2013-9

Force Sensing Surgical Scissor Blades using Fibre Bragg Grating Sensors

Dean Callaghan
Technological University Dublin, dean.callaghan@tudublin.ie

Force Sensing Surgical Scissor Blades using Fibre Bragg Grating Sensors

A thesis submitted to The Dublin Institute of Technology in conformity with the requirements for the degree of Doctor of Philosophy

by

DEAN CALLAGHAN, *BEng.*

Supervisors: Mr. Mark McGrath, Prof. Eugene Coyle and Prof. Gerald Farrell

School of Manufacturing and Design Engineering

College of Engineering and Built Environment

Dublin Institute of Technology

September 2013

Dedicated to:

Catherine, Alex, Elizabeth & Pippa,

the driving forces behind my endeavours.

Abstract

This thesis considers the development and analysis of unique sensorised surgical scissor blades for application in minimally invasive robotic surgery (MIRS). The lack of haptic (force and tactile) feedback to the user is currently an unresolved issue with modern MIRS systems. This thesis presents details on smart sensing scissor blades which enable the measurement of instrument-tissue interaction forces for the purpose of force reflection and tissue property identification. A review of current literature established that there exists a need for small compact, biocompatible, sterilisable and robust sensors which meet the demands of current MIRS instruments. Therefore, the sensorised blades exploit the strain sensing capabilities of a single fibre Bragg grating (FBG) sensor bonded to their surface. The nature and magnitude of the strain likely to be experienced by the blades, and consequently the FBG sensor, while cutting soft tissue samples were characterised through the use of an application specific test-bed. Using the sensorised blades to estimate fracture properties is proposed, hence two methods of extracting fracture toughness information from the test samples are assessed and compared. Investigations were carried out on the factors affecting the transfer of strain from the blade material to the core of the FBG sensor for surface mounted or partially embedded arrangements. Results show that adhesive bond length, thickness and stiffness need to be carefully specified when bonding FBG sensors to ensure effective strain transfer. Calibration and dynamic cutting experiments were carried out using the characterisation test-bed. The complex nature of the blade interaction forces were modelled, primarily for the purpose of decoupling the direct, lateral, friction and fracture strains experienced by the bonded FBG sensor during cutting. The modelled and experimental results show that the approach taken in sensorising the blade enables detailed cutting force data to be obtained and consequently leads to a unique method in estimating the kinetic friction coefficient for the blades. The forces measured using the FBG are validated against a commercial load cell used in the test-bed. This research work demonstrates that this unique approach of placing a single optical fibre onto the scissor blades can, in an unobtrusive manner, measure interblade friction forces and material fracture properties occurring at the blade-tissue interface.

Declaration

I certify that this thesis which I now submit for examination for the award of **Doctor of Philosophy** is entirely my own work and has not been taken from the work of others, save and to the extent that such work has been cited and acknowledged within the text of my work.

This thesis was prepared according to the regulations for postgraduate study by research of the Dublin Institute of Technology and has not been submitted in whole or in part for another award in any Institute.

The work reported on in this thesis conforms to the principles and requirements of the Institute's guidelines for ethics in research.

The Institute has permission to keep, lend or copy this thesis in whole or in part, on condition that any such use of the material of the thesis be duly acknowledged.

Signature Deán Gallagher Date 11th Oct. '13

Candidate

Acknowledgements

First and foremost I would like to express my gratitude to my supervisory team, Mr. Mark McGrath, Prof. Eugene Coyle and Prof. Gerald Farrell for their unwavering input, guidance, patience, insights and positive attitude throughout the duration of this research work. I am eternally grateful to one and all and it has been an honour to work alongside such esteemed colleagues.

I am also indebted to my fellow researchers (past and present) in the DIT Photonics Research Centre. In particular to Ginu Rajan, Sunish Mathews and Yulyia Semenova whom I have worked most closely with throughout this research and other related projects.

I sincerely thank the Head of School of Manufacturing and Design Engineering in DIT, Mr. John Lawlor for endless assistance and support throughout the duration of this research. There was never an obstacle that couldn't be overcome, and always made resources and facilities available when needed to facilitate the research.

I must pay particular thanks to The Head of Research for the College of Engineering and Built Environment Dr. Marek Rebow who is a fantastic inspiration to me as an aspiring researcher. His enthusiasm, dedication and energy have helped foster a great research environment in which to work. Many thanks also to the various post graduate students whom I have the pleasure to share office and lab space with and for providing a stimulating environment in which to work.

Thanks also to the various staff members within DIT who gave their time and assistance, particularly technicians Neil Branigan, Derek McEvoy, Peter O'Farrell and Michael Neary.

I would like to pay tribute to my entire family who have provided immense love, support, understanding and patience throughout this journey. Special thanks to my mother and father for everything down through the years, and particularly to my father who sparked my interest in engineering at a young age.

Finally, I wish to express my sincerest and utmost gratitude to my wife Catherine whose love, devotion, support and encouragement has carried me through this PhD journey. I am eternally grateful for your understanding and tolerance particularly during times of extended absence. To my three children Alex, Elizabeth and Pippa; thank you for reminding me of the important things in life and for providing me with the motivation to continue the journey. I love you all very much.

Acronyms

ASTC	Average Strain Transfer Coefficient
DC	Direct Current
DOF	Degree of Freedom
EFPI	Extrinsic Fabry-Perot Interferometric
ESG	Electrical Strain Gauge
FBG	Fibre Bragg Grating
FEA	Finite Element Analysis
FR	Functional Requirement
FT	Freeze-Thaw
FTS	Force Torque Sensor
GUI	Graphical User Interface
LPG	Long Period Grating
LVDT	Linear Variable Differential Transducer
MEMS	Micro-Electro-Mechanical Systems
MIRS	Minimally Invasive Robotic Surgery
MIS	Minimally Invasive Surgery
MRI	Magnetic Resonance Imaging
MSEN	Modified Single Edge Notch
NOTES	Natural Orifice Transluminal Endoscopic Surgery
PCF	Photonic Crystal Fibre
PET	Polyethylene Terephthalate
P-P	Peak to Peak

PR	Performance Requirement
PVA	Poly Vinyl Alcohol
PVDF	Polyvinylidene Difluoride
SDM	Shape Deposition Manufacturing
TDM	Time-Division Multiplexing
UV	Ultraviolet
VCA	Voice Coil Actuator
WDM	Wavelength-Division Multiplexing

Symbols

C	Blade intersection point
$d\Lambda$	Elastic strain energy
dU	Energy stored in a specimen
$d\Gamma$	Plastic work
E	Young's modulus
F_A	Force applied at scissor handles
F_c	Force at blade intersection point
F_d	Direct force
F_f	Friction force
F_{ff}	Friction and fracture force
F_L	Force on load cell

F_s	Lateral force
I	Second moment of area
J	Fracture toughness
J^*	Effective fracture toughness
k	Calibration constant
L	Blade length
L_c	Length of cut
m	Blade thickness taper ratio
m_o	Strain gradient slope
M_w	Molecular weight
n	Blade width taper ratio
R	Calibration ratio
r_c	Outer radius of Polyimide coating
r_{eff}	Effective radius of adhesive layer (Grooved blade)
r_f	Outer radius of fibre
r_m	Effective radius of adhesive layer
t	Time interval
t_a	Adhesive layer thickness
t_b	Thickness of blade at its base
t_c	Sample thickness
t_{max}	Half the thickness of the blade at its pivot
t_{min}	Half the thickness of the blade tip
t_t	Thickness at blade tip

W	Work done
w	Width of blade
w_g	Distance from cutting face to FBG
x_1	Distance from pivot to strain gauge
x_c	Distance from pivot to blade intersection point
x_g	Distance from pivot to FBG
x_{max}	Point of maximum strain
Xu	Incremental external work done
y_g	Distance from cutting face to centroidal axis
y_{gr}	Width of groove
z_{gr}	Depth of groove

Greek

ϕ	Included angle of blade centrelines
ε	Strain
ε_c	Closing strain
ε_d	Direct strain
ε_f	Friction strain
$\overline{\varepsilon}_f$	Average fibre strain
ε_{ff}	Friction + Fracture strain
ε_o	Opening strain
ε_s	Lateral strain
θ	Included angle of blade cutting edges
μ_k	Kinetic friction coefficient

ν	Poisson's ratio

Subscripts

b	Base
c	Closing
d	Direct
g	FBG
gr	Groove
o	Opening
s	Lateral
surf	Upper surface
t	Tip

Contents

List of Figures

List of Tables

List of Contributions

The primary contribution of this research to the field of sensorised surgical instruments and devices is,

A unique direct interaction-force measurement method for surgical scissor instruments using fibre Bragg gratings as the sensor.

A number of interrelated key contributions to the field are:

i. Measurement of cutting forces using a direct force sensing technique, for the first time, using a FBG sensor bonded to the blades.

ii. A novel strain decoupling method used to determine fracture properties of the material being cut, as well the kinetic friction coefficient between the blades.

iii. Validation of the forces on the blade measured by the FBG against values from a commercial load cell. Results show a close correlation between both.

iv. An analytical model based on double tapered beam theory. This model allows strain distributions to be determined on the blade surface for surface mounted FBG sensors and within the blade structure for embedded FBG sensors.

v. A model and experimental approach for quantifying the affects of adhesive bonding on strain transfer for a partially embedding FBG within the blade.

List of Publications

Book Chapters

Dean Callaghan, Mark M. McGrath, Ginu Rajan, Eugene Coyle, Yuliya Semenova and Gerald Farrell "Analysis of Strain Transfer to FBG's for Sensorized Telerobotic End-Effector Applications" *Advances in Robotic Research. Theory, Implementation, Application.* Springer Verlag, Part 3, Pages 65-75, June 2009, ISBN: 978-3-642-01212-9.

Ginu Rajan, **Dean Callaghan**, Yuliya Semenova and Gerald Farrell "Optical Fiber Sensors and Interrogation Systems for Interaction Force Measurements in Minimally Invasive Surgical Devices" *Smart Sensors for Industrial Applications*, CRC Press, May 2013, ISBN: 9781466568105.

International Refereed Journals

D. Callaghan, Mark M. McGrath, Ginu Rajan, Eugene Coyle, Yuliya Semenova and Gerald Farrell "Investigation and Experimental Measurement of Scissor Blade Cutting Forces using Fibre Bragg Grating Sensors" *Smart Mater. Struct. Journal,* IOP science, Vol. 20, p. 105004, 2011.

D. Callaghan, M.M. McGrath and E. Coyle, "A Force Measurement Evaluation Tool for Telerobotic Cutting Applications: Development of an Effective Characterization Platform " *Int. J. Math Phys. and Eng. Sci.,* vol. 1, pp. 144-150, 2007.

G. Rajan, **D. Callaghan,** Y. Semenova, and G. Farrell, "Photonic Crystal Fiber Sensors for Minimally Invasive Surgical Devices," *Biomedical Engineering, IEEE Transactions on,* vol. 59, pp. 332-338, 2012.

G. Rajan, **D. Callaghan**, Y. Semenova, M. McGrath, E. Coyle, and G. Farrell, "A Fiber Bragg Grating-Based All-Fiber Sensing System for Telerobotic Cutting Applications," *Sensors Journal, IEEE,* vol. 10, pp. 1913-1920, 2010.

Conference Proceedings

D. Callaghan, Mark M. McGrath, Ginu Rajan, Eugene Coyle, Yuliya Semenova and Gerald Farrell, "Comparing FBG and PCF Force Sensors in a Laparoscopic Smart Surgical Scissor Instrument" *Proceedings of the Joint Workshop on New Technologies for Computer/Robot Assisted Surgery,* Graz University of Technology, July 2011.

D. Callaghan, M.M. McGrath and E. Coyle, " Force Measurement Methods in Telerobotic Surgery: Implications for End-Effector Manufacture," *25th International Manufacturing Conference (IMC25),* pp. 389-398, Dublin Institute of Technology, 2008.

D. Callaghan, M.M. McGrath and E. Coyle, "Measurement of Surgical Instrument-Biological Tissue Interaction Forces: Sensor Requirements" *Proceedings of the Fourteenth Annual Conference of the Bioengineering in Ireland,* pp. 53, Sligo, 2008.

D. Callaghan, M.M. McGrath and E. Coyle, "Comparison of Force Sensing Technologies for a Haptic Feedback Application" *Proceedings of the Northern Ireland Biomedical Eng. Society 28th Annual Spring Meet,* P. 10, University of Ulster, 2008.

D. Callaghan, M.M. McGrath and E. Coyle, "Force Measurement & Evaluation for Surgical Cutting Applications: Development of an Effective Characterization Testbed" *Proceedings of the 11th Annual Sir Bernard Crossland Symposium and Postgraduate Research Workshop*, pp. 89–107, University of Limerick, 2008.

G. Rajan, **D. Callaghan,** Y. Semenova and G. Farrell, **"**Miniature Temperature Insensitive Fiber Optic Sensors for Minimally Invasive Surgical Devices", *21st International Conference on Optical Fiber Sensors,* Ottowa, 15-19 May 2011.

S. Mathews, **D. Callaghan,** Y. Semenova, G. Rajan, G. Farrell : "Photonic Crystal Fiber Strain Sensors for Laparoscopic Surgical Devices", *Proc. Photonics Global Conference, Singapore,* 13-16 Dec. 2012.

S. J. Mathews, Y. Semenova, G. Rajan, **D. Callaghan,** and G. Farrell, "Temperature Insensitive Miniature Photonic Crystal Fiber Interferometric (PCFI) Strain Sensors," in *International Conference on Fibre Optics and Photonics*, p. T2C. 4., Dec. 2012.

Chapter 1

Introduction

For centuries open surgery was the standard for performing operations on patients. This technique is traumatic for the patient, results in significant scarring and leads to lengthy and costly recovery times. In the last several decades, minimally invasive surgery (MIS) has revolutionised the way surgeries are performed and has addressed the demand for smaller incisions and shorter recovery times. Despite the obvious advantages that MIS has over open surgery there are a few significant drawbacks to the technique. It is worth noting that the advantages associated with MIS are primarily to the benefit of the patient while almost all the disadvantages affect the surgeon [1]. These disadvantages include, but are not limited to;

- Lost hand-eye coordination
- Increased operating time
- Limited degrees of freedom (DOF)
- Increased training time required
- Loss of tactile and force feedback to the user

Technological advances in MIS have significantly progressed in the past 20 years [2] to the stage where a teleoperated MIS approach is now being adopted worldwide. This telemanipulation technique referred to as minimally invasive robotic surgery (MIRS) allows the surgeon to regain full access to the operating field and overcome most of the disadvantages associated with conventional MIS. However, the mechanically decoupled arrangement of surgeon and patient means that there is a total absence of force and tactile (haptic) feedback to the surgeon, to an even greater extent than conventional MIS [3]. A schematic of a typical MIRS master-slave system arranged as a telerobotic network is shown in Figure 1-1.

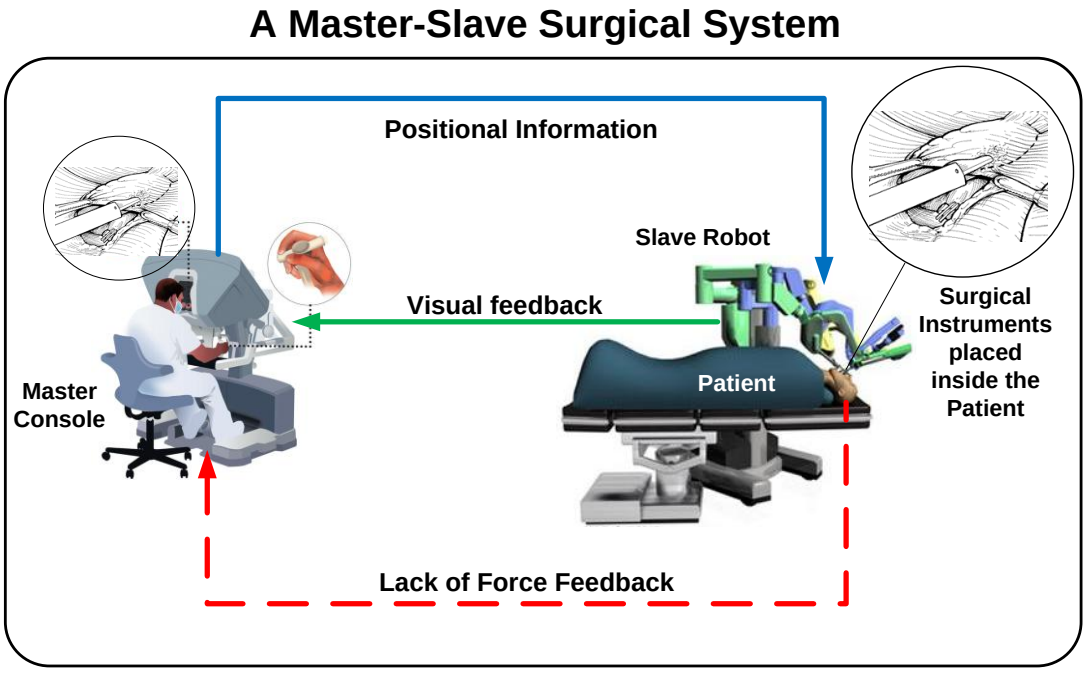

Figure 1-1 A master-slave surgical system showing information flow paths

The function of each subsystem is as follows;

1. The slave robot is the Teleoperator which manipulates surgical instruments by mimicking the movements of the surgeon's manipulators [4]. Sensorised instruments measure the interaction forces arising during surgical tasks and transfer this force data to the master console.
2. The master console is the interface between human and machine which reproduces the measured interaction forces to the user via a haptic display. The haptic display consists of motorised manipulators that provide resistance to the user's movement. This resistance is appropriately scaled to the forces acting on the manipulated instrument at the slave console.

The surgeon views the internal operative field through images from an endoscope (Figure 1-2) which also forms part of the slave console[1].

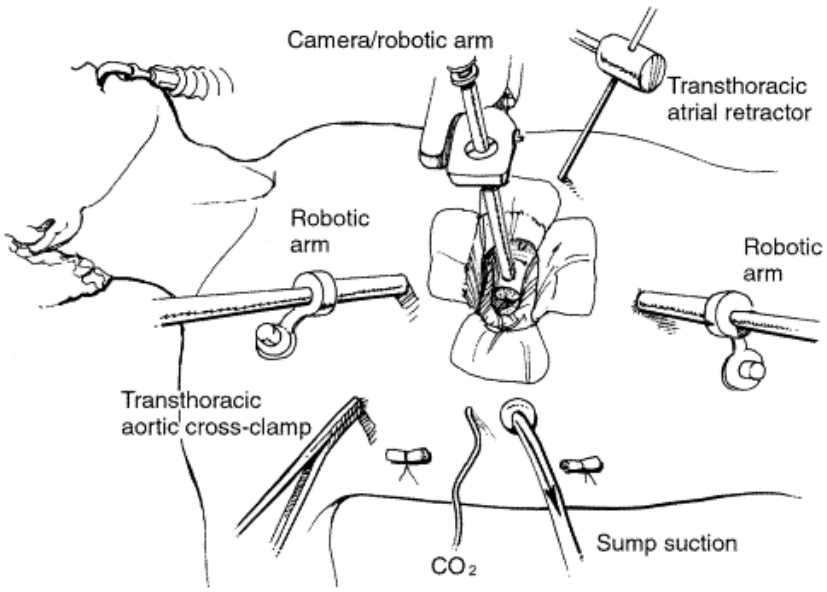

Figure 1-2 A view of a typical setup for robotic mitral valve repair showing the camera (Endoscope), robotic arms (instruments) [5]

[1] Typically two or more manipulator arms carry actuated and sensorised instruments; a third arm controls the endoscopic camera.

In some cases the measured force information can also be viewed on the graphical display either as standalone graphical force information or in conjunction with forces reproduced via the haptic display [6, 7]. However, the challenge that still remains for all MIRS systems is achieving reliable and accurate measurement of the interaction forces that arise between instrument tip and the tissue being palpated, cut, grasped or punctured by that instrument [8-10].

1.1 Motivation for the Research

Many studies have been carried out to develop methods and techniques that can determine forces acting on surgical instruments during surgical procedures [11-15]. The reasons for obtaining such force data vary. In some cases there is a need to provide such force information to the user either visually or mechanically via a haptic interface. Other studies have attempted to use the force information to ascertain whether or not the measurement of such forces is necessary or beneficial to the user. Additionally, researchers who focus on the development of reality-based or empirically-derived models of instrument-tissue interaction require *in-vivo* force information for the purpose of model validation. It is widely acknowledged that the ideal method of collecting such force data is to locate sensors close to the site of force generation. However, this approach comes with many associated challenges, specifically; size constraints, sterilisibility, biocompatibility, mechanism friction and backlash among others. To date, a solution has not been found that meets the requirements for instruments that have the capability to measure tool-tissue interaction forces such as cutting,

grasping and palpation [8, 9, 11]. Therefore, this work proposes the use of a novel force sensing technique employing a fibre Bragg grating (FBG) which will measure the forces arising on a surgical scissor blade for future MIRS applications.

1.2 Thesis Aims and Objectives

1.2.1 Research Aim

This thesis presents an analysis of an unobtrusive and compact direct force sensing scheme incorporating FBGs implemented into surgical scissor blades to quantify instrument-tissue interaction forces during operation for the purpose of force reflection and tissue property identification. In this context, the primary aim of this research work is;

To investigate and experimentally characterise a compact FBG-sensorised scissor blade end-effector as an integrated, direct force measurement solution to the problem of obtaining interaction force values generated at the blade-tissue interface.

1.2.2 Research Objectives

This thesis proposes the integration of FBG sensors onto the surface of a surgical scissor blade to facilitate force measurement during cutting. Parameters such as effective strain transfer from blade to FBG and deciphering the complex force components that arise at the blade-tissue interface will strongly influence the effectiveness of the proposed sensorised blades. Therefore, the objectives of this research are;

i. To design and build a characterisation test-bed that will facilitate the measurement and recording of blade-tissue cutting information from a pair of surgical scissor blades.

ii. To investigate and characterise the nature of the forces generated at the instrument-tissue interface during cutting.

iii. To ascertain the nature and magnitude of strain profiles experienced by the blade onto which a sensor will be placed.

iv. To analyse the factors influencing strain transfer from the blade structure to the FBG core for surface-mounted and embedded configurations.

v. To examine theoretically and experimentally the kinetic friction coefficient between the blades during an empty opening and closing cycle.

vi. To determine the fracture properties of test samples using the proposed force sensing scheme.

vii. To validate the results obtained from the FBG sensor for force and fracture toughness against a commercial load cell.

1.3 Research Methodology

This section provides a brief overview of the methodology adopted in this research in the characterising of a FBG-sensorised scissor blade. The methodology is summarised within Figure 1-3 which outlines the research hypothesis of this research followed by a number of key research objectives.

This is followed by the methodology which outlines the steps taken in the key stages that will facilitate the achievement of the research objectives.

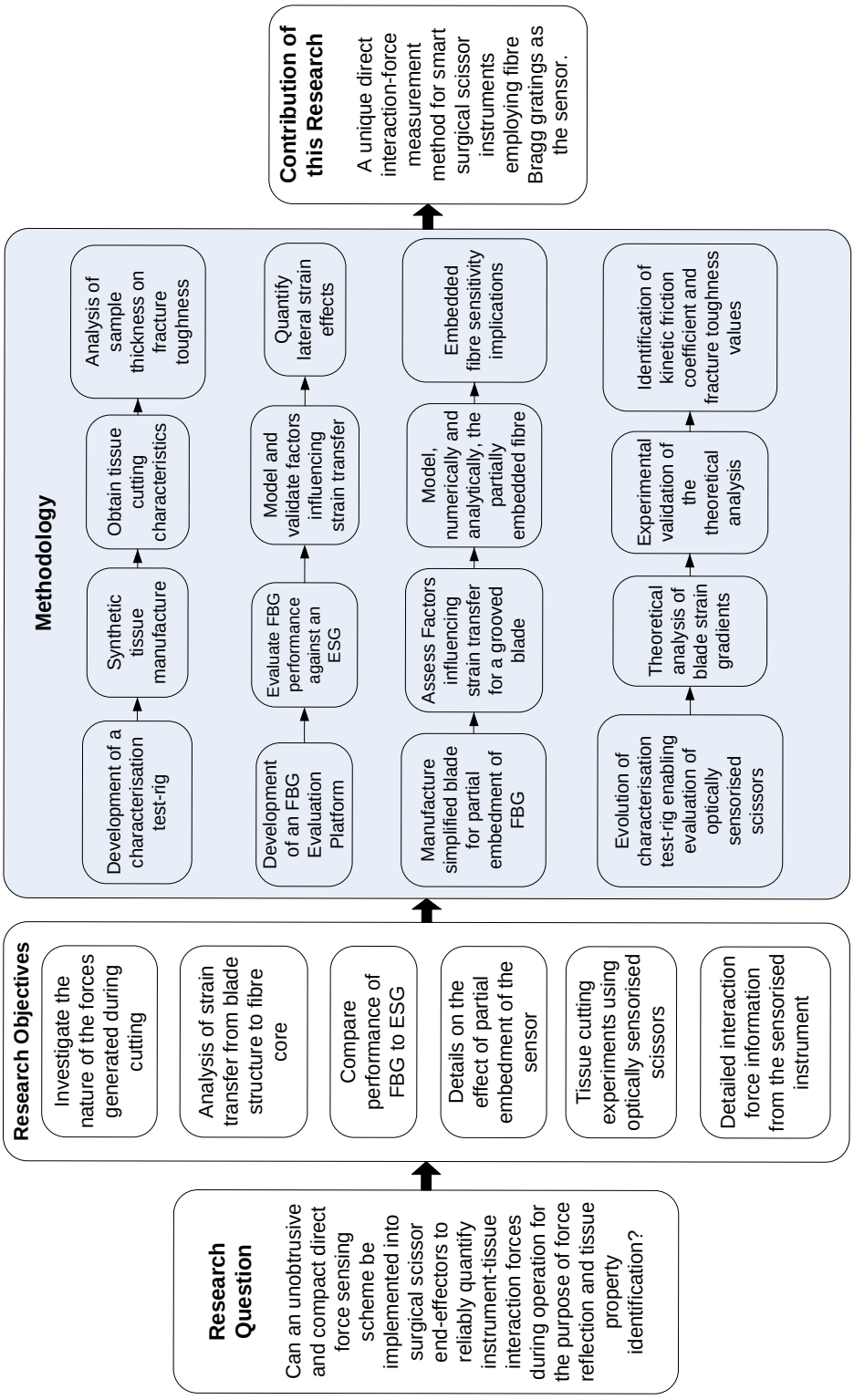

Figure 1-3 Outline of research methodology

1.4 Organisation of the Thesis

The contribution of this thesis will be the development of a unique direct interaction force sensing method for sensorised surgical scissor instruments employing a FBG optical fibre as the sensor. Chapter 1 outlines the aims, objectives and methodology employed for this particular research work.

Chapter 2 discusses the general area of minimally invasive robotic surgery and highlights, in the context of the force measurement problem, how this research work will contribute a solution to the problem. Justifications for the selection of a direct force sensing technique employing FBGs have been laid out. Moreover, the requirements for a direct force measurement scheme of this type will be considered.

In Chapter 3 an investigation into the nature of friction and fracture forces generated during the cutting of synthetic tissue samples is conducted. The development and calibration of the characterisation test-bed used is discussed. Results obtained from the samples are analysed and the fracture toughness determined. A closer examination of the blade structure is carried out to ascertain the sensitivity expected from a directly sensorised blade with an integrated electric strain gauge sensing element.

Chapter 4 details the factors that influence the transfer of blade strain from the blade surface through to the fibre via an adhesive bonding layer. Numerical and analytical modelling of the effect of adhesive bond length and thickness was carried out and the results compared. The results from an experimental investigation into strain transfer are also presented and used in the validation of the theoretical results. Unique details on the effect of partially embedding the

FBG force sensor within the structure of the blade element are all presented. Details on the change in sensitivity of the combined blade-FBG unit for the partially embedded configuration are compared to that of a surface mounted arrangement. The effects of lateral blade loading on the integrated FBG sensor are also analysed and the errors due to lateral loading quantified in this chapter.

Chapter 5 documents the evolution of the characterisation test-bed to include a FBG sensor attached to the surface of the blade for the purpose of measuring the forces arising at the blade-tissue interface. A detailed theoretical model of the strains occurring at the FBG location during lateral and direct loading of the blade is presented. Details are given on a model that shows how the use of a single FBG sensor in the current configuration can enable the kinetic friction coefficient of the blades to be obtained. The limitations of the theory are also discussed. Dynamic experimental results obtained from the sensorised blades are presented and used to validate the theory.

In Chapter 6 presents the conclusions from the analysis carried out on the sensorised blades as well as the limitations of this approach. The major contribution of this research is also presented in this chapter followed by a discussion on the future research stemming from this work.

Chapter 2

State of the Art Review

2.1 Introduction

Presented in this chapter is a concise review of MIRS systems with a specific focus on the end-effectors that are in direct contact with tissue and consequently provide the motivation for this research work. An overview of the various state of the art sensing modalities available to address the lack of force feedback is carried out. Implementation of these sensing modalities can be achieved at different locations on the surgical end-effector units; hence, the advantages and disadvantages of these different locations are discussed. The sensor requirements for an effective direct force sensing scheme are also outlined.

2.2 MIRS – Current Challenges

Minimally invasive surgery (MIS) is an operating technique established in the 1980's. It differs from open surgery in that long slender surgical instruments (ranging from 5 to 14 mm) are inserted into the patient's body through small incisions in the skin. A trocar is placed in the incision to guide the slender

surgical instrument into the abdominal cavity Figure 2-1. The abdominal cavity is filled with gas to expand the volume of the cavity allowing greater freedom of movement of the surgical instrument. This allows the surgeon to manipulate and treat organs, muscle and tissue within the body while observing the images on a 2-D monitor. Most trocars are equipped with a valve that prevent the outflow of gas from the abdominal cavity [16].

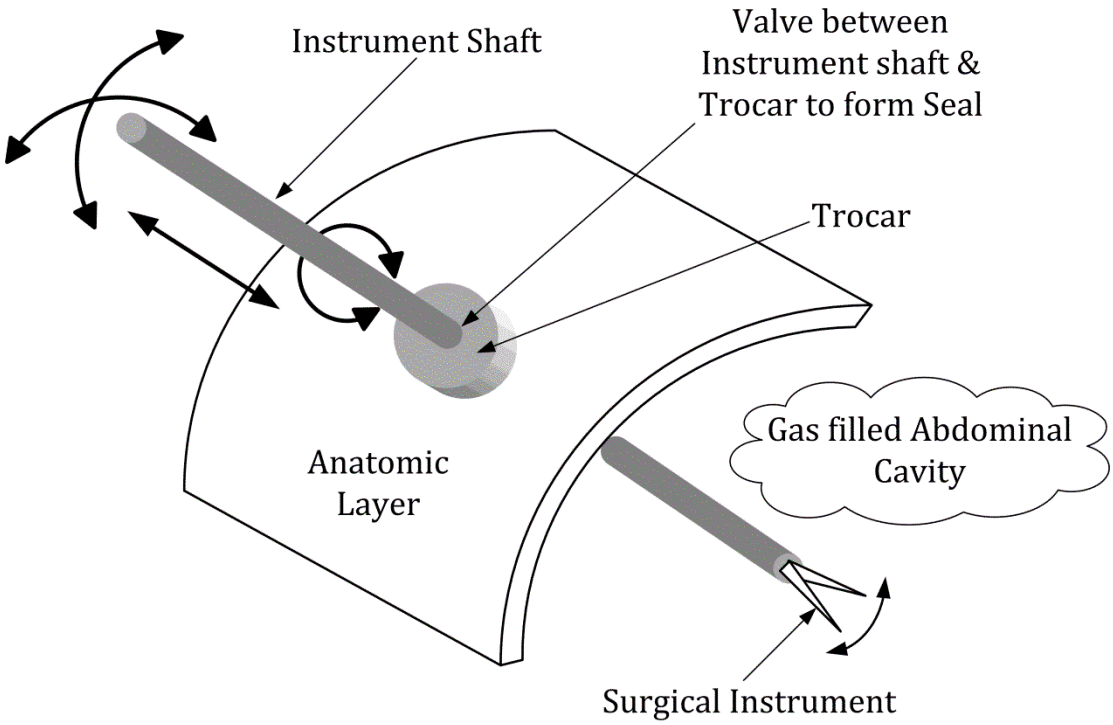

Figure 2-1 An MIS instrument guided into the gas filled abdominal cavity via a sealed trocar which prevents gas leakage.

The primary advantages of this technique include smaller incisions, shorter hospital stays and lower risk of infection. Convalescence is also significantly reduced resulting in better clinical outcomes [11]. However, the disadvantages associated with this technique include the loss of hand-eye coordination,

reduced kinaesthetic and tactile feedback and limited degrees of freedom (DOF) within the abdominal cavity. Moreover, the trocar, abdominal wall, and organs within the abdomen all exert forces on the instrument that result in unrepresentative forces, felt by the user, at the hand-instrument interface. The trocar in particular generates high frictional forces resulting from the instrument shaft rubbing against the valve rubbing while translating along the shaft length and rotating about its longitudinal axis [16, 17].

In the 1990's development began on minimally invasive robotic surgical (MIRS) systems. The first robotic surgery was carried out in 1985 [12] and since then there has been a steady increase in robotic-based surgical systems. Robot-assisted surgery has revolutionised the way in which surgeons carry out minimally invasive surgical procedures. It assists surgeons in overcoming the drawbacks associated with traditional MIS procedures such as hampered dexterity, reduced accuracy, and a loss of 3-D visualisation [12]. As well as addressing the disadvantages of MIS techniques robotic assistance offers new advancements in areas such as; provision of additional degrees-of-freedom (six instead of four), tremor filtering and scaling of motions, particularly in the field of microsurgery [13]. Despite all the advantages, progress in the field of robotic assisted surgery is limited by an unresolved problem; the lack of haptic (force and tactile) feedback to the user [14]. One of the most widely used commercially available minimally invasive robotic surgery (MIRS) systems is the daVinci™ from Intuitive-Surgical® Inc [15]. This system has been evaluated mainly in the field of minimally invasive heart surgery, but further applications will be

established in future. This type of system offers control over tool position/displacement only; there is no force measurement at the slave side as well as no haptic feedback at the master console [15]. This lack of force feedback leads to the difficult task for the surgeon of interpreting organ deformation as a measure of the forces at the slave side. This in turn is quite taxing on the surgeon, which can lead to reduced levels of concentration and increased fatigue. Complications such as accidental puncturing of blood vessels or tissue damage can also be attributed to lack of haptic feedback [18]. There is little doubt that the inclusion of force feedback in a MIRS system leads to improved performance over a system without haptic feedback. Previous work by Tavakoli *et al* [19] has looked at a blunt dissection task where it was found that force feedback reduces the number of errors that lead to tissue damage by a factor of three. A series of experiments on suture tying were carried out by Guthart *et al* [15], with and without, haptic feedback. These experiments indicated conclusively that haptic feedback is advantageous, and therefore desirable, in robot-assisted surgical systems. Thus, for many dexterous manipulations such as cutting, grasping, suturing or dissection, force sensing needs to be incorporated into the surgical instruments being used.

2.3 Feedback Modalities

The term haptic feedback has been broadly defined by Okamura as touch feedback which may include kinaesthetic (related to force and position) and cutaneous (tactile feedback related to the skin) [14]. Kinesthetic feedback is

perceived through direct contact with the object and gives a measure of the forces applied to the patient or tissue by surgical instruments. During open surgery tissue features can be assessed quickly by the surgeon owing to unrestricted access to the operation site. A functional schematic of feedback modalities in open surgery by Schostek [20] is shown in Figure 2-2. It illustrates clearly the feedback and feedforward paths between the surgeon and tissue being manipulated by surgical instruments. Modern MIRS systems are equipped with, and even enhance, visual feedback to the surgeon through the use of high definition 3D depth perception via screens within the user console.

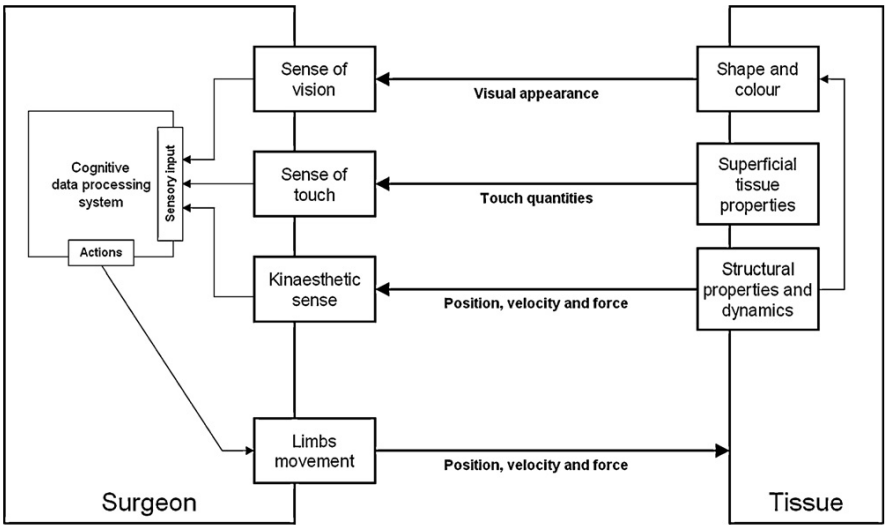

Figure 2-2 Multimodal feedback in open surgery[20].

The lack of force feedback in MIRS is considered to be a safety risk because it can result in accidental tissue damage [20]. Therefore, the majority of research regarding feedback in robotic surgery is aimed at restoring kinesthetic feedback by adding force and torque sensors to the robotic instruments. Kinesthetic

feedback, for most MIRS applications such as knot tying, is sufficient. This is due to the fact that kinaesthetic feedback allows the detection of position, movement and bulk forces acting on the end-effector [21, 22] during interaction with the suture or the tissue being manipulated. Other parameters such as contact force location and pressure distribution information (tactile feedback) may not be necessary to carry out most surgical tasks [23, 24]. However, palpation of tissue is noted as one particular task where the inclusion of tactile feedback in the MIRS system is particularly relevant [25, 26].

Other feedback modalities which have been considered when attempting to measure the interaction forces between instrument and tissue include visual feedback, virtual fixtures and auditory feedback (sensory substitution methods). A novel approach by Fischer *et al* [27] simultaneously measured the force applied by a grasper as well as the tissue blood oxygenation saturation as a means of limiting the maximum force being applied to the tissue. A GUI presents the data to the user in the form of coloured circles which change colour in proportion to the applied force. Reiley *et al* [28] investigated virtual fixtures which is a method of preventing the user applying excessive forces or entering forbidden regions during a surgical procedure by physically restraining the instrument tip. Thorough robotic modelling and control approaches are required for the accurate placement of virtual fixtures. Current research is investigating the uncertainty involving robot position relative to anatomical structures due to unmodelled dynamics [28]. The effects of substituting direct haptic feedback with auditory cues were studied by Kitagawa *et al* [29]. This work concluded

that, although auditory cues gave additional support to the surgeon, it was suggested that such continuous auditory feedback might be disruptive and confusing in an already noisy operating environment.

It is reported that, despite attempts at incorporating feedback to the end-user using virtual fixtures or auditory cues, the most reliable approach is that involving the incorporation of sensors into the tip of the surgical instrument [29]. Such an approach is particularly pertinent while manipulating or handling soft tissues, as the modelling, estimation and subsequent compensation of soft tissue mechanical behaviour during intraoperative conditions is challenging [30, 31].

The direct force measurement approach forms the basis of this research work where we investigate the use of an optical sensor as a means of detecting the forces acting on the tip of a surgical device during operating. The reasons for adopting the direct force sensing approach over indirect force sensing alternatives are;

- Direct force measurement instead of a force estimation
- Forces on blades/jaws are isolated from all other forces
- Mechanical properties of the tissue can be determined
- Fast response without delays or sluggishness
- No complex spatial modelling required
- Integration of real-time end-point sensing into intelligent control schemes [32].

2.4 Force Sensor Locations

The realisation of a successful force feedback scheme requires that the sensing elements must form an integral part of the instrument. Commercially available force sensors are very effective for measuring forces and torques in many MIRS systems, but the surgical environment places severe constraints on size, geometry, cost, biocompatibility, and sterilisability. Although it is difficult to add force sensors to existing robotic instruments some researchers have had success on this front by creating specialised grippers that can attach to the jaws of existing instruments [1, 33, 34]. The surgical environment is a challenging environment in which to sense interaction forces. Sensors would ideally be placed in locations on the robot outside the body of the patient to simplify system design. However, this is problematic for most surgical robots since force sensors placed outside the patient's body will acquire force data not only from the delicate interactions between the instruments and tissue, sutures, etc., but also from sources that are not directly relevant to the surgical task [35]. For example, there are significant friction, body wall forces, and torques applied to the instrument at the insertion point to the patients abdominal cavity. These undesirable forces are large enough to mask the instrument-tissue interaction forces that should be displayed to the surgeon. According to Okamura [35] force sensors would ideally be placed in, or near, the tip of the instrument being placed inside the patient. Additionally, the materials of the sensor must withstand harsh sterilisation procedures and because surgical instruments interact with warm tissues and fluids, sensors must be insensitive to changing

temperature. According to a state of the art review in force and tactile sensing for MIS by Puangmali *et al* [10] there are four location where the sensing elements can be placed on a MIRS laparoscopic instrument (Figure 2-3);

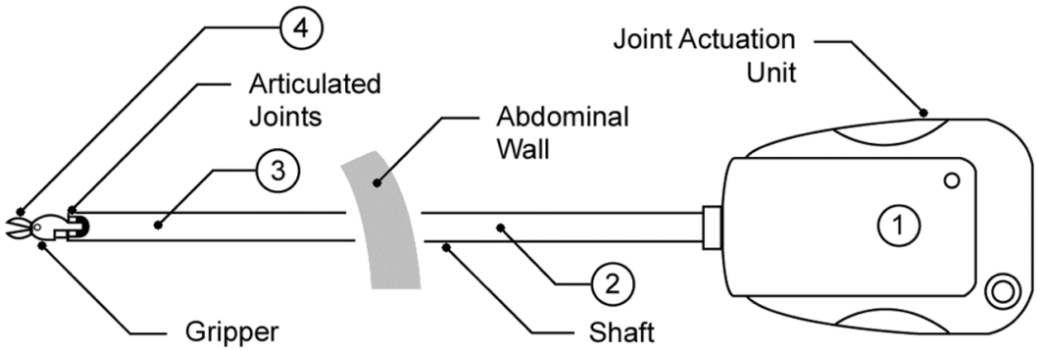

Figure 2-3 Possible sensor locations on a MIRS laparoscopic instrument [9]

1. Near or at the instrument actuation mechanism.
2. Instrument shaft outside the patient's body
3. Instrument shaft inside the patient's body
4. At the instrument tip.

These four sensor locations can be classified into two categories as follows,

- Direct force sensing – sensors placed inside the body on or near to the instrument tip
- Indirect force sensing – sensor placed outside or inside the body but not on the instrument tip.

The advantages and disadvantages of indirect and direct forces are discussed in the sections that follow.

2.4.1 Indirect Force Sensing

One approach to overcoming the adverse frictional effects associated with indirect force sensing (Section 2.2) is being investigated by a number of groups [36-38]. This method involves the use of what is commonly termed "the overcoat method". This is a double barrel arrangement allowing the trocar to be fed into the abdominal cavity, unimpeded by friction, abdominal wall forces [35] and the fulcrum leverage effect [39] at the entry point on the patient. The force sensors are placed outside the abdominal cavity (Figure 2-4) and measure interaction forces between instrument and tissue resulting from pulling, pushing, probing and palpation. Shimachi *et al* [36, 40, 41] developed a system using the overcoat method which can be integrated into the daVinci® robotic surgical system.

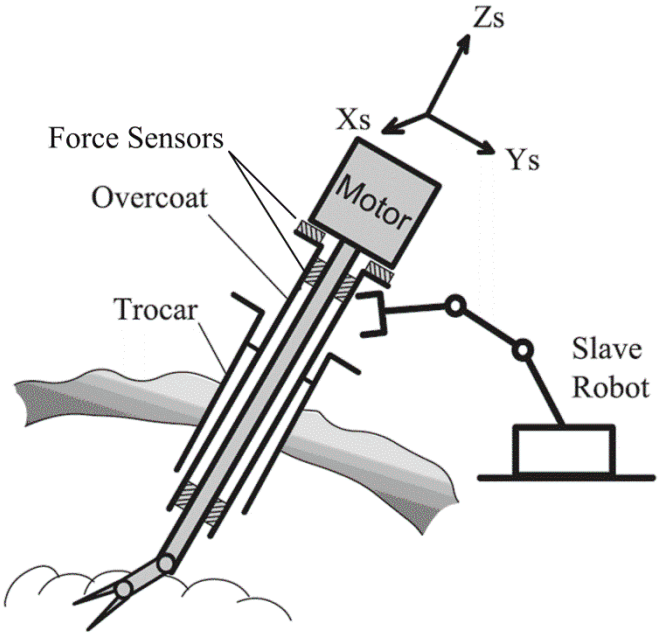

Figure 2-4 Overcoat method of force sensing used by Shimachi et al [40]

However, the total force sensing error is estimated to be 0.5 N as a result of the deformation of the adaptor frame supporting the motion drivers. Studies were also carried out by this group which used accelerometer measurements to cancel out the adverse inertial and gravitational effects of the motion drivers/instrument mass along the axis of the trocar. This method does not consider the grip forces at the jaws of the instrument.

Zemiti *et al* [37] have also investigated the overcoat method; a 6-axis force/torque sensor, having a force resolution of 0.002 N in three dimensions and torque resolution of 25 μNm about the *x,y* and *z*-axes, is mounted outside of the abdominal cavity. Experimental results highlight the robot's potential for the measurement of contact forces at the distal end without being corrupted by the friction between the instrument trocar and the passive guide. Grasping forces are not measured or controlled as the robot currently consists of a manually controlled grasper.

Alternatively, Dobblesteen *et al* [42] estimated the forces arising at the tip of a grasper by carrying out a kinematic analysis of the relationship between the grasper handles and the tip. Results showed a good correlation between the actual tip grasping forces and the estimated tip forces measured at the handles. However, it was concluded that issues with mechanism friction and consequently hysteresis within the actuation mechanism needed to be addressed to improve the method adopted.

2.4.2 Direct Force Sensing

An alternative means of sensing the interaction forces at the instrument-tissue interface is to locate the force transducers at the distal end either close to, or on, the instrument tip. There are two types of force that require measurement at this point, interaction/manipulation forces and grasping/cutting forces. Kuebler *et al* [3] have developed a six-axis resistive-based force/torque sensor utilising a Stewart Platform arrangement which is placed between the gripper and the cardanic joint. Results have shown that the sensor can provide realistic kinaesthetic feedback of the remote interaction forces. The sensor can handle manipulation forces up to 20 N with a resolution of 0.25 N in the z-direction and 0.05 N in the *x* and *y*-directions. The force-torque sensor (FTS) does not cater for the measurement of the gripping forces, this being facilitated independently through the use of a uniaxial sensor.

The most suitable location for the force transducer is on the instrument tip allowing for direct measurement of the grasping forces and the interaction forces, without frictional and transmission disturbances. However, this is technically the most challenging location for placement of a force transducer owing to size restrictions. Other issues include the cost of the sensor as well as preservation of the design so as to ensure functionality is not compromised [3].

A number of different sensing technologies are currently being investigated for suitability as direct force sensing transducers. Tholey *et al* [43] attached a flexible resistive element on to a grasper for the measurement of forces normal

to the gripper surface. During calibration, the arrangement exhibited nonlinear characteristics as well as significant hysteresis up to an applied force of 13 N.

A grasper catering for the measurement of forces being applied in 3-DOFs has been developed by Fischer *et al* [44]. The gripper was manufactured from 2024-0 aluminium alloy instead of stainless steel to increase sensitivity, while strain gauges were bonded on to the gripper for force measurement. The measured forces were displayed to the user via a haptic interface using visual indicators as a measure of the applied force. All electrical components in the device were coated with an appropriate silicon epoxy to ensure biocompatibility as well as sterility. This method does not allow a standard autoclave sterilisation protocol to be used and hence the instrument is sterilised using hydrogen peroxide.

A study into a force reflection scheme by Hemert *et al* [45] found that the forces exerted on tissue by the grasping tips of a pair of forceps should be measured with sufficient accuracy if a bilateral position-force control scheme is to be implemented to control the master-slave system. It was noted that, due to several nonlinearities within the forceps, the force measurement at the handle is less accurate than measurements at the tip. They concluded that an optical force sensor was required to measure the forces at the tip in a safe manner without the influence of nonlinearities such as friction and mechanism backlash.

2.4.3 Benefits of Direct Sensing

It has been discussed in Section 2.4.1 that for indirect force measurement schemes the quality of the estimated forces at the distal end is degraded as a

result of frictional effects, gravity and the inertia of mechanical components. Many research groups have indicated that the ideal location for force sensor placement is as close as possible to the site of interaction [10, 43, 46-48], which for MIRS is at the instrument tip. This implies that augmented instruments employing the direct force sensing method are the most appropriate for accurate measurement of complex instrument-tissue cutting forces. Another benefit of accurate real-time direct force measurement is that the data collected from these instruments is expected to yield more accurate models for surgical simulators used in surgeon training. This can be attributed to the fact that force information measured is a true reflection of the forces exerted on the instrument tip, unmasked by fulcrum friction forces [16, 17]. The benefits provided by a direct force sensing method provide the basis for this thesis where the overall aim is to develop sensorised scissor blades that can detect complex cutting forces at the blade-tissue interface and enable the fracture properties of the tissue be estimated.

2.5 Sensorised Surgical Instruments

The geometries of a range of surgical instruments have been adapted into the design of surgical instruments specifically for use in MIRS. Among these are graspers, forceps, scissors and scalpels, some of which can come with cauterisation capability. Many research labs have explored the possibility of sensorising graspers and forceps [43, 49-51] for the purpose of measuring grip forces occurring between the tips. Scalpels and knives have also been sensorised

to measure multi-axis interaction forces [52, 53] enabling direct haptic feedback during an operation. Limited work has been carried out to date on sensorising scissor blades for acquiring interaction cutting forces during operation.

2.5.1 Surgical Scissors

Scissors represent an indispensable tool for any surgical discipline, in medical practices no less than in clinical departments. It is probably safe to say that among all surgical instruments, scissors are used most frequently – prior, during, and after the operation. Haag *et al* [54] reported that there are few better alternatives when it comes to transecting or dissecting tissue or cutting sutures or any other kind of auxiliary materials. Scissors have been the traditional tool of surgeons for dissection in conventional surgery and have maintained an active role in laparoscopic surgery. This can be attributed to their precise operator-determined action, safety, and low price in comparison with other dissection techniques. Dissection is regarded as a necessary component of many surgical procedures carried out using open, minimally-invasive, or robot-assisted operating techniques. The two-handed scissors-atraumatic forceps technique represents the mainstay of complex laparoscopic surgical dissection [55]. Surgical dissection and transection using scissors are integral to many of the most frequently performed surgical interventions such as adrenalectomy, cholecytectomy, gastric bypass, heller myotomy [56] and prostatectomy [57].

Sharp dissection implies the use of concentrated effort/energy on a relatively small area of tissue to achieve separation with little disruption to surrounding

tissue. This is most readily achieved by dividing homogenous tissue at right angles to lines of tension. Blunt dissection on the other hand separates bulk tissues ideally between tissue cleavage planes [55]. Properly used, scissors stabilise flaccid tissues between the blades during cutting and provide excellent control over both depth and direction of incision. Observations by Mahvash *et al* [58] relating to how surgeons use scissors show that the cutting blades rarely open beyond an angle of 20° and never close completely. Rather, they close the blades to the point where they feel the cut ends which is not when the blades are completely closed as scissor blades rarely taper to a point at their tip. Making small cuts over this small angular region provides the surgeon with a greater sense of feeling and control particularly during delicate cutting procedures.

2.5.2 Previous Studies of Sensorised Scissors

A study by Mahvash *et al* [59] modelled the forces generated on a pair of a Metzanbaum scissor blades based on empirical data collected from a test apparatus. The test apparatus had a load cell placed at the scissor handles but not directly on the blades themselves. A load cell at the scissor handles was sufficient for this particular study as the aim was to measure the forces experienced at the scissor handles. The measured force data was then used to develop cutting models for a virtual haptic interface.

Yang *et al* [60] carried out a study in which a laparoscopic scissors was adapted to measure cutting forces while cutting arterial wall tissue. A force sensor was attached to one of the scissor handles and measured the forces occurring at the

handle. This indirect force measurement method used by Yang *et al* [60] is sufficient for measuring forces on the instrument handle but did require modelling of the linkage mechanism in order for the true forces occurring on the blades to be determined. Changes in the linkage mechanism with time due to changes in frictional resistance and backlash would clearly affect this model and consequently compromise the accuracy of the cutting force values obtained. It is argued that a direct force sensing approach where a suitable sensor formed part of the blade element would eliminate these drawbacks and allow unhindered direct force measurements to be taken.

A study by Trejos *et al* [61] investigated the tool-tissue interaction forces required to manipulate tissue during natural orifice transluminal endoscopic surgery (NOTES). The aim of the study was to measure typical interaction forces acting on the NOTES instruments (grasper and scissors) while performing in-vivo abdominal surgery. To measure the interaction forces, researchers opted for a direct sensing approach, by attaching small strain gauges to the scissor and grasper instruments close to (but not on) the gripper and blades (Figure 2-5). In the case of the grippers, the purpose of the strain gauges was to measure interaction forces perpendicular to the plane of the strain gauges during tissue manipulation. In the case of the scissors, the gauges were used to measure the forces arising during positioning of the instrument but not the forces produced during cutting. It is our view that with suitable miniature sensing technology a similar study could be carried out to measure the cutting forces experienced by the blades during in-vivo abdominal surgery using NOTES. Images from the

Trejos study showed that the scissor blades were approximately 3 mm in length and consequently would require very small narrow sensors to be attached to the blade surface.

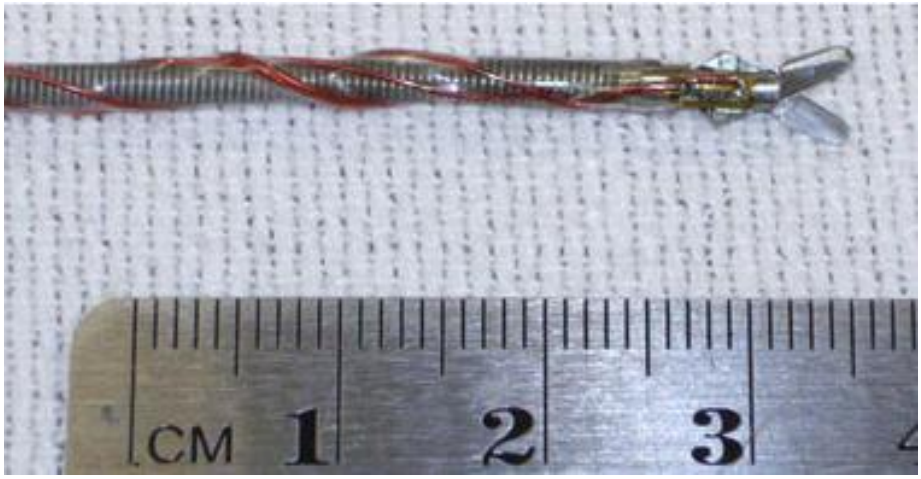

Figure 2-5 Sensorised NOTES scissors [61]

Fundamentally, sensorising scissor end-effectors, using a direct force sensing method, for use in MIRS, NOTES or indeed traditional MIS will bring a number of benefits to the surgeon during operation such as;

- Indicating to the surgeon, with a restricted view of the operating site [61], that an actual cut has been made.
- The accumulation of real-time in-vivo cutting force data to facilitate the creation and validation of soft tissue virtual simulation models.
- Enabling detection of blade slippage during cutting indicating blade bluntness and consequent tissue damage.

- Enabling the collection of in-vivo cutting force information for the purpose of estimating material mechanical properties such as fracture toughness.

2.6 Fracture Toughness

Fracture toughness is a material property that indicates a material's resistance to fracture propagation upon loading [62]. Standard engineering tests used to measure fracture toughness classify fracture into three modes as illustrated in Figure 2-6. Mode I is an opening tensile mode where the crack surfaces move directly apart. Mode II is a sliding (in-plane shear) mode where the crack surfaces slide over one another perpendicular to the leading edge of the crack. Mode III is a tearing (antiplane mode) where the crack surfaces move parallel to the leading edge of the crack.

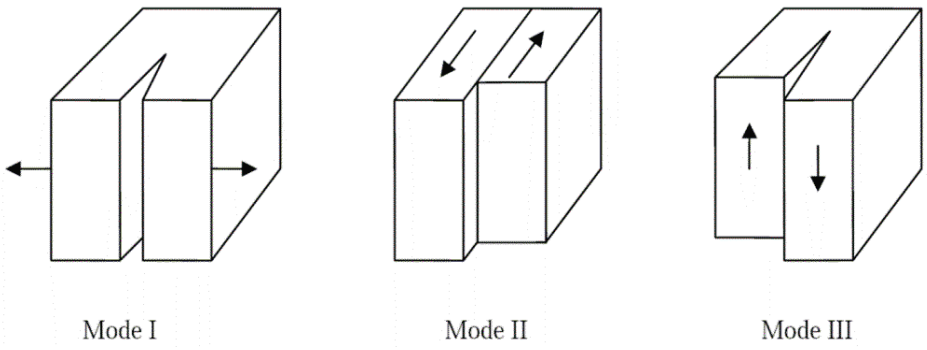

Figure 2-6 Fracture modes [63]

There are a few standard tests that are used to quantify fracture toughness of soft tissue samples. These include:

- A trouser (or tear) test (Mode III) in which a sample is made into a strip and a longitudinal starter crack made in the sample. Each leg of the strip is clamped in a universal testing machine and loaded until it breaks.
- Single edge notched tensile test (Mode I) where like the trouser test a rectangular sample is prepared and a starter notch made mid-way along the sample on one edge. The sample is then clamped in the testing machine and pulled to propagate the crack across the specimen.
- A shearing test (Mode I) in which a blade (preferably angled) is mounted in a universal testing machine crosshead. A second blade is held fixed below the angled blade and the specimen placed between the two. The angled blade is lowered and guillotines the sample.

Other tests that have been adopted to measure the fracture toughness of specific types of biological samples include; the wedge fracture test (food samples), punch-and-die test (leaves and skin), microtome test (histological sections) and the single edged notched bending test (bone and nacre). The scissoring test[2], pioneered by Lucas and Periera [64] has been established as an effective means of measuring the fracture toughness of leaves and mammalian skins. The tests involved mounting a pair of scissors in a universal testing machine monitoring the forces force generated while cutting a biological sample. Friction forces between the blades were accounted for by closing the blades while no tissue was

[2] Scissor cutting is considered to be mixed-mode fracture, although this can be argued against if similar work-of-fracture results are obtained for the same test specimens using the wedge test. In turn this enables results to be interpreted conventionally.

present and work done due to friction only was determined. This friction work was subtracted from the work of cutting which yielded an estimation of the fracture toughness of the sample being cut.

2.6.1 Measuring Fracture Toughness *in-vivo*

The fracture toughness of soft tissue acted upon by the surgical tools plays a critical role in medical procedures, such as catheter insertion, robotically-guided needle placement, suturing, cutting or tearing, and biopsy [65]. These procedures all involve tissue damage to a certain extent, which should be kept to a minimum in order to avoid any medical complications [66]. Thus, knowledge of fracture related material properties, especially the fracture toughness, is of major importance.

Fracture toughness characterises a material's intrinsic resistance to crack initiation and penetration [67]. The measurement of fracture toughness of soft tissues is of interest to many researchers [68] particularly those involved in the development of reality-based tissue interaction models [69-71]. This material property is of importance when estimating or modelling interaction forces on surgical instruments during bisection, shearing and puncturing using scissors, blades and needles. Common methods currently being employed to estimate in-vivo fracture toughness of biological tissue involve the use of material indentation or needle insertion [66, 72]. A review of relevant literature reveals that there are no instrumented scissor instruments currently available that are used specifically to facilitate the collection of fracture property data in-*vivo*.

2.6.2 Fracture Toughness using Scissors

Although there are many types of instrument used in medical intervention that can facilitate the measurement of fracture toughness values, this thesis focuses on the use of scissors. Scissors are an effective and precise instrument for cutting thin tissues in laparoscopic and minimally invasive robotic surgery [54, 55, 65]. The advantages of using scissor blades over scalpels and indenters in the determination of fracture toughness include;

(a) The test is simple to perform.
(b) The cut can be directed as required to pass through the anatomical features of interest.
(c) Material can be held (to a certain extent) by the scissors between its blades.
(d) A reasonably long cut can be achieved.
(e) Friction effects between blades can be quantified before and after a cutting procedure.

Conversely there are a number of documented drawbacks associated with employing a scissoring technique [62]. Specifically;

(a) Friction between the blades can be significant and must be compensated for.
(b) The rate of cutting is non-uniform throughout the cut length increasing toward the tip of the blades.

It is evident that using scissors to estimate fracture toughness requires that adequate measurement and compensation of blade friction forces is required. This is particularly significant when cutting soft tissue as the forces generated from blade friction could be significantly greater than the forces on the blade arising from tissue fracture.

2.7 Forces on Scissor Blades

The number of different scissor and dissector instruments used in laparoscopic, minimally invasive and robot assisted surgery platforms is vast. Consequently, the forces generated on the cutting blades during operation are very much dependent on the mechanical properties of the tissue being cut as well as blade geometry, mechanism linkage, age of instrument and experience of the user. A recent study by Mucksavage [73] *et al* carried out experiments on typical instruments used on three different daVinci surgical platforms types; the standard-platform, the *s*-platform and the *si*-platform. A load cell was placed within a manufactured housing unit (Figure 2-7(a)) onto which the tips of the instruments (including scissor instruments) were placed (Figure 2-7(b)). The instruments clamped the housing and the closing force measured. The forces measured from the three platforms specifically for two scissors instruments are summarised in Table 2-1.

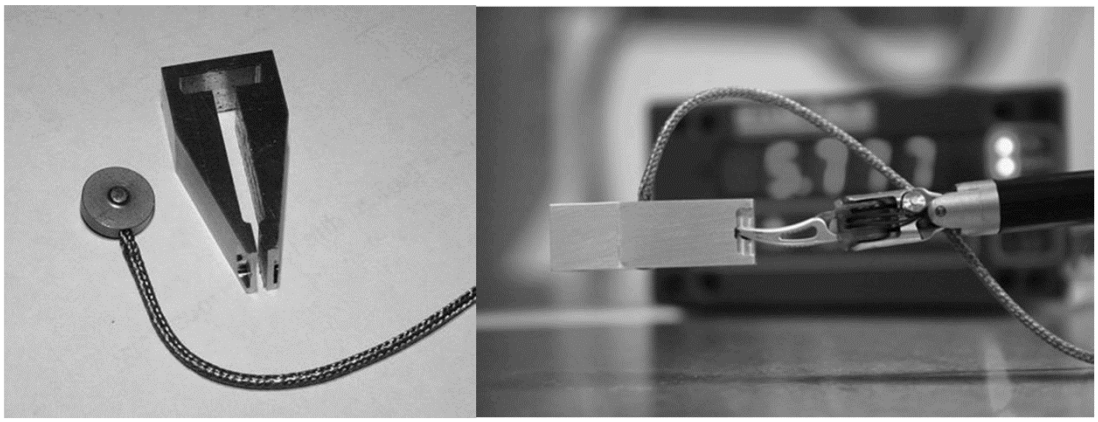

(a) (b)

Figure 2-7 Experimental Force measurement setup (a) Load cell and housing unit (b) A laparoscopic instrument gripping the machined portion of the housing unit.

	Closing forces (N) per platform type		
Scissor Type	*Standard-platform*	*s-platform*	*si-platform*
Round-tip scissors	12.57	10.11	10.04
Monopolar curved scissors	12.10	10.38	10.38

Table 2-1 Measured closing forces of 8 mm laparoscopic scissors [73]

The study concluded that different grip forces were observed for each platform whilst using the same surgical instruments. This reinforces the need for a force measurement scheme that measures the true forces exerted on the instrument tip, free from the influence of system (platform) type, actuation mechanism and geometry. Greenish *et al* [74] have experimentally obtained in-vitro cutting

forces that occur at the handles of Metzenbaum surgical scissors. The main aim of this work was to use the experimentally-derived force data to enable reproduction of realistic force feedback in a virtual haptic scissors force feedback simulator [75]. It was concluded that the forces required to cut the tissue samples remained indeterminate and cited that an improvement to the force sensor was required. The measured force ranges for three different types of scissors used is summarised in Table 2-2.

	Cutting force range per scissor type (N)		
Material cut[3]	*Metzenbaum*	*Mayo*	*Iris*
Empty	3 - 5	5 - 9	5 - 8.5
Liver	3 - 8	7 - 10	12 - 20
Skin	7 - 27	8 - 22	23 - 49
Muscle	6 - 8	7 - 10	15 - 23

Table 2-2 Summary of measured cutting forces by Greenish [74]

It should be noted that the force range signifies the minimum peak force to the maximum peak force obtained from a number of samples of the same specimen. It is not clear, from the data presented in Table 2-1 and Table 2-2 as to whether

[3] Rat and sheep specimen samples

the scissor blades being considered would deflect sufficiently enough under loading and generate enough mechanical strain to load a strain sensor attached to its surface or within its structure. It is believed that the strain generated in scissor blades, particularly smaller blades, would be quite low. Therefore, the sensor chosen must itself have sufficiently high sensitivity to ensure that meaningful strain and force data is obtained from the sensorised blade. Moreover, the location of a sensor on the blades is also important, particularly in the case of scissor blades, as the location of the forces acting on the blade during cutting vary along its length.

2.8 Summary of the Research Problem

It is evident, based on the literature reviewed, that there exists a need for haptic feedback in MIRS. The benefits are twofold;

- Haptic (both tactile and kinaesthetic) feedback enables the user a sense of feel that is otherwise lost due to the remote nature of the master-slave system.
- Real time information in relation to tissue properties while being manipulated may be obtained in-vivo and used for the development and validation of soft tissue models and simulations.

A schematic of a MIRS system is shown in Figure 2-8 along with a view of a surgical instrument illustrating the direct and indirect sensing locations onto which sensors can be placed.

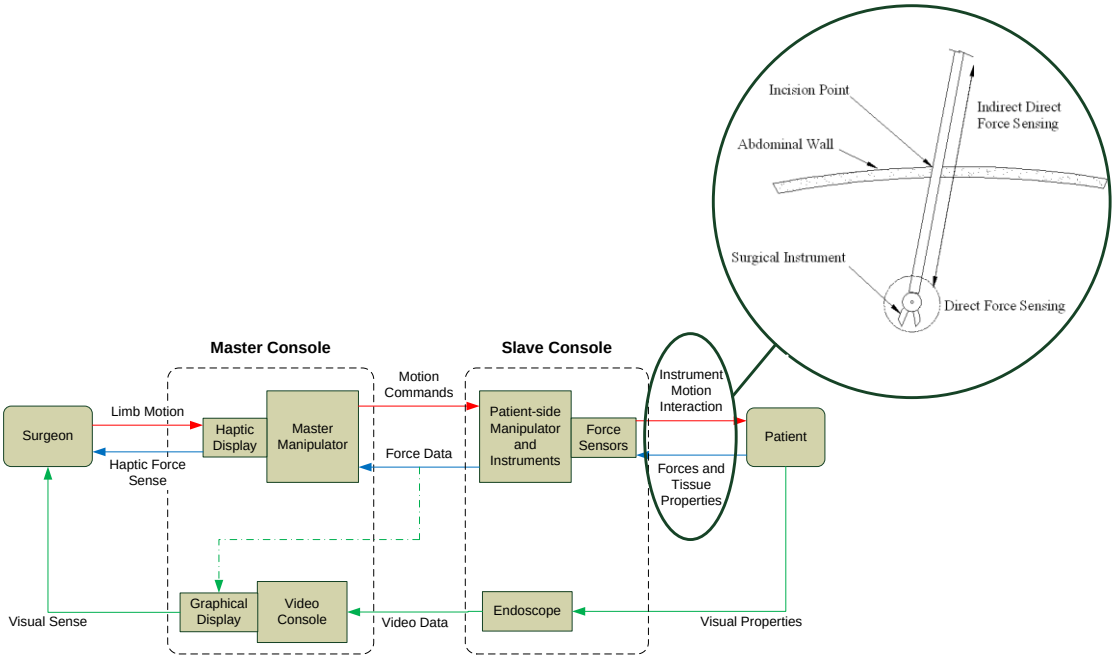

Figure 2-8 Master-slave MIRS system and a slender surgical instrument

Obtaining true information pertaining to the interaction between tissue and instruments which is free from the influence of unwanted frictional and inertial effects dictates that the tip of the instrument is the ideal location for force sensor placement (direct force sensing). This location enables force information to be collected as close as possible to the point where it originates (Figure 2-9).

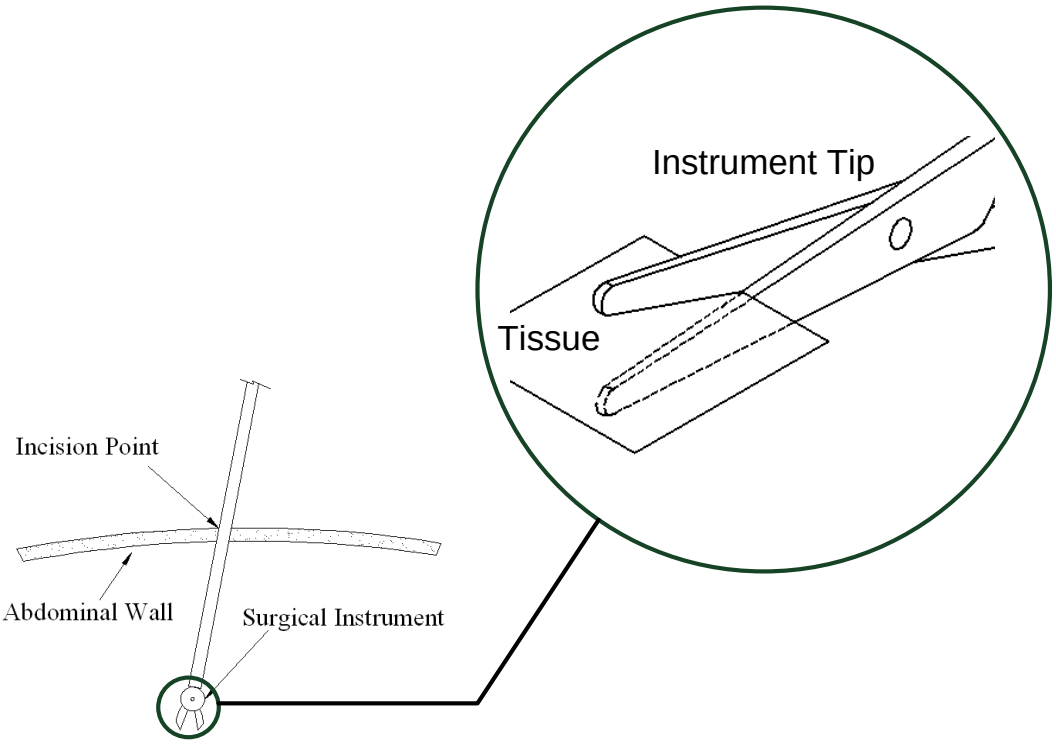

Figure 2-9 Ideal location for sensor placement (Instrument tip)

A number of instruments can be considered for direct force sensing implementation, ranging from graspers and forceps to scissors and dissectors. For this research work Metzenbaum scissors have been selected as the instrument of choice for the following reasons;

- They are an integral part of many of the most frequently performed surgical interventions.
- Straight Metzenbaum scissors are mostly used in laparoscopic surgery for mechanical dissection.
- Metzenbaum scissors are recommended for blunt dissection and for sharp dissection of delicate tissues [76].

The focus of this research therefore is to integrate a force sensing scheme at the surgical scissor blades, enabling delicate soft tissue forces to be quantified while cutting. This approach in which a small sensing element is bonded to or ideally embedded into the scissor blade dictates that the scissor blade itself becomes the sensing element (Figure 2-10)[4]. The benefit of this approach is that only forces occurring in a region between a blades pivot and its tip are measured and are thus unaffected in any way by forces outside the region resulting from mechanism backlash and friction. The challenges associated with implementing a force measurement scheme are;

- Selecting a sensor with sufficiently compact dimensions
- The placement and attachment/bonding of the chosen sensor
- Deciphering the various forces that act on the blade during cutting, i.e. fracture forces, compression forces, and friction forces.

[4] Note that Figure 2-10 shows two integrated sensors. The sensor on the upper surface is the bonded strain sensor while the sensor on the side face is an unbonded temperature sensor if required.

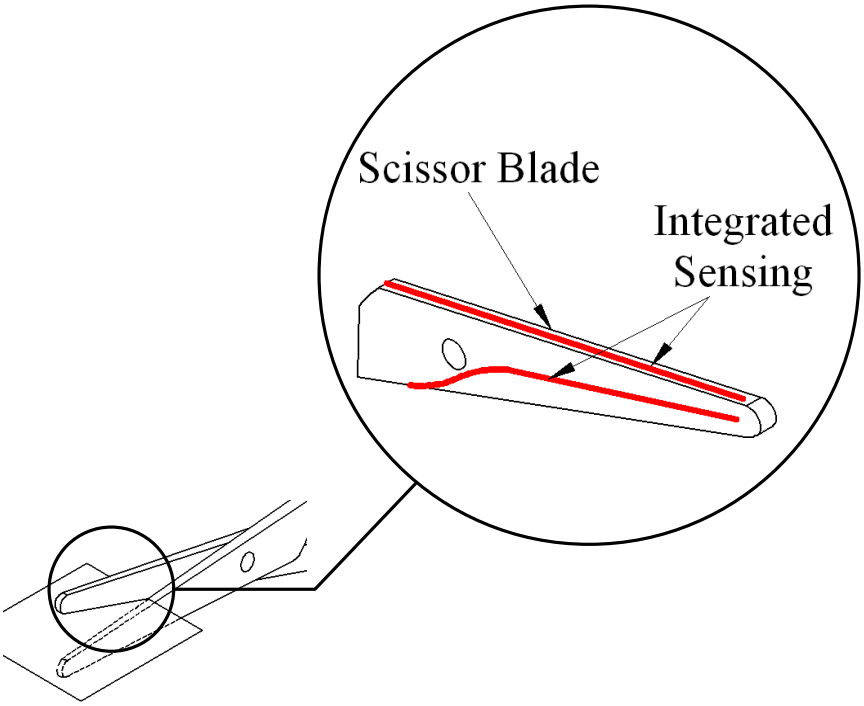

Figure 2-10 Sensorised scissor blade with integral sensing

2.9 Sensor Requirements

There are a number of important issues, specific to a direct force-sensing scheme, which require consideration when assessing the potential of various sensing technologies. The following sections investigate the issues which are deemed important in the integration of a suitable force sensor into a pair of surgical scissor blades. Although many sensors are available that can detect forces and ultimately tissue properties, not all are biocompatible, small, robust and do not hinder instrument functionality [77]. The challenge therefore is to find a sensor that meets all these criteria.

2.9.1 Space Restrictions

Placing sensors directly on to the scissor blades requires that the sensing element be sufficiently small so as to maintain the integrity of the instrument tip. Advances in Micromachining technology has allowed Micro-electro-mechanical systems (MEMS) to be successfully attached onto, or embedded into, surgical instruments [78]. Geometrical constraints, biocompatible material requirements, and assembly complexities of surgical MEMS can make device fabrication quite challenging [79]. An additional constraint with scissor blades is that the blade width is generally narrower than that of a typical grasper, reducing the area on to which a sensor can be attached. Alternatively, a sensor could be placed on the outside faces of the blades as they are wider than the top of the blade but it remains to be seen whether sufficient sensitivity could be achieved with this approach. Scissor blades range in length from 3 mm to 30 mm depending on the scissor type being considered. Most scissor blades taper along their length. The width of the taper at the pivot can range from 1 mm to 5 mm narrowing to sub 1mm at the tip. These sensor placement zones for a single scissor blade are illustrated in Figure 2-11.

Taking the smallest zone (the top zone) on the smallest blades, the sensor needs to have dimensions ideally <1 mm width and a maximum of 3 mm in length. It is worth noting that when the blade dimensions are small, the sensor dimensions also need to be compact. If not, the sensor is measuring strain over an area that may form a large percentage of the placement zone.

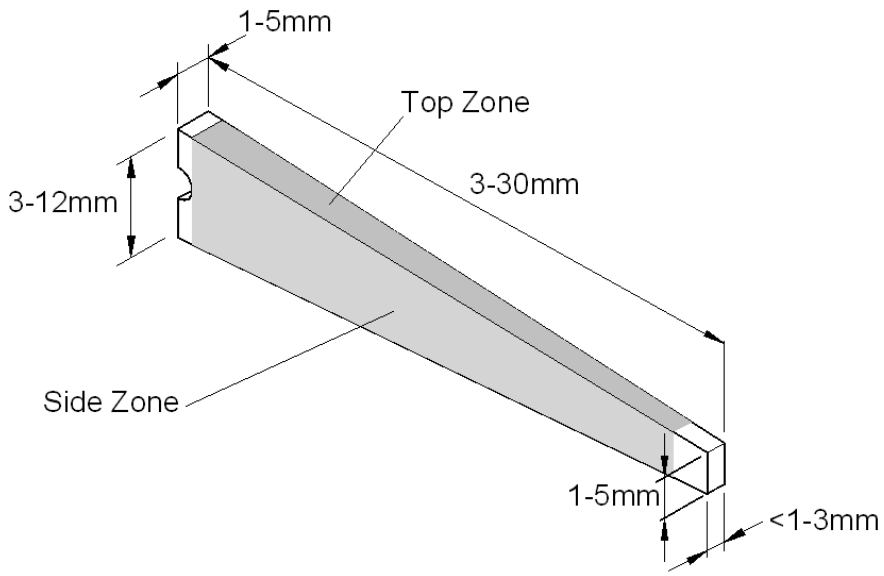

Figure 2-11 Sensor placement zones on a single scissor blade

This would in turn lead to a sensor that is in effect measuring an average strain over its contact area rather than a localised point measurement. Point measurements are preferred as average strain values would result in lower strain sensitivity. To overcome space restrictions and achieve point measurement the sensor must be dimensionally as compact as possible both in width and length.

2.9.2 Sterilisation and Biocompatibility

Surgical instruments that are used inside the body need to be thoroughly sterilised to ensure complete destruction of microorganisms (e.g. spores). Steam sterilisation in an autoclave, at approximately 121°C and 205 kPa absolute pressure, is the standard sterilisation protocol used for most surgical

instruments [80, 81]. Steam autoclaving between 132°C and 134°C is recommended by Intuitive Surgical® for sterilisation of the daVinci® surgical instruments. Therefore, it is imperative that a transducer placed at the instrument tip is capable of withstanding these elevated temperatures for between 4 and 15 minutes to ensure all spores are eliminated. It is also important to note that if the sensor is to be bonded to the instrument then the bonding agent should also be able to withstand these temperatures and pressures. All electrical components placed on to the instrument tip must be appropriately sealed and protected. This is achieved through application of an appropriate epoxy that is again sterilisable as well as compatible with the conditions in which it is to operate. If suitable adhesives and epoxies are not available an alternative sterilisation protocol using Ethylene Oxide, Hydrogen Peroxide or other chemical agents may be more suitable. Ortmaier *et al* has suggested that, as a result of unanswered questions dealing with sterilisability of electrical components, alternatives such as optical methods may have to be used for measuring and transmitting information [53].

2.9.3 Modular Design

Commercially available MIRS systems have instruments that are modular in design and allow the instrument tip to be disposed of after approximately 12 to 20 uses. Integrating a force sensor on to the instrument tip would increase its complexity and cost. This requires consideration at the design stage so as to create an instrument that has an extended life and is thus reusable or

alternatively can be manufactured at a cost that is acceptable enough to allow disposal of the instrument after one use.

2.9.4 Sensor Integration

The majority of previous research efforts which focused on direct force sensing have attached the sensor onto the surface of the instrument. Studies by a number of researchers have used electrical strain gauges attached to the surface of their instruments [44, 82]. Strain gauges have the advantage of low cost, proven performance and are available off-the-shelf and are easy to attach to the surface of instruments. However, the use of surface mounted strain gauges on an instrument used clinically offers up different challenges compared to that of a lab setting. Among these challenges is the fact that surface mounted sensors may impede the surgeons view of the operating site and could impede the function of the device if the attached sensor increases the geometry of the instrument by a significant amount.

A viable alternative may be to embed the force measurement transducer into the instrument during the manufacturing process. This method ensures no contact between sensor and tissue, and as a result eliminates issues involving sterilisation and compatibility. Verimetra Inc. has successfully embedded MEMS sensors into microgrippers. This eliminates the need for glue and adhesion layers which improves sensitivity and reduces errors due to creep [79]. A miniature polymeric gripper developed by Dollar *et al* [49] has six strain gauges embedded within its structure enabling three-axis force measurement. The

shape deposition manufacturing (SDM) technique was used to manufacture the gripper arms which incorporate the embedded sensors. This technique proved to be a quick, inexpensive and robust manufacturing method. The gripper output is sensitive to temperature with a drift of 0.15 N in the output arising from temperature variation over a 5 minute period; indicating that temperature compensation may need to be considered during embedding of force sensors using SDM.

2.9.5 High Speed Dynamic Sensing

Realistic modelling and simulation of tissue deformation is an ongoing area of research as a result of the complexity of human organs and the challenges associated with the acquisition of tissue parameters [83]. The real-time collection of in-vivo instrument-tissue interaction data can be used to validate the accuracy and realism of these models. It is proposed that sensors used in the collection of this interaction information should have high-speed dynamic sensing capabilities enabling the measurement of force information.

2.10 Overview of Force Measurement Sensors

There are a wide range of sensors available that have the potential to be used as the sensing element of a sensorised surgical scissor blade. Some of the most commonly available sensor types are considered in this section. A number of state-of-the-art review publications were consulted [84] to facilitate the evaluation of suitable sensors for the proposed sensing scheme in a clinical

application. These various force sensing technologies can be summarised and grouped into the following sensing categories;

Sensing category	Sensor technologies	Force Measurement method
Displacement based	LVDT, potentiometer, VCA	Force is estimated from difference between two displacement measurements.
Current based	DC motor	Force inferred from motor current measurement.
Resistive based	Strain gauges, MEMS	Structural strain induces change in electrical resistance proportional to force.
Capacitance based	Capacitive sensor element arrays	Force applied perpendicular to film results in change of capacitance[5].
Piezoelectric based	Ferroperm Piezoceramics, PVDF	Force causes stress in the PVDF film, polarisation charges which produce voltage signals are generated.
Optical based (Extrinsic)	Fabry-Perot Interferometer (EFPI)	Force/strain moves the transduction element altering the reflected light spectrum which is transmitted along the optical fibre to a detector.
Optical based (Intrinsic)	Fibre Bragg grating (FBG), Long period grating (LPG)	Strain is applied to the optical fibre which itself modulates and reflects the light spectrum to the detector.

Table 2-3 Common sensing categories used in the detection of strain/forces

Each of the sensing categories outlined in Table 2-3 have benefits and limitations particularly in the context of sensorised surgical devices for use in clinical applications. Table 2-4 summarises the pros and cons of what are adjudged the most suitable force sensing technologies from Table 2-3. Displacement

[5] Best suited to tactile force sensing applications

technologies are not considered due to the inferred nature of the sensing method, i.e. not strictly a direct force sensing technique.

Technology	Advantages	Limitations
Strain Gauges	• Small size and can be sealed in a waterproof environment. • Multi-axis measurement is easily achieved.	• Sensitive to electromagnetic noise and temperature changes leading to drift and hysteresis. • Trade-off between the sensitivity of the measurement and the stiffness of the structure.
Measurement of actuator input	• The system is no longer limited by the sensor bandwidth (which can make a control or feedback system unstable), and it is not necessary to incur the cost of force sensors. • Does not rely on force sensors, which often do not operate properly when exposed to high temperatures and humidity.	• Very sensitive to uncertainties so if the system cannot be properly modelled (due to high joint friction, for example), the estimation error can be significant
Capacitive-based sensing	• Limited hysteresis, better stability and increased sensitivity compared to strain gauges.	• They need more complex signal processing and are more expensive.
Piezoelectric sensing	• Since these materials generate their own voltage, no additional power supply is needed. • They have high bandwidth, high output force, compact size and high power density.	• They are very temperature dependent and subject to charge leakages. This results in a drifting signal when static forces are applied, thus making them suitable for the measurement of dynamic loads only.
Optical Sensors	• Forces can be measured in as many as six DOFs. • They can be used inside magnetic resonance imaging (MRI) scanners. • They can detect changes with high sensitivity and reproducibility.	• Sensitivity to light intensity changes caused by bending of the cables or misalignment. • Optical fibres cannot typically achieve small bending radii.

Table 2-4 Summary of force sensing technologies by Trejos [38]

The selection of a sensor from Table 2-4, that is suited to a device employing a direct forcing technique, can be achieved by assessing each one against the following proposed criteria; 1) General sensor requirements, 2) Requirements specific to a sensorised surgical instrument being used clinically.

1) *General criteria;*
    - High sensitivity and resolution
    - Robustness
    - Minimal zero and sensitivity drift
    - Temperature insensitivity

2) *Application specific criteria;*
    - Biocompatibility
    - Small dimensions
    - Sterilisibility
    - Embedibility
    - Electromagnetic immunity
    - Disposability/cost

While most of the sensing technologies outlined in Table 2-4 would be similar in terms of general criteria, it is the application-specific criteria that will, to a great extent, determine sensor selection. On these grounds, the optical force sensing transducers would appear to be superior to their electrical counterparts. Optical based sensors are typically manufactured from silica, itself an inert material

which satisfies both the sterilisibility and biocompatibility criteria. Moreover, intrinsic optical sensors offer the following additional advantages over their resistance, piezo and capacitive-based commercially available counterparts [85];

a) Wavelength Encoded
b) Self-referencing
c) Linear Output
d) Small and Lightweight
e) WDM & TDM Multiplexing
f) Mass producible
g) Durable
h) Single & Multi-Point Distributed Sensing

These benefits are of great interest to researchers involved in the investigation, prototyping and manufacture of sensorised surgical devices and instruments. Additionally, researchers investigating small compact devices for use in NOTES and microsurgery [32] as well as sensorised instruments that can operate in an MRI environment [86, 87] could benefit. However, there are drawbacks that need consideration when using optical-based sensors for strain and force measurement. Namely;

- Thermal sensitivity
- Transverse strain sensitivity
- Limited suppliers of optical sensors
- Lack of standards available

Technical issues such as thermal sensitivity and transverse strain sensitivity can be addressed with the inclusion of an additional temperature sensor for localised temperature readings [88] and calibration of the strain sensor to enable compensation for lateral strain effects. The lack of standards at present means that optical sensors such as fibre Bragg grating sensors are not manufactured in standard sizes and do not come as pre-packaged transducers that can be bonded to a device or instrument. However, despite the drawbacks associated with optical sensors, the advantages outlined in page 48 offer significant potential for a new generation of augmented sensorised instruments such as scissors, dissectors, graspers, needles and forceps.

2.10.1 Optical Fibre Sensor Selection

The discussion in Section 2.10 has shown how optical based sensors meet both the general and application-specific criteria for sensorised surgical instruments. However, it is also important to assess the mechanical conditions likely to be experienced by an optically based sensor to establish its suitability for sensorised surgical scissor blades. There are number of different optical based strain sensors available. Four of the most common types have been compared by Rao [89] and are summarised in Table 2-5. It can be seen that the FBG sensor has advantages over its counterparts of high mechanical strength (~1375 kPa after gratings have been written into the fibre) and short gauge length (1 – 5 mm). Moreover, FBG sensors have a strain measurement range between 0 - 10,000 με [90] which make them very suitable for the measurement of high strain values.

However, it is generally recommended that the service strain be ~30% of 10,000 με to ensure a 20 to 40 year lifespan for the FBG sensor [90]. Additionally, Rao [89] published details on the physical and optical properties of FBG strain sensors as outlined in Table 2-6.

	Fibre Bragg Grating (FBG)	**Fabry-Pérot (FP)**	**Two- Mode (TM)**	**Polarimetric (PM)**
Linear Response	yes	yes	yes	yes
Absolute Measurement	yes	yes	yes	yes
Range of Resolution	high	high	low	low
Sensor Gauge Length	short	short	long	long
Mechanical Strength	high	low	high	high
Multiplexing	yes	yes	yes	yes
Mass Production	yes	yes	yes	yes
Potential Cost	low	low	low	low

Table 2-5 Comparing optical fibre strain sensors [89]

A few of the key properties of a typical FBG are assessed in Table 2-7 against the requirements for the sensorised scissor blades used in this research. The expected strain and stress values were obtained from a finite element analysis on the blade that will be used in the experimental section of this thesis [91].

Physical Properties	
Ultimate strength	> 200 kpsi (~1379 MPa)
Failure time	> 1 million cycles
Thermal stability	< 3000 °C
Response time	< 1 μs
Optical Properties	
Spectral bandwidth	0.1 - 0.2 nm
Reflectivity	0 - 100 %
Excess loss	-30 dB

Table 2-6 Physical and optical properties of a nominal fibre Bragg grating [89]

	Blade	FBG	Suitable for application?
Strain	0 - 500 με (expected)	0 – 10,000 με [92]	Yes
Dimensions	Placement Area: 3 x 39 mm	125 μm x 5 mm	Yes
Temperature	0 - 40 °C (expected)	< 3000 °C [89]	Yes
Stress	71 MPa (expected)	UTS: 1379 MPa [89]	Yes

Table 2-7 Comparing FBG properties against application requirements

The data presented in Table 2-7 coupled with the fact that FBGs are sterilisable [93, 94], biocompatible [95], embeddable [96] and electromagnetically immune [97] make them an appropriate transducer to sensorise a pair of Metzenbaum scissor blades. The compact dimensions and inert nature of the sensor make it attractive for both microsurgery and MRI applications. Purchasing the sensors as non-prepackaged devices dictates that sensors can be integrated onto or within the tip of the blades to achieve a compact sensing element.

2.10.2 FBG Principle of Operation

An elementary fibre Bragg grating comprises of a short section of single-mode optical fibre in which the core refractive index is modulated periodically using an intense optical interference pattern [98], typically at UV wavelengths. This periodic index modulated structure enables the light to be coupled from the forward propagating core mode into backward propagating core mode generating a reflection response. The light reflected by periodic variations of the refractive index of the Bragg grating, having a central wavelength λ_G, is given by [89],

$$\lambda_G = 2n_{eff}\Lambda, \tag{2.1}$$

where n_{eff} is the effective refractive index of the core and Λ is the periodicity of the refractive index modulation.

The basic principle of operation of any FBG-based sensor system is to monitor the shift in the reflected wavelength due to changes in measurands such as strain and temperature. A schematic of a FBG interrogation system is shown in Figure 2-12.

The sensitivity of the Bragg wavelength to temperature arises from the change in period associated with the thermal expansion of the fibre, coupled with a change in the refractive index arising from the thermo-optic effect. The strain sensitivity of the Bragg wavelength arises from the change in period of the grating coupled with a change in refractive index arising from the strain-optic effect.

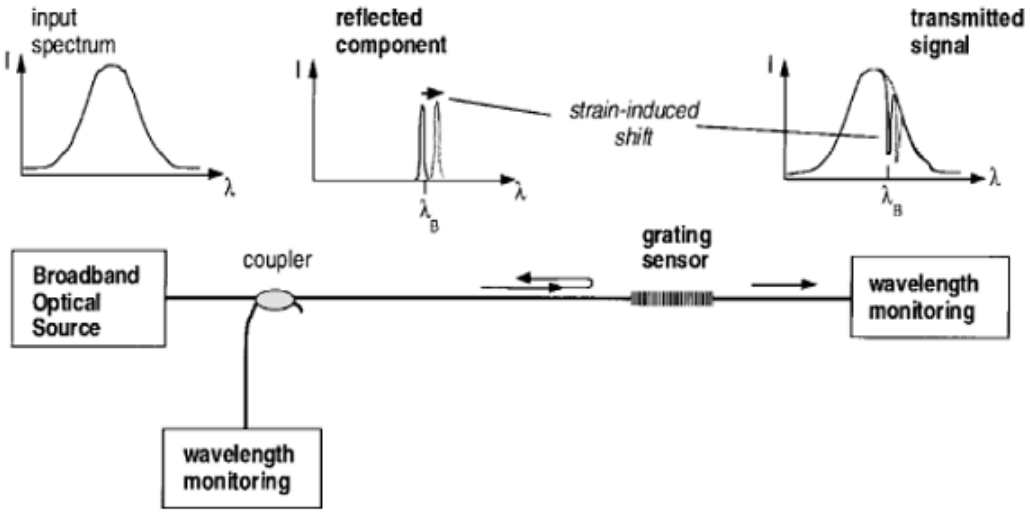

Figure 2-12 A FBG interrogation system

The wavelength shift, $\Delta\lambda_T$, for a corresponding change in temperature measurement, ΔT, is given by,

$$\Delta\lambda_T = \lambda_G(\alpha + \xi)\Delta T, \tag{2.2}$$

where α is the coefficient of thermal expansion of the fibre material and ξ is the fibre thermo optic coefficient. The wavelength shift, $\Delta\lambda_S$, for the measurement of applied uniform longitudinal strain, $\Delta\varepsilon$, is given as,

$$\Delta\lambda_S = \lambda_G(1-\rho_\alpha)\Delta\varepsilon \tag{2.3}$$

where ρ_α is the photo elastic coefficient of the fibre given by the formula,

$$\rho_\alpha = \frac{n^2}{2}\ \rho_{12} - \upsilon(\rho_{11} - \rho_{12}) \tag{2.4}$$

where ρ_{11} and ρ_{12} are the components of the fibre optic strain tensor and υ is the Poisson's ratio. For a silica core fibre the value of (1 - ρ_α) is usually 0.78. Thus, by measuring the wavelength shift, using techniques such as those described in [89], changes in temperature or strain can be determined depending on which

parameter the FBG sensor is expected to measure. A FBG sensor has a strain sensitivity of 1.2 pm $\mu\varepsilon^{-1}$ and a temperature sensitivity of 10 pm/°C.

2.10.3 System Costs & Implementation

An important issue with fibre Bragg grating sensors is the detection scheme for wavelength-shift. For most biomedical applications the resolution required is very high and the conventional spectrometers do not fulfil the requirement adequately [95]. A number of interrogation schemes such as edge filter, tuneable filter, interferometric scanning and dual-cavity interferometric scanning have been reported for high-resolution wavelength-shift detection [89]. In conventional robotics applications, the chief drawback is that the optical interrogator that reads the signals from the FBG cells is larger and more expensive (< €30,000) [99, 100] than the instrumentation used for foil or semiconductor strain gauges. The interrogation system cost is typically dictated by the measurement resolution required and the number of FBG sensors that can be read simultaneously (multiplexing). However, the costs of optical-fibre interrogation systems are dropping steadily and in applications, such as MIRS applications, the capital costs are amortised over many operations [86]. Developing low cost interrogation systems is currently an active research area. Wan *et al* [101] for example, have developed a prototype ratiometric wavelength interrogation system designed for FBG strain sensing. It is believed that the complete measurement system can be produced for ~ €350. Typical interrogation units are relatively small and compact (~ 280 × 170 × 55 mm).

These dimensions would facilitate the practical integration of the interrogation unit into the slave subsystem of current or new MIRS systems. Post processing of the signals from the interrogation unit can be done using a LabVIEW or MATLAB based platform [86]. This data can then interfaced with MIRS systems software to provide force information to the surgeon's hands via the haptic interface on the master console.

Currently, the one-off cost of a single FBG in a standard 125 μm silica single mode fibre with a ~12 μm polyimide recoat over the sensor region is ~€ 200. In large quantities, the price can be reduced significantly. Overall, these costs are small in comparison to most disposable and reusable devices for MIS and MIRS procedures. Furthermore, the price of FBGs is expected to drop in the next five years, making the integration of FBGs into augmented surgical instruments more financially achievable.

2.11 FBG-Sensorised Surgical Devices

Several groups are investigating the use of optical sensing techniques which facilitate the measurement of instrument-tissue force interactions in biomedical applications. Examples include the NeuroArm neurosurgical robotic system [102], a six degrees of freedom force-torque-sensor [103], a 2-D fibre optic sensorised hook instrument for retinal surgery [104], a sensorised surgical needle for use in a MRI environment [105] and a three degree of freedom modular sensor placed between instrument tip and shaft [87]. A recently developed micro-forceps by Kuru *et al* [106] bonded three FBG sensors onto the

shaft of the forceps. The instrument was designed to measure the lateral bending forces on the forceps while removing an inner shell membrane which mimicked a thin membrane layer on a retina surface. The grasping forces exerted on the tissue by the grasper were not measured.

The aforementioned applications consist broadly of grasping, hooking and needle instruments for robotic surgery. This thesis will expand the current range of optically sensorised instruments by investigating, both analytically and experimentally, the interaction forces generated during surgical cutting. It is proposed that the FBG sensor forms an integral part of the scissor blade and is capable of detecting the directly applied forces resulting from the cutting process. Factors influencing these forces typically include inter-blade friction opposing the motion of the blades and the work required to fracture the material between the blades. Additionally, the lateral forces generated along the blade due to its curvature (Figure 2-13) will need to be quantified, as the FBG cannot discriminate them from the directly induced forces.

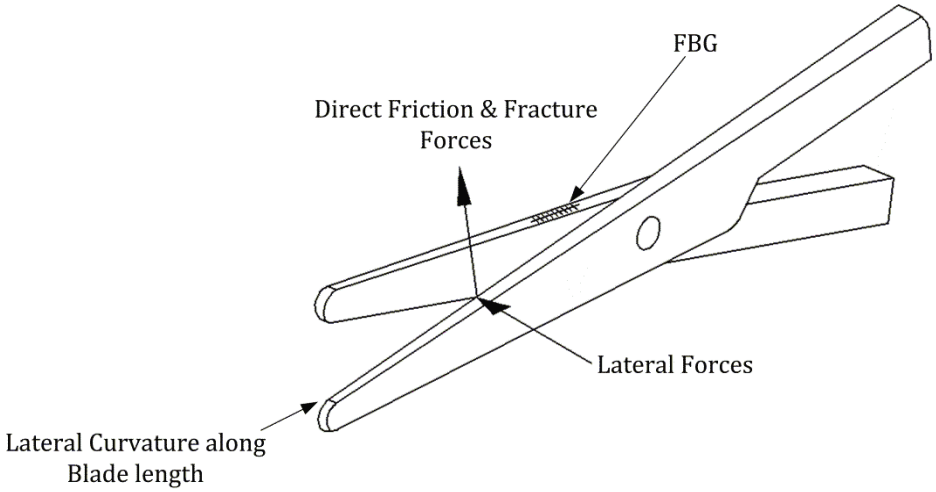

Figure 2-13 Direction of direct and lateral forces acting on the blades

The attachment of the FBG at this distal location will serve to more accurately reflect the force information generated at the blade-tissue interface during cutting without any disturbance forces resulting from mechanism friction and backlash.

2.11.1 Interaction Friction Forces

In general the interaction between a rigid tool and a body involves friction, deformation of the body and possibly fracture, damage or other physical irreversible phenomena [7]. The importance of friction modelling and friction compensation when attempting to acquire fracture properties has been discussed by a number of researchers [69, 72, 107, 108]. Some instruments such as scissors necessitate high friction forces between the blades to ensure that the blades maintain contact during operation resulting in clean, burr-free cuts. A high friction coefficient and subsequently high contact friction forces are due to blade curvature along their length. From Atkins work on general guillotining of materials [109] it is assumed that the lateral forces between the blades due to curvature or 'setting' is constant throughout the cutting cycle. This is reasonable as the blade cross-section and curvature are uniform along the blade length. It was also stated that the lateral forces between the blades may vary with blade angle owing to the form of spring loading. Scissor blades are a typical example of this in which the lateral forces experienced between the blades differ along the blade length depending on the way in which the geometry of the blades change from pivot to tip. Modelling the forces generated during cutting with scissors

was carried out by Mahvash *et al* [59]. Their investigations focused on the forces generated due to fracture of the material being cut. Friction occurring between the blades was not modelled; instead the friction forces were measured and added to the model for forces generated during fracture of the material only. This was deemed effective for haptic rendering of cutting with a pair of scissor blades in a virtual environment.

2.12 Summary

Many researchers are actively engaged in developing methods to measure and restore force information that is currently not available in MIRS systems. The details presented in this review chapter outlined the current state-of-the-art sensing technologies being investigated in the field of sensorised surgical instruments. Particular attention was given to sensorising scissor instruments using a direct force sensing technique in which the sensor is placed as close as possible to the point where forces are being generated. This approach presents technical difficulties in relation to size restrictions, sterilisation issues thus possibly compromising instrument functionality. A review of the most popular resistive, piezoelectric and capacitive based sensing technologies show that, while they can meet most of the requirements for effective force sensing, issues still exist in relation to electromagnetic interference, temperature fluctuation and drift. Optical sensing technologies were explored as an alternative to capacitive and resistance options and it was found that they not only address the shortcomings of traditional sensors but bring the added benefits of

electromagnetic immunity, biocompatibility and sterilisibility. The focus of this work therefore is to investigate the use of FBGs to sensorise a Metzenbaum scissor blade and establish them as a viable choice when sensorising future surgical instruments and devices.

The interaction forces occurring between a surgical scissor blade and the tissue is complex, consisting of fracture forces and blade friction. A direct force sensing method by its nature should facilitate the measurement of accurate fracture and friction forces. The most common methods to date, of obtaining *in-vivo* fracture properties of biological tissue consist of indentation and needle insertion. The use of scissors has only been explored ex-vivo using commercial load cells. It is proposed that a directly sensorised scissor device employing a FBG could enable the collection of accurate tissue fracture information *in-vivo*. A set of tissue cutting experiments are required to establish the nature of the forces and strains that are likely to be experienced by the FBG sensor. A test rig has been developed for this purpose, the details of which are discussed in the following chapter.

Chapter 3

Scissor Cutting Characterisation & Evaluation of Soft Tissue Forces

3.1 Introduction

The design and development of an experimental test-bed incorporating a pair of sensorised surgical scissors has been carried out. This test-bed will form the basis for determining the nature of forces occurring on the scissor blades as well as facilitating the future analysis of FBG sensorised blades during the cutting of synthetic tissue samples.

The functional and performance requirements of the test-bed are outlined in Section 3.3 followed by details on the calibration of the apparatus. Calibrating scissor blades for forces generated along its length is complicated by the fact that the forces generated move along the blade length during cutting. The maximum force acting on scissor blades during a cut occurs at the intersection point between the two scissor blades [58, 75]. Due to the variation of the included angle between the two blades a relationship between the intersection point of the blades and the blade angle needs to be established. This chapter establishes

this relationship experimentally and analytically for the Metzenbaum being used. To date there is no data available pertaining to the magnitude and nature of the strain on the surface of scissor blades arising from cutting. Sensorising the blades using established strain sensing technologies such as electrical strain gauges is required to obtain this information.

In addition to analysing the nature of the force profiles arising during surgical cutting, methods of determining the fracture properties of the samples being cut are also explored. Characteristics that are unique to obtaining fracture properties using the scissor method are discussed and the limitations of such a method are presented.

3.2 Related Research

To date little research has been undertaken to investigate the interaction between a pair of scissor blades and the tissue being cut with a view to developing a real-time force feedback solution. A study carried out by Greenish [75] to measure the forces generated while cutting a range of anatomical tissue concluded that exact quantitative measures for the forces required to cut tissues remained indeterminate. However, the force data obtained was subsequently used by [58, 71] for virtual simulation of tissue cutting.

Test rigs developed by Darvell [110] and Pereira [108] used scissors to ascertain the fracture toughness of various biological tissues. Forces acting on the blades were measured by the placement of a load cell between the scissor handles and an actuator. No force sensors were placed on or close to the blades.

Mahvash *et al* [59] constructed a test rig to measure forces generated on a pair of Metzenbaum scissor handles while cutting for the purpose of validating an analytical model of the forces generated during cutting. No force sensors were attached to the blades of the scissors as only the force occurring at the handles of the scissors were of interest.

Other test-beds of varying configurations have been developed previously to measure the mechanical properties of biological and synthetic materials as well as the forces generated at the interaction between tissue and instrument. Tholey *et al* [51] for example, developed an automated laparoscopic grasper for the characterisation of grasping and cutting tasks. The jaws of the grasper were calibrated by placing a load cell against one of the jaws and forming a relationship between forces and actuating current to ensure accurate measurement of the cutting forces. The grasper set-up was evaluated by grasping hydrogels of varying elasticity and distinguishing between each one based on the force feedback from the grasper. Further tests were carried out on the samples to assess repeatability of the measurement system with good results being obtained.

Equipment for measurement of the forces and torque exerted on a scalpel blade during one degree-of-freedom tissue cutting was developed by Chanthasopeephan [111]. The acquired force displacement graphs highlighted a characteristic deformation followed by a localised crack extension pattern. This data was later used to verify finite element models that would be used to create a reality-based model for real-time medical simulation.

Studying the test-beds developed by other researchers enabled a set of design and functional requirements to be created that met the needs of this particular research work.

3.3 Test-Bed Design Requirements

This research focuses on the direct measurement of contact forces between a surgical instrument tip, in this case a pair of scissor blades, and the tissue with which it makes contact. In order to facilitate this, the requirements for a force measurement evaluation test-bed specific to scissor cutting needed to be established. The primary requirements of the test-bed were categorised into functional and performance requirements and are outlined in Table 3-1 and Table 3-2.

	Functional Requirements
FR.1	The test rig shall actuate a pair of Metzenbaum scissors through a complete open-close cycle.
FR.2	The test rig shall facilitate the measurement of interaction forces occurring at the blade-tissue interface.
FR.3	Facilitate the measurement of the blades intersection point position.
FR.4	Be controlled using a standard PC and data acquisition system.
FR.5	Enable the secure attachment of soft synthetic test samples ranging in thickness from 1 mm to 5 mm.

Table 3-1 Test-rig functional requirements

	Performance Requirements
PR.1	The scissor blades shall have an open and closing rate of between 7 °s^{-1} and 50 °s^{-1} [75].
PR.2	The test rig shall have a force measurement range up to 50 ± 0.1 N.
PR.3	Be capable of measuring the included angle of the scissor blades between 0° and 50°.
PR.4	The data acquisition system shall be capable of sampling signals from the force and angular displacement transducers at a rate of 1kHz to ensure that all complex cutting force information can be obtained.
PR.5	The clamping mechanism shall have the capacity to apply transverse tension to the samples enabling an increase in % strain up to 10%.

Table 3-2 Test-rig performance requirements

3.3.1 Test-Bed Development

The functional and performance requirements in Table 3-1 and Table 3-2 were laid out at the test-bed design stage so that the rig could be deemed a suitable force measurement, characterisation, and evaluation tool. This test-bed will be used in future work to assess new sensing technologies in the measurement of the contact forces at the instrument-tissue interface. It is therefore logical to take initial force readings using tried and tested sensing methods such as bonded resistance strain gauges. It is imperative that the test equipment can differentiate in a quantifiable manner between tissue samples with differing mechanical properties. To achieve this, a series of PVA cryogels of increasing

elastic modulus were cut and the force/angular-displacement characteristics recorded using a data acquisition system. A number of cutting experiments were performed on each of the different tissue samples in order to establish the repeatability of the measurements.

All aspects of the characterisation test-bed development (Figure 3-1(a)), including design, manufacture, data acquisition (DAQ) and software writing was implemented in-house. A typical pair of scissor blades that are geometrically similar to scissor blades used in MIS were examined to facilitate the characterisation of the cutting process. The complexity of the system was minimised by mounting the scissors in a rigid fixture allowing 1-DOF (blades opening and closing) movement only (Figure 3-1(a)(b)). This approach was appropriate in this investigation as only the contact forces perpendicular to the edges of the scissor blades are of interest.

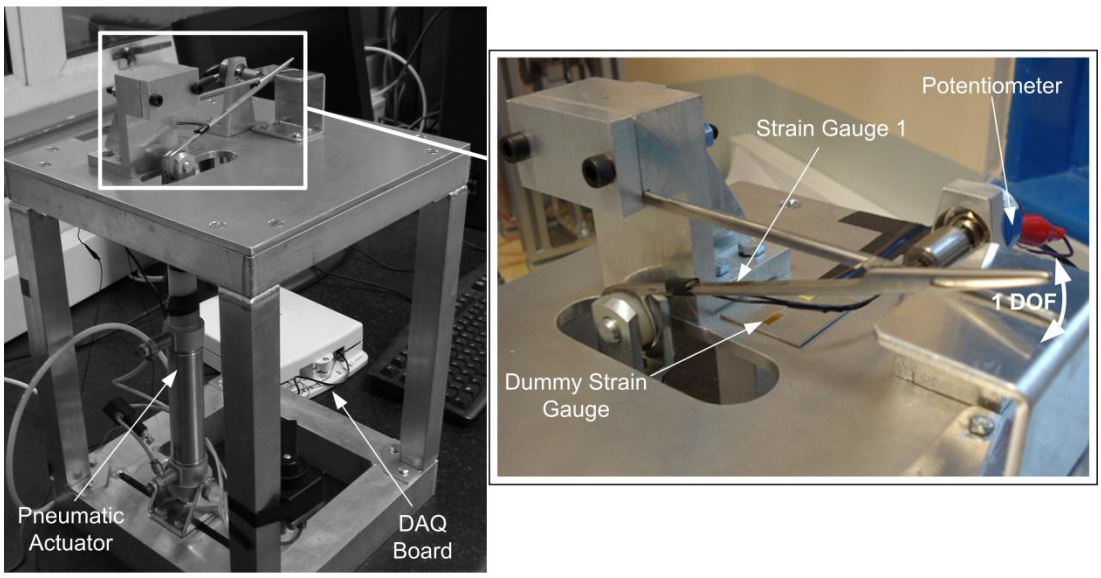

Figure 3-1(a) Characterisation test-bed (b) Location of strain gauges and potentiometer

A pair of 18 cm straight blade Metzenbaum-Nelson scissors (nopa® instruments) were used as the cutting instrument for this investigation. These scissors were deemed appropriate as they have been used in previous force measurement investigations [75] and therefore data is available for comparative purposes. An electrical resistance strain gauge (RS 632-124 N11-MA2-120-11) was bonded to the inner surface of the lower scissor arm (strain gauge 1) as shown in Figure 3-1(b). The inner surface was chosen because it is a flat, even surface compared to the outer surface which is convex. The gauge has a nominal resistance of 120 Ω and base dimensions of 9 mm × 3.5 mm, small enough to be attached to the inner surface of the scissor arm. The upper arm of the scissors is securely fixed while the lower arm is free to rotate about its fulcrum. The actuation of the lower arm is achieved by means of a 32 mm diameter double acting pneumatic cylinder (Festo, model DSNU-32-100-P-A) with a maximum force output of 322 N. Adjustment of a unidirectional flow control valve at the entry to the cylinder upper and lower chambers controls the linear velocity of the piston rod. A single turn conductive plastic precision potentiometer (Vishay Spectrol® model 357), for the measurement of the angular displacement of the blade cutting edges, was fixed to the scissor fulcrum via a coupling device. Fully closed, the scissor cutting edges form an included angle θ of 6.5° (Figure 3-2), however, with the strain gauge bonded to the inner surface of the handle this angle is increased to 7.5°. The cutting angle range of the scissor blades is from 40° to 7.5° with the cutting process completed at 10°. The design and construction of the cutting assembly offers a robust arrangement ensuring that

the forces measured by the strain sensor are only those occurring during the interaction between blades and tissue.

3.3.2 Data Acquisition

The data acquisition unit used in this system collected analogue signals from the active strain gauge (strain gauge 1) and the precision potentiometer. As a result of limited space on the scissor arm the strain gauges were arranged in a quarter bridge configuration with a dummy strain gauge (Figure 3-1(b)) for temperature compensation. This three-wire arrangement was connected to a National Instruments® (NI) SCC-SG02 strain gauge module, which provided bridge completion. The signals are filtered through a 1.6 kHz lowpass filter and amplified by 100 to give readable strain values. Bridge offset nulling was also included in the module by adjustment of a built-in potentiometer. This strain gauge module was inserted into an NI SCC 68 module holder, which also accepted analogue output signals from the precision potentiometer. These analogue signals were converted into useable digital readings by connecting the SCC 68 module holder to a PCI-6221 NIDAQ card, which was installed on a standard PC (Dell optiplex GX150). The software used included NIDAQ MAX 8.3, which configured the devices, sub-devices and channels, as well as set up tasks. LabVIEW® 8.0 was used to condition and display the acquired data.

3.3.3 Test-Bed Calibration

Calibration of the force measurement system was carried out to ensure meaningful force readings were obtained from the strain gauge bonded to the scissor arm. To achieve this, a relationship was established between the point of intersection between the blades C and the strain readings ε obtained from strain gauge 1 (Figure 3-2). This was accomplished by placing a miniature button load cell, measuring 9.52 mm in diameter and 6.35 mm high (model SLB-25 from Transducer Techniques®), between the blades using two specially designed securing units which allowed the forces F_L to be directed perpendicular to the load cell surfaces (Figure 3-3). The upper arm of the scissors was secured in a clamping mechanism while a series of forces F_A were applied to the scissor arms using a miniature translation stage.

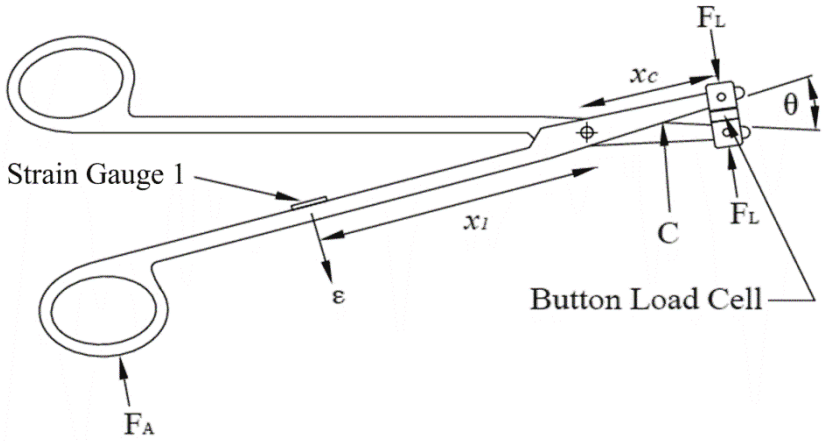

Figure 3-2 Scissor calibration arrangement

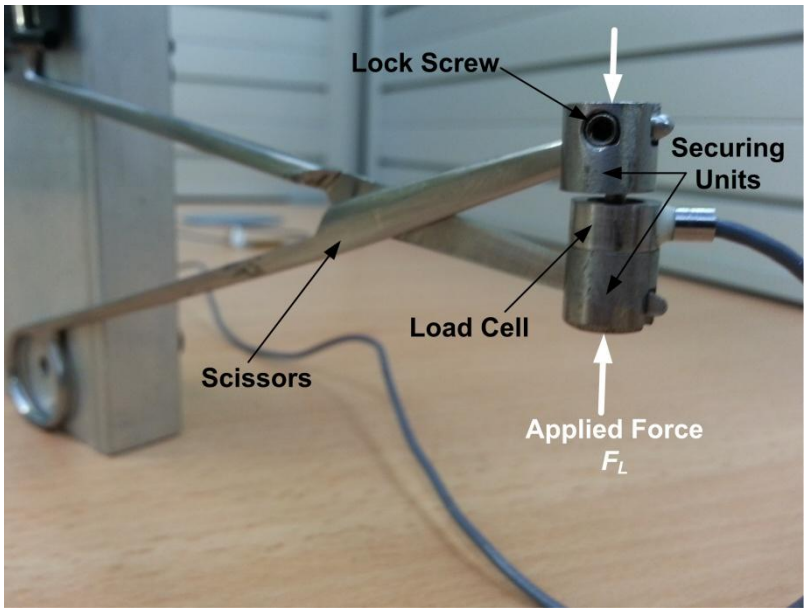

Figure 3-3 Close up view showing the load cell held between the securing units which are clamped to the scissor blades by a lock screw

The strain gauge and the load cell readings were recorded for each force increment applied to the scissor arms. This resulted in a constant of proportionality k (N/με) between the load cell output at x_c (mm) along the scissor blade and the strain gauge readings at x_1 being obtained. This procedure was repeated with the load cell placed at three different locations along the blades resulting in three different k values. However, the dimensions of the load cell placed a restriction on how close the load cell could be placed to the pivot of the blades with the result that k values close to the fulcrum could not be measured directly. The unknown k values were obtained as follows; the three known values were plotted and extrapolated over the working length of the scissor blades (Figure 3-4) resulting in the linear equation,

$$k = -0.0059x_c + 0.3072 \tag{3.1}$$

This equation yields a k value for any position x_c along the cutting edges of the blades.

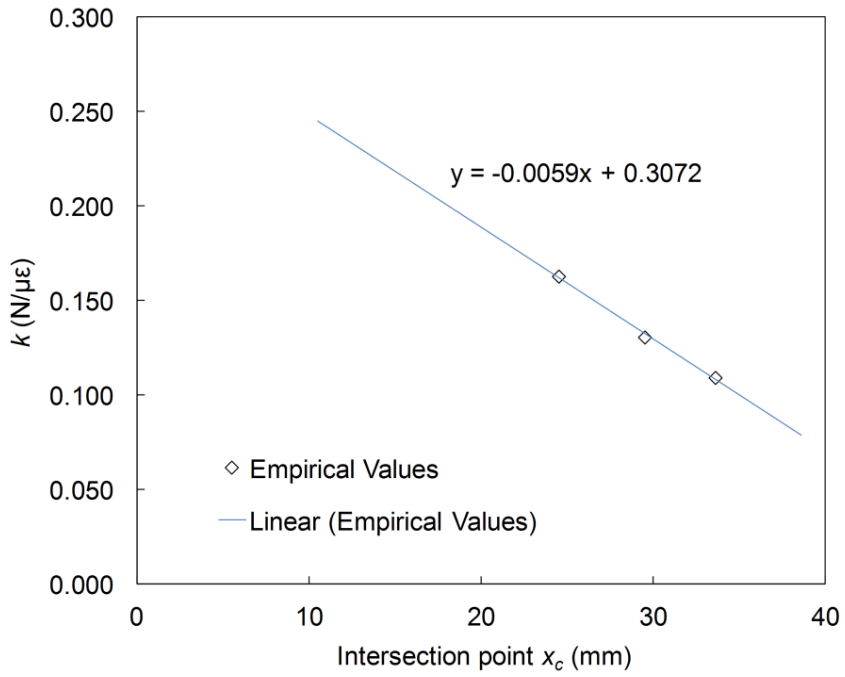

Figure 3-4 Extrapolation of the k-values over the full blade length

The angle θ can be measured directly, hence, a relationship between this angular displacement and x_c allows a value for k to be assigned to any angle and consequently any distance x_c along the length of the blade. Both θ and x_c were recorded at incremental steps of 2° over the cutting range of the blades (40° to 7.5°). When plotted the results yielded the following power relationship,

$$\theta = 560.38 x_c^{-1.1069} \tag{3.2}$$

A comparison can be made between the empirically-derived relationship in (3.2) and the theoretical relationship by examination of the blade geometry in Figure 3-5 using [112],

$$x_c = \frac{t(l)}{\sin\left(\frac{\phi}{2}\right)} \tag{3.3}$$

Where *t(l)* is the thickness of the scissor blades which varies along its length and ϕ is the angle between the centre lines of the blades. It is assumed that *t* varies linearly between t_{max} and t_{min}, thus yielding,

$$t(l) = t_{\max}\left(\frac{Tan(\frac{\phi}{2})}{Tan(\frac{\phi}{2}) + \frac{t_{\max} - t_{\min}}{l}}\right) \tag{3.4}$$

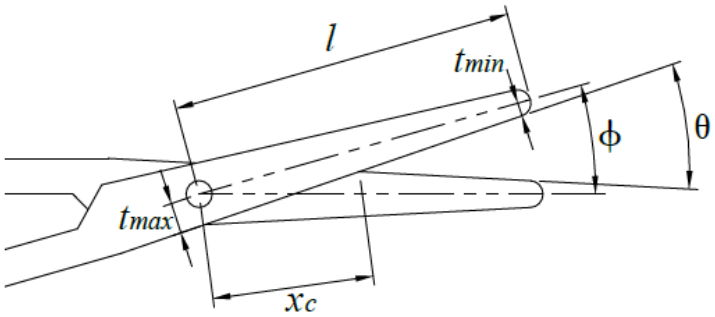

Figure 3-5 Scissor blade geometry

Comparing the theoretical and measured values (Figure 3-6) it can be observed that there are small variations between the measured and theoretical values due to the assumption that the blade cutting edges are perfectly straight. Examination has shown that there is a slight irregular curvature along the length of the blade. However, the close correlation signifies that the location of the

blade intersection can be reliably obtained when the angle of the blades is known.

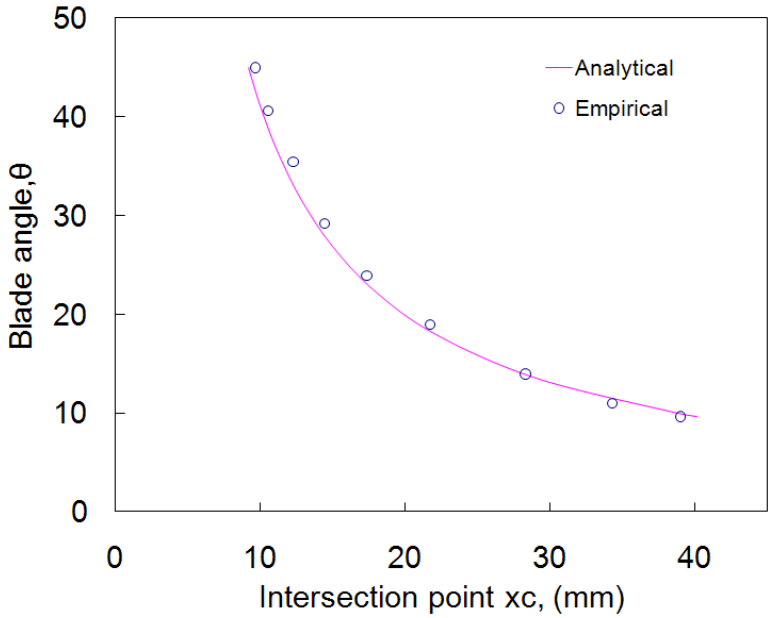

Figure 3-6 Measured and analytical intersection point and blade angle relationship

A database was created wherein the appropriate k value was assigned to each angle in increments of 0.001° between 40° and 7.5°. The resultant force F_c at the point of contact C is therefore expressed as,

$$F_c = \text{Measured strain} \times k(\theta) \tag{3.5}$$

where k is a function of the measured blade angle θ.

3.4 Poly-Vinyl Alcohol (PVA) Hydrogel Test Samples

Hydrogels are a cross-linked network of hydrophilic polymers that are insoluble in water [113]. Poly-vinyl alcohol (PVA) hydrogels, for example, can be made using a freeze-thaw (FT) method which creates crystallinity to bond the

structure [114]. Hydrogels have been used in a variety of applications including drug delivery devices [115], scaffolds for tissue engineering [116] and as tissue phantoms [117, 118]. PVA cryogels in particular are very suitable as phantom materials because they can be produced with realistic tactility and mechanical properties and possess long term structural stability. Synthetic tissues are used in the assessment of instrument-tissue interaction forces as a practical substitute to *in vivo* or *in vitro* biological tissue samples [117, 119]. Real biological tissues were not chosen for this study due to their anisotropic and heterogeneous nature [120] making it difficult to highlight the sensitivity of the characterisation rig in ranking specimens of differing stiffness and fracture properties. Homogeneous synthetic PVA tissue samples were chosen so that fracture properties and characteristics could be identified without the influence of cells, blood vessels, lymphatics, nerves, collagen elastin fibres etc. typical of living tissue [109]. This type of homogeneous sample would enable a reasonable degree of repeatability in the results to be obtained from the test-bed.

3.4.1 PVA Compressive Modulus

A range of homogeneous samples of differing elastic properties are produced using a carefully mixed solution and exposing them to a varying number of freeze-thaw cycles (1FT cycle to 5FT cycles). A 99+% hydrolyzed Polyvinyl Alcohol (PVA) power from Sigma-Aldrich was used with a weight-average molecular weight (M_W) of between 85,000 and 124,000 g/mol. A 10 wt.% PVA cryogel solution was achieved by dissolving 40g of PVA powder in 360g of

deionised water. The solution was mixed on a magnetic stir plate at 90°C for 30 minutes, then removed and stirred for a further 30 minutes until cooled to room temperature. Once cooled the solution was weighed and additional de-ionized water added to ensure a 10 wt.% was achieved. Five samples were prepared by pouring the PVA solution into five identical moulds giving a sheet of PVA tissue 180 mm × 80 mm × 3 mm. A cylindrical test sample, measuring 22 mm × 20 mm diameter, was exposed to the same freeze-thaw cycle as each of the tissue sheets. These cylindrical specimens were included so that mechanical properties could be obtained using appropriate testing procedures. A secant modulus [121] value was obtained for each cylindrical sample by subjecting them to standard compression testing using a materials testing machine (Lloyd Instruments™ LRK30) with a 500 N load cell. The stress-strain relationship for a cylindrical sample (5FT) subjected to 30% compressive strain is plotted in Figure 3-7. The secant modulus is calculated by taking the slope of a secant drawn from the origin through the stress-strain curve at 30% (0.3) strain. A 30% compressive strain was the maximum that all samples were tested to. The experimentally obtained stress-strain values for all PVA samples are plotted in Figure 3-8 and the calculated Secant modulii presented in Table 3-3. This range of modulus values (18.35 to 193.6 kPa) is comparable to that of a range of *intra-vitam* bovine biological tissues such as Liver, Spleen and Kidney (10 to 85 kPa) that were measured by Maaß [122].

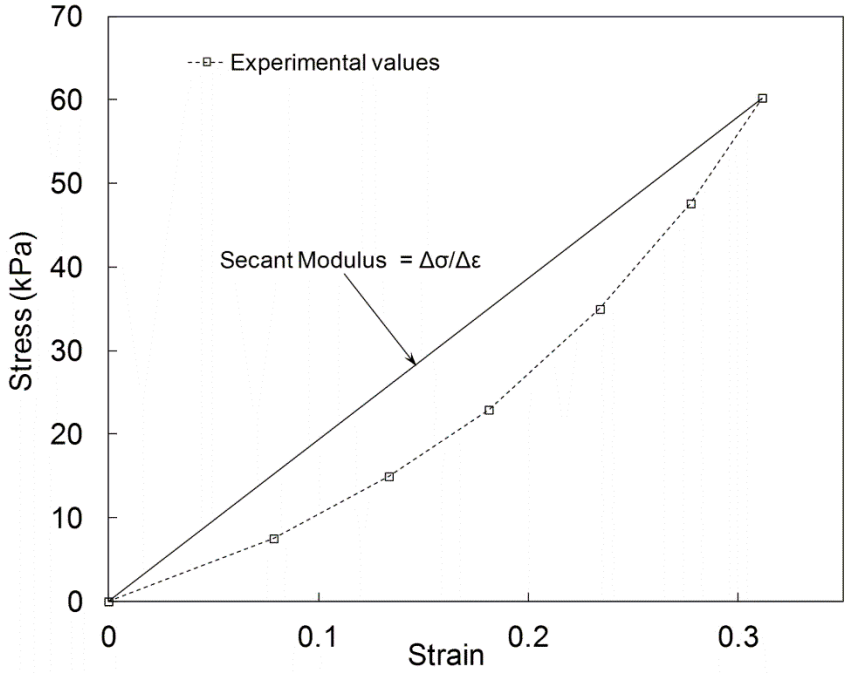

Figure 3-7 Obtaining the compressive secant modulus for a PVA cryogel sample

Number of freeze-thaw (FT) cycles	Secant modulus at 30% compressive strain (kPa)
5	193.6
4	149.14
3	130.29
2	85.95
1	18.35

Table 3-3 Secant modulus values for the five PVA samples

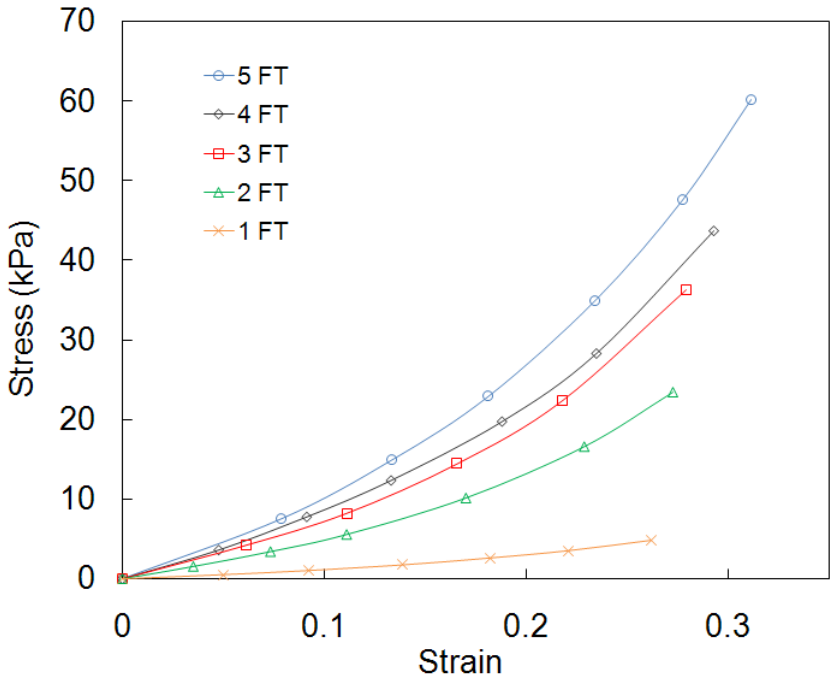

Figure 3-8 Compressive stress-strain data for all PVA samples

It can be seen that due to the nonlinear nature of the PVA, the compressive stress-strain relationship varies as the percentage strain changes. To quantify this variation a tangent modulii were calculated at ~5% strain increments between 2% and ~27% strain. The tangent slope was calculated by measuring the slope between two localised data points at each percentage strain increment [123]. The variation in compressive tangent modulus shown in Figure 3-9 illustrates the variation in the compressive properties between the respective samples.

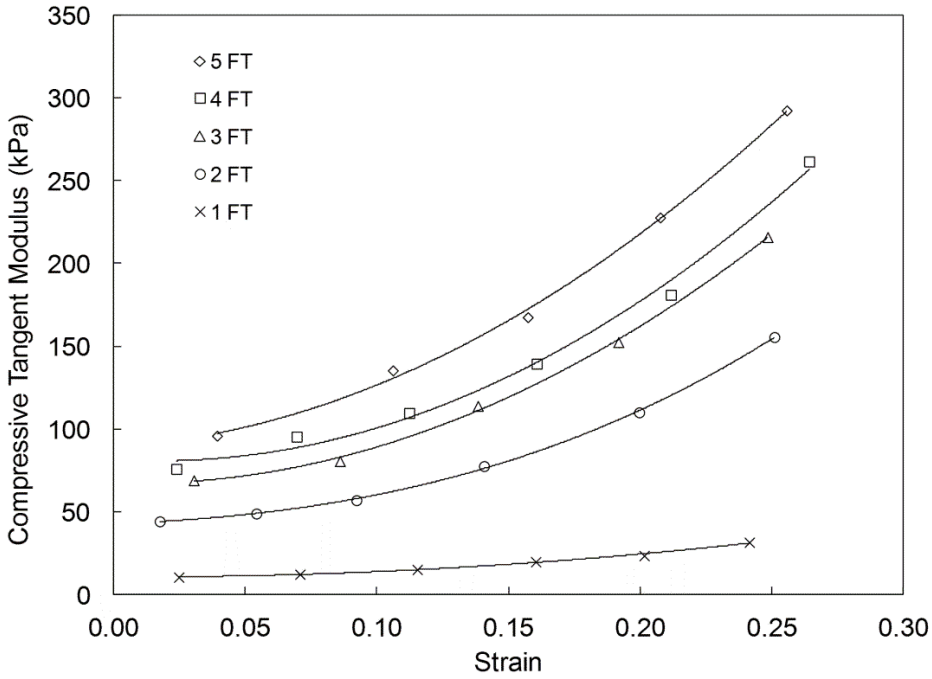

Figure 3-9 Variation in compressive tangent modulus for all PVA samples

3.4.2 Repeatability of Tissue Samples

Cutting measurements were obtained from each of the samples immediately after they had been removed from the de-ionized water to prevent dehydration, which would result in changes in tissue properties. The angular velocity at which all samples were cut was maintained constant at 22.7 deg·s^{-1} to ensure that the conditions would be as consistent as possible, and allow comparisons to be made between samples. The velocity was maintained constant by adjusting the air flowrate to the pneumatic actuator which in turn closed the scissor blades. The change in angular displacement ($\Delta\theta$) was plotted against the time taken (Δt) for the blades to close fully. The slope of the graph was the angular velocity of the blade. A speed of 22.7 deg·s^{-1} was chosen based on data collected by Greenish [75] which found that the average speed during actual surgical cutting

procedures was found to be in the range from 7 deg·s^{-1} to 44 deg·s^{-1} depending on the material being cut. Each sample was subjected to one complete cutting cycle involving the blades closing from 40° to 7.5° and returning to the fully open position again, resulting in a 32 mm long cut. Data from three different cuts from each sample set were compared to establish the repeatability of the measurement system. An example of the closeness of agreement after three cuts for one sample set is illustrated in Figure 3-10.

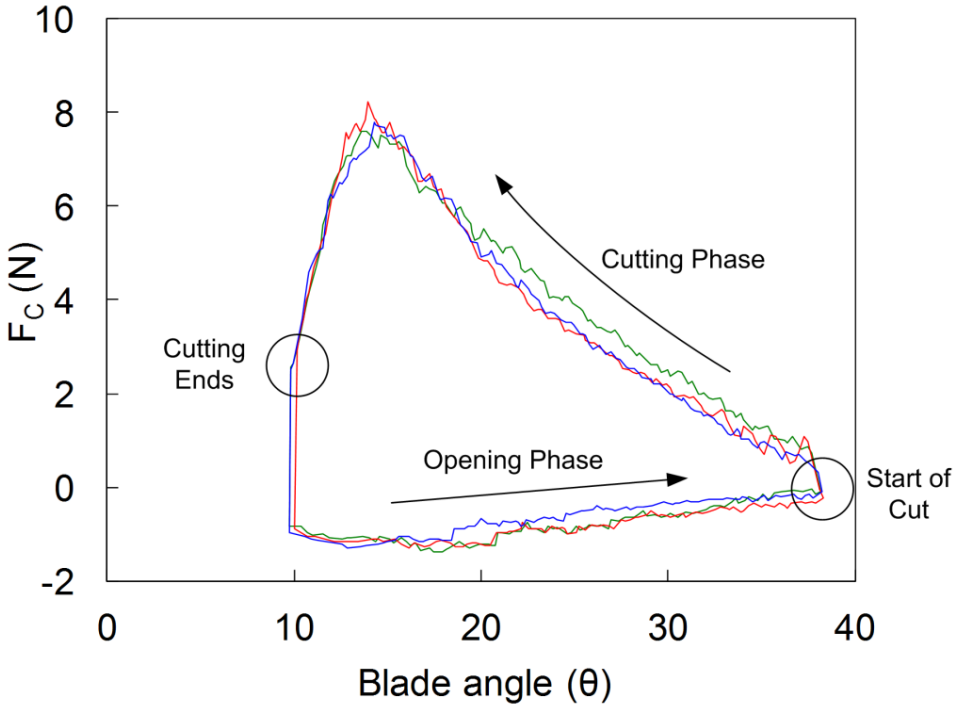

Figure 3-10 Repeatability graph for three cuts of sample 3FT

3.4.3 Analysis of Force Profiles

Each cutting cycle consists of a number of different stages [55]. Engagement is the initial phase, where by the blades make contact with the tissue. This is illustrated in Figure 3-11 by the sudden rise in the force reading at t = 0.01 s.

From this point onward there is a combination of phases such as plastic deformation and intercellular fracture followed by separation along the line of the scissor blades. This process continues along the cutting edges, until the end of the cut is reached at 10°. Beyond this angle, the forces generated from 10° to the fully closed position of 7.5° are not as a result of contact forces but are due to frictional forces between the blades only. Force-displacement curves were created using the data collected from the sensorised scissors while cutting each of the five different tissue samples (Figure 3-12). It is observed that the force distribution along the blades for the softest sample (one freeze-thaw cycle) followed a similar profile to that for the empty cut with only a slight increase in magnitude. This was expected as the Young's modulus value for this sample was quite low and also highlights the capability of the test-bed to detect low level force values arising from softer samples.

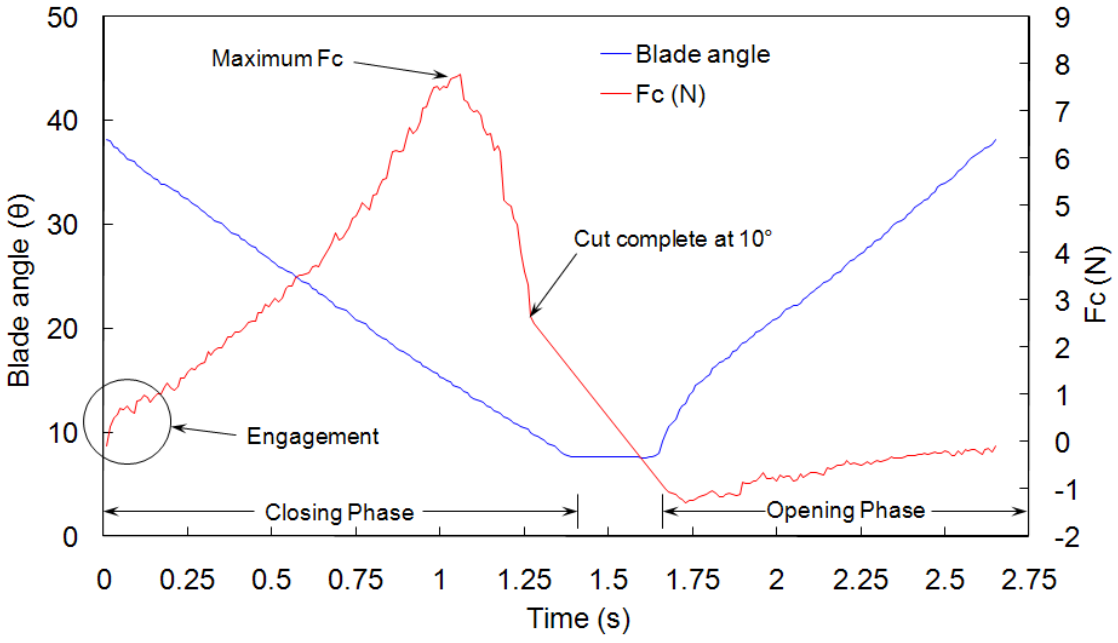

Figure 3-11 Typical soft tissue cut characteristics

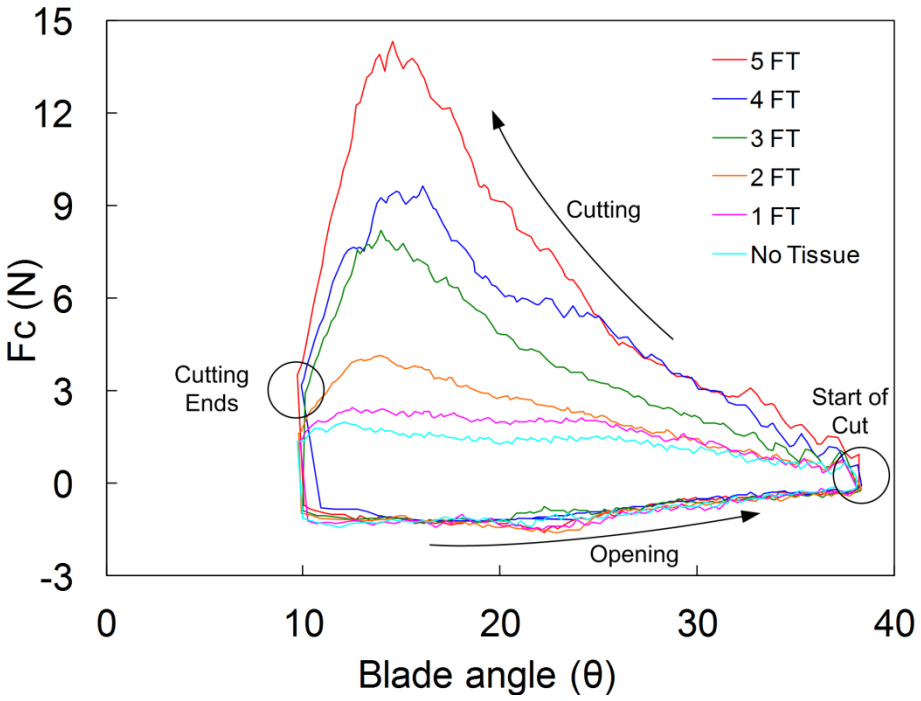

Figure 3-12 Cutting force profiles for five PVA samples obtained from the characterisation testbed

For each of the other samples, the contact force continuously increases along the blade length, with a significant increase in the maximum force towards the end of the cutting cycle. This may be due to the fact that as the angle of the scissor blades decreases it has the effect of squeezing the tissue resulting in an extended plastic deformation phase before fracture and separation stages [75]. It is reasonable to assume that the forces generated due to deformation of the tissue with the blades would be greater than those generated during fracture, warranting further investigation. It was expected that the location of the maximum contact force would be at the tip of the blades corresponding to an angle of 10°, however, it can be seen from Figure 3-12 that the maximum force occurs before the end of the cut. An explanation for this may come from the fact

that, during cutting, the tissue is being pushed forward slightly due to the longitudinal components of the forces acting on the blades. Towards the end of the cut the tissue may slide off the blade tip instead of being cut, accounting for the sudden drop in contact force after the maximum is obtained.

3.5 Strain on Blade Surface

A direct force sensing approach requires placement of a strain-force sensor directly onto the blades as close to the point of force generation as possible. It is important, therefore, that the nature of the strains at the location of the sensor is understood. To ascertain the nature of the strains generated on the blade surface, a miniature strain gauge (RS 632-124 N11-MA2-120-11) (strain gauge 2 in Figure 3-13) was bonded to the upper edge of one blade to directly measure the strains experienced by the blades during cutting.

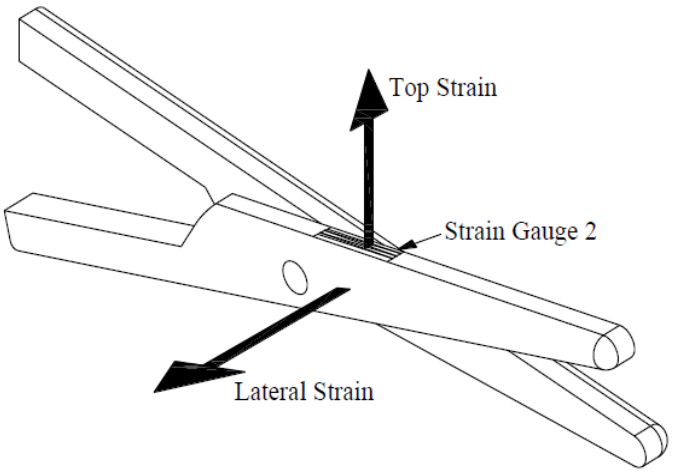

Figure 3-13 Direction of strains acting on the blade upper surface

Results from strain gauge 2 (Figure 3-14) show that the measured strain ranges from +62 με for the softest sample to -121 με for the stiffest sample. It is

interesting to note that even though the top surface of the blade onto which the strain gauge is attached experiences compressive strain resulting from tissue cutting, the strain readings for the first two samples (1FT and 2FT) are positive values. The strain values for 3FT to 5FT are negative as expected and increase in magnitude as the sample stiffness increases. On close examination of the blades during a cutting cycle it was observed that lateral deflection of the blades, due to blade curvature along its length, was significant. This lateral deflection in turn induced lateral strain at the location where the strain gauge was attached. Therefore, the strain values being measured by the surface-mounted strain gauge were not exclusively as a result of cutting forces but a combination of cutting, friction and lateral forces.

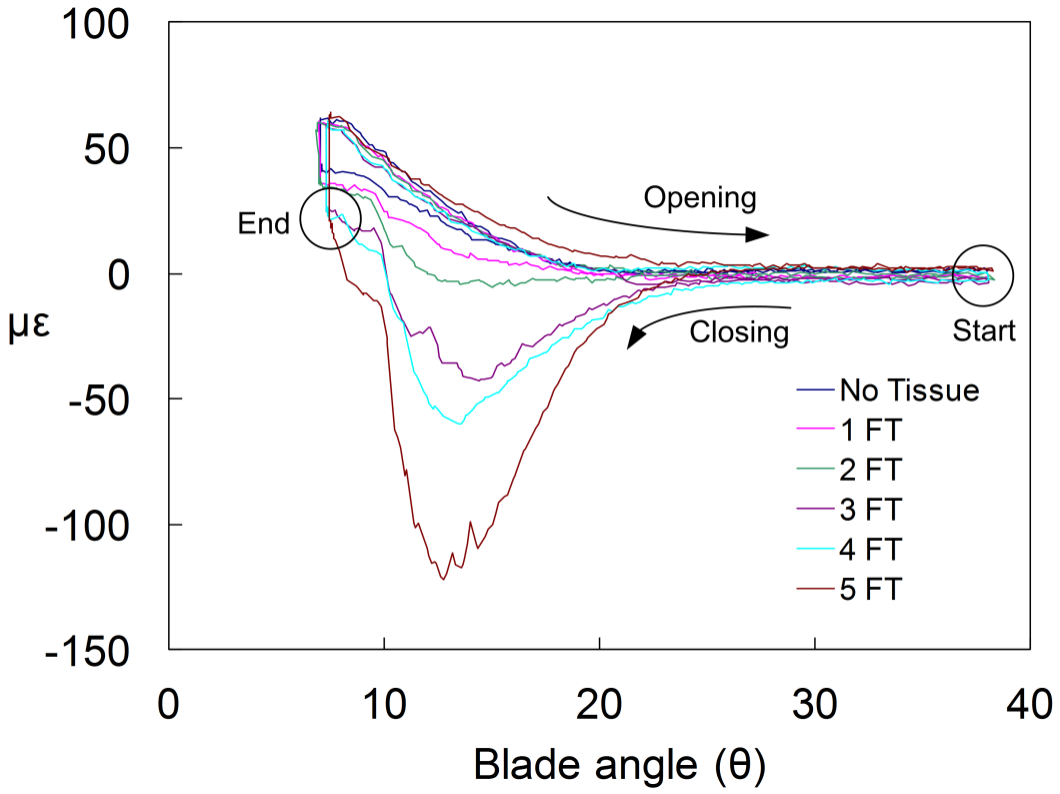

Figure 3-14 Experimentally obtained blade strains during soft tissue cutting

It is clear that the integration of a force sensing element into the tip of the scissor blades will require detailed analysis of the effect of the various strain components on the required force readings. Consideration needs to be given to the decoupling of these various strain components particularly if accurate tissue fracture properties are to be obtained from the measured force data. Forces due to cutting of the tissue are the primary forces of interest; therefore, a means of eliminating the inadvertent lateral blade forces needs to be established. It is important to note that in terms of sensor selection, the resolution of the measurement system is of greater significance over the working range (25° to 10°) as this is the portion of the blade primarily used by surgeons while cutting as documented by Greenish [75]. This equates to the surgeon utilising approximately 56% of the blade length cutting edge measured from the tip. This would suggest that, from the point of view of sensor placement, the remainder of the blade (44%) towards the blade pivot can be regarded as a sensor placement zone. From Figure 3-12 it can be seen that the maximum measured force for all tissue samples occurs between 12° and 18°. Clearly this cutting region of the blade is where the greatest force sensitivity is occurring and gives credence as to why surgeons prefer using it.

3.6 Limitations of Test-Rig

It was felt that collecting force data from the characterisation rig using a calibrated strain gauge attached to the scissor arm was not an optimal method as there was still a degree of inference required in the values obtained. The

purpose of the characterisation test rig is to form a basis for assessing and validating new sensing technologies against more established off-the-shelf technologies such as strain gauges and load cells. To this end, an evolution of the test rig configuration was carried out in which a commercially available load cell was incorporated into the characterisation test rig. The benefits of this arrangement were twofold;

- A commercially available precalibrated load cell would be used as a benchmark against which force measurements from the proposed FBG sensing arrangement could be validated.
- The placement of the load cell unit at the scissor handle actuator ensured that external forces acting on the scissor handle could be measured directly.

Measuring externally applied forces on the scissor handles offers a reliable means of calculating the work done due to intrablade friction and fracture during cutting. These externally applied forces are of particular importance when using scissor blades to estimate the fracture toughness of the material being cut as the total external work done W during fracture is calculated using,

$$W = \int_{a}^{b} (F_{ff} - F_f) dz \tag{3.6}$$

where dz is the infinitesimal displacement of the scissor actuation mechanism and b-a is the total displacement of this mechanism during a cut [108]. F_{ff} is the

force due to combined fracture and blade friction and F_f is the force due to blade friction only. The acquisition of accurate force measurements dictated that the rig be modified to incorporate a commercial load cell located at the point of scissor actuation enabling real-time force readings to be obtained. This approach in turn would serve as a means of validating cutting force readings from miniature force sensors placed on the scissor blades. Force values can be compared directly to values obtained from the commercial load cell. An inline load cell (DSM 50 from Transducer Techniques) was used as shown in Figure 3-15.

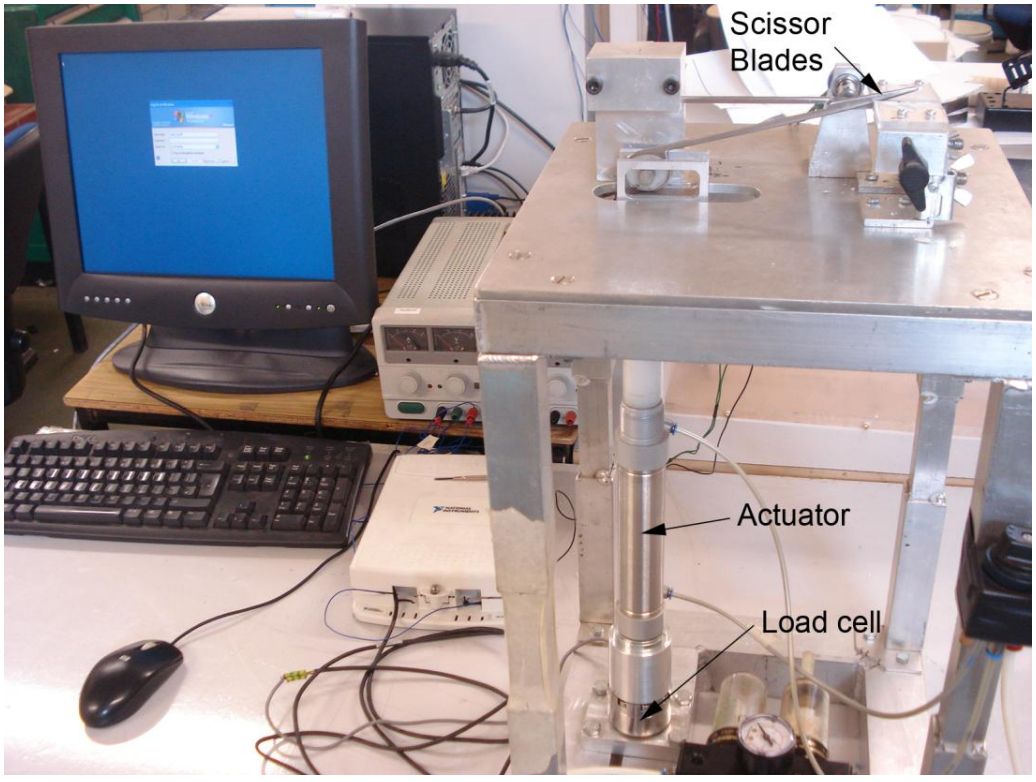

Figure 3-15 Modified characterisation test-bed showing location of load cell

3.7 Obtaining Fracture Toughness Values

The sensitivity of the modified test-bed to forces generated from cutting synthetic tissue samples with differing fracture properties and dimensions is assessed in this section. A series of cutting tests were carried out using the test-bed. The objectives of the tissue cutting tests were to examine the following:

1. The effect of tissue thickness on forces generated on the scissor blades.
2. The effect of tissue stiffness on the forces acting on the blades.
3. The effect of tissue fracture toughness on the forces acting on the blades.
4. The effect of pretensioning the samples being cut.
5. The effect of two different analysis methods for the estimation of fracture toughness values.

3.7.1 Preparing PVA Samples

The synthetic PVA samples used were prepared and manufactured using the method outlined in Section 3.4. The work done in fracturing a tissue sample is a dependent on the net fracture force, the length of the cut and the thickness of the material being cut [109]. Therefore, it was decided to use PVA samples over a range of thicknesses and stiffnesses, where the stiffness of each sample is determined from the number of freeze-thaw cycles it was put through during manufacture. Medium (3 FT) and high (5 FT) stiffness PVA samples were chosen for these experiments with each sample having thicknesses of 1, 3, and 5 mm. Previous work by Chu [124] showed that increasing the number of FT cycles results in reduction in the sample dimensions due to a loss of moisture content.

This decrease can be as much as 20% in some cases. Examination of the cylindrical specimens used in Section 3.4 indicated that there was a clear decrease in the specimen diameters as the number of freeze-thaw cycles increased. To quantify the decrease in sample diameter the original inner diameter of the mould was measured (18.6 mm) and used as a reference diameter for each of the five specimens. The percentage change in diameter for each specimen is illustrated in Figure 3-16. The relatively linear nature of the decrease between one and four freeze-thaws correlates with findings by Chu [124] where the wall thickness of a PVA aortic phantom decreased linearly up to 5 freeze-thaw cycles. Thereafter, up to 10 freeze-thaw cycles, the reduction in thickness was minimal.

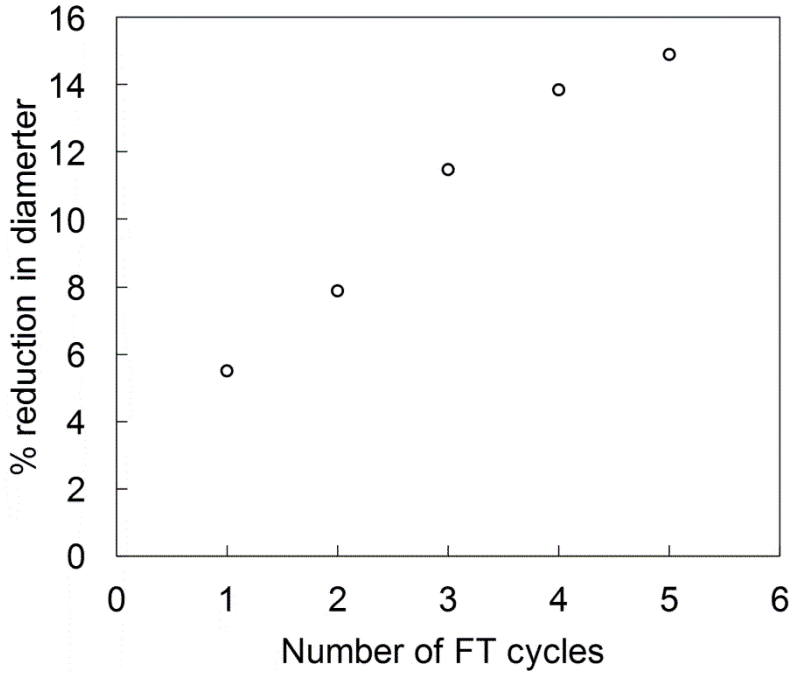

Figure 3-16 Percentage reduction in PVA sample diameter as the number of FT cycles increase

The nylon moulds were machined deeper than the target thickness of the sample to allow for shrinkage and to ensure that the required PVA sample thicknesses of 1, 3 and 5 mm were obtained. One mould for each sample thickness was manufactured as opposed to one mould per FT cycle per sample thickness as the shrinkage difference between 3 FT and 5 FT was approximately 3.5%. This was deemed small enough to have minimal effect on the final thickness of the finished sample. A summary of the mould dimensions and the final sample thicknesses are presented in Table 3-4. It can be seen that the final sample thicknesses are in good agreement with the target thicknesses. Moreover, the use of the original cylindrical samples to estimate the percentage increase in the new mould dimensions was a suitable technique in achieving accurate sample thicknesses.

Target Sample Thickness (mm)	FT Cycles	Mould Depth (mm)	Final Sample Thickness (mm)
1	3	1.15	1.1
	5		0.97
3	3	3.4	3.1
	5		3.06
5	3	5.7	5.1
	5		5.09

Table 3-4 Target and actual PVA sample thicknesses

3.7.2 Fracture Characteristics of Synthetic Samples

Literature suggests that measured fracture toughness (J) is sensitive to the type of test performed [125]. This is consistent with the fact that tests carried out on

rat skin using both a trouser test and a scissor test showed that J values obtained from the scissor test were an order of magnitude lower than that obtained from the trouser test. This is believed to be due to the fact that scissor tear tests maintain a sharp crack tip ahead of the blades [125].

The forces measured at the scissor handle for all six PVA samples are presented in Figure 3-17. It can be seen that the force profiles from samples 1 mm_3FT to 3 mm_3FT (and to some degree sample 3 mm_5FT) are relatively smooth through the cutting cycle from the point of initial contact with the tissue, through the compression-fracture phase up to the point of tissue failure. It is interesting to note that this smooth profile is similar to the force values[6] obtained in Section 3.4.3 where all the sample thicknesses were constant at 3 mm. Comparing force profiles for samples < 3 mm to the profiles of the 5 mm samples, it can be seen that the 5 mm force profiles are not smooth but contain a number of very distinctive compression-fracture peaks. In the case of the 5 mm_3FT and the 5 mm_5FT samples it is obvious that the magnitude of these peaks increase from approximately $\theta = 23°$ to the end of the cut at $\theta = 12°$. This suggests that as the angle between the blades decreases and becomes more acute through the cutting cycle the tissue experiences a lot of compression between the blades before the force is sufficiently high to further propagate fracture [125].

[6] Original values represent forces acting on the blade and not at the scissor handle.

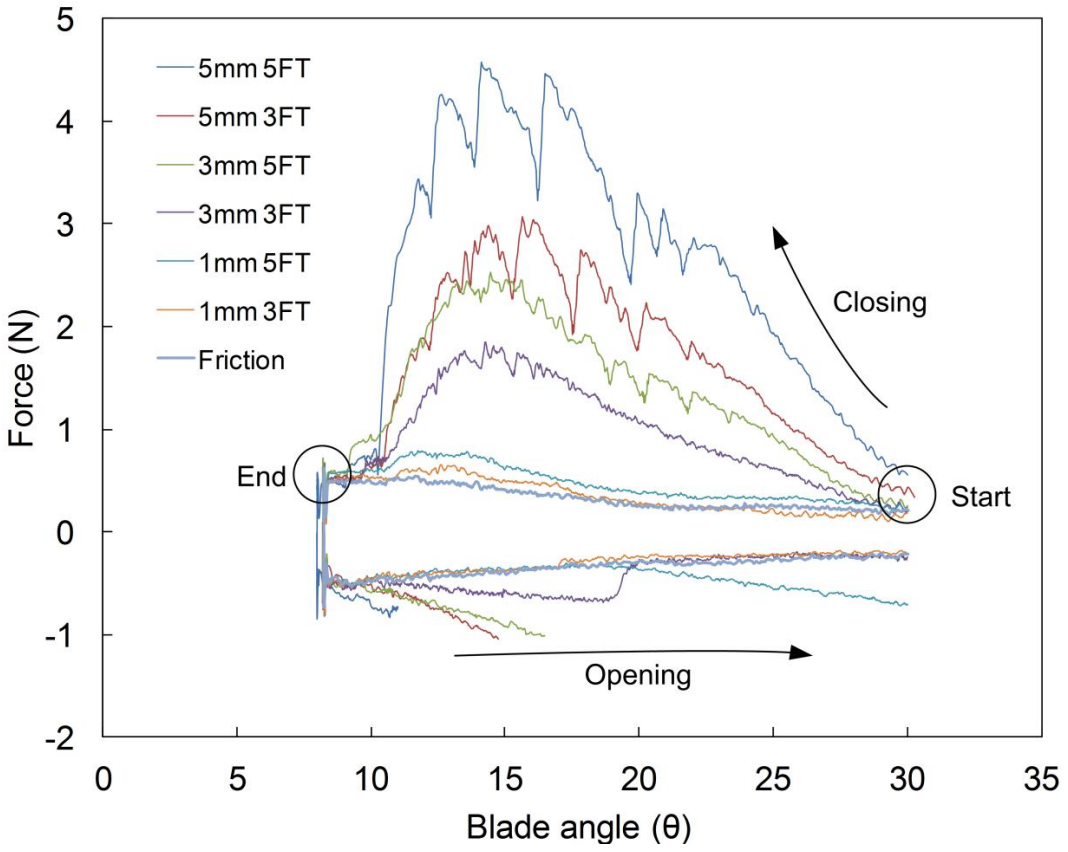

Figure 3-17 Experimental cutting force profiles from six PVA samples[7]

Moreover, at the beginning of the cutting cycle, at θ = 30°, the wide blade angle will have the effect of pushing the tissue ahead of the blade intersection point before it actually begins to fracture it. As the blade angle reduces this so called slice-push ratio [126] decreases and so the combined compression-fracture forces increase due to;

- the compression of the tissue between the blades inducing a clamping effect on the tissue, and,

[7] The negative force values shown for some samples is due to the tip of one of the blades slipping under the clamped sample at the end of the cut and snagging it during the blade opening phase of the cycle.

- the residual forces present in the tissue due to the initial pushing are now acting in the opposite direction to blade motion keeping it pressed against the blade intersection point.

During guillotining, deformation and subsequent fracture of the material occurs over the small region around that part of the blade in contact with the material being cut [126]. Analysis of this region (Figure 3-18) shows how the non-steady state force vs blade stroke for orthogonal cropping can be used to estimate the steady state force component of guillotining in the cut plane of intense shear.

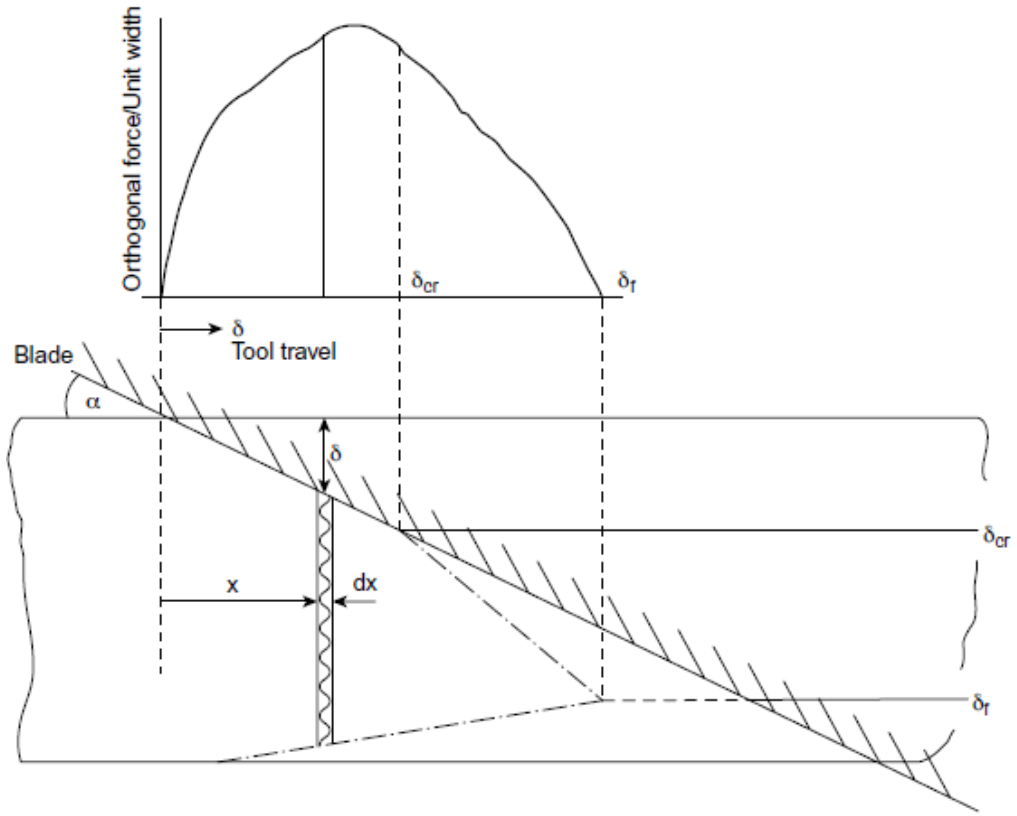

Figure 3-18 Non steady force vs blade stroke during cropping with a guillotine [109]

The mean total work per area performed over the cut face from $\delta = 0$ to $\delta = \delta_t$ consists of the indentation plastic work from $\delta = 0$ to $\delta = \delta_{cr}$ followed by the subsequent fracture between $\delta = \delta_{cr}$ and $\delta = \delta_t$. This mean total work per area is defined by Atkins [126] as the effective fracture toughness (J^*) in the plane of intense shear.

Results obtained from the characterisation test-bed while cutting PVA tissue samples also exhibit this type of non-steady force behaviour, particularly values obtained from the thicker stiffer samples (Figure 3-19). Although scissor cutting and guillotining are not exactly the same in the way in which the blades move relative to one another there are obvious similarities between the way in which the PVA samples fracture during cutting and the way in which metal plates fracture during guillotining. This is illustrated in Figure 3-19 where the close up view highlights the various stages of work being carried out during the cutting phase of the cycle which corresponds closely to the plastic indentation and fracture characteristics identified in Figure 3-18.

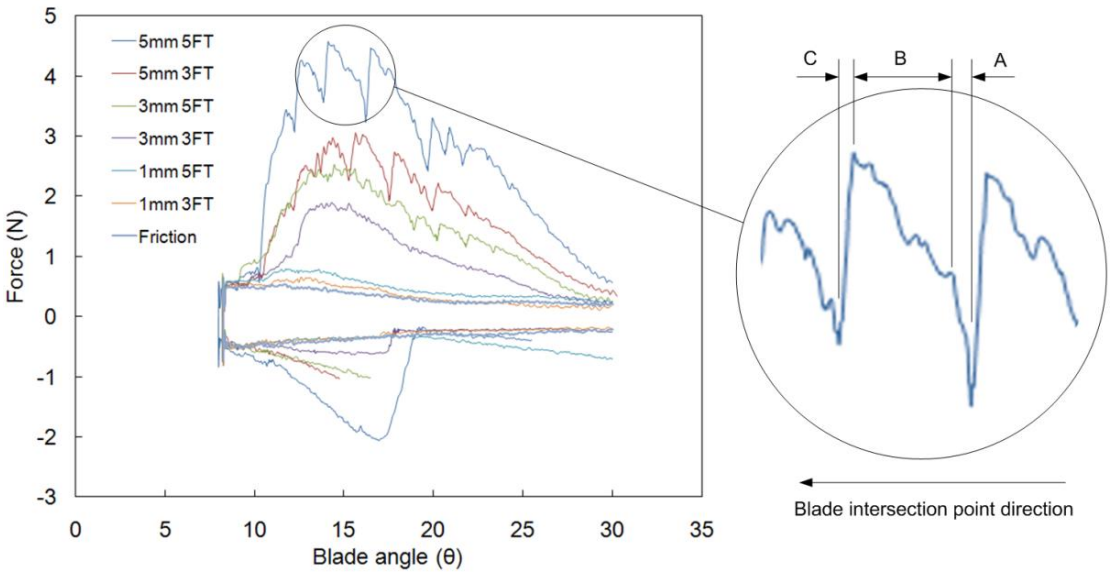

Figure 3-19 Compression and fracture characteristics of PVA sample

Phase A, for example, highlights the tissue sample is being compressed between the blades of the scissors without obvious fracture of the sample. Phase B suggests that while there is plastic indentation of the sample following compression, there also appears to be small fractures (at a microstructural level) occurring throughout the phase as the blades closes. The magnitude of the forces generated during these compression and indentation phases are greater towards the end of the cuts (between θ=16° and θ=12°) owing to the acute angle between the blades having a greater compressive effect on the samples. At the end of phase B, where the indentation force is at its maximum, the small cracks within the microstructure of the sample eventually coalesce under the increased load and fracture of the sample occurs. This localised fracture is evident in phase C and occurs over a small displacement of the scissor handles and related translation of the blade intersection point along the sample. The sum of the work

done over the three phases A, B and C is the effective fracture toughness J^* of the PVA samples being cut using scissor blades. This is not to be confused with the true specific essential work of fracture (fracture toughness) J, which does not reflect the inclusion of remote plastic work (B) nor compression work (A) both of which have nothing to do with the process of fracture [109].

3.7.3 Pretensioning Tissue Samples

It has been reported that tensioning a sample being cut by blades has the effect of reducing the cutting force require to fracture the specimen due to the lateral tension assisting fracture propagation [62]. This in part may be due to the fact that tensioning the material reduces the friction force between the material and the blades doing the cutting, hence a reduction in friction and not forces arising from fracture may be the cause of the force reduction. The reduction of the net force and its effect on the repeatability of the measurements can be assessed using the test-bed. The method of clamping the synthetic PVA samples into the test-bed involves securing the sample between two clamping jaws that can subsequently be moved away from one another to apply a degree of pretension to the sample (Figure 3-20). A method of obtaining the effective fracture toughness for these tensioned and untensioned samples is outlined in Section 3.7.4.

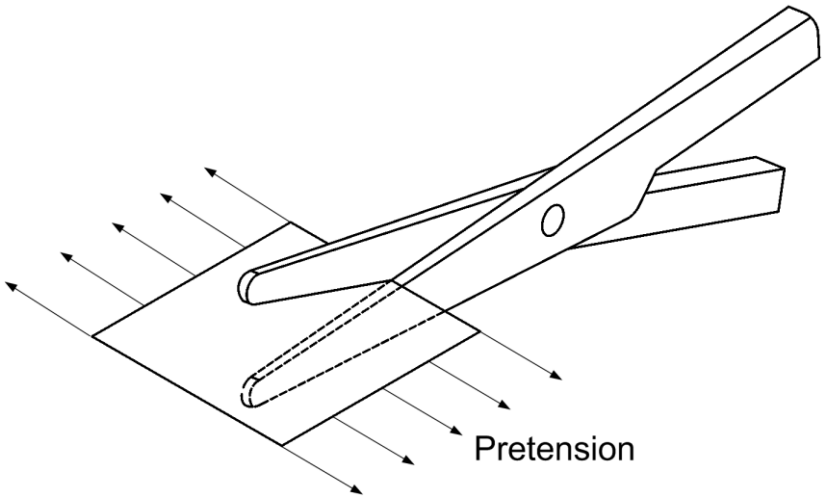

Figure 3-20 Direction of the applied tension in relation to the scissor blades

3.7.4 Obtaining J* (Method 1)

To determine J* an approach similar to that used by Pereira *et al* [108] is used. The method of obtaining the effective fracture toughness of the samples used in these experiments is outlined in Figure 3-21 where each stage is broken down as follows;

(a) PVA samples of thicknesses 1 mm, 3 mm and 5 mm (two of each thickness) were prepared as described in Section 3.4. Half the samples were put through 3FT cycles and the other half were put through 5FT cycles giving a total of six samples of varying stiffness and thickness.

(b) Force data was collected from the characterisation test-bed for all the samples. Each sample was glued to the clamping surfaces using cyanoacrylate glue to ensure that there was zero slippage of the sample during a cutting cycle. Additionally the clamps were designed so that they

could be translated away from one another allowing controlled tensioning of sample to be carried out.

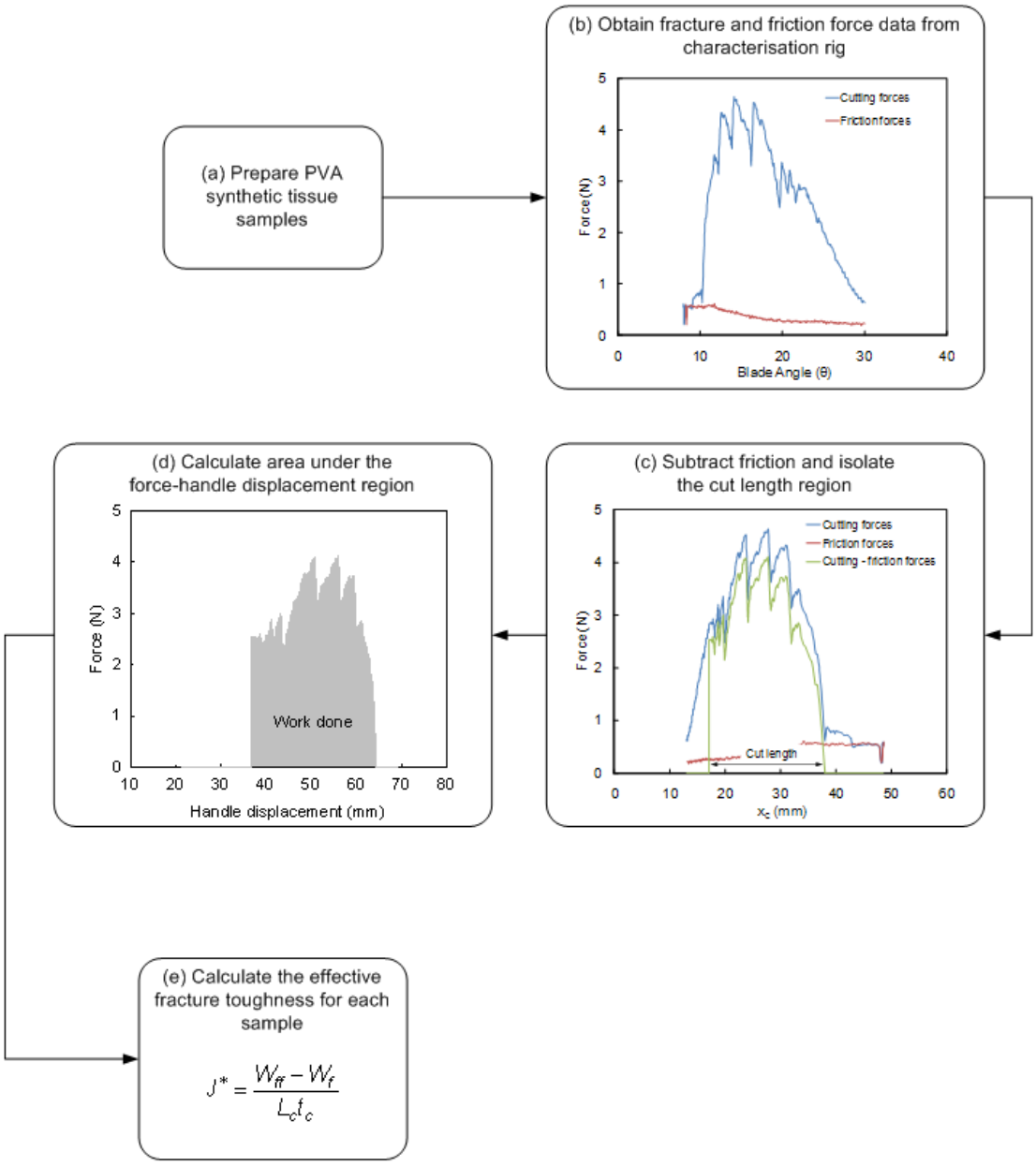

Figure 3-21 Method 1; obtaining effective J values using the entire cut length*

(c) Three cuts were made for each sample; one with zero tension, one with 5% strain applied by the clamping mechanism and one with 10% strain applied. This enabled the forces acting on the scissors to be assessed for each tensioned sample and to ascertain if the tension affected the magnitude of the forces.

The friction forces generated between the blades devoid of tissue were measured before each cut was carried out. Due to the low velocities involved, the minimal contact area between the two blades and the stiff nature of the blades, it is reasonable to assume that the friction forces generated during an empty cycle of the blades remained the same during a tissue cutting cycle. It should be noted that work carried out by [108] shows, that for some materials, the friction force profile before and just after cutting a specimen can vary. This can be attributed to micro particles being deposited on the blade cutting surfaces. It is believed that fragments deposited during the cutting of biological samples had adhered to the blades and altered the surface roughness, resulting in a change in the friction profile. Non biological samples e.g. PET plastic, which is tougher and more homogeneous, does not produce as many fragments during cutting. This results in a friction profile that does not deviate as much from the empty pass after cutting.

(d) Friction forces generated for an empty pass of the blades are subtracted from the combined fracture-friction force profile resulting in a force profile without the influence of friction. The force-displacement area calculated

under this profile is the work done during tissue fracture. The cut length L_c can be estimated when the force profile is plotted against the displacement of the blade intersection point x_c. All cuts end at x_c = 38 mm (1 mm from the blade tip[8]). The beginning of the cut can be established through identification of the first primary fracture which initiates separation of the tissue along the length of the blade cutting edges. Each cut was measured (using a pair of digital vernier calipers) to confirm the cut length estimated from the force data. Work done to fracture the tissue sample is defined as the product of the externally applied load and the displacement of the scissor handles where the load is applied. The area under this force-displacement profile was calculated using the numerical Trapezoidal integration method.

(e) The effective fracture toughness for each sample is calculated using,

$$J^* = \frac{W_{ff} - W_f}{L_c t} \tag{3.7}$$

where $W_{ff} - W_f$ is the work done due to fracture of the sample only, and t is the sample thickness.

3.7.5 J* Results (Method 1)

The J* results for each set of samples are presented in the box and whisker plot shown in Figure 3-22. The upper and lower limits of each box represent the 75th

[8] Between x_c = 38mm and x_c = 39mm the blade tips are rounded resulting in the blades passing one another without shearing the tissue.

and 25th percentile respectively (the interquartile range), with the median being the horizontal line in the box.

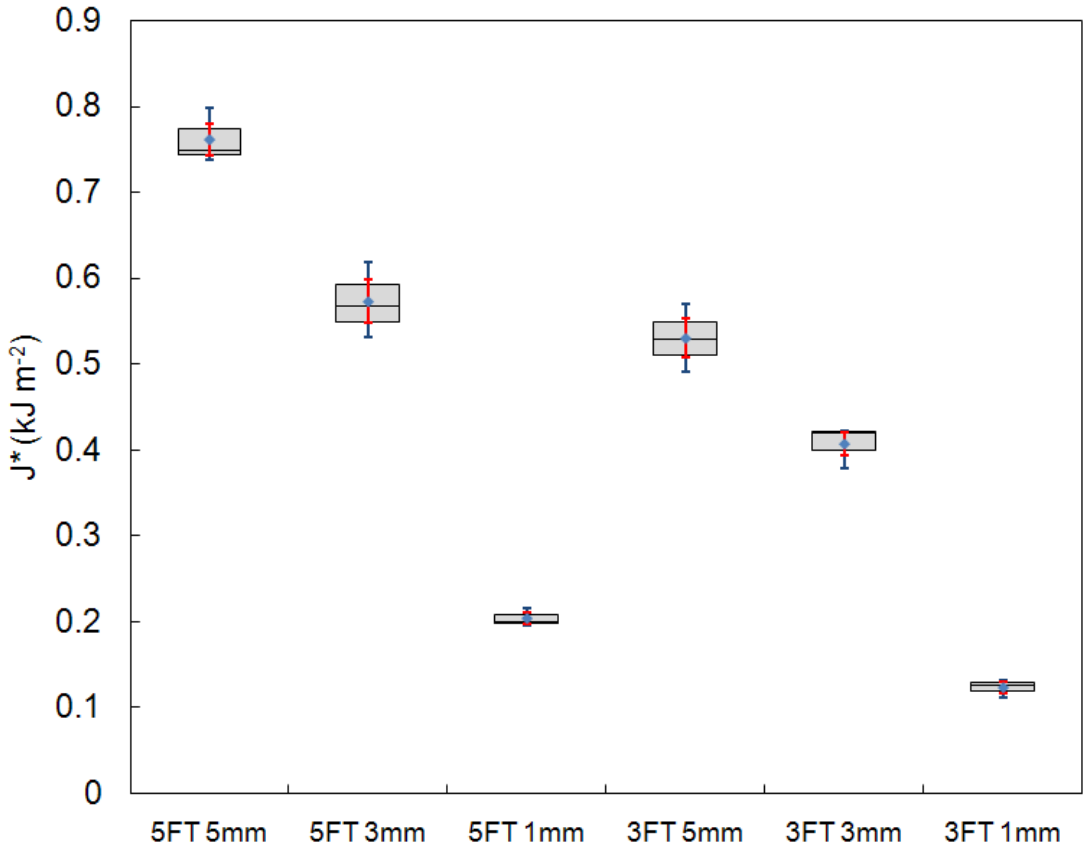

Figure 3-22 Mean J for samples experiencing varying degrees of pretension*

The ends of the blue whiskers denote the maximum and minimum values of the data set. The blue diamond represents the mean in the range. The red error bars denote the standard error of the mean value. The low standard error for each set of samples indicates that there is little difference between the J* values for an individual sample, whether tensioned or untensioned. However, there is significant difference between samples of the same stiffness but different thicknesses. It has been shown by [127] that there was no difference in the true

fracture toughness between thin (0.7 mm) and relatively thick (2.7 mm) specimens using a modified single edge notch (MSEN) test. Therefore, the use of a shearing technique to obtain fracture properties requires further understanding of the complex interaction occurring between the specimen being cut and the scissor blades. A reason for the variation in J* values could be attributed to variations in strain energy induced in a sample during a cutting cycle. Strain energy within a soft tissue sample during scissor cutting arises from the tissue being 'clamped' between the blades during a cutting cycle. As the blades go through a cutting cycle the angle between them changes and as a consequence the level of compression experienced by the tissue between the blades also changes. Furthermore, thicker samples are likely to experience a greater degree of clamping from the blades which in turn induces a higher level of strain energy. As quantitative strain energy values are difficult to obtain it is unclear to what extent the strain energy contributes to the J* values.

3.7.6 Obtaining J* (Method 2)

The methodology outlined in Section 3.7.4 (method 1) for obtaining J* is based on calculating the external work done over a complete cut length. This approach indicated that while the effective fracture toughness can be obtained, the nature of the cutting process means that J* is not independent of material thickness. An alternative method is investigated to ascertain whether J* values can be obtained independently of the thickness of the sample being cut. Method 2 differs from method 1, in the determination of J*, as the full cut length is not considered when

calculating the work of fracture but rather the work done over a number of individual fractures is calculated. This method of obtaining the work of fracture for a series of fractures while cutting a 5FT 5 mm sample is illustrated in Figure 3-23.

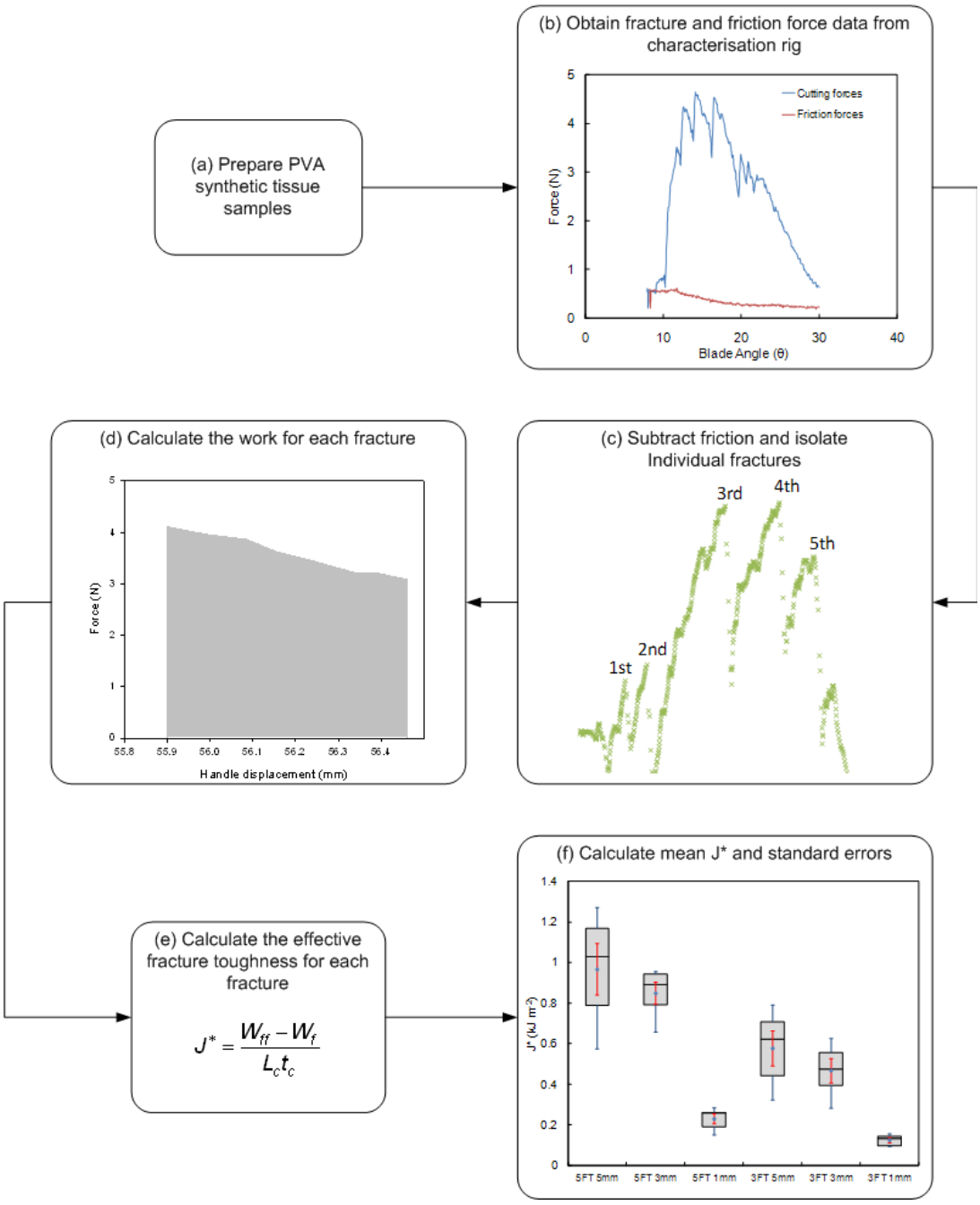

Figure 3-23 Method 2; Obtaining J using the individual fracture approach*

The key elements of this approach are the identification of the fractures to be analysed (Figure 3-23(c)) and the calculation of the work done during the propagation of the fracture (d). The fracture toughness equation (3.7) was used to calculate the localised J* where W_{ff} – W_f is the area under an individual fracture and L_c is the length of the crack over which the work was calculated. L_c was measured by taking the location of the blades intersection point at the start of the fracture from the location at the end of the fracture. The difference was deemed to be the fracture length L_c.

3.7.7 J* Results (Method 2)

The results obtained for J* using method 2 are presented in Figure 3-24. Higher J* values for the 3 mm and 5 mm samples are observed when compared with the 1 mm samples. The mean J* values obtained using method 2 are generally higher than values obtained using method 1 as shown in Figure 3-25 with an average 15% difference. This would indicate that method 2 is possibly more sensitive to the thickness of the material being cut as well as the nature of the scissor cutting method.

This is supported by the fact that for samples 5FT1mm and 3FT1mm the difference in J* is negligible and the standard error is low. From the results obtained it is believed that the respective J* for 5FT1mm and 3FT1mm are closer to the true fracture toughness of the material than the values obtained for the stiffer, thicker samples. Similar results have been observed by Atkins [128] while guillotining thin sheets of metals of different thicknesses. It was stated that the

higher J* value reflects the inclusion of remote plastic work which has nothing to do with the work of fracture.

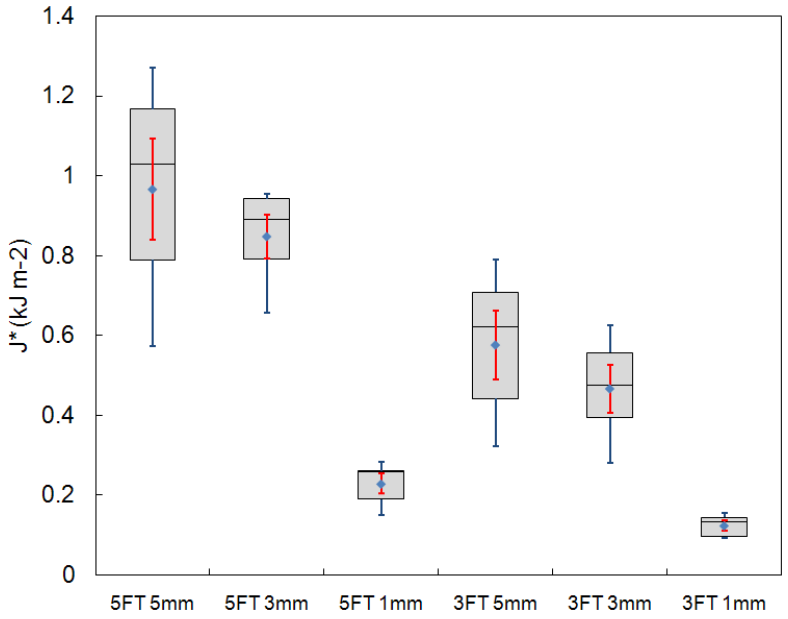

Figure 3-24 Mean J values obtained using method 2*

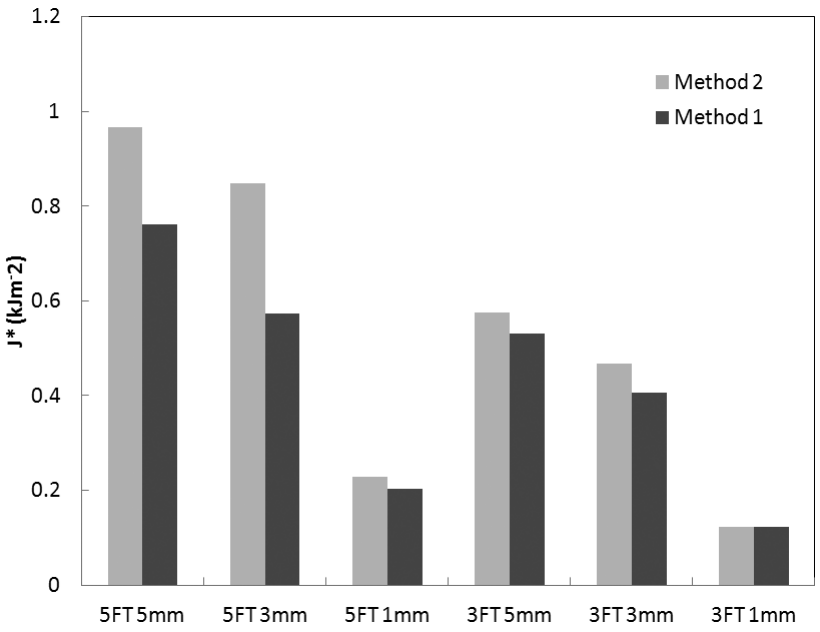

*Figure 3-25 Comparing both methods of obtaining J**

3.7.8 Discussion on Fracture Results

It has been observed, that at the beginning of a cutting cycle, the tissue is pushed in front of the blade intersection point before the initial material fracture occurs. This initial localised pushing is due to the large opening angle of the blades and the gap of 30 mm between the support clamps in which the sample is secured. This localised pushing combined with material compression between the cutting edges of the blades is evident in Figure 3-17 between θ = 30° and 23°. However, after the initial primary fracture occurs it is not clear to what extent the sample returns to its original prefracture condition. There appears to be a percentage of the original pushing force present throughout the remainder of the cut materialising as strain energy. This in turn changes the deformation pattern around the crack tip as it propagates through the material. Evidence of this residual strain energy was observed at the end of each cut when the portion of the sample just ahead of the tip of the scissor blades slipped back over the blade upon cut completion. The extent to which the sample slipped over the blade tip appeared greater as the sample size and stiffness increased. Attaining values for the specific work of fracture, independent of the effects of residual strain energy, requires a detailed investigation into the contribution of residual strain energy in determining J* of a sample. An energy balance equation proposed by [129] for the determination of fracture toughness is,

$$J = \frac{(Xu - d\Lambda) + dU - F_f u - d\Gamma}{dA} \tag{3.8}$$

where Xu is the incremental external work done, $d\Lambda$ is the elastic strain energy stored in the specimen, $d\Gamma$ is the incremental plastic work, dU is the energy stored in the specimen due to transverse loading and $F_f u$ is the work resulting from contact between tissue specimen and the blade surface. In most cases where sharp cutting (assumed to be quasi-static) is used to determine fracture toughness $d\Lambda$ and $d\Gamma$ are typically neglected [130]. This is reasonable if the cutting edges of the tools are considered sharp, leading to the assumption that the elastic energy stored in the specimen is much smaller than the irreversible work due to fracture, in turn limiting the measurement error. Experimental force-displacement graphs obtained by [59, 72, 120, 130] showed that the elastic strain energy had the effect of shifting the curves along the y-axis but did not affect the slope of the curve and hence can be ignored in the calculation of J. However, when making cuts with scissor blades the included angle of the blades is continually changing and therefore the amount of strain energy present in the material is also changing as the blades progress through the tissue. This is due to the contact region between tissue and blade increasing as the blades close as shown in Figure 3-26.

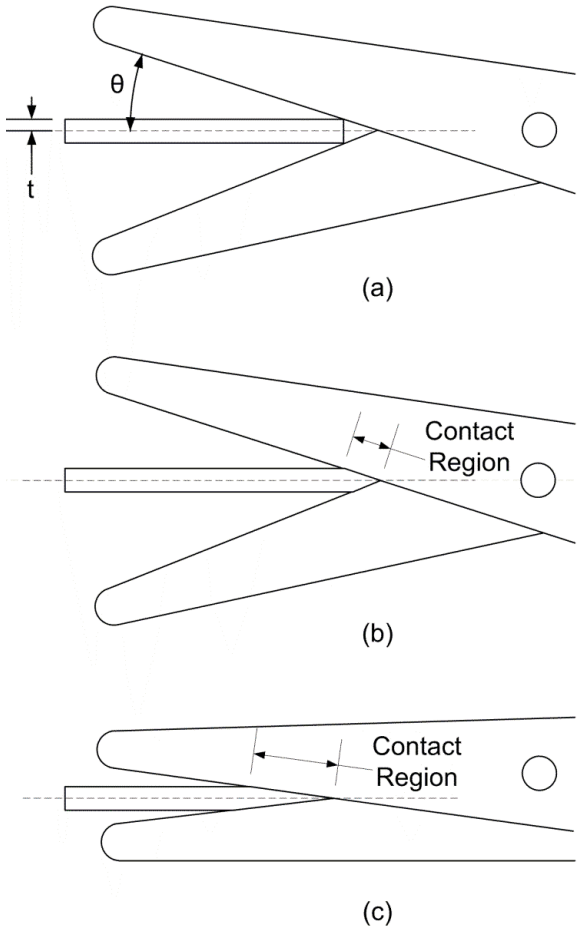

Figure 3-26 Change in contact region between blade and tissue throughout cut

In Figure 3-26(a) there is no contact between tissue and blades; in (b) the blades compress the soft tissue creating a moderate contact region from the blade intersection point. Clearly as the blade closes, this contact region increases as shown in (c) inducing greater strain energy in the tissue being cut.

3.8 Summary

In this chapter a force measurement evaluation apparatus has been designed and developed which can cater for the characterisation of scissor-cutting

procedures on synthetic tissue samples with known elastic properties. The major system requirements were measurement and acquisition of:

(i) the forces experienced by the scissor blades,

(ii) the angular displacement of the blades, during the cutting procedure.

The test apparatus was found to be robust, accurate and capable of discriminating between homogeneous tissue samples of varying mechanical properties.

The force-displacement curves obtained from the test-bed exhibited typical scissor cutting characteristics such as tissue engagement, elastic deformation, plastic deformation, fracture and separation. It was observed that the maximum force during a cut, occurred before the cut was completed, indicating tissue slippage towards the tips of the blades. Data showed that the cutting apparatus was clearly able to distinguish between the range of tissue samples used. The force displacement profiles are in general agreement with those published in other literature. Fracture toughness values have been estimated using two different methods. Both methods highlight the complexities associated with obtaining fracture properties from soft tissue.

The key conclusions of this chapter can be summarised as follows:

- The application specific test-bed developed is capable of facilitating the characterisation of interaction forces occurring between tissue sample and surgical scissor blades. It forms the basis of a test rig which can be further developed to assess alternative and new force sensing technologies for surgical cutting instruments.

- The range and nature of the forces likely to be experienced by the scissor blades have been measured. Based on this data, loads not exceeding 30N will be used in future modelling and experimental work.
- Strain values measured by a surface mounted sensor cannot exclusively measure fracture induced forces but rather a combination of fracture, friction and lateral forces. The integration of a force sensing element into the tip of the scissor blades will require detailed analysis of the effect of the various strain components on the strain arising during tissue fracture. Decoupling of these various strain components will be required.
- The determination of fracture properties for soft tissue samples using scissors is complex. Effects such as, compression of the tissue by the blades, and tissue being pushed ahead of the blades during cutting, make ascertaining true fracture property data challenging. It is therefore proposed that the energy required to fracture the tissue sample during cutting be referred to as the effective fracture toughness, incorporating strain energy arising from tissue compression as well as true fracture energy.

Chapter 4

Strain Transfer from Blade Structure to Fibre Core

4.1 Introduction

This chapter investigates the parameters which affect strain transfer from the blade structure to the core of a bonded FBG sensor. Two cases are considered; a surface mounted FBG attached to the blade upper surface and a FBG partially embedded within the blade. This study is necessary as FBG sensors, unlike ESG sensors, are not manufactured in modular units complete with a polyimide backing strip allowing the strain gauge to be bonded to a structure. Therefore, consideration needs to be given to the factors which influence the transfer of strains which arise in and on the blade structure during cutting. This chapter presents details of the main factors affecting strain transfer to the FBG sensor. Preliminary investigations focus on bonding the FBG to the upper surface of a mocked up scissor blade and estimating the theoretical average strain transfer coefficient (ASTC) between the blade and the core of the FBG. FEA simulations of

the FBG bonded to the blade surface are carried out for a range of adhesive layer thicknesses (10 – 200 μm) and bond lengths (5 – 13 mm). Experimental validation of the FE results was achieved using an application-specific test rig incorporating a simplified geometrical realisation of an actual surgical scissor blade. The rig design allows for the bonding of an electrical strain gauge (ESG) and a FBG sensor simultaneously, enabling their respective performances to be evaluated. Loading the blade will induce strain in the blade allowing the effectiveness of strain transfer from blade structure to the FBG sensor to be assessed. A study is also carried out on a FBG which is partially embedded within a groove machined into the mocked up blade. The ASTC is assessed both analytically and numerically and results verified experimentally. Additional factors such as transverse strain gradients through the groove and lateral loading of the blade are also investigated. The sensitivities of the surface mounted FBG and the embedded FBG are examined to assess what effect embedding the FBG has on the sensor performance.

4.2 Strain Transfer Theory

Initial theoretical investigations into the strain transfer from a host matrix to a cylindrical fibre were carried out by Cox [131]. The resultant derived solution is adapted in this work to a four-layer cylindrical model for the purpose of identifying the strain transfer parameters which influence strain transfer between host material (the blade) and fibre (FBG) core.

A bare FBG encapsulated within a protective coating, adhesive layer and the blade material is illustrated in Figure 4-1. The blade is the only element to which an axial load (x-direction) is directly applied.

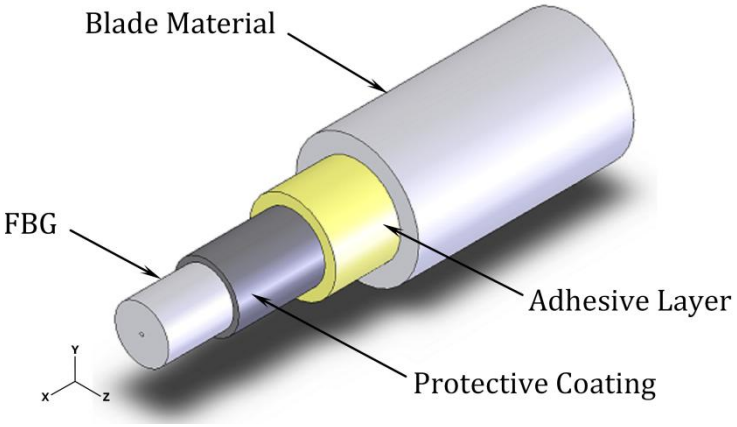

Figure 4-1 A FBG fully embedded within the blade

The resulting strain is transferred to the bare FBG as a result of shear strain developed within the two intermediate layers. The average strain transfer coefficient (ASTC) is defined as the ratio of the average strain over the bonded FBG to that of the blade (ε_m) and can be calculated using the following expression,

$$\bar{\alpha} = \frac{\bar{\varepsilon}_f}{\varepsilon_m} = 1 - \frac{\sinh(kL)}{kL\cosh(kL)} \tag{4.1}$$

where L is the length of the FBG sensor and k is the shear lag parameter encapsulating the material and geometric properties of the FBG, coating and adhesive layers and is given by,

$$k^2 = \frac{2}{E_f r_f^{\,2}\left[\frac{1}{G_c}\ln\left(\frac{r_c}{r_f}\right)+\frac{1}{G_a}\ln\left(\frac{r_m}{r_c}\right)\right]} \tag{4.2}$$

where G_c and G_a are the shear modulii values for the protective coating and adhesive layer respectively and E_f being the Young's modulus of the FBG material (Silica). The terms r_f, r_c, and r_m refer to the radii of the FBG, the FBG coating and the adhesive layers respectively (Figure 4-2). These equations show that the strain in the FBG core is influenced by the bonded length of the FBG as well as the geometric and material properties of the FBG and intermediate layers.

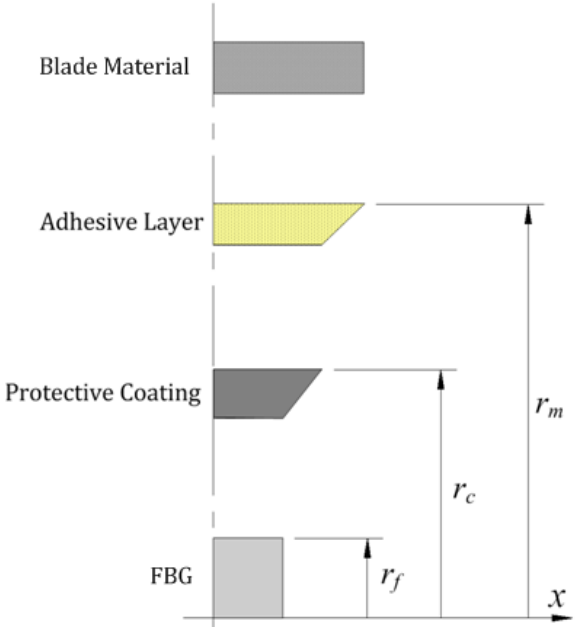

Figure 4-2 FBG, coating, adhesive and blade material layers

A surface mounted FBG sensor differs from an embedded FBG in that the host material does not fully encapsulate the coated FBG (Figure 4-3).

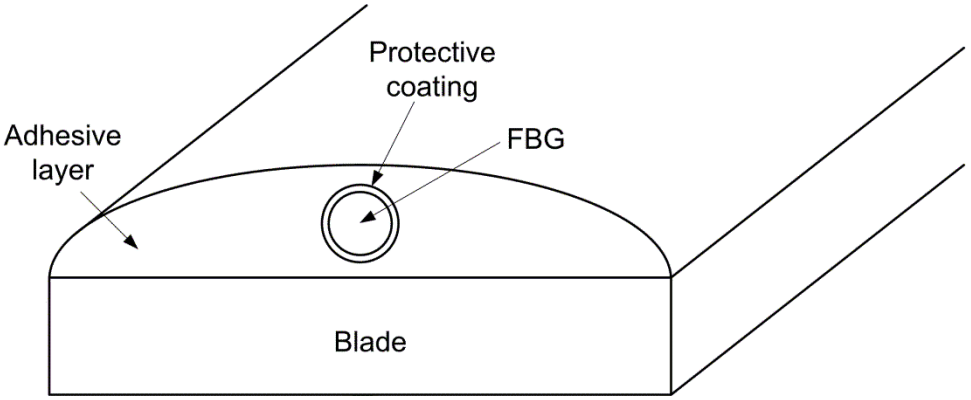

Figure 4-3 FBG sensor surface bonded to the blade

The coated FBG is instead bonded to the surface of the host material (blade) by the adhesive. The adhesive between the blade and the FBG coating does not exhibit an annular cross sectional profile, but can be approximated as a semi-elliptical profile. It is obvious for a semi-elliptical adhesive layer that a concentric adhesive outer radius r_m does not exist and as a consequence equations 4.1 and 4.2 are not applicable when considering a surface mounted fibre. Therefore, it is proposed that a numerical simulation be used to model the surface mounted FBG and incorporate the fact that it is not fully embedded within the blade.

4.3 Numerical Simulation of Surface Mounted FBG

In practice, the adhesive layer tends to take up a flattened profile which is approximated as an ellipse for the purpose of this numerical model. A previous study by Wan *et al* [132] demonstrated that variation in side width and top thickness of the elliptical profile had negligible effect on the strain transfer from

host material to FBG core. It was shown, however, that the adhesive thickness, t_a, between the protective coating and the host material surface greatly influenced the average strain in the FBG core.

4.3.1 Details on the FBG sensor

The finite element model was created with reference to the FBG being used in concurrent experimental work in which the FBG was bonded to the surface of a replica scissor blade. This experimental work is discussed in detail in Section 4.4. The FBG used was manufactured from a length of SMF 28 single mode fibre. The fibre has a (cladding) diameter of 125 ± 0.7 μm, a core diameter of 8.2 μm and an effective refractive index n_{eff} of 1.4682 at a wavelength λ_G of 1550 ± 0.5 nm (Figure 4-4).

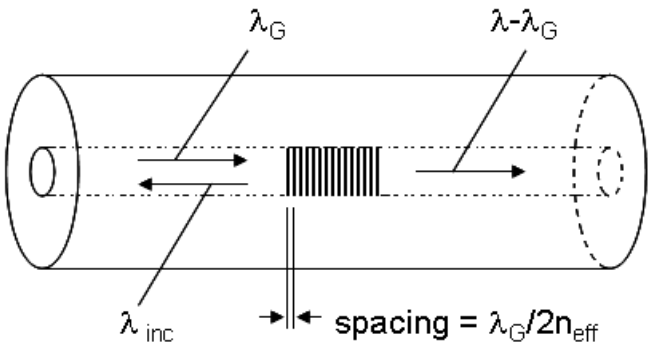

Figure 4-4 A fibre Bragg grating [133]

The gratings were written into the FBG by Smart Fibres Ltd. using spatially-varying patterns of intense UV laser light; this is known as a phase mask technique [89]. A phasemask is a diffractive element that can be used to form an interference pattern laterally, i.e. Bragg grating pitch, with the light beams which

are spatially phase modulated and diffracted by the phase-mask, as shown in Figure 4-5. This interference pattern is then used to imprint a refractive index modulation into the photosensitive fibre. The phase-mask method has several advantages over other FBG writing techniques:

- The Bragg wavelength of an FBG is determined by the pitch of the phase-mask and is independent of the wavelength of the UV laser.
- As phase-masks are fabricated under a computer controlled photolithographic imprinting process through an original phase-mask, this technique is suited to mass production with good repeatability at low cost.
- This single-beam writing method improves the mechanical stability of the FBG.
- Low spatial and temporal coherence lasers can be used instead of highly coherent, very expensive UV lasers used by other writing methods.

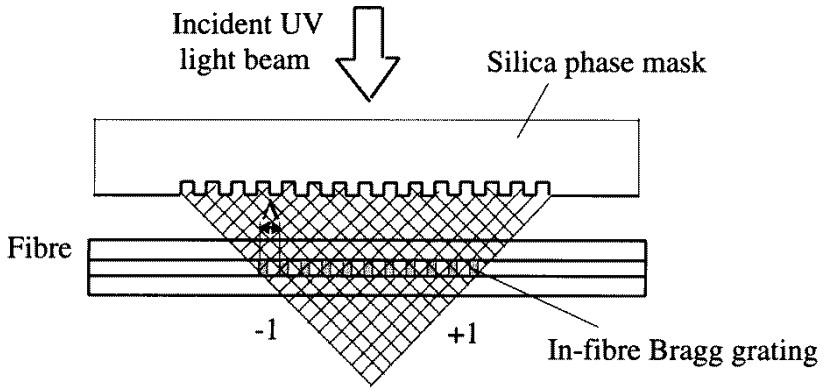

Figure 4-5 Schematic of the phase-mask writing process [89]

The optical properties of the FBG were supplied by the manufacturer and are given in Table 4-1.

5 mm long FBG with 10 ± 2 μm polyimide recoat over the sensor region	
Central wavelength (λ_G)	1550 ±0.5 nm
Reflectivity	≥ 70%
Full width at half maximum (FWHM)	< 0.7 nm

Table 4-1 Optical properties of the FBG obtained from the manufacturer

4.3.2 The Effect of Adhesive Thickness on the ASTC

An FE model has been created to study the effects of varying the adhesive layer thickness, bond length and elasticity on the ASTC in a manner more representative of a surface mounted FBG. The symmetry of the model geometry, as well as the applied strain, allows a half model to be created (Figure 4-6) reducing computational convergence time. The compound arrangement is 5 mm long representing the bonded length of the FBG sensor. Other FBG and isotropic material parameters employed in the FE model are presented in Table 4-2. The 3-D model is solved using ANSYS 12 simulation software. The materials are all assumed to be linear, elastic and isotropic. SOLID185 quad elements offering enhanced strain formulation were used in each of the model components. All surfaces between FBG, adhesive and blade are assumed to be in perfect contact with no slippage occurring.

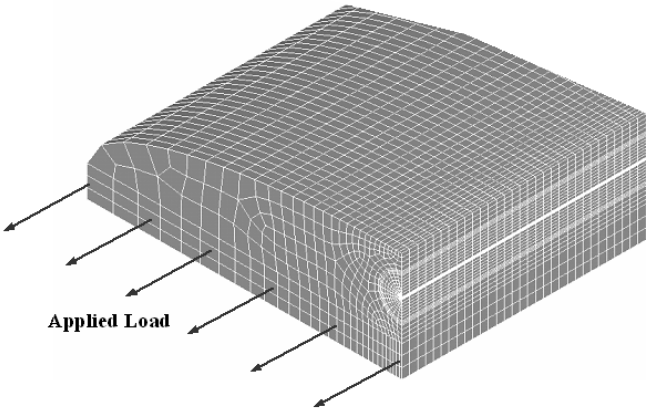

Figure 4-6 The finite element model cross-sectional isometric view

A 0.03% uniform strain was applied to the blade in the axial direction for each simulation. The following parameters were varied and the strain distribution along the FBG core assessed after each simulation:

(a) The thickness of the adhesive layer between FBG coating and blade was varied from 10 μm to 200 μm.

(b) The Young's modulus of the adhesive was set at either 2 GPa or 3 GPa [134].

The strain distribution along the FBG core for an adhesive Young's modulus of 3 GPa over a range of thicknesses from 10 μm to 200 μm is shown in Figure 4-7. The effect of increasing the adhesive layer thickness is evident, with the effects becoming more pronounced at greater thickness values.

Description	Identifier	Value
Outer Radius of FBG (µm)	r_f	62.5
Outer Radius of Polyimide Coating (µm)	r_c	75
Adhesive Layer Thickness (µm)	t_a	10 - 200
Young's Modulus (GPa)		
FBG	E_f	72
Polyimide Coating	E_c	3
Adhesive Layer	E_a	2-3
Blade	E_m	193
Poissons Ratio		
FBG	ν_f	0.17
Polyimide Coating	ν_c	0.35
Adhesive Layer	ν_a	0.35
Blade	ν_m	0.30

Table 4-2 Table of material and geometric properties used in the FE model

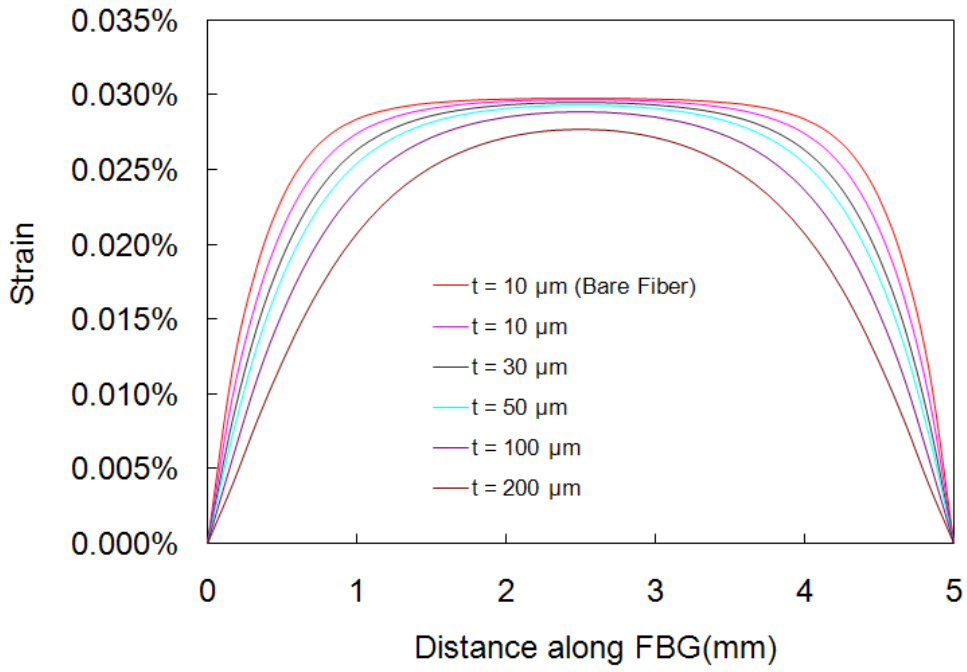

Figure 4-7 FE strain along FBG core for a range of adhesive thicknesses

Shear effects through the adhesive and protective coating layers dictate that 100% uniform strain over the FBG length is unattainable by bonding the FBG length only. Therefore an adhesive bond length of some percentage greater than the length of the FBG length is necessary to ensure complete strain transfer from blade to the core of the FBG. The ratio of the average FBG strain to that of the blade (ASTC) is plotted in Figure 4-8 for five different adhesive layer thicknesses and Young's modulus values of 2 and 3GPa. The analytical ASTC values were obtained from equations 4.1 and 4.2 where an effective value for r_m was obtained using the following equation developed by Wan *et al* [132],

$$r_m = \sqrt{(r_c + t_a)^2 + r_c^2} \tag{4.3}$$

It can be seen that the analytically obtained ASTC values are over-estimated by an average of 10% compared with the values obtained using FE. This can be attributed to the approximate nature of equation 4.3 which does not completely reflect the influence that t_a has on the ASTC.

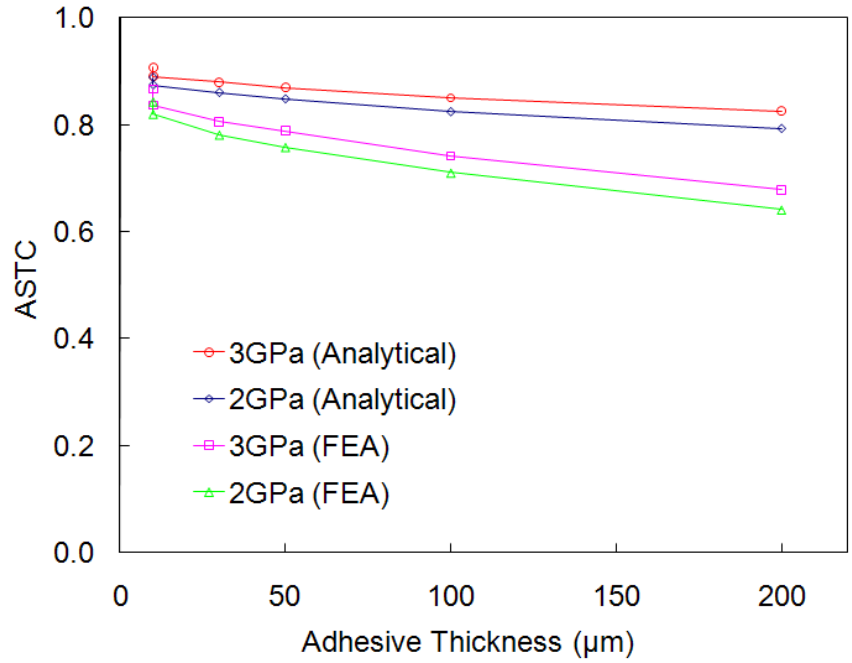

Figure 4-8 Comparing analytical and FE ASTC results for a range of adhesive thicknesses

Table 4-3 compares the ASTC values using both methods and it can be seen that the most effective strain transfer is achieved (for both methods) when the adhesive layer thickness is thinnest (10 μm) and its Young's modulus is greatest (3 GPa). Reducing the stiffness of the adhesive from 3 GPa to 2 GPa has the effect of reducing the ASTC by an average of 2%. It is noted also that there is a significant difference between the ASTC values obtained using FE and analytical methods using the same adhesive stiffness. The consistently lower ASTC values obtained using FE were expected as the geometry of the surface adhesive layer dictates that the shear effects are concentrated between the bottom of the FBG and the host material. In contrast, the analytical equations assume that the strain is transferred circumferentially around the FBG resulting in a higher ASTC value.

	3 GPa Adhesive Modulus			2 GPa Adhesive Modulus		
Adhesive Thickness	Analytical ASTC	Finite Element ASTC	% Difference	Analytical ASTC	Finite Element ASTC	% Difference
10 μm (Bare Fibre)	0.907	0.866	4.52	0.888	0.843	5.07
10 μm	0.890	0.836	6.07	0.874	0.820	6.18
30 μm	0.879	0.805	8.42	0.860	0.781	9.19
50 μm	0.869	0.788	9.32	0.848	0.758	10.61
100 μm	0.850	0.741	12.82	0.824	0.710	13.83
200 μm	0.825	0.678	17.82	0.793	0.641	19.17

Table 4-3 FE and analytical ASTC values for two different Young's modulus values and a range of adhesive thicknesses

4.3.3 The Effect of Adhesive Bond Length

It was shown in Section 4.3 that the ASTC is influenced by the material properties of the FBG, its coating and the adhesive. Moreover, geometrical properties such as adhesive layer thickness also affect strain transfer. The length of the adhesive that bonds the FBG also influences the effectiveness with which the blade strain is transferred to the FBG core. A FBG strain sensor measures the shift in its reflected wavelength which is proportional to the strain being experienced. Achieving accurate strain measurement necessitates that a uniform strain distribution is obtained along the 5 mm grating length. This ensures that:

(a) The strain sensitivity of the FBG (1.2 pm $\mu\varepsilon^{-1}$) is valid, as this value is based on the assumption of strain uniformity.

(b) No spectral broadening or distortion of the reflected wavelength spectra occurs which can result in errors.

FE analysis was carried out to ascertain the minimum FBG bond length which ensures strain uniformity over the 5 mm grating. Five FE models were created of a surface bonded FBG in which the adhesive bond length was the only variable. Simulations showed that for an adhesive layer thickness of 60 µm, and a 4 µm thick polyimide coating, a minimum bond length of 11 mm (55 % longer than the FBG) ensures a uniform strain distribution across the 5 mm FBG (Figure 4-9).

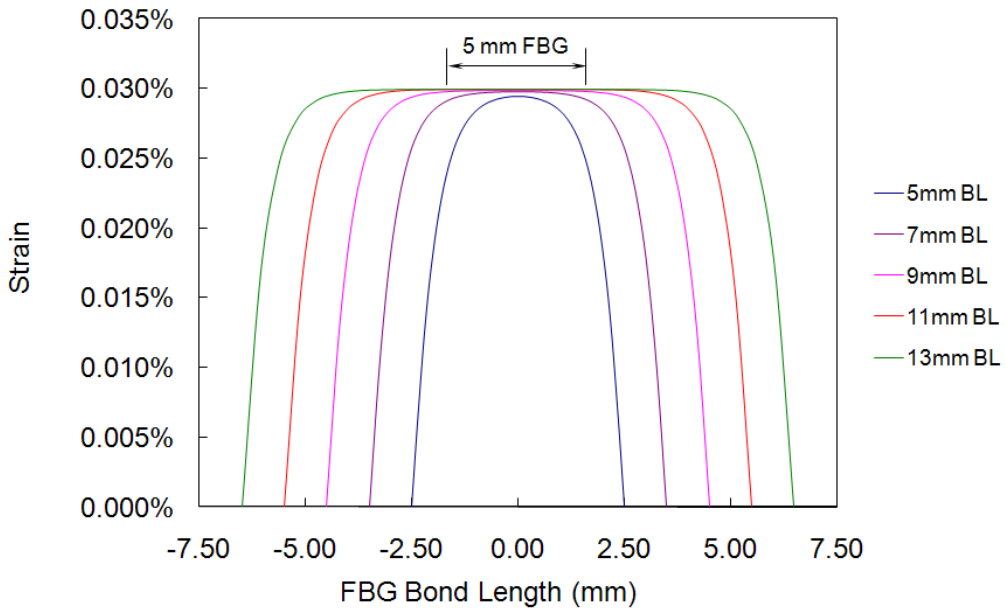

Figure 4-9 FE strain distribution for various bond lengths

Practical limitations restrict the dimension to which the adhesive layer thickness can be reduced. A thickness, t_a, of 62.5 µm (Figure 4-10(a)) was chosen as an achievable value based on the dimensions of the actual FBG polyimide and acrylate coatings used in our experiments (Figure 4-10(b)). The original coating radius was 125 µm and the recoated fibre radius 62.5 µm, therefore, the

adhesive thickness is maintained at 62.5 μm whenever the original coating is resting on the blade surface.

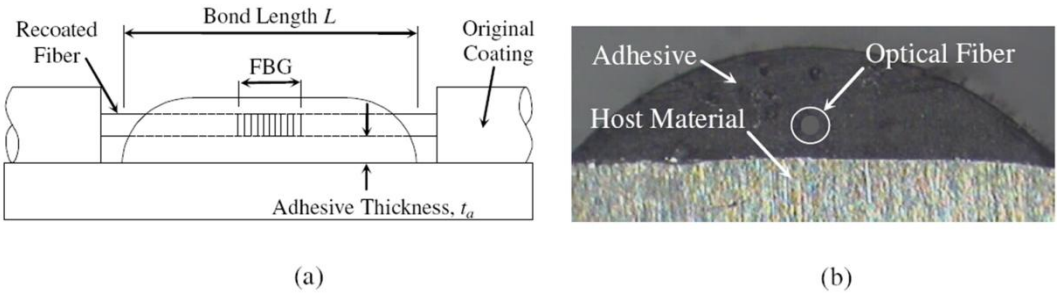

Figure 4-10 (a) Surface mounted FBG (b) A FBG sensor within the adhesive layer

4.4 Experimental Test Rig (Surface Mounted FBG)

An experimental testing platform has been developed for the initial investigation and characterisation of the strain distribution along a replica stainless steel scissor blade. The test rig consists of a simplified blade arrangement which is representative of one blade of a stainless steel scissor end effector. The blade is symmetrical about its pivot point allowing for the simultaneous evaluation of FBG and electrical strain gauge sensors under the same conditions. The blade protrudes 39 mm either side of its pivot point. Two FBG sensors are attached to the blade, one on the top of the blade for direct strain measurement and the other, used for temperature compensation, is attached but not bonded to the lateral side of the blade. A close-up view of the 5 mm FBG attached to the top surface of the blade is shown in Figure 4-11.

Figure 4-11 A 5 mm FBG attached to the upper surface of the blade

An ESG is attached at the equivalent position on the opposite, symmetrical, side of the blade to facilitate comparison with the results obtained from the FBG. Loads were applied using a micrometer translation stage with a load cell attached to the end of the micrometer as shown in Figure 4-12. The data from the load cell is collected using a National Instruments load cell module SG-24, which is connected to a data acquisition board NI6221. The data from the strain gauges is obtained using a strain gauge module SG-03. The system is monitored and controlled using LabView 8.0.

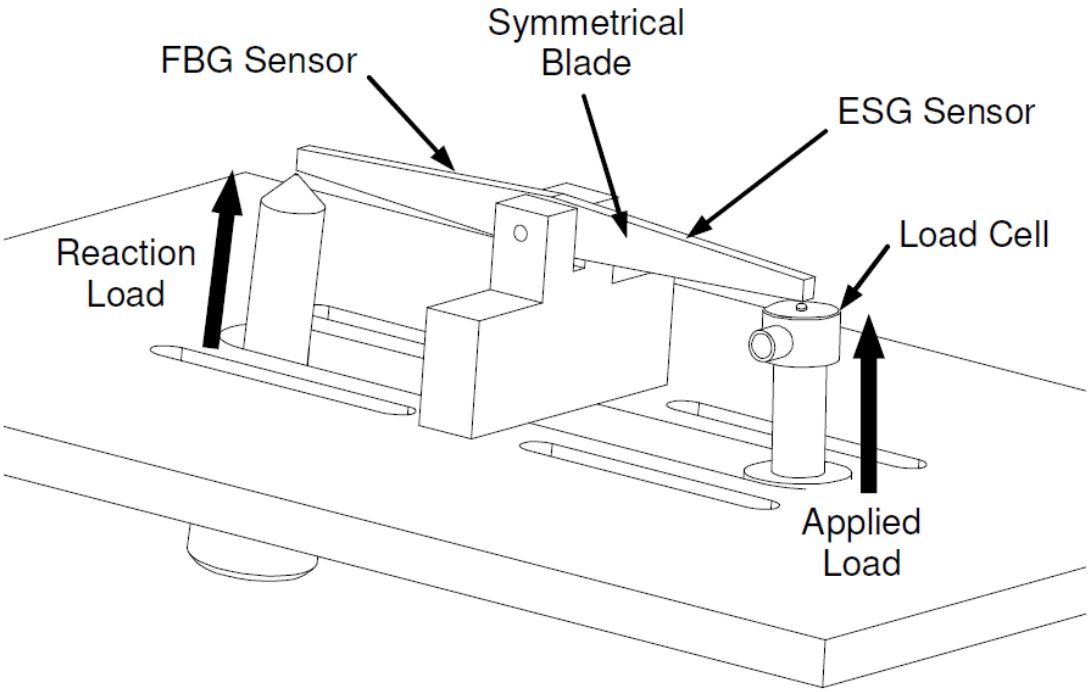

Figure 4-12 Symmetrical blade test arrangement showing locations of the FBG and ESG

4.4.1 FBG Placement

Due to the small dimensions of the blade used (39 mm in length) and the high modulus of elasticity of the blade material (193 GNm^{-2}) it was important that the sensitivity of the sensorised blade was maximised. This was achieved by analytically modelling a series of loads applied to the blade at a number of locations along its length and finding the subsequent point of maximum strain on the blade upper surface. The geometry of one half of the symmetrical blade model is shown in Figure 4-13.

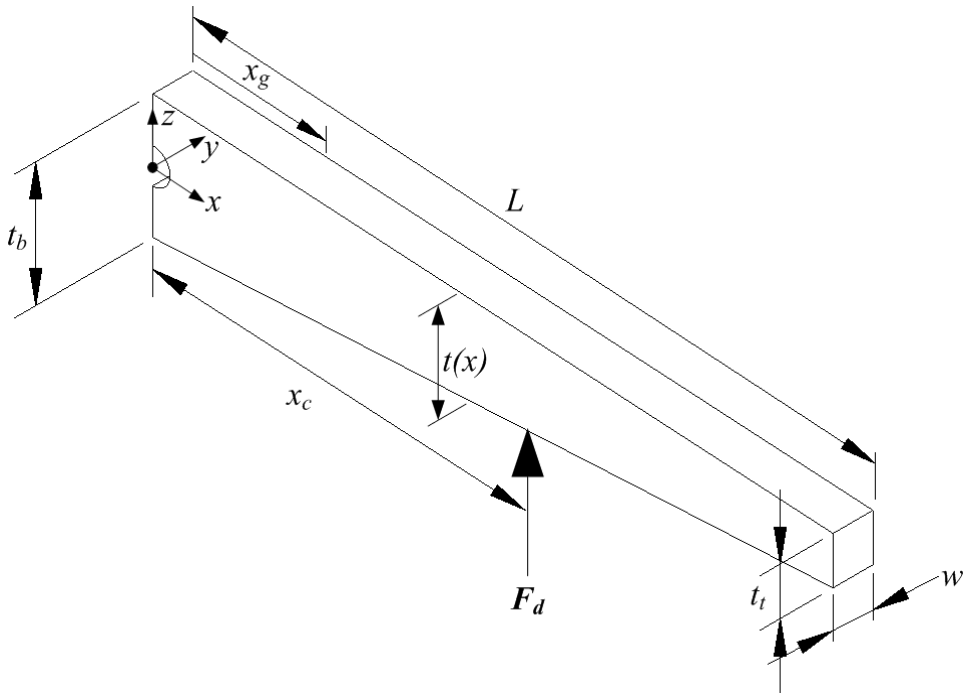

Figure 4-13 Blade geometry

The strain along the blade upper surface ε_d, as a function of x, can be defined from elementary beam theory as,

$$\varepsilon_d(x) = \frac{F_d(x_c - x_g)t(x)}{2EI(x)} \tag{4.4}$$

where $t(x)$ is the depth of the blade at any location x along its length and can be written as,

$$t(x) = mx + t_b \tag{4.5}$$

Where t_b is the width of the blade at its pivot and m is the slope of the blade, taken to be,

$$m = \frac{t_t - t_b}{L} \tag{4.6}$$

and t_t is the width of the blade at its tip and L is the total length of the blade. As the second moment of area $I(x)$ of the blade section is not constant it is taken as,

$$I(x) = \frac{w\ (mx + t_b)^3}{12} \tag{4.7}$$

Subbing $I(x)$ into equation 4.4, the equation which allows the strain to be estimated at any location along the blade length becomes,

$$\varepsilon_d(x) = \frac{6F_d(x_c - x_g)}{Ew(mx + t_b)^2} \tag{4.8}$$

where x_c is the distance from the pivot to the point of application of the load F_d, x_g is the distance from the pivot to where the strain is to be estimated ($0 < x_g > L$), w is the width of the blade and E is the Young's modulus of the blade material. To find the location of the maximum strain, let $\frac{d\varepsilon_d}{dx} = 0$, therefore,

$$\frac{d\varepsilon_d}{dx} = \frac{6F_d(2x_c m - mx + t_b)}{Ew(mx + t_b)^3} = 0 \tag{4.9}$$

When a load is applied at the blade tip then the maximum strain occurs at,

$$x_{max} = 2x_c + \frac{t_b}{m} \tag{4.10}$$

Finite element simulations were used to confirm the location of maximum strain on the blade upper surface. This is illustrated in Figure 4-14 where the blade is loaded to 30 N at its tip and the strain profile along the upper surface is plotted against the strain obtained from the analytical analysis.

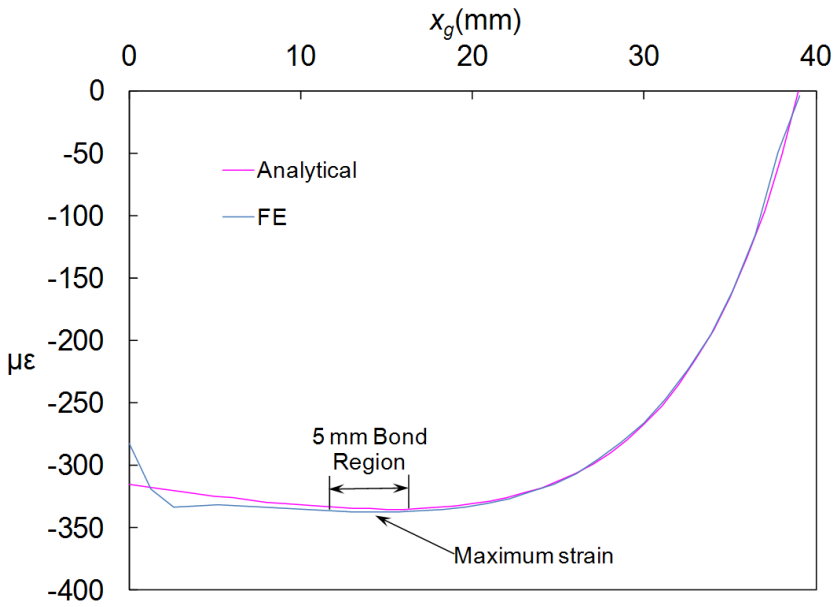

Figure 4-14 Location of maximum strain on one half of the symmetrical blade

Figure 4-15(a) and (b) shows a range of strain profiles over a range of loads up to 30 N applied at the blade tip (x_c = 39 mm). The maximum strain consistently occurs at x_g = 14 mm from the pivot point. Figure 4-15(c) and (d) considers the effect of moving the applied load along the blade length. The maximum load of 30 N is applied at a series of locations from the blade tip (x_c = 39 mm) to the blade pivot (x_c = 0 mm). It can be seen that as the blade is loaded at each location, strain is induced on the blade upper surface between the point of application of the load and the blade pivot point. The blade upper surface region between the point of application of the load and the tip of the blade does not

experience any strain from the applied load. Placing a FBG sensor at x_g = 14 mm means that it is within the 44 % region (equating to x_g = 17 mm) of the blade upper surface that is available for sensor placement as outlined in Section 3.5.

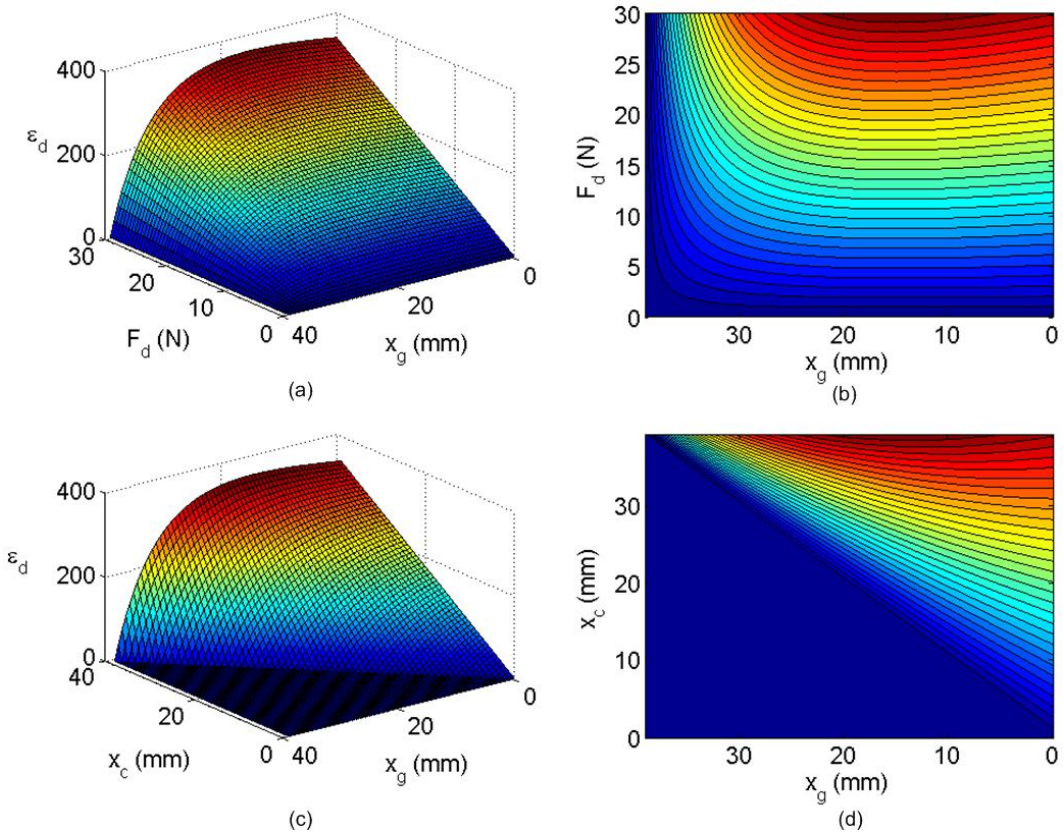

Figure 4-15 Strain distribution along blade top surface obtained using analytical equation 4.8 where in (a) and (b) a 0 N to 30 N load range is applied to the tip of the blade only and in (c) and (d) the loads are applied at a number of locations x_c along the blade length.

4.4.2 Attaching the FBG Sensor

Bonding of the FBG sensor to the surface of the blade was achieved using a special fixture incorporating four linear stages. This fixture allows the fibre to be fixed at one location while the blade is aligned in the *x, y* and *z* planes prior to the

addition of the adhesive layer. After satisfactory alignment, the blade is lowered and the adhesive layer is manually applied over the bond length (11 mm). The blade is then raised to its original position where it meets the fibre which is held in position by an applicator containing a 250 μm deep groove. This groove ensures that the fibre is placed securely to the blade without squeezing the Acrylate coating at the points of contact between applicator and blade (either side of the recoated fibre). This technique is important since squeezing of the Acrylate coating during bonding results in curvature of the recoated fibre and consequently an inconsistent adhesive thickness along the adhesive bond length.

4.4.3 Comparing FBG and ESG Sensors

A range of loads in increments of 2 N between 0 and 30 N were applied to one end of the symmetrical blade resulting in an equal load being applied at the opposite end (Figure 4-12). This technique induces equal strain fields in each side of the blade. As a result the ESG and the FBG sensors located at the same location on each blade experience the same strain due to the blade being directly loaded. The reflected central wavelengths of the FBG sensor were measured using an optical spectrum analyzer (Agilent 86140B). The measured wavelength for zero strain and maximum applied load have the same bandwidth with peak shift, due to the induced strain only, being observed (Figure 4-16). This confirms that uniform strain is being induced over the grating length, as an appropriate bond length of 11 mm is being used.

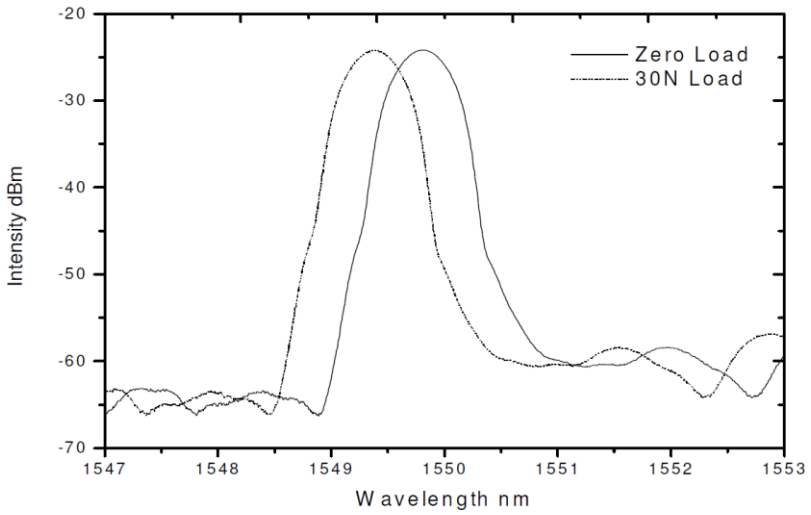

Figure 4-16 Spectral shift at zero and maximum load

The experimental data from the FBG and the ESG over the loading range of the blades are presented in Figure 4-17. Blade strains obtained using FE and elementary beam theory are also presented.

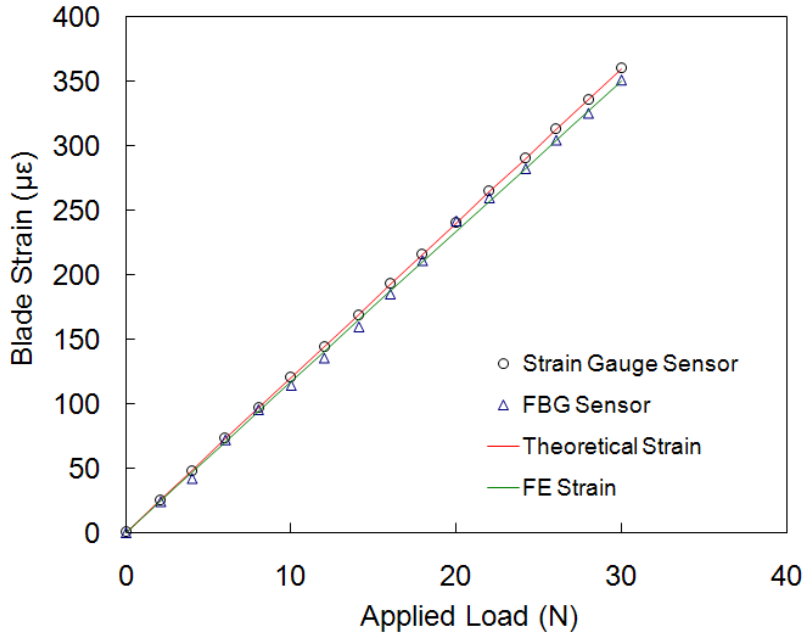

Figure 4-17 FBG and ESG measured strain

The strain values from the FBG sensor are in good agreement with those from the surface mounted ESG with a maximum of 2.8% variation in strain being observed over the full range. The theoretical ASTC is estimated from equation (4.1) where the uniform strain $\bar{\varepsilon}_f$ is the actual strain measured by the FBG and ε_m is the uniform strain on the blade surface. The FE simulation indicates that an ASTC of 1 is obtainable using an appropriate bond length, adhesive layer thickness and coating thickness. The experimentally obtained strain readings for both the FBG and ESG were plotted against one another as shown in Figure 4-18. By letting the FBG strain readings represent $\bar{\varepsilon}_f$ and the ESG[9] readings representing ε_m an estimate of the ASTC value can be obtained.

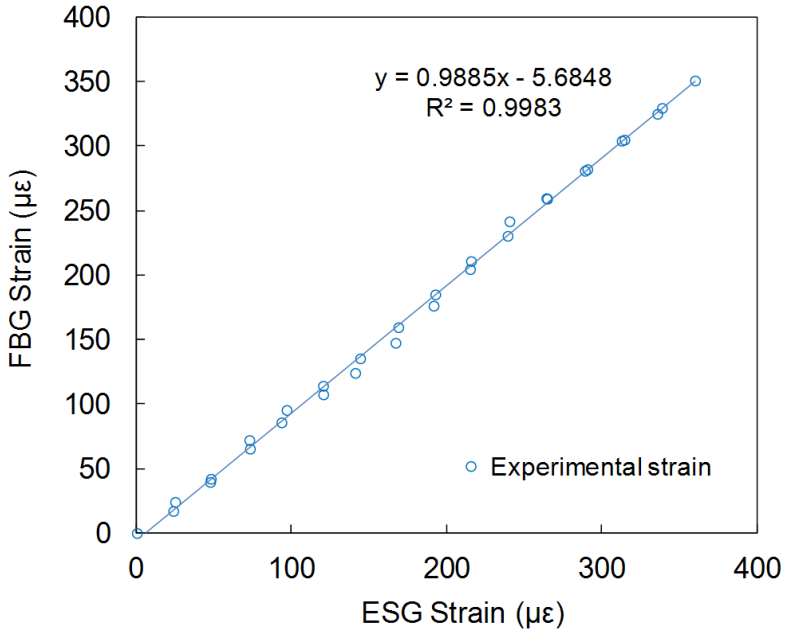

Figure 4-18 Obtaining ASTC from FBG and ESG strain readings

[9] Gauge factor tolerance ±1% and Resistance tolerance ±0.5%

It is seen that closeness of agreement between the FBG and ESG strain values is very good and consequently an ASTC of 0.98 is obtained from the slope of the graph. This comparison also indicates the performance of the FBG, in terms of its sensitivity, is comparable to that of the more established ESG technology reinforcing its suitability for the proposed measurement application. It is observed that the strain values from the FBG sensor correlate closely with both the analytical and FE values which also indicate that a high level of strain transfer from blade to FBG is attained.

4.5 Partial Embedment of the Fibre

The purpose of partially embedding the FBG sensor within a host structure is to protect the fibre from damage during operation and to simulate somewhat a fully embedded fibre arrangement. The accuracy of the FBG measured strain is dependent on the bonding characteristics between the host structure, fibre protective coating and the silica fibre itself. Ideally, the embedded FBG should output a signal in proportion to the strain generated in the blade structure in the vicinity of the FBG sensor. The theoretical analysis into the effect of the adhesive bond length and thickness has not been examined for a partially embedded fibre scenario. These parameters are important when considering the implementation of a FBG strain sensor into small structures experiencing relatively small strains. Minimising the fibre bond length to ensure that the combined fibre-adhesive length is as short and compact as possible facilitates the integration of FBG sensors in small compact surgical instruments and devices. Furthermore,

embedding a FBG sensor close to the neutral axis of its host structure, affects the overall sensitivity of the sensorised structure. Bonding FBGs to the surface of the host structure maximises the distance between the neutral axis and the point of maximum strain measurement. Embedding the fibre below the surface of the blade will result in a reduction in the sensitivity of the sensorised blade and therefore the depth of sensor embedment should be kept to a minimum. Work by Iordachita *et al* [104] in which partially embedded FBGs were integrated into a retinal surgery device has been carried out but investigations into the reduction in sensitivity and the effects of local strain gradients at the location of FBG were not carried out. Park *et al* [86, 135] have reported hysteresis as an issue during the operation of a sensorised biopsy needle incorporating partially embedded FBG. This reinforces the importance of understanding the effects of the bonding interface between an instrument and a FBG.

The following sections will quantify the reduction in sensitivity of a blade with a partially embedded FBG sensor, taking into consideration transverse strain variations through the fibre during blade loading. Recalculation of the minimum adhesive bond length is required due to the geometrically different way in which the FBG is adhered to the blade structure. This is achieved by modification of the surface analytical strain transfer model to include an effective adhesive radius analogous to that of a fully embedded fibre. Numerical analysis will be used to verify the modified strain transfer analytical model.

4.5.1 Limitations of ASTC Equations

Cox [131] originally developed equations for the embedment of a cylindrical element embedded in a host material being subjected to an axially applied uniform strain field. These equations assume that the fibre being strained is encapsulated fully by the surrounding host material and by the intermediate adhesive layer bonding the fibre to the structure. However, as seen in Figure 4-19 which represents a partially embedded fibre placed within a groove in the host structure, the encapsulating adhesive layer is not axisymmetrical. Incorporating a fibre into a host structure in this way means that the adhesive thickness is not uniform between the fibre protective coating and the loaded host structure. Hence, the strain being transferred from the host structure through the adhesive layer will not be uniform at different circumferential locations around the fibre outer surface.

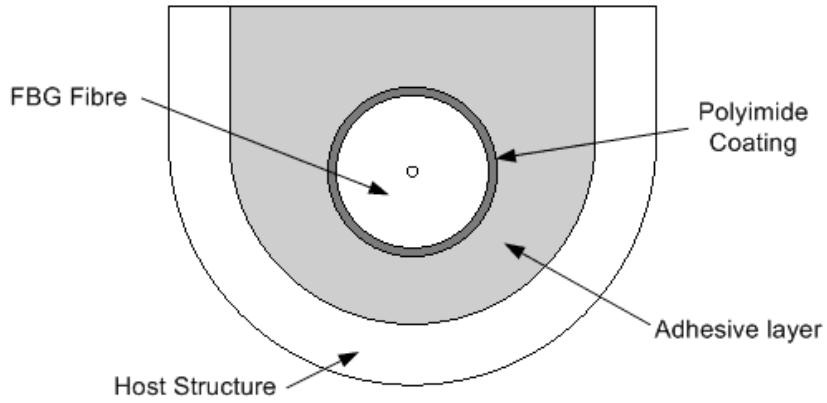

Figure 4-19 Coated FBG partially embedded within the host structure

These limitations of Cox's equations will not allow accurate estimation of the adhesive bond length and strain transfer coefficient to be obtained for a partially embedded fibre as it is only applicable to a fibre fully encapsulated within the host material.

4.5.2 The Effect of Adhesive Thickness and Bond Length

Modification of the ASTC equation (4.1) for a fully embedded FBG fibre to account for the axisymmetrical nature of a partially embedded fibre is proposed. As the geometry of the adhesive effects the strain transfer from host structure to fibre core, a re-evaluation of the shear lag parameter k is required. It is clear from equation 4.1 that the outer radius of the annular adhesive layer, r_m, does not exist for a partially embedded fibre. It is proposed that the radial dimension r_m be replaced with an effective radius, $r_{eff,}$ to account for the non-axisymetrical nature of the adhesive layer encapsulating the fibre within the groove (Figure 4-20).

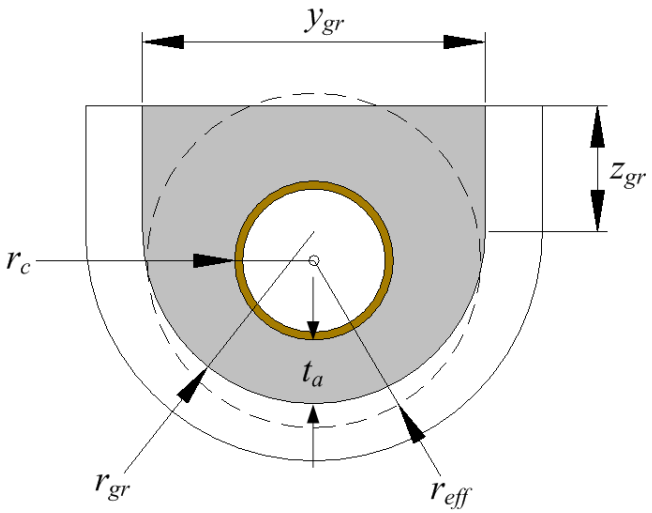

Figure 4-20 Embedded fibre and effective radius r_{eff} of adhesive

This effective radius was estimated by equating the cross sectional area of the adhesive within the groove to the cross sectional area of an annular adhesive ring representative of a fully embedded fibre within the blade structure resulting in an effective adhesive radius r_{eff} defined as,

$$r_{eff} = \left[\frac{y_{gr} z_{gr}}{\pi} + \frac{(r_c + t_a)^2}{2} \right]^{1/2} \tag{4.11}$$

where t_a is the effective adhesive thickness between the bottom of the fibre coating and the base of the groove into which it is bonded. It is observed that t_a has an impact on the ASTC for a partially embedded fibre similar to that of a fully embedded fibre. This is illustrated in Figure 4-21 where the effect of varying the nondimensionalised BL/t_a for a range of bond lengths between 5 mm and 13 mm is shown. A high BL/t_a ratio results in a high ASTC over the bonded region, signifying that t_a is kept to a minimum and the BL is maximised.

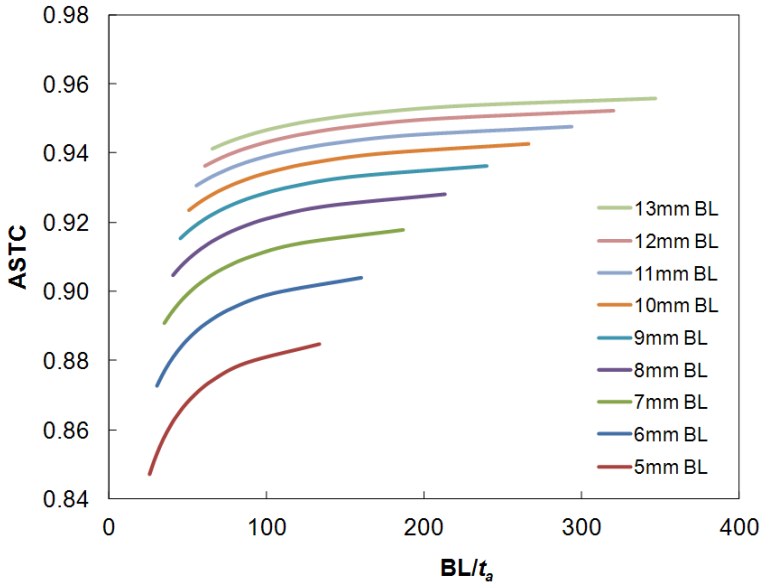

Figure 4-21 The effect of the BL/t_a ratio on the ASTC

It should be noted that the ASTC values presented in Figure 4-21 are obtained by taking the ratio of the average strain in the fibre over its bonded length to the strain experienced by the host material. However, the plots in Figure 4-21 do not give any indication of the ASTC over the actual FBG length present within the bonded length. The only plot in figure 4-19 that gives the ASTC over the FBG length is the 5 mm BL plot where the adhesive is applied over the length of the 5 mm FBG only. Simulations show that a t_a of 2-3 μm would be required to achieve an ASTC of 0.95 for a 5 mm FBG with a 5 mm BL. However, there is uncertainty as to whether an adhesive layer of this thickness would remain intact under loading.

Holding t_a at a fixed value (62.5 μm) and varying the BL yields the fibre strain distribution shown in Figure 4-22.

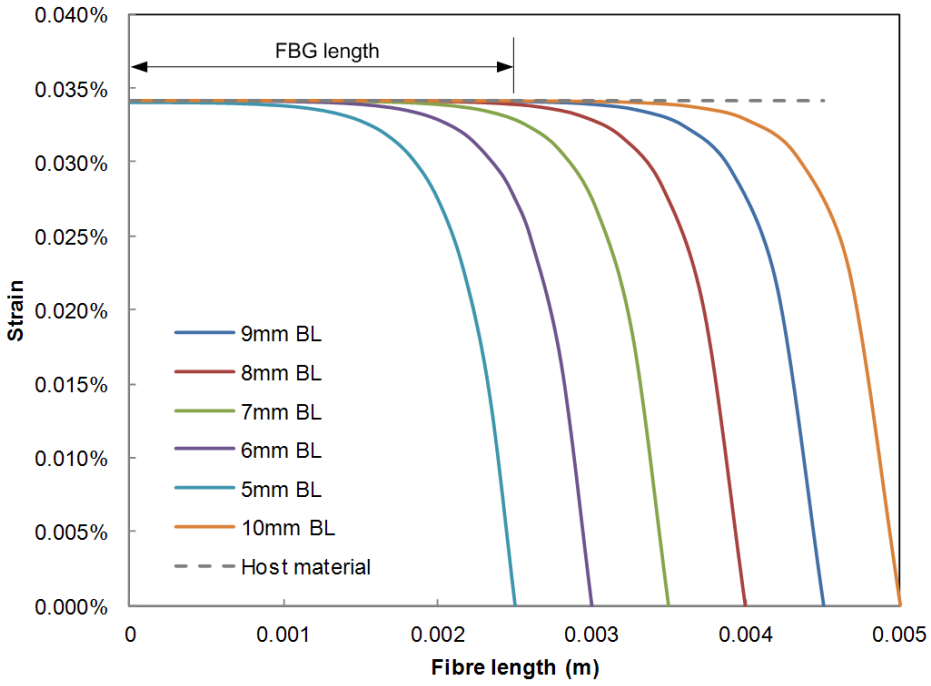

Figure 4-22 Strain distribution over the FBG length (half length)

It is seen that the 5,6,7 and 8 mm bond lengths do not transfer 100% of the host material strain in the to the FBG. Therefore, the minimum BL for which an ASTC of unity is achieved for a partially embedded fibre with t_a = 62.5 μm is 9 mm. This BL is 45% greater than the length of the FBG being used. Using FBG sensors for the purpose of low value strain measurement arising in small surgical instruments requires compact packaging of the sensor onto or into the instrument. It is therefore imperative that the fibre itself is as small as possible and that the method of attaching the sensor to the instrument also has minimal impact on the overall dimensions of the sensing element.

4.5.3 Numerical Simulation of Partially Embedded Fibre

A numerical simulation of the FBG strain sensor embedded within a groove in the host material was developed for two reasons;

1. To validate the effectiveness of using the modified analytical equation incorporating r_{eff}, as a means of estimating a bond length which ensures complete strain transfer from blade to fibre core.
2. To investigate, for transverse strain gradients through the groove, whether or not the FBG measures the strain in a horizontal plane coincident to the centreline of the fibre core.

A 3-D finite element model of the 5 mm FBG sensor placed within the groove was created using ANSYS 12 numerical simulation software. A half model was used as it is symmetrical about a vertical plane along its longitudinal axis thus enabling mirror symmetry to be implemented (Figure 4-23).

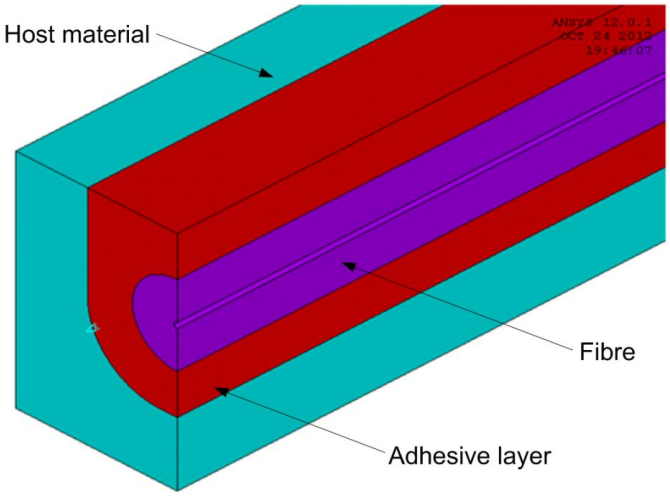

Figure 4-23 Model of fibre embedded within the host material

The interfaces between the fibre, adhesive and host material are bonded in the FE simulation software. Initial investigations into how the contact surfaces between fibre, adhesive and host material would be bonded in the model considered the use of TARG and CONT elements. The TARG and CONT elements allow a more detailed contact model to be created. The surfaces in contact were configured so that high cohesive sliding resistance and frictional resistance conditions were established between them. However, this configuration set up nonlinearities at these contact surfaces which resulted in long convergence times for the model. The model was run again with the surface areas glued using the ANSYS glue function. The glue function assumes a perfect contact between the surfaces. Strain results from both methods were compared and it was found that there was negligible difference in the results. It is reasonable to assume that the three materials being used in the model would remain within their elastic

limits during loading and unlikely to experience any yielding at the contact interfaces. For this reason the glued contact option was deemed suitable for this particular model.

4.5.4 Parameters for the Numerical Model

As outlined in the theoretical analysis in Section 4.5.2 the bond length of the adhesive which adheres the fibre to the host structure must be some percentage greater than the length of the FBG being used. Finite element analysis is employed here to validate the modified ASTC equation (4.1) and to confirm that the minimum adhesive bond length of 9 mm results in an ASTC of unity. Five different bond lengths were compared ranging from 5 mm to 10 mm. The fibre was located within the groove with a t_a of 62.5 μm. This t_a was measured from the experimental set-up and dictated by the geometric restrictions placed on the fibre depth by the radius of the original Acrylate fibre coating which was retained either side of the polyimide recoated portion of the fibre (Figure 4-24).

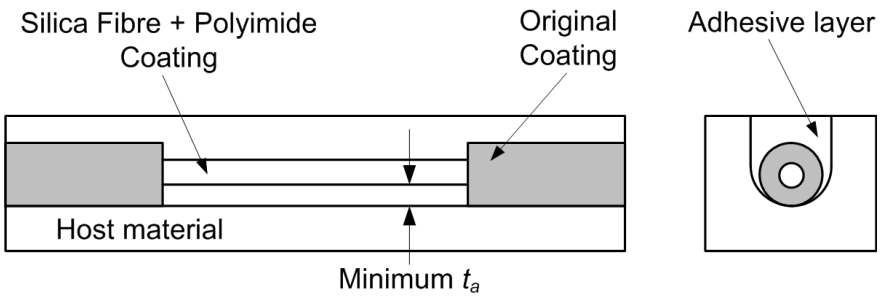

Figure 4-24 A coated fibre within the host material

The original coating measured 250 μm in diameter and the coated silica fibre into which the FBG was written measured 125 μm. This dictated, therefore, that between the base of the groove and the protective coating of the fibre, t_a is 62.5 μm. This value for t_a was used in the numerical simulation model.

4.5.5 Numerical and Analytical ASTC Results

The material properties used for the embedded fibre simulation are the same as the properties used for the surface mounted fibre. The host material was strained to 0.0341% strain longitudinally. The strain distribution through the adhesive layer into the fibre is shown in Figure 4-25 where an obvious region of low strain is observed towards the end of the adhesive layer.

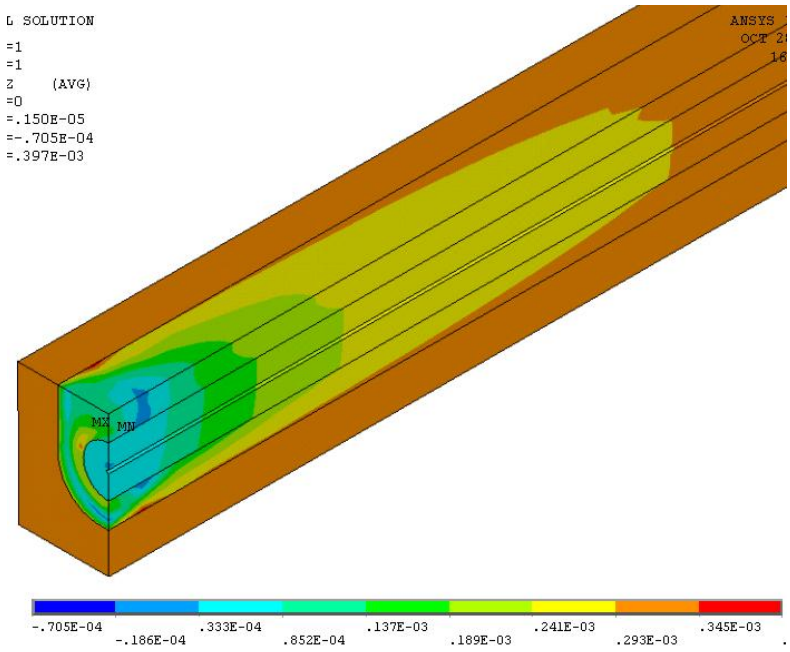

Figure 4-25 Numerical simulation showing areas of low strain towards end of the bonded region

The strain in the adhesive and fibre eventually converge at the centre of the bonded region to match the strain being experienced by the host material. This strain distribution is similar in characteristic to the strain profiles obtained analytically in Figure 4-22. A path was created in the numerical model along the centre of the fibre from one end of the BL to the other. The longitudinal strain was mapped onto this path and is plotted against the analytically obtained values in Figure 4-26 for 5 different bond lengths between 5 and 10 mm.

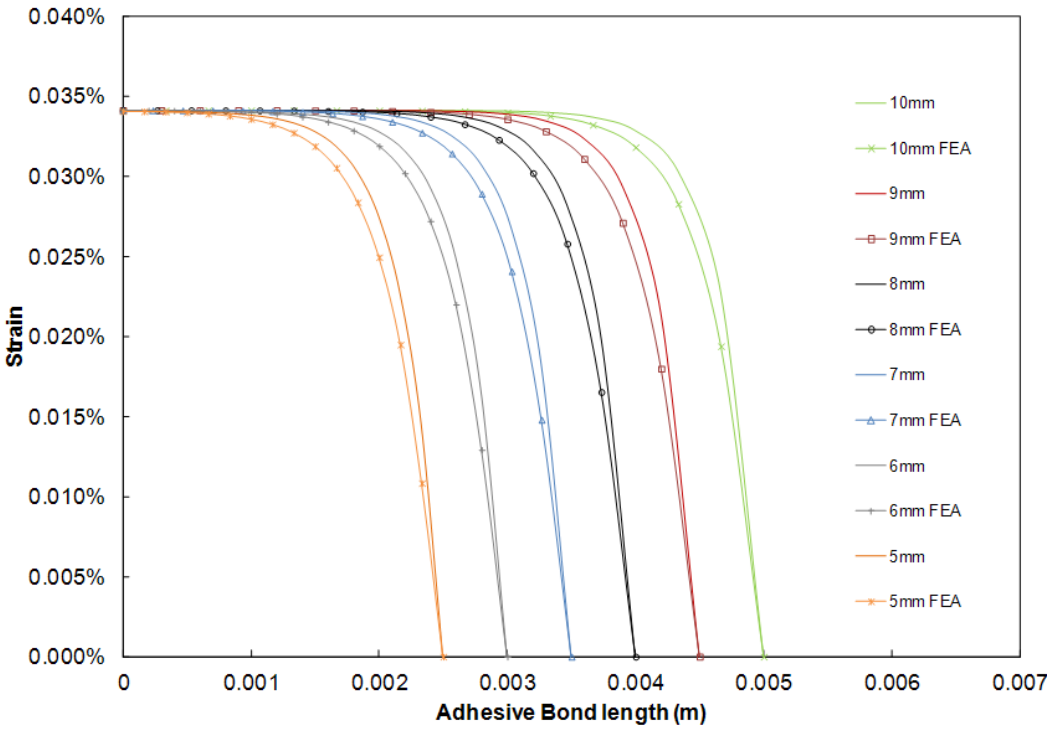

Figure 4-26 FEA and analytical strain distribution for a range of BL

It can be seen from Figure 4-26 that there is good correlation between the strain profiles obtained using FE and the modified analytical equations. Close examination of the FE strain profile shows that, like the analytical analysis, an

ASTC of 1 is obtained with a BL=9 mm. This length ensures that there is uniform strain over the entire 5 mm FBG sensing region of the fibre.

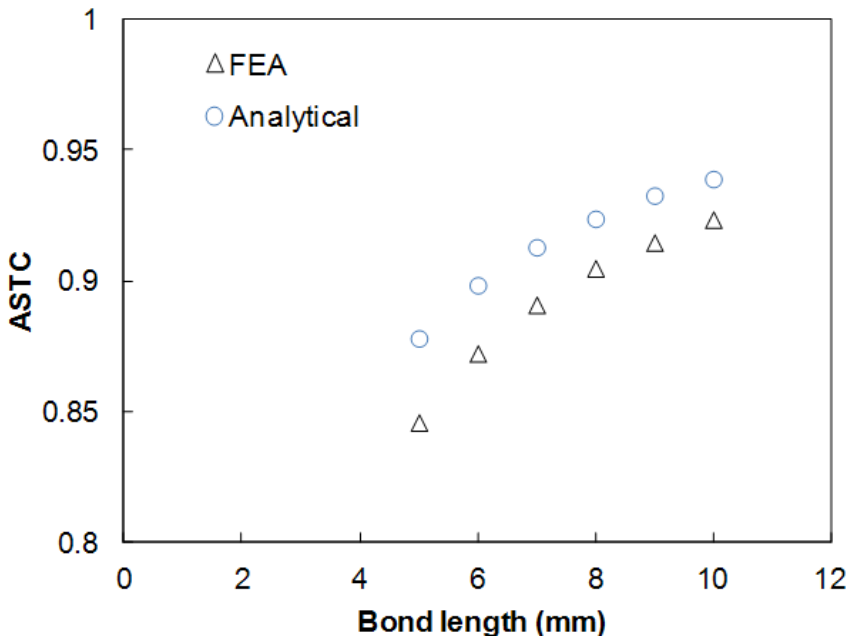

Figure 4-27 Comparing FEA and analytical ASTC

The closeness of agreement between the ASTC values obtained through analytical and FE methods is shown in Figure 4-27. The average percentage difference between the ASTC obtained using the FE and analytical equations was found to be 2.4% with a 1.9% at BL=9 mm. It can be concluded that the modified analytical model, to include an effective radius, gives a reasonable estimation of the minimum bond length for a FBG fibre embedded within a host material.

4.6 Transverse Strain Gradients within the Groove

The FE analysis of the fibre within the groove was carried out by loading the host material longitudinally to a specified percentage strain value. This approach dictates that the strain throughout the host material is uniform at all points throughout it cross-section. However, further analysis of the strain distribution throughout the tapered blade cross-section shows that the longitudinal strain is at its maximum at the blade upper surface and gradually decreases towards the blades neutral axis. An estimation of the strain variation between the blade upper surface and the bottom of the groove (260 µm) is shown in Figure 4-28(a). These strain profiles were created using the elementary beam theory previously discussed in Section 4.4.1 where 30 N was applied at the blade tip.

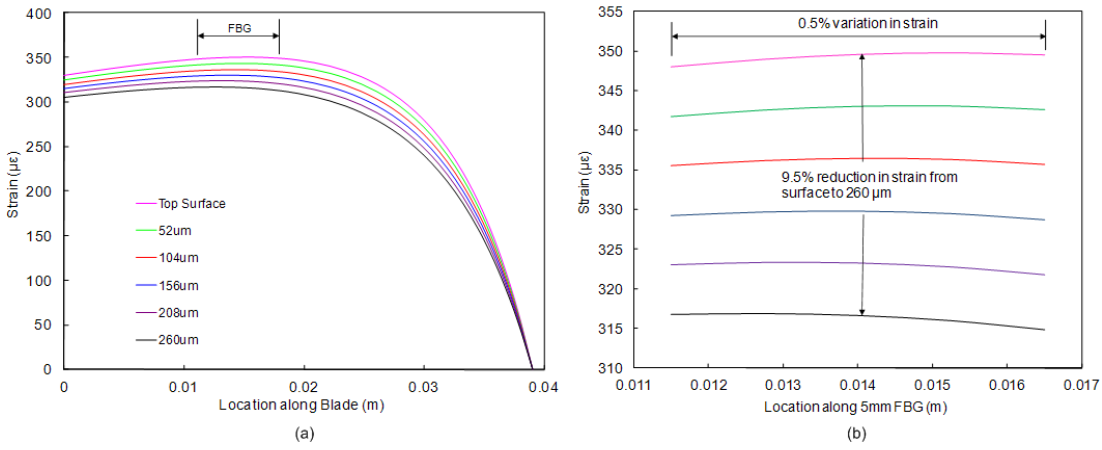

Figure 4-28 (a) Strain variation over blade length from upper surface to base of groove (b) Strain variation along 5 mm FBG length only.

A closer look at the longitudinal and transverse strain variations over the 5 mm FBG only shows that there is 0.5% variation in longitudinal strain and a 9.5%

variation in the transverse strain. While FBGs are sensitive to nonuniform longitudinal strain it is believed that 0.5% is negligible and unlikely to cause significant spectral broadening or multiple reflected peaks [136]. Little is known however on the effect of the transverse strain variation on the readings obtained from the FBG sensor. It is assumed that for a fully embedded fibre the strain measured by the fibre is the strain coincident with the centreline of the fibre. This is justifiable as the strain in the host material is being transferred circumferentially to the fibre via a fully encapsulated adhesive layer. However, when the fibre is partially embedded not all of the host material strain is being transferred circumferentially but primarily concentrated at the bottom and sides of the adhesive layer with the top of the adhesive being open to the environment. Therefore, for a partially embedded FBG, an investigation is required to ascertain whether the strain being measured is the strain coincident with the centreline of the FBG or whether it is affected by the transverse strain gradient throughout the groove depth.

4.6.1 Defining Transverse Strain Gradient

The numerical model used in Section 4.5.5 was modified and used to assess the effect of introducing a transverse strain gradient through the groove. A 9.5% change in displacement between the top of the groove and the base of the groove was applied to the face of the host material. This in turn induced a 9.5% linear strain gradient representative of the variation found in Figure 4-28(a). The change in the longitudinal strain $d\varepsilon_x$ is now a function of the distance dy from the

upper surface of the blade (y = 0) where the constant of proportionality linking both variables is m_o, the slope of the line as shown in Figure 4-29. The term ε_f is the strain expected to be read by the FBG sensor at distance y_f from the blade upper surface.

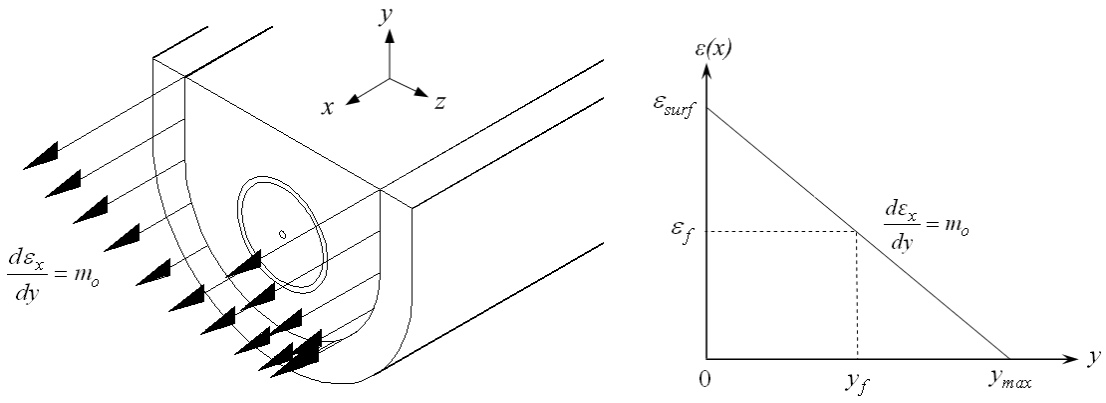

Figure 4-29 Nature of the applied strain gradient to the host material in the finite element simulation

Inducing the strain gradient required that a displacement function was imported into ANSYS which related displacement of the host material at a specific distance from the top surface of the blade of the form,

$$\Delta x = m_o y + x_{surf} \tag{4.12}$$

Δx is the displacement of the host material and x_{surf} is the displacement at the blade upper surface. Since,

$$\varepsilon_x = \frac{\Delta x}{BL} \tag{4.13}$$

where BL is the bond length of the host material, then the induced strain at distance y from the blade upper surface is calculated as,

$$\varepsilon_x = \frac{m_o y + x_{surf}}{BL} \tag{4.14}$$

An ANSYS model of the partially embedded fibre with a BL of 9 mm was created. A 9 mm BL was chosen as this is the BL that ensures 100% of the strain from the host material is transferred to the fibre core. The adhesive thickness below the fibre t_a was maintained at its practical minimum value of 62.5 μm. An image of the loaded model is shown in Figure 4-30 where the applied strain gradient can be seen by the change in colour of the contour lines in the host material. A slope m_o of 1.167 μm/μm was used in this model to induce a 9.5% strain gradient from the upper surface of the host material to the bottom of the groove in which the fibre was embedded.

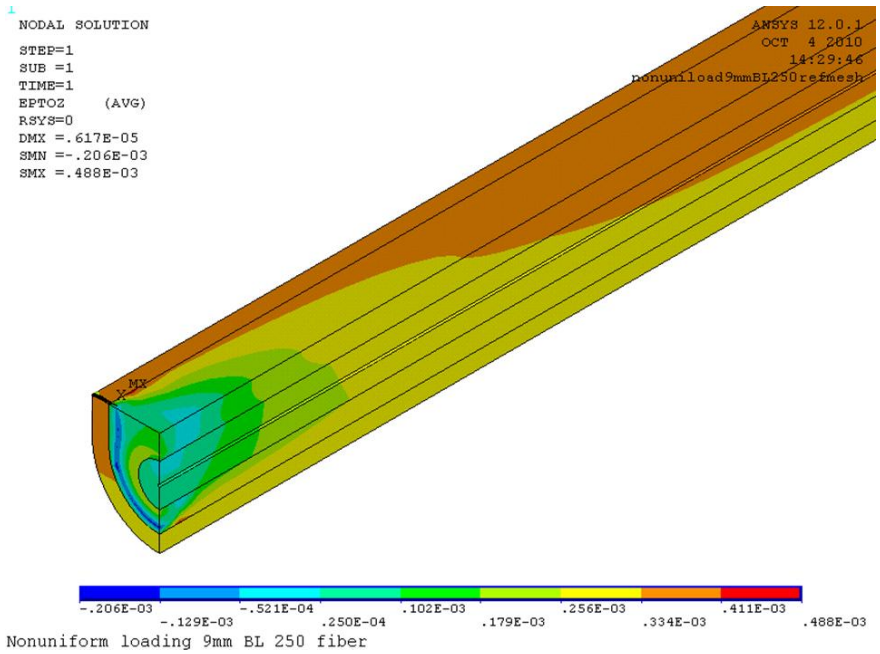

Figure 4-30 Transverse strain gradient applied to the finite element model

Post processing of the results from the FEA model was carried out by creating strain measurement paths at six locations in the model; the upper surface of the host material, 135 µm down from the surface, 260 µm down from the surface, and the top, bottom and centre of the partially embedded fibre. Strain measurements at 135 µm are significant as this is the depth in the host structure which is coincident with the centreline of the bonded fibre. The longitudinal strain readings that were mapped onto the six paths are presented in Figure 4-31. It can be observed that the strain measured along the centreline of the fibre, located 135 µm from the upper surface of the host material, corresponds with the strain within the host material at the same distance from the upper surface.

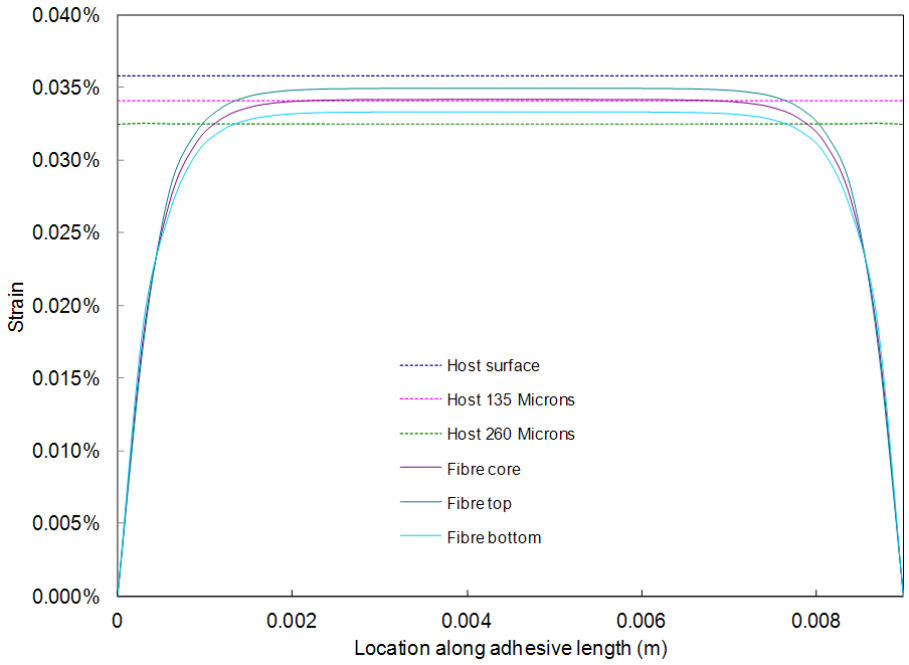

Figure 4-31 Strain readings through host material and embedded fibre

Five further simulations were carried out where the transverse strain gradient was incrementally increased from 9.5% to 90%. The results from each simulation showed that, at each strain gradient the strain measured at the fibre centreline location was the same as the strain at that depth in the host material. These results do suggest that the strain in the core of the fibre over the length of the FBG sensor (5 mm) is the strain experienced by the host material at a location coincident with the fibre centreline even if there is a significant transverse strain gradient through the groove.

4.6.2 The Grooved Blade

The experimental rig used in Section 4.4 in the analysis of a surface mounted FBG sensor was modified to accommodate a FBG sensor embedded within a groove in the blade. A high speed milling machine with a 300 μm wide ball-nosed cutting tool was used to machine the groove into the upper surface of the mocked up symmetrical blade (Figure 4-32(a)).

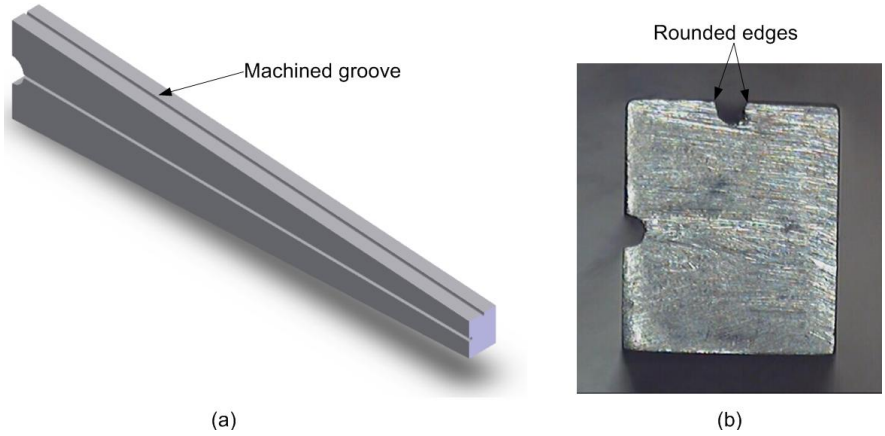

Figure 4-32 (a) Model of the machined blade (b) close-up section view of grooves

An additional groove was put into the blade to accommodate an additional unbonded FBG for the purpose of localised temperature measurement and consequent temperature compensation if needed. The depth of the grooves was 260 μm, which matched the geometry of the FE model. When measured, the widths of the grooves were found to be 340 μm at the top and not 300 μm as originally specified. A close-up view of the grooves (Figure 4-32(b)) showed that the top edges of the grooves had become rounded. It was concluded that this was probably due to swarf catching the top edges of the groove while being removed during the machining process. Even though the rounded edges were slightly different to the corresponding edges in the FE models, it was believed that this would have no affect on the ASTC.

4.6.3 The Recoated FBG

The FBG used was a single mode silica fibre with a 5 mm FBG written into its core. The original Acrylate coating was stripped over a 10 mm region to allow the FBG to be written. The stripped region was then recoated with a polyimide layer used to protect the delicate fibre from damage and breakage. The final outer dimensions of the recoated portion and the original coating of the fibre are shown in Figure 4-33. It should be note that the manufacturing tolerances used in the recoating process are quite low and as a consequence it has been found that there can be quite a variation in the diameter of the recoated fibre from one sensor to the next. This is also evident in Figure 4-33(b) which shows the diameter of the recoated 5 mm FBG region of the fibre. It can be seen that the

diameter over this region is greater than the region close to the original coating by ~6 μm. Therefore, the adhesive thickness between the base of the recoated fibre and the base of the groove is ~55 μm when the fibre is bonded in the groove. This differs from the value used in the analytical and numerical analysis where the adhesive thickness was taken to be 62.5 μm. The thinner adhesive thickness in the experimental setup should not have any detrimental effect on the results obtained other than to enhance the transfer characteristics between FBG and the blade.

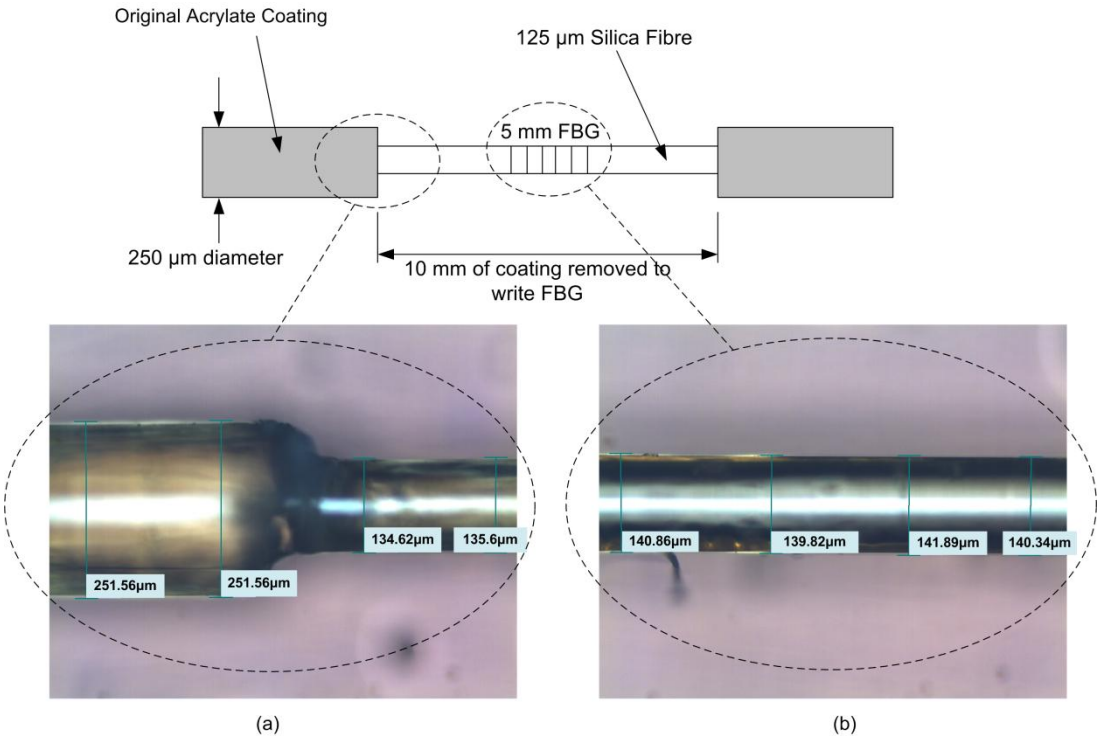

Figure 4-33 (a) Original Acrylate coating and recoated fibre (b) Finished diameter of the recoated fibre at the 5 mm FBG location

4.6.4 Experimental Verification of Coincident Strain

The numerical analysis carried out confirmed that the strain being experienced by a partially embedded FBG is the same as the strain within the host structure coincident with the centreline of the FBG. To verify this, the symmetrical blade used for the surface mounted investigations was modified to include a groove on one half of the blade for embedding the FBG and a machined region on the other half of the blade to accommodate an electrical strain gauge at a depth of 135 μm from the upper surface (Figure 4-34). This machined region will experience the same strain at a depth coincident with the location of the FBG in the other half of the blade. The centre of the machined region was located at 14 mm from the blade pivot point to ensure that the strain gauge was located at the same location as the FBG on the other half of the blade.

The experimental procedure for loading the blade and collecting the FBG and ESG strain information was the same as the procedure described in Section 4.4.3 for the surface mounted FBG.

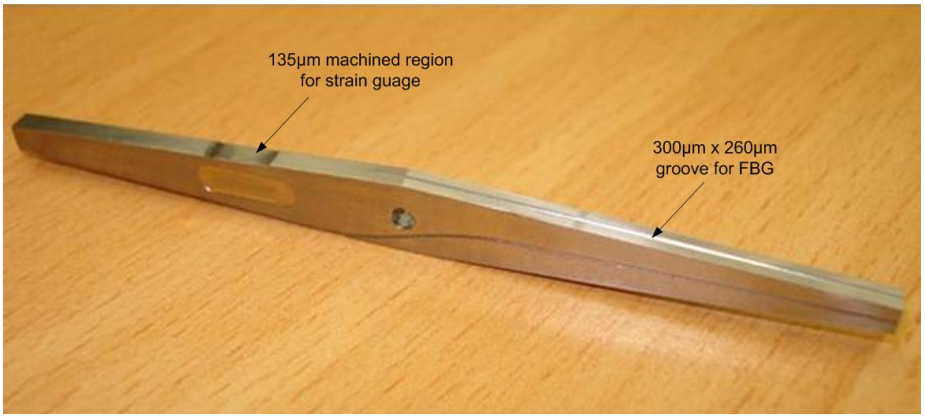

Figure 4-34 Modified symmetrical blade

The results comparing the strain values obtained from the ESG, FBG and analytically are shown in Figure 4-35. The results show the strain readings taken while loading and unloading of the blade between 0 and 30 N. It is notable that there is a very good correlation between both sets of results up to ~15 N. Thereafter there is a decrease in the sensitivity of the FBG sensor while the ESG sensitivity remains constant. It was suspected initially that this change at ~15 N may be due to inadequate bonding of the fibre in the groove. However, the strain values while unloading the blade match exactly the loading readings with no evidence of hysteresis. This would suggest that the bonding is adequate.

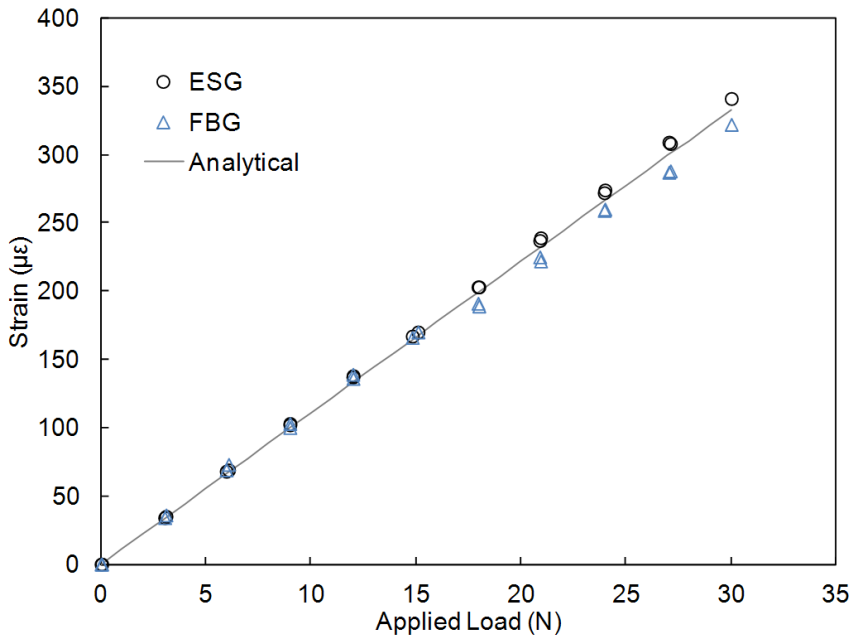

Figure 4-35 Results comparing ESG, FBG and analytical strain values

To check that the mechanical loading of the blade was not causing the issue, the blade was reversed and the experiment carried out again. The readings were found to match those in Figure 4-35 very closely and the change in sensitivity at

~15 N was still evident. It was observed from analysis of the FBG strain readings that noise in the signal appeared to change as the load applied to the blade changed between 0 and 30 N. Therefore, an investigation was carried out to establish if there was a correlation between the noise observed in the signal and a change in the FBG strain readings.

4.7 Fluctuations in the FBG Strain Readings

Reading the load cell force values and the FBG wavelength shift, while the force was being applied at various locations, was carried out by taking 100 samples over a 2 second time period and logging the information. Each set of 200 samples was then averaged to give the force applied to the blade by the load cell and the corresponding strain measured by the FBG sensor. It was observed that the peak-to-peak (p-p) fluctuation in some of the FBG readings, at certain load values, was different to others. Closer analysis of the p-p fluctuation in the signals showed that, at lower load values, it was relatively low (p-p fluctuation of 6 με) but as the loads increased the p-p fluctuation also increased (Figure 4-36).

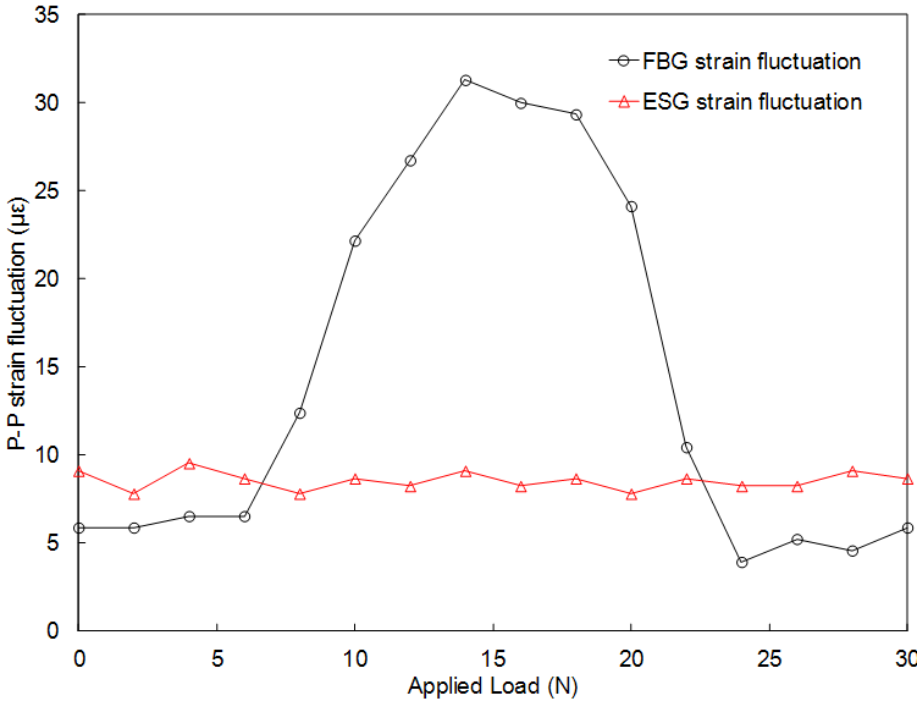

Figure 4-36 Peak to peak strain fluctuation in the FBG readings

A maximum p-p fluctuation of 31 με occurred at 14 N load before decreasing to ~5με thereafter. By contrast the p-p fluctuation measured from the corresponding ESG readings remained constant at ~8.5 με. It was not clear exactly why the p-p fluctuation in the FBG was behaving like this, so a series of experiments were carried out to assess:

1. The influence of FBG bonding on the strain fluctuation.
2. If the blade material affected the fluctuation.

4.7.1 Point Bonding Experiment

It was thought that there could be unknown issues at the contact region between the FBG and the adhesive that may in some way affect the strain transfer to the

fibre. Therefore, is was decided to carry out the same loading experiment as before but change the way in which the fibre was bonded to the blade surface. The experiments carried out in Section 4.4.3 used a FBG bonded to the blade surface over its length. The adhesive bonded the length of the 5 mm FBG plus 3 mm either side to ensure complete strain transfer from the blade surface. To assess whether or not there was an issue with fully bonding the FBG in this way, a new fibre was bonded at the exact same blade location as the previous one. However, the new fibre was bonded to the blade by placing two regions of adhesive on either side of the FBG instead of along its length. This meant that there was no contact between the FBG and adhesive yet the fibre could still be strained by inducing tensile strain on the blade upper surface. The tensile strain was induced in the FBG by turning the symmetrical blade (shown in Figure 4-12) upside down in the test rig and applying the loads at the blade tips as described in Section 4.4.3. The p-p fluctuation was again measured for each applied load and the results are shown in Figure 4-37. There is little difference between the results for the fully bonded and the point bonded FBGs and consequently we concluded that the influence of a fully bonded adhesive layer had no impact on the strain fluctuation. Moreover, strain results taken from the fully bonded FBG were compared under tensile and compression loading but similar p-p characteristics were observed in each case as shown in Figure 4-37.

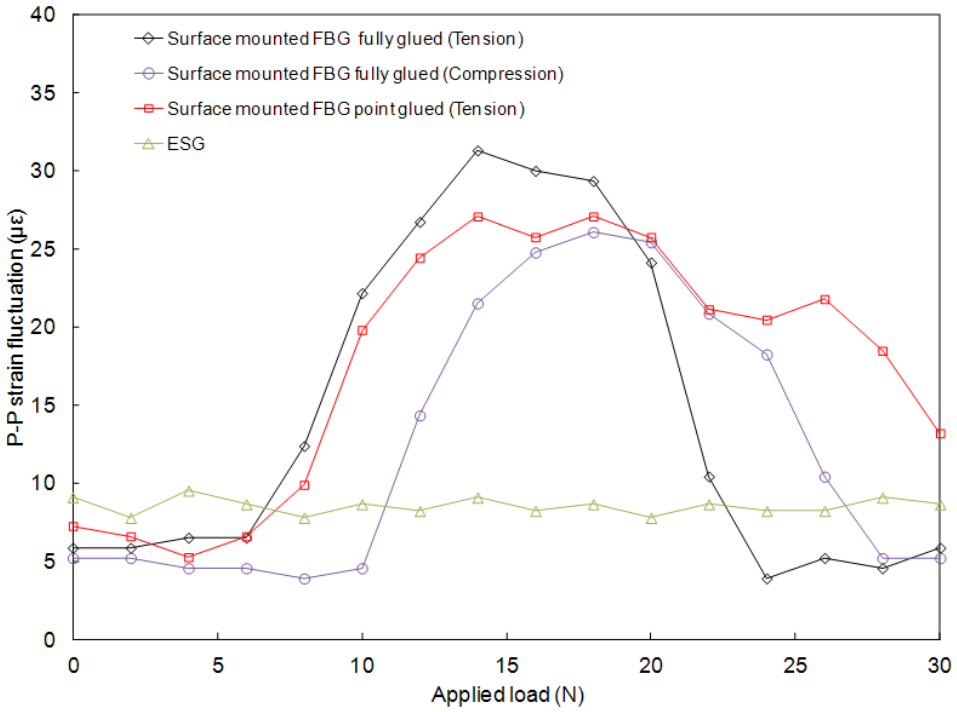

Figure 4-37 P-P fluctuation for point bonded and fully bonded FBGs

4.7.2 Modified Test-Rig

It could be concluded from the experiments carried out in Section 4.7.1 that adverse effects due to bonding, the adhesive material, strain gradients in the vicinity of the FBG and the nature of the loading were not causing the irregular p-p strain fluctuation. Other possibilities were proposed such as the possibility of a resonant vibration occurring in the blade material at a particular load. Therefore, a second symmetrical blade was manufactured from aluminium instead of stainless steel and the experiments repeated with a new FBG bonded at the same location as previous FBGs. The p-p fluctuation results obtained corresponded very closely with results from the stainless blade suggesting that the blade material was not causing the issue.

To assess the possibility of the rig itself introducing inadvertent lateral or transverse loads into the blade during application of the forces, the rig setup was changed. The symmetrical blade was held securely in a rigid translational stage (Figure 4-38) and the blade translated against a solid column which in turn applied the loads to the blade. The results obtained were identical to the previous rig setup which suggested that the original rig set-up was probably not the cause of the strain fluctuations.

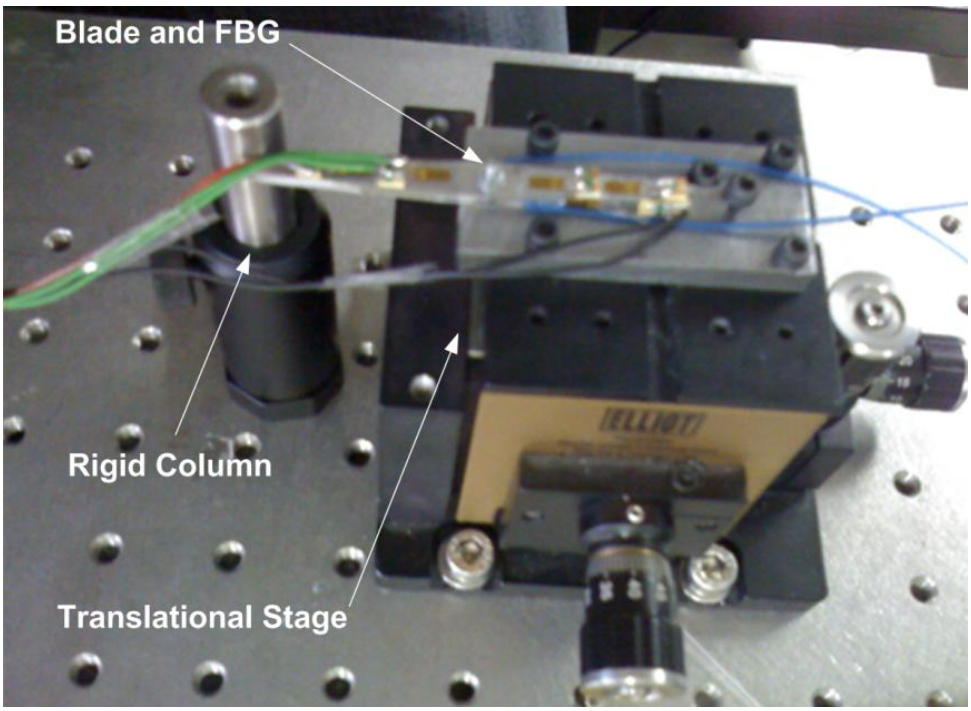

Figure 4-38 Alternative blade loading fixture

4.7.3 Macrobend Interrogation Unit

Having investigated the possibility of mechanical or bonding issues causing fluctuations in the strain readings, attention was turned to the interrogator used

in the detection of the reflected wavelength from the FBG and the shift in reflected spectrum when loaded. The strain readings in previous experiments were obtained using a Wx-02 commercial interrogator unit from the Smart Fibres Company. The Wx-02 unit has a high output power, electrically tunable, solid state laser source with a 2500Hz scan rate enabling real time data acquisition. Using an interrogator based on a tunable-filter method, a broadband source is followed by a filter that can be periodically scanned over the whole wavelength operating range of the sensor. This method of interrogation allows the use of the system in a closed-loop operation, enabling it to track the centre wavelength of the light reflected by a single sensor. Alternatively it could be used in a sweep mode, allowing the interrogation of several sensors simultaneously [137]. This interrogation unit was changed, for the purpose of this experiment, to a macro-bend fibre edge filter ratiometric system developed by Wang *et al* [101]. The schematic structure of a ratiometric wavelength measurement system is shown in Figure 4-39 which includes a splitter, an edge filter, a reference arm and two photodetectors. The edge filter discriminates the wavelength of the input signal with the transmission measured by photodetector A.

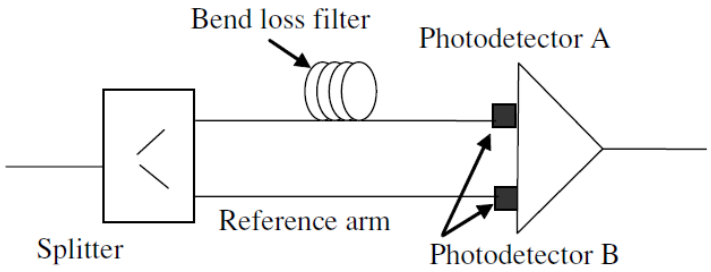

Figure 4-39 Schematic of a ratiometric wavelength measurement system [138]

The reference arm is used and based on the ratio between the measured powers from two arms, it can discriminate the wavelength of the input signal regardless the power of the input signal for an ideal input light (monochromatic) and photodetectors (no noise) [138].

The original test-rig was again used to load the blade and the FBG connected to the macrobend interrogation unit. The results obtained from both units are presented in Figure 4-40. Clearly by using the macrobend interrogator the irregular nature of the p-p fluctuation through the loading range is no longer evident.

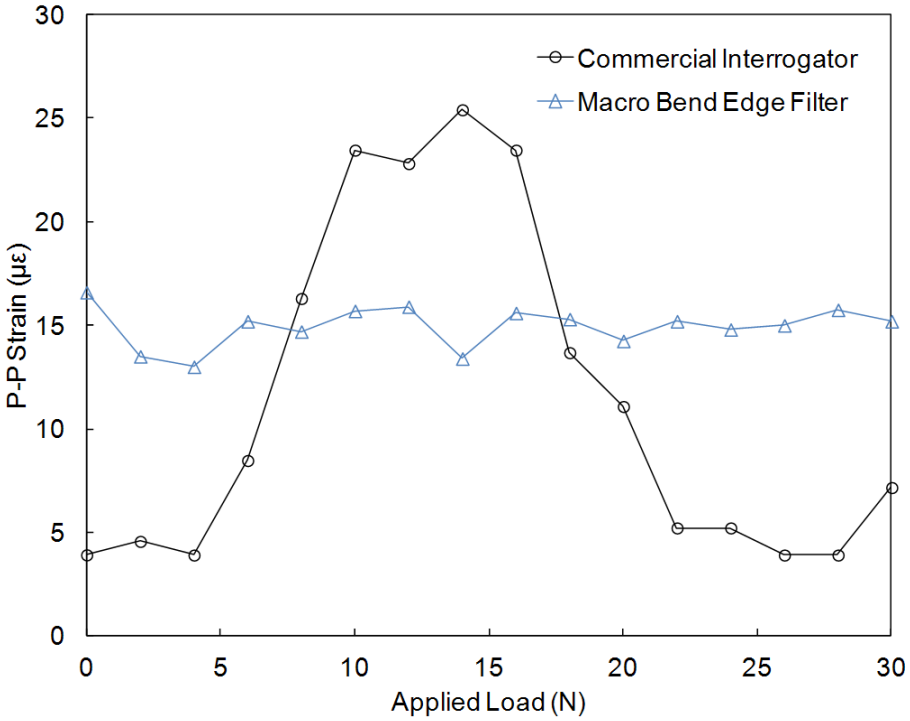

Figure 4-40 Commercial and macrobend interrogator p-p fluctuation

This suggests that the means by which the commercial interrogation unit measures the reflected spectrum could be the reason for the variation in the p-p strain fluctuation. It is not clear if the problem is due to the hardware used in the measurement of the wavelength shift or a software related issue that interprets the measured information. The fluctuation of the signal could be reduced by averaging or filtering the signal. However, the resolution of the overall system is restricted by the maximum p-p fluctuation of ~31 με occurring at particular loading values.

4.8 Lateral Loading of the Grooved Blade

In practice, during a typical cutting cycle, scissor blades experience laterally applied loading due to the curved nature of the blade. The sensitivity of the embedded fibre to these lateral loads is examined. Lateral loads were applied to the blade along its length, with the FBG located at the same longitudinal position, 14 mm from the pivot. Loads in the range 0-12 N were applied at multiple locations along the lateral side of the blade, from the tip (39 mm) towards the location of the FBG (14 mm) in 3 mm increments. The strain measured by the FBG resulting from the laterally applied loads is shown in the Figure 4-41.

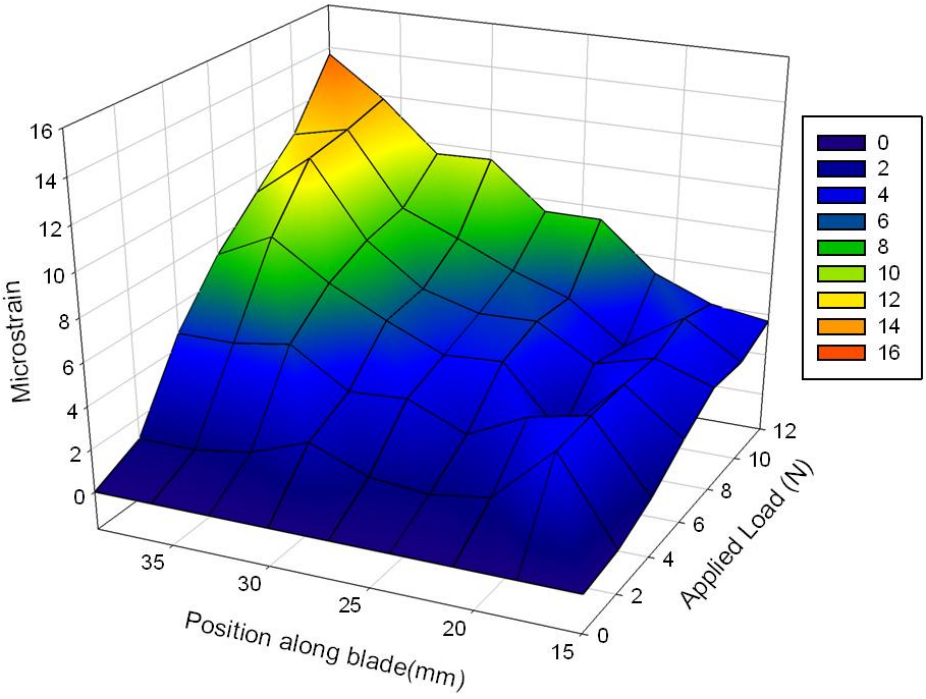

Figure 4-41 Measured FBG lateral strain over a range of loads

It is clear that the lateral loading of the blade will impact the FBG strain readings obtained from direct loading. Although the FBG sensor is less sensitive to the lateral loading, it is still significant enough to cause errors in the direct measurements which arise due to blade friction, tissue fracture and compression. A maximum lateral load of 12 N applied to the tip of the blade introduces a maximum error of 14 με in the measured direct strain. The value of error decreases when the applied load shifts towards the blade pivot due to smaller lateral deflections. Thus, the accuracy of the direct strain measurement is limited due to the inadvertent lateral loading arising from the deflection of the blade during cutting. However, this could potentially be minimised by characterising the lateral strain for a dry cut (without any tissue) and using the

results to form a calibration correction factor to eliminate the impact of the lateral loads.

Theoretically, if the blade groove and consequently the FBG sensor were located exactly on the neutral axis of the blade, the strain readings from the FBG due to lateral loading would be zero. The location of the centreline of the groove relative to the neutral axis of the blade was measured and found to be offset by 80 μm. An analytical equation (4.16) was developed from elementary beam theory which predicted the lateral strain being experienced by the FBG when placed a distance x_g (14 mm) from the blade pivot and a distance w_g (1.063 mm) from the blade cutting face.

$$\varepsilon = \frac{6F(L - x_g)(w - 2w_g)}{Ew^3(mx_g + t_b)} \tag{4.15}$$

F is the lateral load, L the length of the blade, w is the width of the blade, t_b is the thickness of the blade at the pivot, E is the Young's modulus of the blade material and m is the slope of the blade given as;

$$m = \frac{t_t - t_b}{L} \tag{4.16}$$

where t_t is the thickness of the blade at its tip.

Comparing the theoretical lateral strain with the experimental values in Figure 4-42 it can be seen that they correlate closely up to a maximum load of 12 N applied at the tip.

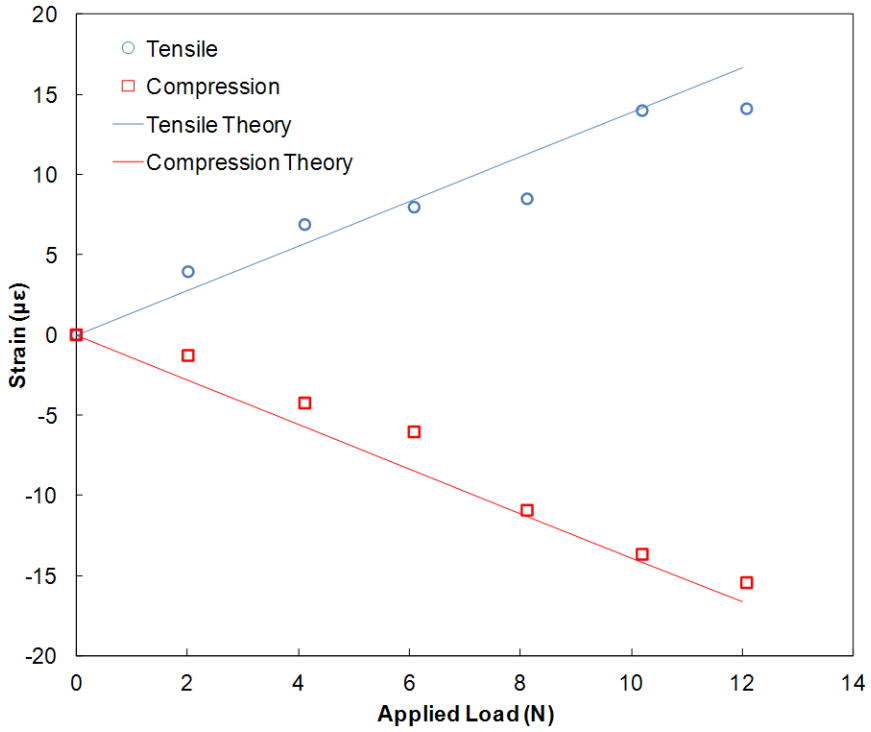

Figure 4-42 Tensile and compressive lateral loading of FBG from laterally loading the blade in opposing directions

The results also highlight that there is a slight discrepancy between the strains measured when the blade is loaded laterally in one direction (Figure 4-43(a)) and then in the opposite direction (Figure 4-43(b)) due to the FBG being offset from the centreline by 80 μm. The sensitivities for each loading direction were found to be 1.13 με N^{-1} and -1.37 με N^{-1} by taking a best fit linear line through the experimental data points.

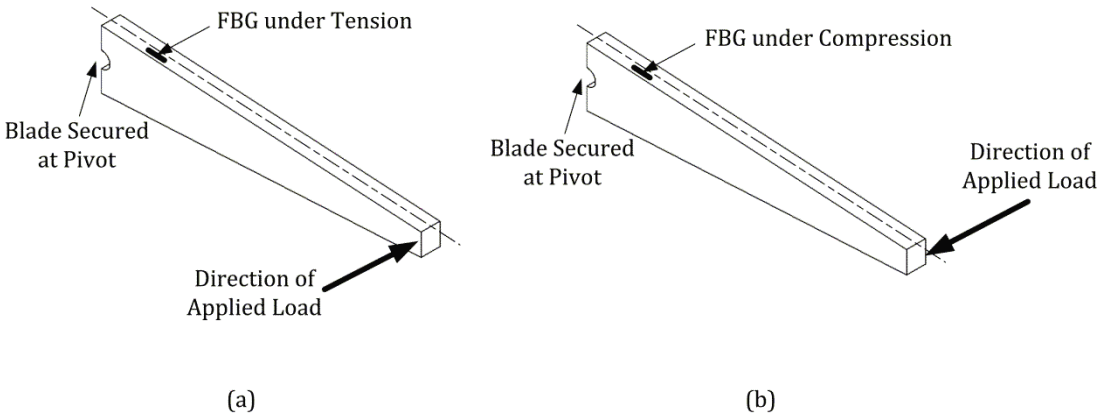

Figure 4-43 Blade showing FBG (offset from blade neutral axis) (a) applied load inducing tensile strain on the FBG (b) applied load inducing compressive strain on the FBG

Comparing the lateral sensitivities of both configurations (Figure 4-44) it is notable that the sensitivities of the surface mounted configuration are generally higher than that of the grooved configuration. This can be attributed to the location of the FBG centreline axis relative to the neutral axis of the blade. The centreline of the FBG embedded within the groove was measured to be offset from the blades neutral axis by ~80 μm (w_g = 1.063 mm) while the surface mounted FBG was measured to be ~100 μm (w_g = 1.043 mm) from the neutral axis. These measurements were used in the equation (4.15) to estimate the theoretical strain being experienced by the FBG in their respective configurations.

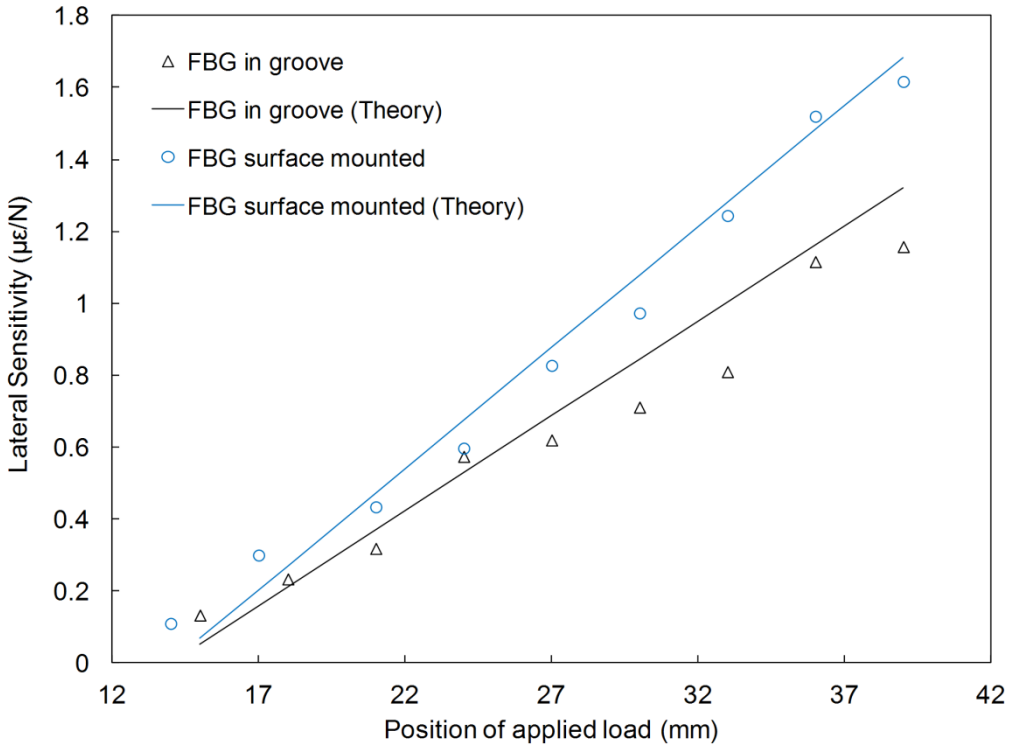

Figure 4-44 Measured and theoretical lateral sensitivities for surface mounted and embedded FBG configurations

4.9 Direct Sensitivities of Surface Mounted and Partially Embedded Blades

Partially embedding the FBG into the structure of the blade moves the fibre away from the location of maximum strain which occurs at the blade surface. It has been established in Section 4.4.3 that the strain read by a surface mounted FBG sensor is in good agreement with established strain sensing technology when the blade is loaded directly. The experimentally measured FBG strain values between the blade tip (39 mm) and FBG location (14 mm) over a 30 N load range are shown in Figure 4-45. The values exhibit good linear characteristics over the length of the blade. Likewise, the partially embedded fibre also exhibits good

linearity as well as close agreement to the theoretically determined values. It is evident that there is a reduction in the sensitivity of the partially embedded fibre arrangement compared with the surface mounted arrangement.

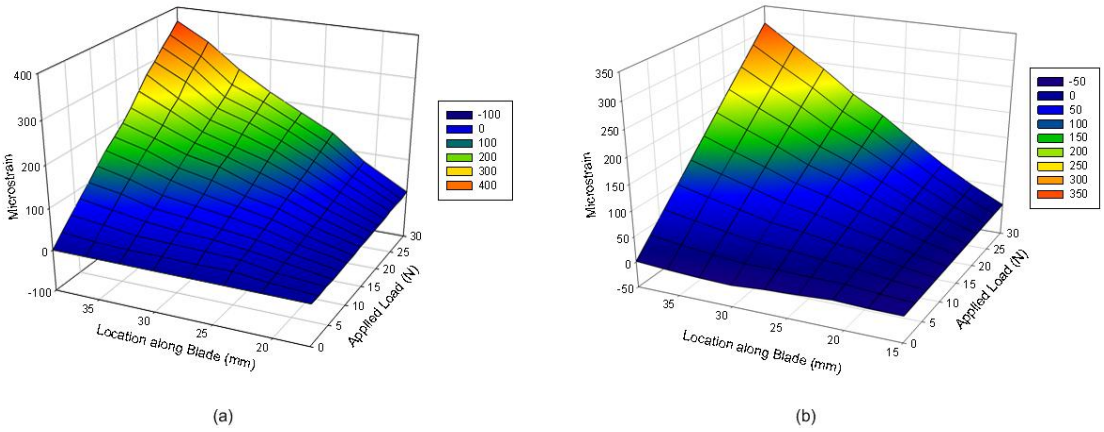

Figure 4-45 (a) Surface mounted FBG strain and (b) partially embedded FBG strain

The determination of the respective sensitivities is achieved by analysing the strain/force ratio for each configuration when the load range (0-30 N) is applied over the region between tip (39 mm) and FBG location (14 mm). Comparing each experimental sensitivity with its respective theoretical value in Figure 4-46 shows that there is a good correlation between them. A difference of 9.2% exists between the surface mounted FBG (5.88 με N^{-1}) and embedded FBG (5.34 με N^{-1}) arrangements when comparing the experimental sensitivity values. The corresponding theoretical sensitivities, based on elementary beam theory, were 5.36 με N^{-1} for the surface mounted and 4.91 με N^{-1} for the partially embedded fibre giving an average difference of 8.4%. It can be seen that the FBG sensitivity values for the embedded fibre correspond very closely with the theoretical

values with good linearity being attained. The surface mounted FBG corresponds more closely to the theoretical values when the loads are applied at blade locations between 24 mm and 39 mm with a slight deviation from linearity between 24 mm and 15 mm.

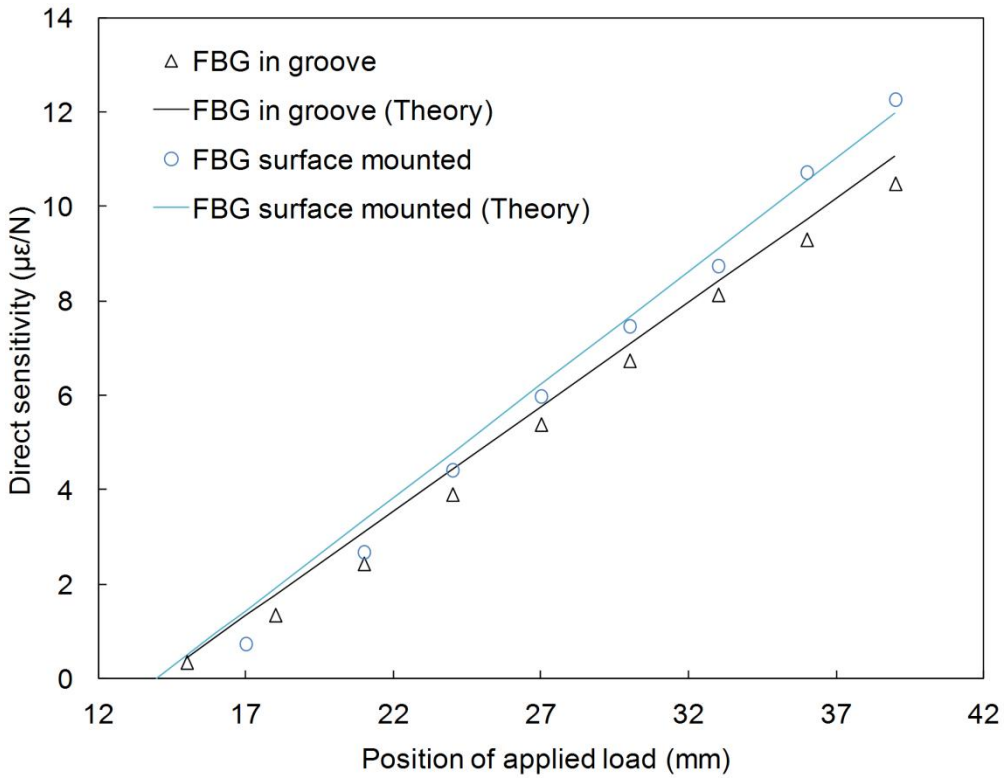

Figure 4-46 Direct loading sensitivities for surface mounted and embedded FBG configurations

The ratio of the direct-to-lateral sensitivity values for both surface mounted and grooved configurations are compared in Figure 4-47. The theoretical results show that the direct-to-lateral sensitivity ratio should remain constant along the blade length. However, the experimentally obtained values show that direct-to-lateral sensitivity ratio remains relatively constant from the blade tip (39 mm) to

~24 mm corresponding to ~38% of the blade length. In the region between 24 mm and the location of the FBG (14 mm) the sensitivity ratio is clearly erroneous. This could be attributed to the lower (direct and lateral) sensitivities in this region being affected by the p-p strain fluctuation discussed in Section 4.7 leading to inaccuracies in the measured values. However as documented by Greenish [75] surgeons typically use the first one third of the blade (from the tip) which is the region in Figure 4-47 where the direct-to-lateral sensitivity ratio is relatively constant.

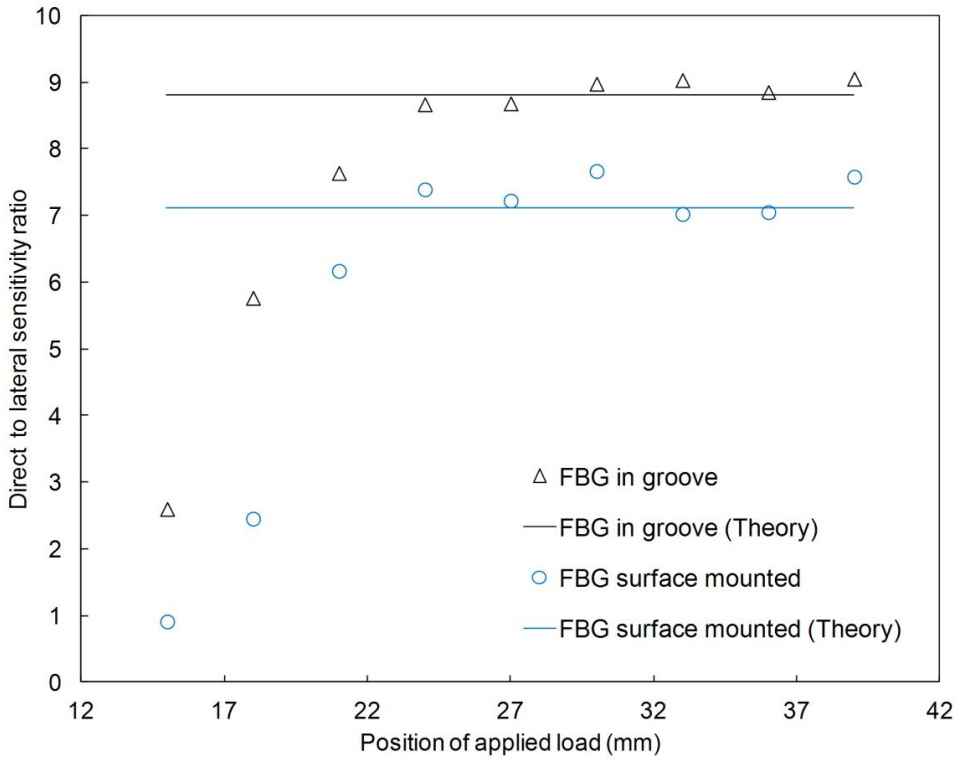

Figure 4-47 Measured and theoretical direct to lateral strain ratio for both surface mounted and grooved configurations

4.10 Summary

In this chapter the transfer of strain from the scissor blade to the core of a FBG sensor bonded to the blade was investigated. FBG sensors are not available as pre-packaged modular sensors; therefore, the bonding of the fibre to the host structure requires consideration as a non-uniform strain distribution across the FBG sensor will lead to spectral broadening and distortion of the reflected spectrum.

An average strain transfer coefficient (ASTC) theoretical model developed by Cox *et al* for a fully encapsulated FBG was used to estimate the adhesive bond length required to ensure complete strain transfer from host to FBG. A numerical model was developed to more accurately simulate the ASTC for a surface mounted fibre.

A study was carried out where a FBG was partially embedded within the structure of a mocked up scissor blade to assess the effects of adhesive bond length and adhesive thickness as well as the sensitivity of the partially embedded sensor arrangement. No theoretical models existed for a partially embedded fibre so the model for a fully encapsulated fibre was modified to account for a change in adhesive between the bottom of the fibre and the base of the groove.

The study also investigated whether or not the presence of transverse strain gradients through the host material had any effect on the strain reading obtained from the FBG sensor.

The key conclusions of this chapter can be summarised as follows;

- A series of adhesive bond lengths and adhesive thicknesses for a surface mounted FBG sensor were assessed using the numerical model. It was found that for an adhesive thickness of 62.5 μm a bond length of 11 mm (55% longer than the FBG) ensures 100% strain transfer and uniform strain across the 5 mm FBG length.
- A novel evaluation test-bed was developed which allows FBG and ESG strain readings to be assessed simultaneously. Results show that the sensors are in good agreement with a maximum variation of 2.8% between respective strain readings. The ratio of the strain measured by the FBG to that of the ESG was found to be 0.98. This was defined as the ASTC.
- Analysis of the reflected FBG spectrum at zero and maximum load reveals that no errors occurred in the FBG strain measurements as a result of strain non-uniformity along the grating. This confirmed that 11 mm is an appropriate bond length for the 5 mm FBG used, allowing strain uniformity and complete strain transfer to be obtained.
- A numerical model was developed for the partially embedded FBG and it was found that the modified analytical model compared favourably. Using an adhesive thickness of 62.5 μm it was found that the adhesive bond length for a partially embedded FBG could be reduced to 9 mm compared to 11 mm for the surface mounted FBG. An 18% reduction in bond length is desirable from the point of view of ensuring the sensing arrangement is as compact as possible.

- Numerical simulations, where a series of strain gradients up to 14% were applied, showed that the strain measured by the FBG is the strain coincident with the FBG centreline. However, it is believed that there is a need for more detailed knowledge of the adhesive properties being used in the simulations to more accurately reflect the complex interaction between fibre, adhesive and host material. Experimental results show that the coincident strain measured by the FBG correlated well with results from an electrical strain gauge and the numerical simulations. There was an irregularity in the results from the FBG midway through the loading range. It was proposed that these errors in reading could be due to noise fluctuation observed in the measured signal at different loading values. An alternative interrogation technique confirmed that the peak-to-peak fluctuation observed appeared to be caused by the commercial interrogator unit used in the study.
- The sensitivity of the FBG sensor to lateral loading, whether surface mounted or partially embedded, was investigated. The results show that the FBG is sensitive to both direct loading and lateral loading of the blade. The strain effects of lateral loading must be compensated for as the laterally induced strain will introduce errors into the direct force readings. These laterally induced errors have particular importance when the forces being measured are to be used in the measurement of tissue elastic and fracture properties.

Chapter 5

Dynamic Cutting Analysis of the Sensorised Scissor Blade

5.1 Introduction

The strain experienced by an actual scissor blade onto which a FBG sensor is attached is investigated and modelled, through the use of elementary beam theory (EBT). A theoretical analysis is presented, followed by experimental verification, of the strains that occur coincident with the FBG position on the blade due to the blade being loaded directly and laterally during operation. The model demonstrates how the complex strains generated during blade opening and closing will contribute to the total strain readings obtained from the FBG sensor. Moreover, a means of decoupling the lateral and direct forces is modelled and validated using data obtained from the sensorised characterisation test-bed. The model employs the use of double tapered beam theory to represent the blade [139-142]. From this, a theoretical calibration ratio can be developed allowing estimations to be made in relation to the sensitivity of the sensorised

blades. The calibration ratio is verified experimentally and subsequently used to facilitate the measurement of forces generated at the interface between tissue and blades at any location along the blade. This will enable analysis of the variation of forces acting on the blade as the blades open and close [107, 108]. To validate the accuracy of the force results obtained from the FBG sensorised blade, results are compared to those obtained from a commercial load cell.

5.2 Blade-Tissue Interaction

Inter-blade friction and the fracture properties of the material being cut are the primary factors affecting the magnitude of blade-tissue interaction forces. Our approach aims to integrate the sensor into the actual scissor blade at the blade-tissue interaction site. This arrangement provides for excellent transmission of resulting blade strains to the sensor. This ensures that measurements are not adversely influenced by factors such as mechanism friction and backlash [6]. This increased accuracy provides the basis for improved analysis of the resultant force components.

Sharp dissection implies the use of concentrated energy on a relatively small area of tissue to achieve separation with little disruption to surrounding tissue. The scissor cutting method consists of two sharpened blades rotating about a common pivot location during closing. The blades are curved along their longitudinal axis such that, upon passing, there is a point contact between the cutting edges of both blades [74]. This is the point at which all the external input energy, from scissor actuation, is concentrated. This point is referred to as the

blade intersection point as shown in Figure 5-1. This intersection point moves along the blade length as the included angle of the cutting edges changes through a cutting cycle. As a result, two coincident friction force components (direct and lateral) are occurring at the intersection point as it moves through the cycle. Implementing a FBG sensing element as part of the blade structure means that both the lateral and direct force components are measured simultaneously. However, it is the direct loading forces that are of primary interest in this work as they are the forces acting perpendicular to the blade cutting edges, giving a sense of feeling to the user. The approach taken in the development of a set of sensorised scissor blades capable of facilitating the measurement of these direct forces is shown in Figure 5-1.

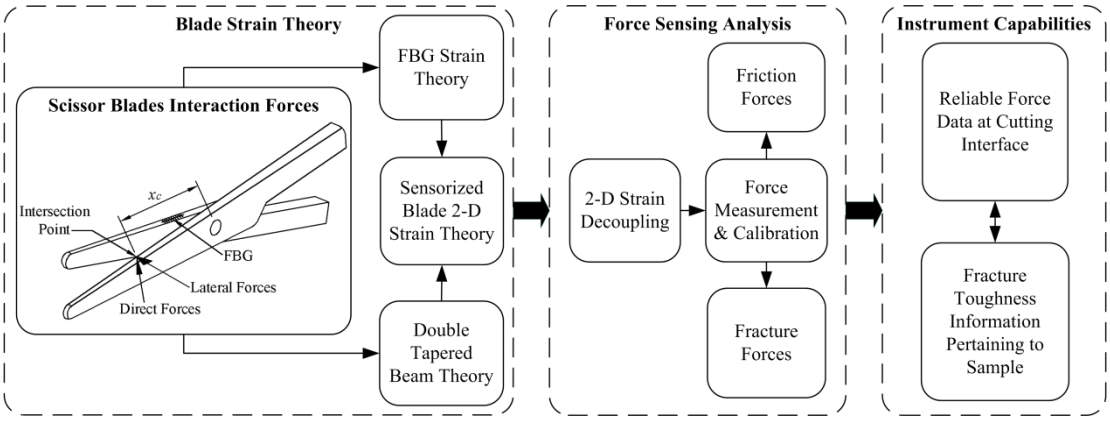

Figure 5-1 Proposed method of measuring blade-tissue interaction forces

5.2.1 The Effect of Eccentric Blade Loading

A finite element analysis of eccentric loading was carried out on a model of a blade to assess the applicability of employing elementary double tapered beam

theory during blade strain analysis. Firstly, the blade was loaded directly (F_d) at the location of the blade neutral axis (Figure 5-2(a)), then, the load was offset from the neutral axis to the cutting edge. Secondly, a similar evaluation was carried out during lateral loading where F_s was applied both at the neutral axis and offset to the cutting edge. F_d and F_s were set to 30 N and 10 N respectively and applied at the blade tip to induce maximum bending moments.

The strain distributions resulting from F_d being applied at the neutral axis, then offset by 0.76 mm (half the blade width at its tip) to the blade cutting edge, are shown in Figure 5-2(b). The strain values were measured at two locations on the blade upper surface; at the centreline axis (green and purple) and at the cutting face plane (red and blue). Results show that there is no discernible error between the strain plots at these locations under the described loading conditions.

During lateral loading, F_s was applied at the blade neutral axis and subsequently offset from the neutral axis by 1.345 mm (half the blade thickness at the tip) as shown in Figure 5-3 (a). Strain distributions were measured on the blade upper surface at the cutting face plane as well as 0.38 mm and 0.76 mm from the cutting face plane Figure 5-3 (b). Analysis of the strain at the three locations found that the impact of eccentric loading induced negligible twisting of the blade. It is reasonable therefore, to assume that the use of elementary beam theory, in which the loads are applied at the blade neutral axis, is representative of a scissor blade being loaded eccentrically along its cutting edge.

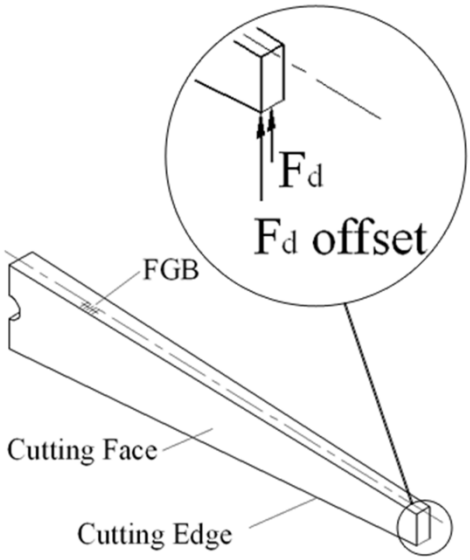

(a)

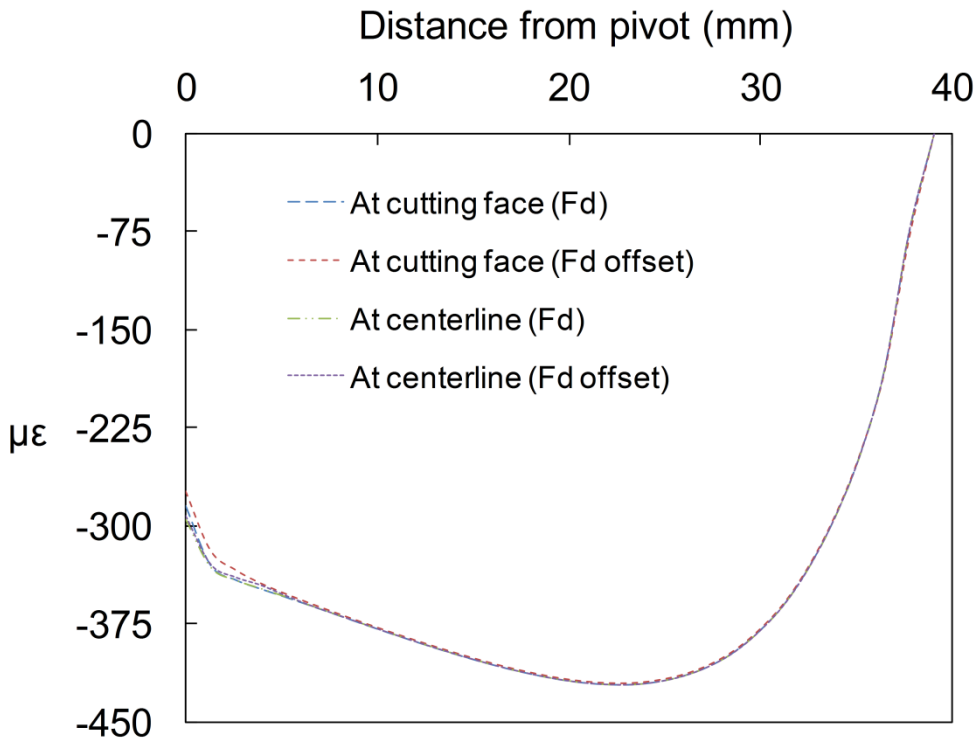

(b)

Figure 5-2 (a) The Finite Element model being loaded at the blade centreline (F_d) and at the cutting edge (F_d offset), (b) Strain profiles along the blade top surface for both direct loading configurations.

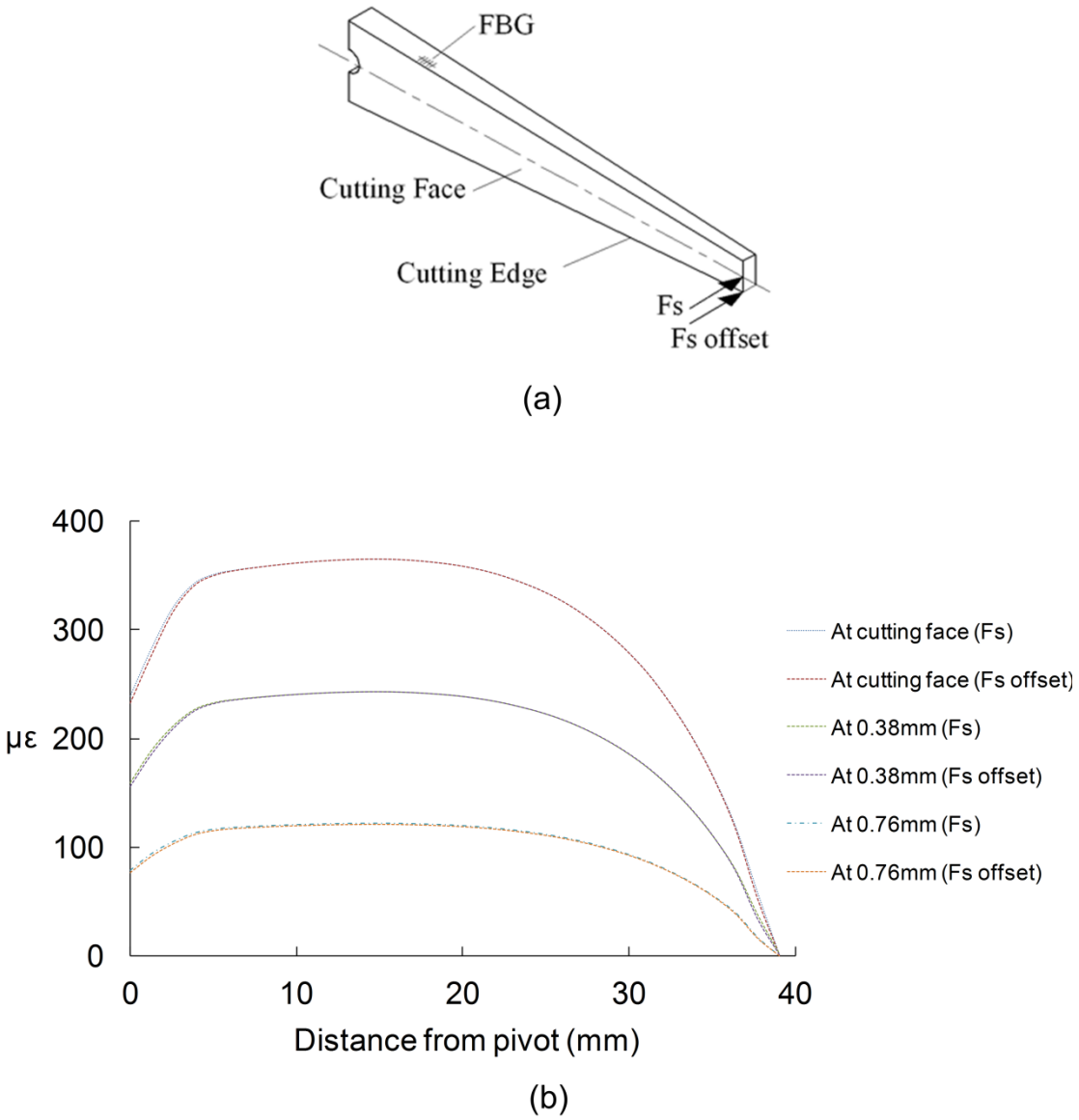

Figure 5-3 (a) The Finite Element model loaded laterally at its centreline (F_s) and offset to the cutting edge (F_s offset), (b) Strain profiles at three locations along the blade top surface for both lateral loading configurations.

5.2.2 Tapered Blade Strain Analysis using EBT

The scissor blade onto which a FBG strain sensor is to be attached can be approximated as a cantilever beam tapering uniformly in two planes (Figure 5-4). The blade is loaded both laterally and directly to investigate the nature of

the 2-D strains experienced at the location of the FBG. The FBG sensor is located on the blade upper surface so as not to interfere with blade functionality during opening and closing. Using elementary beam theory, the resultant strain ε at any location x along the blade length for a given direct force input F_d can be estimated from equation (4.4).

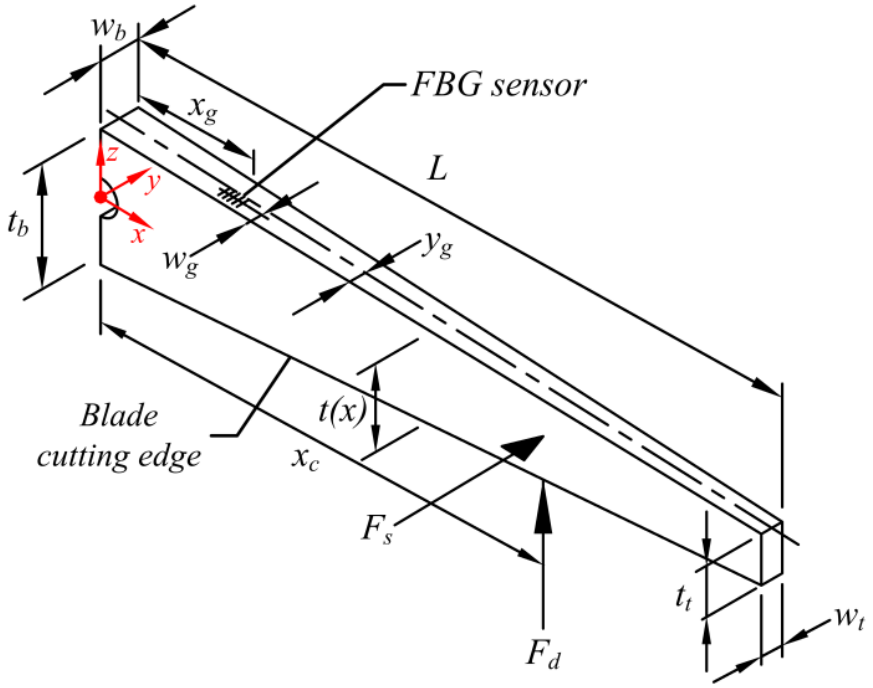

Figure 5-4 Geometry of a double tapered scissor blade

The blade section varies linearly in both planes and consequently the Second Moment of Area $I(x)$ of the section can be expressed as,

$$I(x)=\frac{nx+w_b \quad mx+t_b}{12}^{3} \tag{5.1}$$

where the blade width w(x) is given as,

$$w(x)=nx+w_b \tag{5.2}$$

with the width taper ratio n given as,

$$n = \left(\frac{w_t - w_b}{L} \right) \tag{5.3}$$

Substituting (5.1) into (4.4) results in the strain as measured by the FBG at location x_g due to direct loading at x_c and is given as,

$$\varepsilon_d = \frac{6F_d(x_c - x_g)}{E(nx_g + w_b)(mx_g + t_b)^2} \tag{5.4}$$

Direct force loading of the blade during an empty cut arises from frictional contact between the blades while they are opening and closing. When the blades are passing one another during this empty cut cycle there is effectively a point contact at their point of intersection due to the blades curving along their length in the xy plane. It is therefore reasonable to assume that forces during opening and closing are generated perpendicular to the blade cutting edges at x_c. The curved profile also causes lateral deflection resulting in lateral forces on the blades during a cutting cycle. This lateral deflection influences the FBG readings as the fibre is bonded to the upper surface of the blade. The lateral strain ε_s is estimated using an approach analogous to that for calculating the direct strain and is presented as,

$$\varepsilon_s = \frac{6F_s(x_c - x_g)}{E(mx_g + t_b)(nx_g + w_b)^2} \tag{5.5}$$

The fibre lateral location, y_g, which can be varied between the blade centreline and blade cutting surface, is according to equation 5.5 assumed to be located at the blade cutting edge where,

$$y_g = \frac{nx_g + w_b}{2} \tag{5.6}$$

This is an undesirable location as placing the fibre at the blade cutting face interferes with blade functionality as well as compromising the protection of the FBG during operation. Modification of equation 5.6 to include the term w_g permits the measurement of strain values at any location between the blade cutting edge and its centre axis to be evaluated according to,

$$y_g = \frac{(nx_g + w_b) - 2w_g}{2} \tag{5.7}$$

Substituting (5.7) into (5.5) results in equation (5.8) and describes the lateral strain induced in a FBG strain sensing element attached to the upper surface of a blade. Therefore,

$$\varepsilon_s = \frac{6F_s(x_c - x_g)((nx_g + w_b) - 2w_g)}{E(mx_g + t_b)(nx_g + w_b)^3} \tag{5.8}$$

where x_g and w_g are the longitudinal and lateral locations respectively of the fibre on the blade upper surface. The resultant total strain ε from the FBG sensor subjected to F_d and F_s inputs at coincident locations along the blade length is therefore the sum of ε_d and ε_s. It is evident that to obtain relevant direct force information perpendicular to the cutting edges, ε_s needs to be decoupled from the total strain readings.

5.2.3 Decoupling Strains

Extracting pertinent force information from the total FBG strain requires a means of decoupling $\varepsilon_s(\theta)$ from $\varepsilon_d(\theta)$. It is proposed here that the use of a single

FBG on the blade can facilitate the measurement of both $\varepsilon_s(\theta)$ and $\varepsilon_d(\theta)$. These individual strain components acting on the FBG sensor are separated using a novel decoupling technique. This is the first time that this decoupling technique has been implemented and consequently offers a new contribution in the field of FBG sensing in surgical instruments. Decoupling can be achieved by analysing the total strain measured by the FBG during blade opening and closing to allow for the extraction of reliable estimates of $\varepsilon_s(\theta)$ and $\varepsilon_d(\theta)$. To distinguish between strain measured by the FBG during opening and closing the direct strain $\varepsilon_d(\theta)$ will be denoted as $\varepsilon_o(\theta)$ during opening and $\varepsilon_c(\theta)$ during closing. Note, that when closing the blades without any tissue present between them (empty pass), the direct strain $\varepsilon_d(\theta)$ becomes $\varepsilon_f(\theta)$ which is the strain resulting from blade friction forces only. The strain values measured by the FBG during the closing phase are therefore expressed as,

$$\varepsilon_c(\theta) = \varepsilon_s(\theta) - \varepsilon_f(\theta) \tag{5.9}$$

where $\varepsilon_f(\theta)$ is negative due to compression of the blade upper surface resulting from friction forces being applied to the blade at x_c. During the opening phase the direction of the friction force is reversed inducing tension in the blade upper surface, hence,

$$\varepsilon_o(\theta) = \varepsilon_s(\theta) + \varepsilon_f(\theta) \tag{5.10}$$

The inherent lateral curvature of the scissor blades dictates that the blade will deflect outward during closing whilst returning to their original shape upon opening. It is reasonable to assume from this that, over a complete opening and closing cycle, the net $\varepsilon_s(\theta)$ equates to zero. Therefore, utilising equations (5.9)

and (5.10) results in an expression which estimates $\varepsilon_f(\theta)$ directly from the total strain measured by the FBG without need for further manipulation, as follows,

$$\varepsilon_f(\theta) = \pm \frac{\varepsilon_o(\theta) - \varepsilon_c(\theta)}{2} \tag{5.11}$$

The strain profiles for a cut cycle using typical force values for an empty cut are illustrated in Figure 5-5, where the blade cutting edge angle θ is a function of x_c and can be calculated as,

$$\theta = 2\tan^{-1}\left(\frac{t_b}{2x_c}\right) \tag{5.12}$$

This suggests that from a theoretical perspective, accurate $\varepsilon_f(\theta)$ and $\varepsilon_s(\theta)$ values can be obtained via a single FBG sensor located on the blade. The resultant strains are proportional to the applied loads and as a result the friction-to-lateral strain ratio is defined as the kinetic friction coefficient μ_k. Therefore,

$$\mu_k = \frac{\varepsilon_f}{\varepsilon_s} \tag{5.13}$$

It is notable from Figure 5-5 that when the blades are closed to a blade angle of ~10° there is a difference in the opening strain value, $\varepsilon_o(\theta)$, and the closing strain value, $\varepsilon_c(\theta)$, of 30 με under these particular loading conditions.

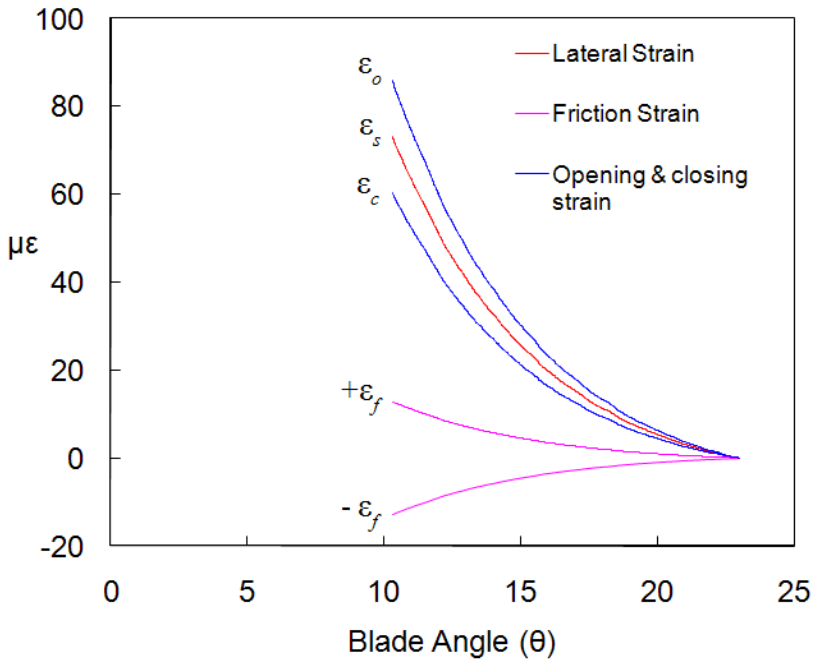

Figure 5-5 Theoretical lateral, friction and total strain values for an empty pass

Consequently, the nature of the strains being experienced by the FBG changes from compressive (closing cycle) to tensile (opening cycle). This is due to the normal force between the blades holding them together and inducing a friction torque that causes the blade to hog when the external opening torque is applied to the scissor handles. The hogging blade creates tensile strain on its upper surface which materialises as tensile strain readings from the FBG.

5.2.4 Fracture Induced Strain

The strain profiles illustrated in Figure 5-5 are representative of an empty cut devoid of any material between the blades. However, the cutting of material during the closing phase creates additional compressive effects on the blade upper surface. This further compresses the fibre and reduces the total strain

measured by the FBG in proportion to the generated fracture forces. This change in measured strain will allow friction as well as fracture force information to be obtained during cutting (Figure 5-6). This enables accurate force reflection of forces generated at the cutting interface and facilitates the collection of material property data pertaining to the fracture toughness of the materials being cut.

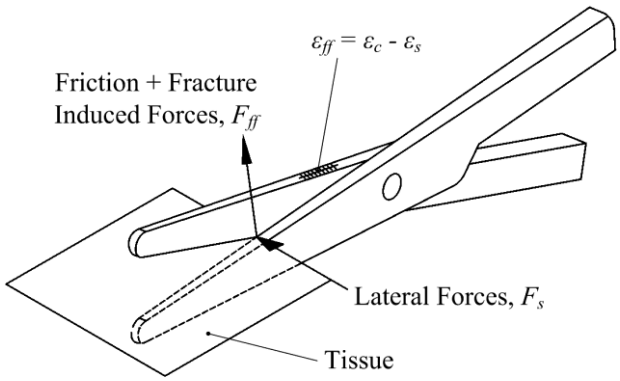

Figure 5-6 Friction, fracture and lateral forces acting on the scissor blades

The use of scissor blades is a convenient means of obtaining material fracture toughness by using equations 3.6 and 3.7. The respective force values F_{ff} and F_f are obtained from the decoupled FBG measured strains, $\varepsilon_{ff}(\theta)$ and $\varepsilon_f(\theta)$, which are independent of the inherent lateral strain effects. To obtain strain resulting from tissue cutting, the total FBG strain during closing is modified using the following,

$$\varepsilon_{ff}(\theta) = \varepsilon_c(\theta) - \varepsilon_s(\theta) \tag{5.14}$$

where $\varepsilon_s(\theta)$ was found to be constant during both empty and material cutting cycles. Theoretical strain profiles based on the cutting of standard copier paper with a measured fracture toughness of 4.36 kJ/m^2 are presented in Figure 5-7.

The total FBG strain data in Figure 5-7(a) contains three coupled strain effects, $\varepsilon_s(\theta)$, $\varepsilon_{ff}(\theta)$ and $\varepsilon_f(\theta)$ resulting from their corresponding force inputs to the blade F_s, F_{ff} and F_f. Since $\varepsilon_s(\theta)$ is readily ascertained by combining equations (5.9) and (5.10) it can be subtracted from $\varepsilon_c(\theta)$ to leave strain information pertaining to F_{ff} over the blade length as shown in Figure 5-7(c). Comparing $\varepsilon_{ff}(\theta)$ in Figure 5-7(c) to $\varepsilon_f(\theta)$ in Figure 5-5, there is approximately a 40% increase in $\varepsilon_d(\theta)$ due to the additional forces required to fracture the paper sample. It should be noted that during the cutting of dry paper samples there is no lubricant present between the blades and as a consequence F_f remains constant throughout the cycle. It is reasonable to claim that the presence of fluids while cutting real tissue may alter the kinetic friction coefficient compared to dry conditions. However, experiments carried out by [74] on three different types of scissor blades demonstrated that for each pair of scissors, the same friction force readings were obtained during dry and lubricated conditions. The hydrodynamic effects are limited during cutting owing to the low velocities involved as well as the very small contact area between the blades. However, further experiments should be carried out using a range of lubricant types to ascertain the extent to which the friction coefficient remains constant.

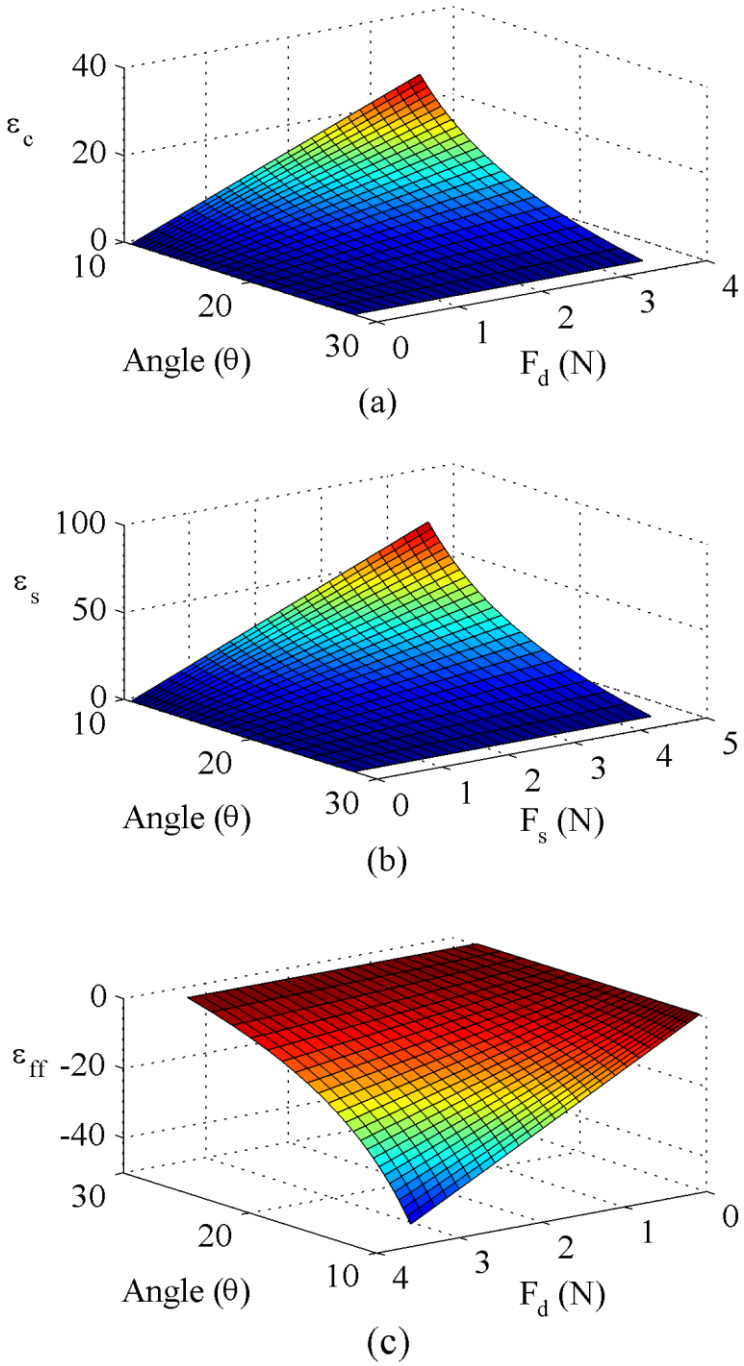

Figure 5-7 (a) Theoretical total FBG cutting strain (b) lateral strain only (c) combined fracture and friction strains decoupled from $\varepsilon_s(\theta)$

Experiments carried out by Atkins [143] on the guillotining of ductile metal plates also demonstrated that the force component present between the blades

due to friction was virtually the same for dry and lubricated cuts. The friction force component, however, was small in comparison to the shear, fracture and bending components which may have masked any discrepancy between the lubricated and dry friction force values.

5.3 Sensorised Blade Experimental Setup

The characterisation test-bed described in Section 3.6 [144] was modified to include a FBG force sensor attached to one of the scissor blades. A set of experiments were carried out using the sensorised blade to:

1. Validate the effectiveness of the strain decoupling technique employed to segregate the various strain components acting on the FBG.
2. Validate the direct force measurements obtained using the sensorised blades against the values obtained from the commercial load cell.

A standard single mode 125 μm diameter FBG sensor (similar to the fibre used in Section 4.6.3) was bonded to the upper surface of one of the cutting blades in the test-bed (Figure 5-8). A surface bonded FBG configuration (as opposed to a embedded FBG configuration) was deemed adequate for the purpose of validating the decoupling theory and validating the sensorised blade against a commercial load cell. The commercial load cell used in the test-bed will allow a direct comparison to be made between force values measured by the FBG and those measured by the load cell. A temperature compensation FBG located on the blade can be used to counteract temperature variation. However, in the

present case the internal temperature sensor of the FBG interrogation unit has been used to compensate for the influence of fluctuating ambient temperature effects on the strain readings.

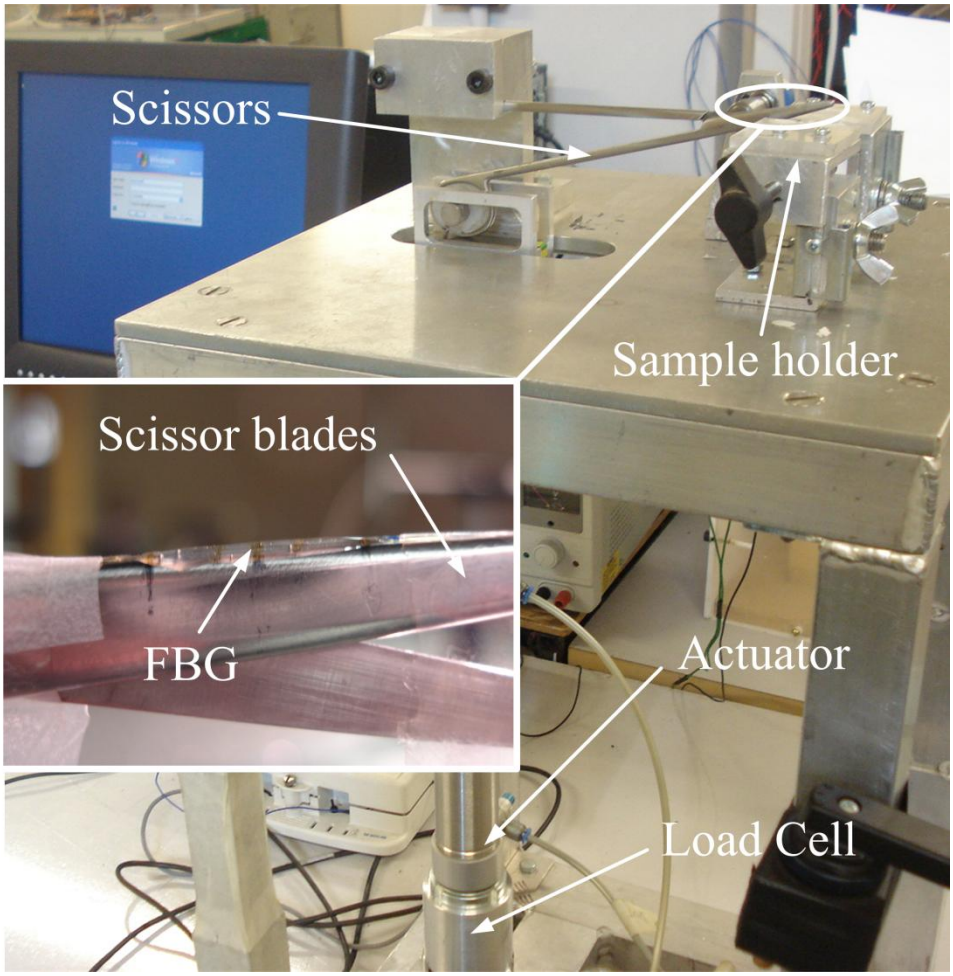

Figure 5-8 Experimental characterisation test-bed showing the location of the FBG on the blades

This method of compensation was deemed suitable for this study as the duration of the cutting cycles are short (approximately 9 seconds) and temperature fluctuation over that duration was minimal. Moreover, the ambient temperature sensed by the interrogation unit is similar to that of the FBG due to the close

proximity of the interrogator to the blades. Future work will address this shortcoming by incorporating an unbonded FBG temperature sensor into the sensorised instrument. The unbonded FBG will sense localised temperature changes enabling compensation to be implemented. This is imperative when FBGs are being used in an environment where there are significant fluctuations in the localised temperature [95]. Moreover, the integration of a FBG for temperature measurement must also be done so as not to impede the functionality and performance of the instrument. Partially embedding the (unbonded) FBG within the instrument is a solution that could address this problem.

5.3.1 Blade Calibration

Calibration of the sensorised scissor blade was carried out over the maximum available cutting range of the scissor blades (25° to 10.4°). This angular range is a function of linear distance along the blade cutting edge x_c from the pivot to the point of intersection of the blades (16 mm to 39 mm). The calibration procedure involved securing the scissor blades in a clamping fixture and applying a series of static loads at a number of locations along the prescribed cutting envelope. A miniature button load cell was coupled to a micrometer load applicator unit which in turn is connected to a linear precision stage enabling translation of the load cell from blade tip to pivot (Figure 5-9). Direct loads F_d were applied normal to the blade cutting edge, in 2 N increments over a 0-30 N load range, representing direct loading of the blade structure during closing.

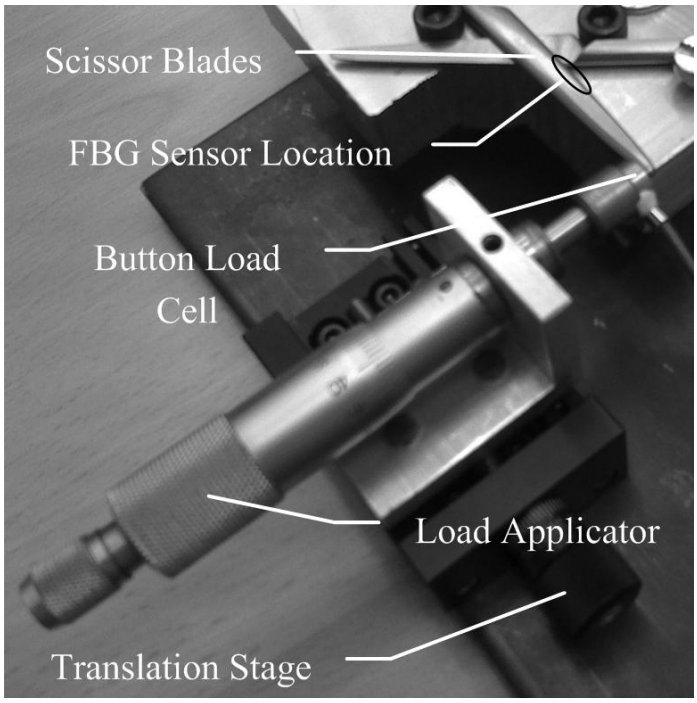

Figure 5-9 Blade calibration set-up for static direct loading conditions

The button load cell was then translated along the blade cutting edge in 3 mm increments. The corresponding load cell force readings and strain measured by the FBG were subsequently taken. The relationship between F_d and $\varepsilon_d(\theta)$ measured by the FBG was found to be linear at each load application point along the blade. The ratio of F_d to $\varepsilon_d(\theta)$ *at* location x_c is defined as the calibration ratio *R.* This theoretical input-output ratio can be estimated by rearranging equation 5.7 such that,

$$R = \frac{F_d}{\varepsilon_d} = \frac{E(nx_g + w_b)(mx_g + t_b)^2}{6(x_c - x_g)} \tag{5.15}$$

Experimental values for R and blade sensitivity are plotted along with their respective theoretical values in Figure 5-10. A close correlation is obtained,

indicating that the representation of the blade as a double cantilever structure is reasonable.

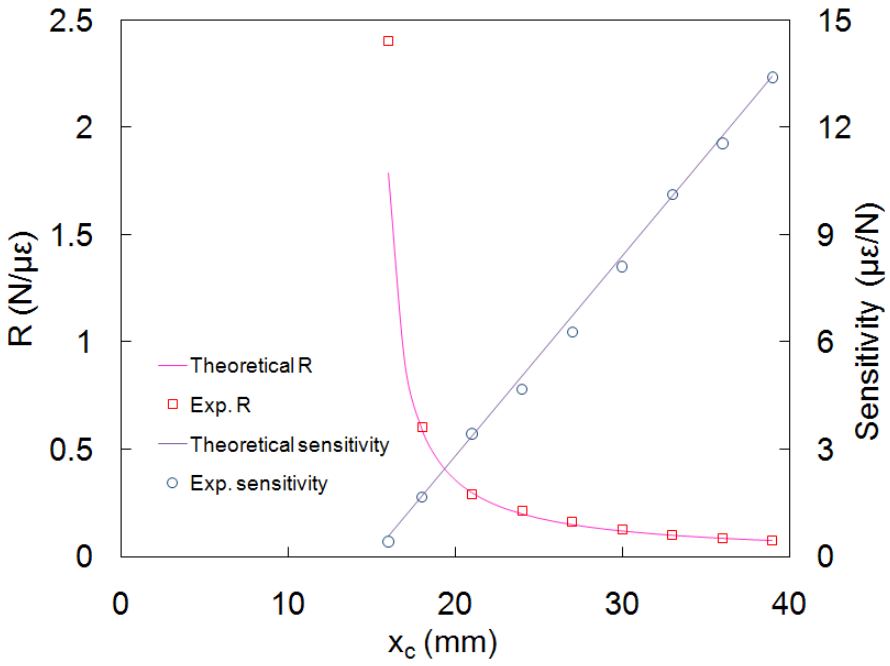

Figure 5-10 Experimental and theoretical direct force-strain calibration ratio and blade sensitivity

It can be seen from these results that the sensitivity of the sensorised blade is high from blade tip up to x_c =20 mm. Thereafter, there is a decrease in blade sensitivity as the applied loads approach the FBG sensor location (x_c =14 mm). Since surgeons typically operate scissors over the first one third of the blade length (26 mm to 39 mm) [75] there is little concern about the lower sensitivity beyond this region.

5.3.2 Lateral Strain Sensitivity

Using the experimental setup described in Section 5.3.1, direct strain on the sensorised surgical blade, with the 5 mm FBG, can be measured with a load

applied at multiple points along the blade from its tip towards the pivot. The measured direct strains for different loads applied at different blade positions for the surgical blade are shown in Figure 5-11. It can be observed that the maximum strain measured by the FBG occurs when the load is applied to the tip of the blade. The strain response is linear with respect to the applied load. However, during a typical cutting cycle the forces on the blades vary along its length over a typical working envelope between 10° and 23°. This is equivalent to a linear range of between 0 mm and 26 mm from the blade tip. In practical cutting applications the load position, $x_{c,}$ can be obtained if the blade opening angle is known hence the corresponding strain can be measured.

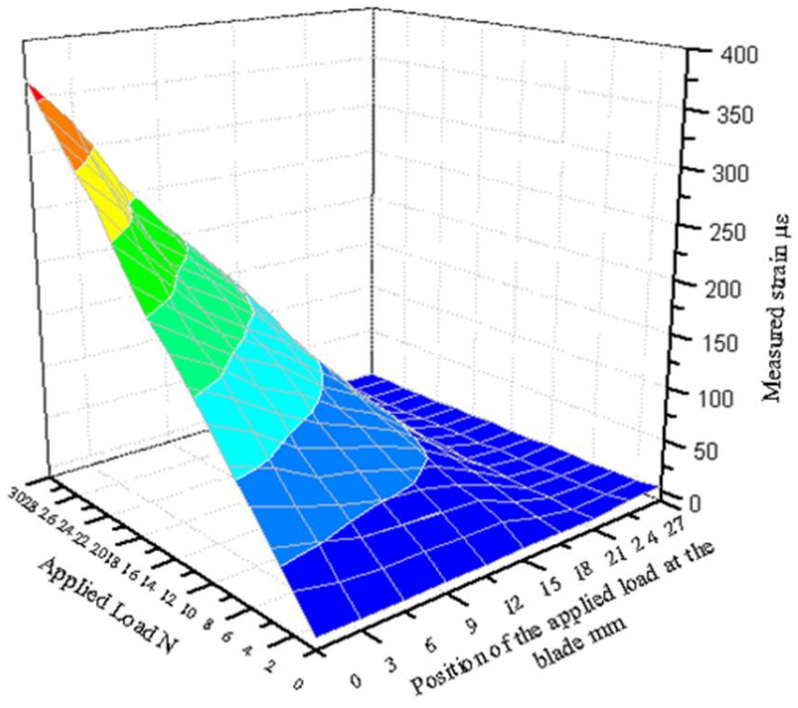

Figure 5-11 Direct strain measured along the blade length

During a typical cutting cycle, scissor blades experience laterally applied loading due to the curved nature of the blades along their length. The strain resulting from the lateral load measured by the FBG attached to the top side of the blade is shown in the Figure 5-12. Loads are applied, at 3 mm intervals, in the range of 0-10 N along the lateral side of the blade from the tip towards the pivot. Although the FBG sensor is less sensitive to the lateral load, it is clear that the lateral loading of the blade affects the direct strain output from the FBG sensor. A lateral load of 10 N applied to the tip of the blade introduces a maximum error of 16 με in the measured direct strain.

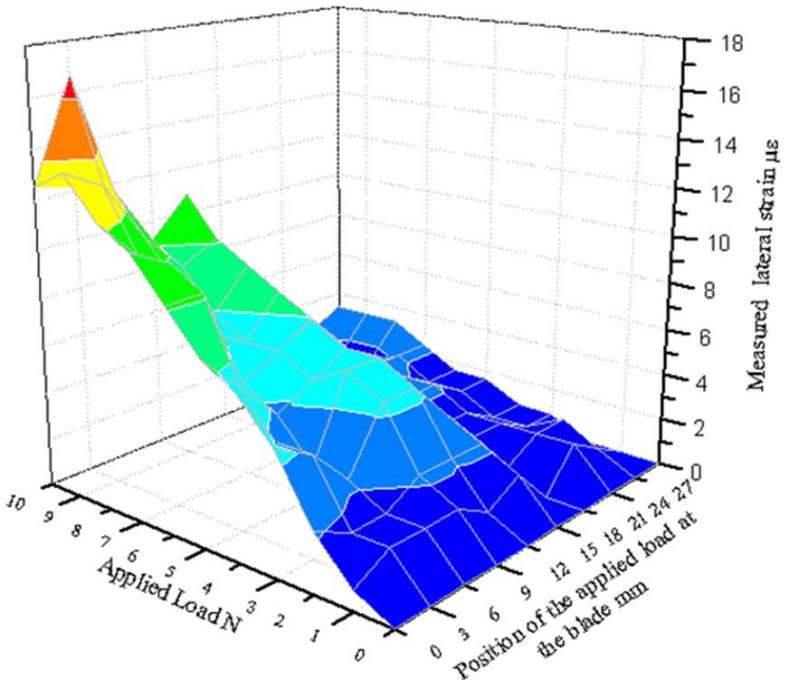

Figure 5-12 Measured lateral strain from lateral loading of the blade along its length

The magnitude of the error decreases when the applied load moves towards the blade pivot. Thus, the accuracy of the direct strain measurement is limited due to the inadvertent lateral loading arising from the deflection of the blade during cutting. However, this can be minimised by characterising the blade for a dry cut (without any tissue) and using the results, a calibration correction factor established to eliminate the influence of the lateral force.

5.3.3 Experimentally Obtained Friction Strain

Investigations into the nature of the strains expected from the FBG involved the opening and closing of the blades without any tissue being cut. Friction between the blades is an inherent part of scissor functionality and therefore an understanding of how kinetic friction forces contribute to the overall force measurement is required. The blades were secured in the characterisation test-bed with opening and closing achieved via pneumatic actuation. Opening and closing rates were kept constant at a rate of 6 degrees·s^{-1}. The Wx-02 commercial FBG interrogator unit measured the reflected wavelength shift at a rate of 1500 samples·s^{-1} with the corresponding strain being obtained with a strain sensitivity of 1.2pm·$\mu\varepsilon^{-1}$ [71]. The strain results for one complete cycle of the blades are presented in Figure 5-13. The total strain measured by the FBG (blue) is the sum of $\varepsilon_f(\theta)$ (friction strain) and $\varepsilon_s(\theta)$ (lateral strain). The positive and negative $\varepsilon_f(\theta)$ profiles are extracted by implementing a simple algorithm based on equation 5.11. Strain values increase towards the end of the cut as expected, due to the blade curvature deflecting the blade laterally. It can be

observed from the data presented in Figure 5-13 that the $\varepsilon_f(\theta)$ to $\varepsilon_s(\theta)$ ratio is consistent throughout the cutting cycle. This is the kinetic friction coefficient μ_k between the blades during a dry cutting cycle and was found to be 0.23 for the particular scissor blades used in these experiments.

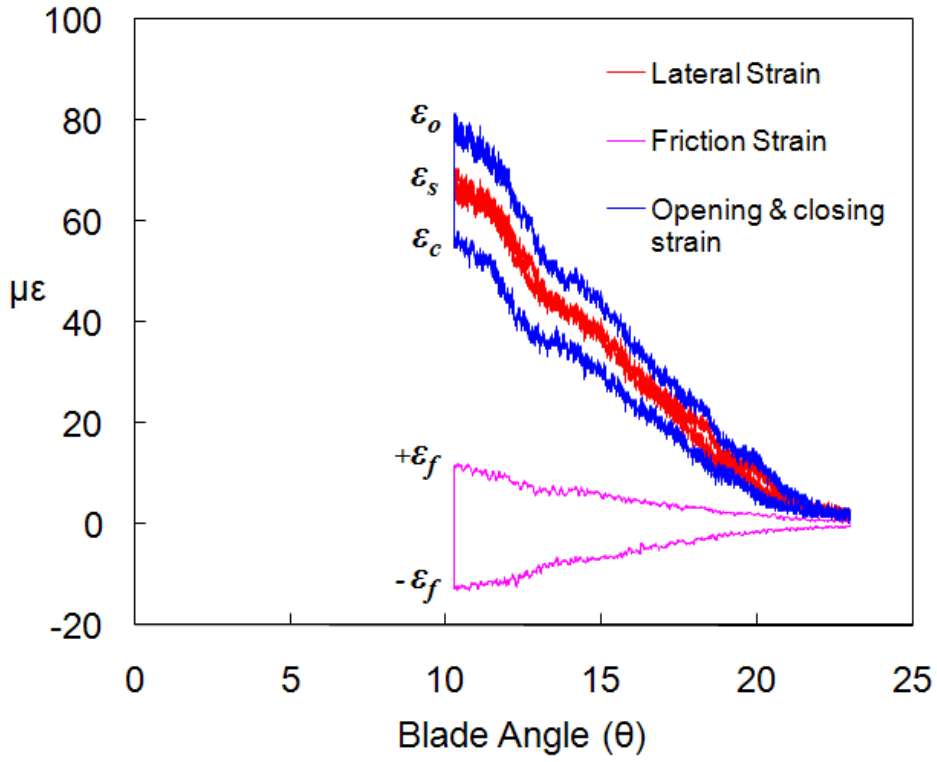

Figure 5-13 Experimental strain data, for an empty pass, obtained from a single FBG attached to the scissor blade

5.3.4 Cutting Paper Samples

A number of cutting experiments were carried out on paper samples to evaluate the performance of the FBG sensor during the cutting cycle. Paper was chosen for these experiments over soft synthetic samples as paper does not have the elastic properties which introduce high levels of strain energy in the sample

being cut. This allows the fracture toughness of the paper sample to be obtained using the force measurements from the FBG without residual strain energy within the sample affecting the efficacy of the results. In turn this enables a direct comparison to be made between force values obtained from the FBG attached to the blade and values obtained from the commercial load cell.

Cuts were carried out within the maximum working envelope of the cutting blades (23° to 10.4°). Paper samples measuring 100×60×0.1 mm were securely fixed between the blades. The total FBG strain (blue) resulting from combined F_s, F_{ff} and F_f over a complete opening and closing cycle are shown in Figure 5-14. Analysis shows that there is a distinct decrease in ε_c during closing, resulting from forces required to fracture the paper in front of the blade intersection point. However, this strain decrease is a combination of uncoupled $\varepsilon_s(\theta)$, $\varepsilon_{ff}(\theta)$ and $\varepsilon_f(\theta)$. From the perspective of accurate force reflection to the user and the acquisition of material property data sets, decoupling of the strain components is required. The $\varepsilon_{ff}(\theta)$ is obtained by subtracting $\varepsilon_s(\theta)$, for an empty cut, from $\varepsilon_c(\theta)$. These strains ($\varepsilon_{ff}(\theta)$) reflect the forces expected to be felt by the user during cutting due to F_{ff} being exerted on the blade.

It was observed that the cuts made were clean, free from burring and material dragging. These observations, combined with the high blade stiffness, suggest that any additional lateral deflection of the blades during paper cutting is negligible compared to that of an empty cut. It is reasonable to assume that a sharp scissor blade cutting a soft tissue will be exposed to negligible lateral deflection in addition to that incurred during empty cuts. Any additional

increase in the blade lateral deflection and strain would introduce errors into the estimated fracture toughness values. This is due to the fact that accurate strain decoupling requires that the lateral strain remains constant for both empty and tissue cutting cycles.

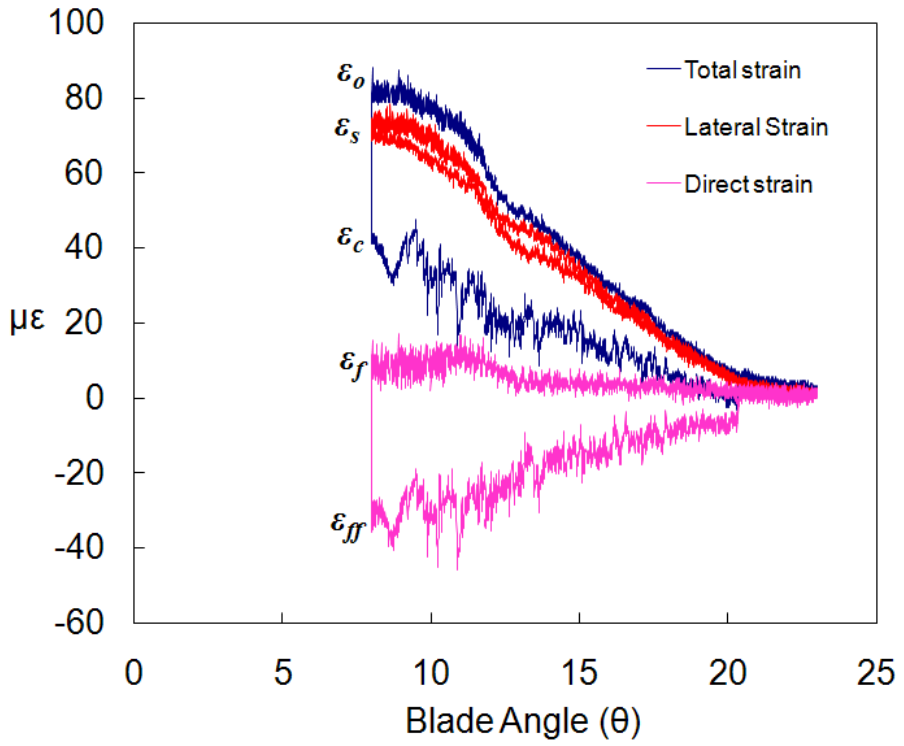

Figure 5-14 Experimental data obtained from the FBG during paper cutting

5.3.5 Force Measurement Validation

Quantifying the direct forces F_d exerted on the blade is carried out using the calibration equation (equation 5.15 in Section 5.3.1) where $\varepsilon_d(\theta)$ is the strain as measured by the FBG due to F_f or F_{ff}. Comparing the direct forces measured by the FBG to those measured by the load cell on the test-bed (Figure 5-15), it can be seen that there is a close correlation between the two. This shows that the

methodology employed, of decoupling $\varepsilon_d(\theta)$ from $\varepsilon_s(\theta)$ and using the calibration ratio R, is an effective means of determining typical cutting characteristics during cutting. It is clear from both force profiles that the point at which the blades make initial contact with the paper occurs at approximately 21°. At this point a sudden increase in force from 0.3 N to 2 N is measured as the blades compress the paper sample prior to fracture. From 21° to 10° characteristic peaks, representing a series of localised compression, deformation and fracture sequences, can be observed. The peaks are not present during the opening sequence as no material is being cut but there are fluctuations due to blade frictional contact.

Based on observations of the fluctuation in the measured strain signal (±3 με approx.) caused by noise in the interrogation system, the force resolution over the first third of the blade was calculated. At θ=15° the resolution is ±0.48 N, however, as sensitivity increases towards the blade tip the estimated resolution improves to ±0.23 N. These values are based on the change in sensitivity of the sensorised blade at different locations along its length. The location of the blade intersection point x_c is 26.36 mm at θ=15° and from Figure 5-10 the calibration ratio R at this point is 0.1613 N $\mu\varepsilon^{-1}$. This equates to an error of ±0.48 N when interrogator noise of ±3 με is considered. Likewise the error at the blade tip is calculated to be ±0.23 N based on a calibration ratio of 0.0754 N $\mu\varepsilon^{-1}$. The error bars shown in Figure 5-15 represent the force resolution variation over a complete cutting cycle. These results show that, with adequate filtering of the

FBG readings, the forces measured are comparable to those obtained from the load cell.

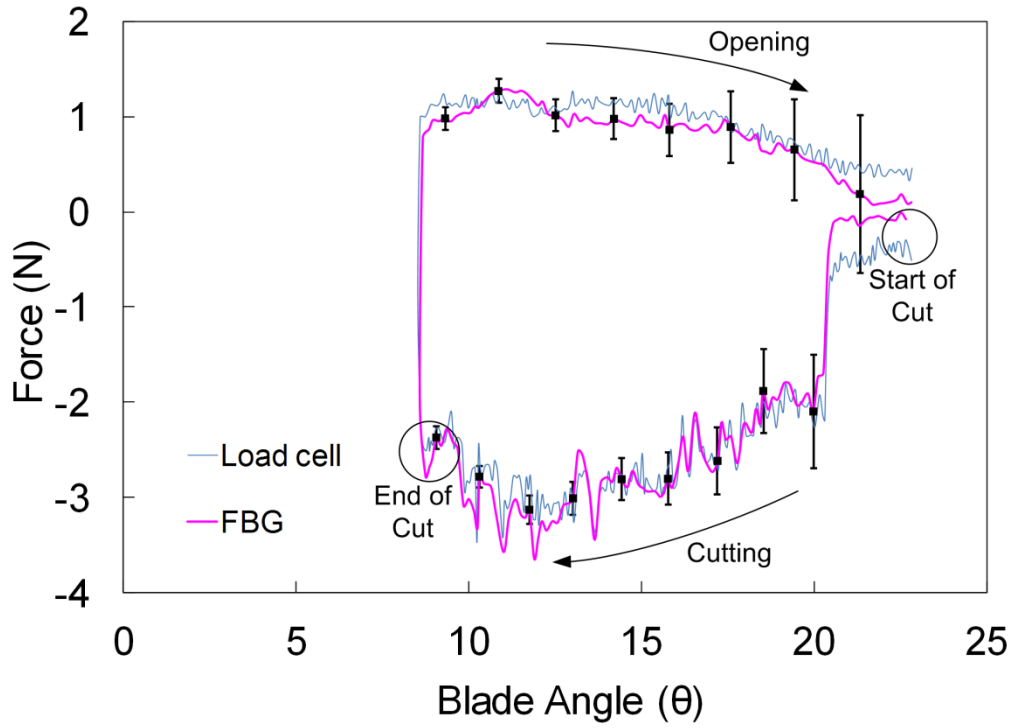

Figure 5-15 Comparing fracture and friction forces obtained from the FBG sensorised blade and a commercial load cell

5.3.6 Fracture Toughness Estimation

F_f and F_{ff} values at the scissor handles were inferred from the corresponding forces on the blade and used to determine the fracture toughness of the paper samples used. Using equation 3.6, the external work done due to combined fracture and friction, W_{ff}, was obtained by integrating under the fracture force-displacement profile in Figure 5-16. Similarly, the external work done due to friction only, W_f, was obtained and subtracted from W_{ff} resulting in work done due to material fracture only. The cut length, L_c, of the sample was acquired by

subtracting the distance x_c at the start of the cut from x_c at the end of the cut resulting in a cut length of 18.8 mm. This was verified by measuring the length of the slit in the sample after cut completion. A fracture toughness value of 4.36 kJ/m^2 was obtained using equation 3.7, comparable to that found in other literature [59]. Error bars are included to convey the force resolution, which improves towards the end of the cut as the blades are closed by the scissor handles. These results show that the FBG sensorised instrument is capable of reliably measuring the intrinsic cutting forces and as a result, the fracture toughness of the material can be obtained.

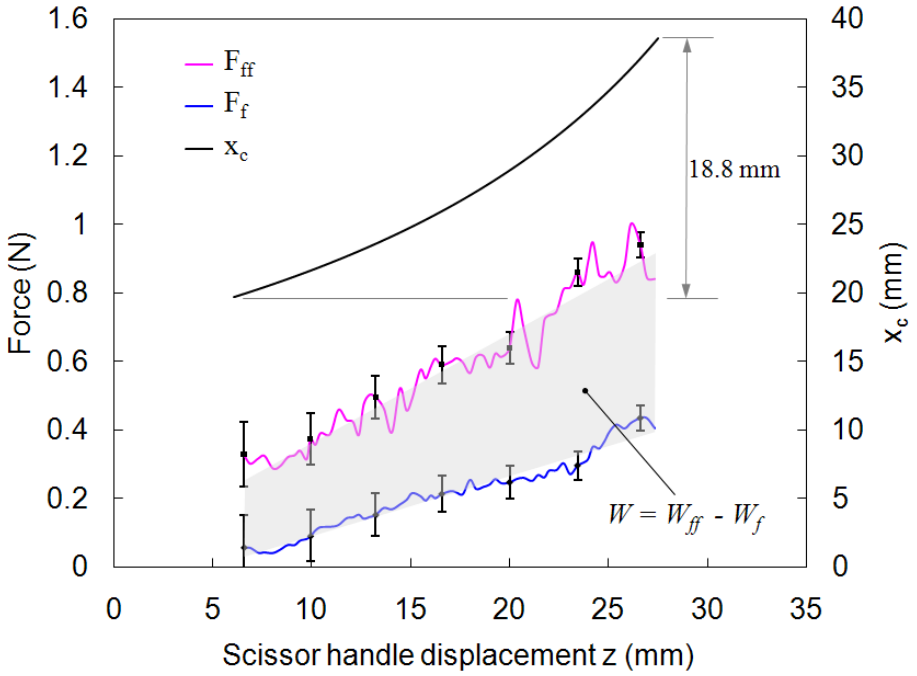

Figure 5-16 Fracture and friction force values at the scissor handles

5.3.7 Summary

This chapter has reported on the preliminary evaluation of sensorised surgical scissor blades employing a FBG sensor attached to the blade surface. The FBG

force sensing element is placed as close as possible to the site of force generation. The closeness of the sensor to the cutting interface ensures that 2-D interaction force information is obtained independent of any external force influences other than inherent friction forces present during scissor cutting. This inter-blade friction has considerable impact on the total interaction force measurement and this work quantifies these effects. The combined blade-sensor arrangement facilitates the estimation of the kinetic friction coefficient between the blades during operation, through the acquisition of both lateral and friction induced strain effects. The nature of the direct and lateral strains experienced by the smart sensing structure, during a typical cutting cycle, was explored by representing the blade as a double cantilever beam element. A theoretical means of decoupling the lateral and friction strain effects was presented and verified experimentally using an application-specific test-bed. A unique feature of scissor instruments compared to most other surgical instruments is that forces occur along the blade length as opposed to a single location at the instrument tip. Calibration of the sensorised blades over the entire blade length ensures that accurate interaction force details can be obtained through a cutting cycle particularly over the high sensitivity region preferred by surgeons. The force information obtained can be reflected to the user in a telerobotic application ensuring a greater sense of user immersion. Additionally, the acquired force information can be utilised in the evaluation of tissue properties such as fracture toughness. The experimental data presented compares the force information obtained from the FBG sensorised blade with that of a commercially available

load cell. Good correlation is observed between the two sensing modes with typical contact and fracture characteristics being evident.

The key conclusions from this chapter can be summarised as follows;

- Modelling the scissor blade using double tapered elementary beam theory allows accurate estimation of lateral and direct strains resulting from direct and lateral loading of the blade. The double tapered model can also be used to estimate the sensitivity of particular blade geometry with a FBG attached at any location on or within its structure.
- A method of decoupling total, lateral and direct strain using a single FBG attached to the blade is demonstrated theoretically and verified experimentally. Decoupling is particularly important when attempting to ascertain the true forces acting on the blade arising from tissue fracture, blade friction and blade curvature.
- A novel means of estimating the kinetic coefficient between the blades was demonstrated using a single FBG attached to one blade. The ability to accurately estimate blade friction coefficient will have significance for researchers attempting to understand the complex interactions between scissor blade and the tissue with which they interact.
- The fracture toughness of samples cut using the sensorised blades can be estimated using this direct force sensing technique which employs a FBG as the sensing element. However, noise due to the sensitivity of the blade-FBG combination limits the resolution of the current system to ±0.48 N close to the location of the FBG.

Chapter 6

Conclusions and Future Research

This chapter presents the overall conclusions of the research carried out. The work presented in this thesis investigated in detail the implementation of a direct force sensing solution for minimally invasive surgical cutting instruments used in MIRS. The approach adopted required the integration of a FBG sensor onto the blades enabling the blade itself to act as a sensing device. A direct sensing approach facilitates the acquisition of cutting force data that greater reflects the actual forces occurring at the interaction site in comparison to non direct sensing methods.

6.1 Conclusions

The overarching aim of this work was to investigate and experimentally characterise a compact FBG-sensorised scissor blade end-effector as an integrated, direct force measurement solution to the problem of obtaining

interaction force values generated at the blade-tissue interface. The specific conclusions of this work are as follows;

- A characterisation test-bed was successfully implemented enabling forces acting on a pair of scissor blades to be obtained. Force data obtained from the test-bed while cutting synthetic tissue samples showed typical soft tissue cutting characteristics such as sequences of compression and fracture profiles consistent with other literature. The test apparatus was found to be repeatable and capable of discriminating between homogeneous tissue samples of varying mechanical properties.
- The effect of blade curvature on the accuracy of the measured cutting forces was measured by attaching miniature strain gauges to the blade surface. Results showed that the placement of a small force sensor on the blades upper surface could detect direct forces generated during cutting but also inadvertently detected lateral strain components due to the blades deflecting laterally while opening and closing. This proved that while the combined blade-sensor arrangement has sufficient sensitivity, further work was required in decoupling the lateral strain components from direct strain components.
- Two methods of determining the effective fracture toughness (J*) of soft tissue samples using scissor cutting were assessed. Method 1 estimated J* by considering the work done during cutting over the full cut length while method 2 estimated the average work done over a series of individual fractures. The mean J* values obtained using method 2 were generally

higher than values obtained using method 1 with an average 15% difference. This would indicate that method 2 is more sensitive to the thickness of the material being cut as well as the mechanics of the scissor cutting method.

- A surface mounted fibre was modelled using numerical simulations and it was shown that a minimum adhesive thickness coupled with an adhesive bond length at least 55% longer then the FBG length was required to ensure that an ASTC close to unity was achieved. Experimental results confirmed that a bond length 55% greater than the FBG does achieve an ASTC of close to unity (0.98). Analysis of the reflected FBG spectrum at zero and maximum load revealed that no errors occurred in the FBG strain measurements as a result of strain non-uniformity along the grating.
- A close correlation was obtained (2.4% difference) between ASTC results obtained from the analytical model compared to results from the FE model for a partially embedded fibre. Numerical simulations of the partially embedded FBG showed that the bond length could be reduced by 18% when compared to the surface mounted FBG. Reducing the bond length facilitates more compact packaging of the sensor on the blade.
- Partially embedding the FBG within the blade structure also results in a reduction in sensitivity when compared with the surface mounted FBG under direct loading conditions. A reduction in sensitivity of 9.2% was found between the blade with a surface mounted FBG (5.88 με/N) and

one with an embedded FBG (5.34 με N^{-1}). The closer the sensor is placed to the blades central longitudinal axis the greater the reduction in blade sensitivity.

- Experiments where a surface mounted and a partially embedded FBG was loaded laterally showed that the sensor-blade combination was sensitive to both lateral loading as well as direct loading. The strain effects of lateral loading must be compensated for as the lateral-induced strain will introduce errors into the direct force readings. These laterally induced errors have particular importance when the forces being measured are to be used in the measurement of tissue elastic and fracture properties.
- Numerical simulations where a series of strain gradients up to 14% were applied showed that the strain measured by the FBG is the strain coincident with the FBG centreline. However, it is believed that there is a need for more detailed knowledge of the adhesive properties being used in the simulations to more accurately reflect the complex interaction between fibre, adhesive and host material. Experimental results show that the coincident strain measured by the FBG correlated well with results from an electrical strain gauge and the numerical simulations.
- Modelling the scissor blades using double tapered elementary beam theory accurately estimates lateral and direct strains resulting from direct and lateral loading of the blade. The proposed double tapered model can also be used to estimate the sensitivity of a particular blade geometry with a FBG attached at any location on or within its structure.

- A method of decoupling total, lateral and direct strain using a single FBG attached to the blade was modelled theoretically and verified experimentally. This is a key element when integrating a FBG sensor directly onto the scissor blades which takes advantage of the lateral sensitivity of the FBG sensor. Decoupling is particularly important when attempting to ascertain the true forces acting on the blade arising from tissue fracture, blade friction and blade curvature during dynamic cutting.
- A further benefit of the decoupling process was that a novel means of estimating the kinetic coefficient between both blades was demonstrated using a single FBG attached to one blade. It is proposed that the effect of lubricating the blades be assessed further to determine its impact on the accuracy of the results obtained. The ability to accurately estimate blade friction coefficient will have significance for researchers attempting to understand the complex interactions between scissor blades and the tissue with which they interact.
- The fracture toughness of paper samples that were cut using the sensorised blades were estimated using this direct force sensing technique. The results obtained correlated closely with values obtained in literature. The decoupling technique used to accurately ascertain the fracture toughness values was validated against data obtained from a commercial load cell used in the characterisation test-bed. Noise due to the sensitivity of the blade-FBG combination limits the resolution of the current system to ±0.48 N close to the location of the FBG.

6.2 Summary of Key Conclusions

The key conclusions from this research are;

- An instrumented characterisation test-bed is a viable way of determining the nature of the complex interaction forces generated between surgical scissor blades and soft tissue samples.
- Inadvertent lateral strain arising from blade curvature is a key factor when considering a direct force sensing approach. The lateral strain effects need to be compensated for to enable the true friction and fracture interaction forces to be obtained.
- Strain energy within soft tissue samples is a parameter that affects the accuracy with which the true fracture toughness of the samples can be obtained. Strain energy is significant during scissor cutting owing to the way in which the blades compress the tissue during the cutting process.
- Adhesive bond length, stiffness and thickness are key elements which effect strain transfer from the blade structure to the core of a FBG sensor whether surface mounted or partially embedded. Partially embedding the FBG within a groove in the blade reduces the bond length assuming the same adhesive thickness and stiffness.
- Decoupling the strains obtained from a single FBG sensor is a key method in the determination of the friction and fracture forces arising between scissor blades and the samples being cut.

6.3 Future Research Challenges

The work presented in this thesis explored the factors that need to be taken into consideration when employing a direct force sensing technique using a FBG on surgical scissor blades. Areas of future research have been identified from this work and are presented as follows;

1. **Soft Tissue Fracture Toughness Estimation**: During this research work a greater understanding was obtained of how interaction forces between scissor blades and soft tissue arise during cutting. It was assumed that the maximum forces occurred at the intersection point between the blades. However, due the changing angle of the blades during closing the tissue experiences a degree of compression between the blades cutting edges. To collect true fracture data in relation to the tissue being cut a greater understanding of the distribution of the forces along the tissue compression region is required. This will enable the separation of the forces required to fracture the tissue from the forces that are compressing the tissue and which contribute in no way to the work of fracture. It is proposed that a detailed FE model be developed which mimics scissor blade cutting edges cutting soft tissue samples. The tissue models would incorporate empirically derived tissue properties such as stiffness, viscoelasticity and fracture toughness. The overall aim of this strand of research would be to ascertain the degree of strain energy experienced by the tissue in the vicinity of the blade intersection point.

The current characterisation test-bed could be used in parallel with the modelling research to collect pertinent force data for model validation.

2. **Strain Transfer Modelling:** The analytical FE models developed in this research assume linear elastic material properties. While this is reasonable for the FBG material (Silica) and perhaps the FBG coating (Polyimide) it may not be reasonable to assume linear elastic properties for the adhesive used to bond the FBG. This could be particularly relevant at higher strain values or as the adhesive experiences heating-cooling cycles due to a series of sterilisation cycles over the instruments lifetime. This research showed that the strain values in the blade are quite low and unlikely to cause nonlinearities or hysteresis during the strain transfer process. However, the effect of the sterilisation process on the adhesive properties does warrant investigation.
3. **Embedding the Sensor:** This research investigated the effects of partially embedding the FBG senor within a groove machined into the blade. Results have indicated that the possibility of fully embedding the FBG is feasible once consideration is given to the adhesive layer length, the adhesive layer thickness and the position of the FBG relative to the centreline of the blade. The challenge associated with a fully embedded approach would be in machining a blind hole in the blade to accommodate the fibre. A coated fibre has a diameter of ~125 μm to 140 μm; therefore, the required hole diameter would need to be slightly greater to accommodate an adhesive thickness. Achieving this diameter

along a length long enough to accommodate the FBG would prove challenging and would be influenced by the length of the blade under consideration. A micromachining or EDM process may prove to be suitable for creating the tunnel but the suitability of these processes and others would need to be explored. An advantage associated with a fully embedded approach would be the unobtrusive way in which the sensing is achieved. Moreover, the fibre would be fully encapsulated within the blade enhancing further its sterilisability and biocompatibility.

4. **Future Sensorised Devices:** In this thesis a FBG sensor was used as the primary sensing element in the sensorised scissor blades. Current advancements in the field of optical sensing include sensors that have strain sensitivities comparable to FBGs but are insensitive to change in localised temperatures. An example of this particular sensor type is a Photonic Crystal Fibre (PCF). Temperature insensitivity would bring additional benefits for future smart-sensing instruments and devices and consequently should be explored further. Moreover, the length of a PCF based sensor can be considerably smaller than its FBG counterparts. Recent research [145] has shown that a PCF sensor as small as 200 μm can be successfully attached to a traditional single mode fibre and used for the measurement of interaction forces acting on the arms of a clip applicator. This further demonstrates that optical sensing will play a significant part in the development of smart sensing surgical instruments that may in time be used in modern MIRS systems.

References

[1] U. Seibold, B. Kuebler, and G. Hirzinger, "Prototypic force feedback instrument for minimally invasive robotic surgery," *Medical robotics,* pp. 377-400, 2008.

[2] P. Dario, B. Hannaford, and A. Menciassi, "Smart Surgical Tools and Augmenting Devices," *IEEE Transactions on Robotics and Automation,* vol. 19, pp. 782-792, 2003.

[3] B. Kuebler, U. Seibold, and G. Hirzinger, "Development of actuated and sensor integrated forceps for minimally invasive robotic surgery," *Int. J. Med. Rob. Comp. Assist. Surg.,* vol. 1, pp. 96-107, 2005.

[4] R. D. Howe and Y. Matsuoka, "Robotics for Surgery," *Annual Review of Biomedical Engineering,* vol. 1, pp. 211-240, 1999.

[5] A. P. Kypson and W. R. Chitwood Jr, "Robotic mitral valve surgery," *The American Journal of Surgery,* vol. 188, pp. 83-88, 2004.

[6] G. Tholey, A. Pillarisetti, and J. P. Desai, "On-site three dimensional force sensing capability in a laparoscopic grasper," *Industrial Robot,* vol. 31, pp. 509-518, 2004.

[7] M. Mahvash, "Haptic Rendering of Tool Contact and Cutting." vol. PhD Montréal: McGill University, 2002.

[8] R. V. Patel, *Haptics For Teleoperated Surgical Robotic Systems*: World Scientific, 2008.

[9] G. Dogangil, B. L. Davies, and F. Rodriguez y Baena, "A review of medical robotics for minimally invasive soft tissue surgery," *Proceedings of the Institution of Mechanical Engineers, Part H: Journal of Engineering in Medicine,* vol. 224, pp. 653-679, May 1, 2010.

[10] P. Puangmali, K. Althoefer, L. D. Seneviratne, D. Murphy, and P. Dasgupta, "State-of-the-art in force and tactile sensing for minimally invasive surgery," *IEEE Sensors J.,* vol. 8, pp. 371-380, 2008.

[11] A. L. Trejos, "A Sensorized Instrument for Minimally Invasive Surgery for the Measurement of Forces during Training and Surgery: Development and Applications," in *Department of Electrical and Computer Engineering*. vol. PhD: The University of Western Ontario, 2012.

[12] A. R. Lanfranco, A. E. Castellanos, J. P. Desai, and W. C. Meyers, "Robotic Surgery: A Current Perspective," *Annals of Surgery,* vol. 239, pp. 14-21, 2004.

[13] F. Tendick, S. S. Sastry, R. S. Fearing, and M. Cohn, "Applications of micromechatronics in minimally invasive surgery," *Mechatronics, IEEE/ASME Transactions on,* vol. 3, pp. 34-42, 1998.

[14] A. M. Okamura, "Methods for haptic feedback in teleoperated robot-assisted surgery," *Industrial Robot,* vol. 31, pp. 499-508, 2004.

[15] G. S. Guthart and J. K. Salisbury, Jr., "The Intuitive telesurgery system: overview and application," in *Robotics and Automation, 2000. Proceedings. ICRA '00. IEEE International Conference on*, 2000, pp. 618-621 vol.1.

[16] T. Horeman, F.-W. Jansen, and J. Dankelman, "An Isolator System for minimally invasive surgery: the new design," *Surgical Endoscopy,* vol. 24, pp. 1929-1936, 2010.

[17] M. Zhou, J. Perreault, S. Schwaitzberg, and C. Cao, "Effects of experience on force perception threshold in minimally invasive surgery," *Surgical Endoscopy,* vol. 22, pp. 510-515, 2008.

[18] C. R. Wagner, Stylopoulos, N., Howe, R. D., "The role of force feedback in surgery: analysis of blunt dissection," in *Haptic Interfaces for Virtual Environment and Teleoperator Systems, 2002. HAPTICS 2002. Proceedings. 10th Symposium on*, 2002, pp. 68-74.

[19] M. Tavakoli, A. Aziminejad, R. Patel, and M. Moallem, "Tool/tissue interaction feedback modalities in robot-assisted lump localization," in *Engineering in Medicine and Biology Society, 2006. EMBS'06. 28th Annual International Conference of the IEEE*, 2006, pp. 3854-3857.

[20] S. Schostek, M. O. Schurr, and G. F. Buess, "Review on aspects of artificial tactile feedback in laparoscopic surgery," *Medical Engineering & Physics,* vol. 31, pp. 887-898, 2009.

[21] G. De Gersem, "Kinaesthetic feedback and enhanced sensitivity in robotic endoscopic telesurgery," *Catholic University of Leuven,* 2005.

[22] G. L. McCreery, A. L. Trejos, M. D. Naish, R. V. Patel, and R. A. Malthaner, "Feasibility of locating tumours in lung via kinaesthetic feedback," *The International Journal of Medical Robotics and Computer Assisted Surgery,* vol. 4, pp. 58-68, 2008.

[23] G. T. Sung and I. S. Gill, "Robotic laparoscopic surgery: a comparison of the da Vinci and Zeus systems," *Urology,* vol. 58, pp. 893-898, 2001.

[24] M. Hashizume, M. Shimada, M. Tomikawa, Y. Ikeda, I. Takahashi, R. Abe, F. Koga, N. Gotoh, K. Konishi, S. Maehara, and K. Sugimachi, "Early experiences of endoscopic procedures in general surgery assisted by a computer-enhanced surgical system," *Surgical Endoscopy,* vol. 16, pp. 1187-1191, 2002.

[25] A. M. Okamura, "Haptic feedback in robot-assisted minimally invasive surgery," *Current opinion in urology,* vol. 19, pp. 102-7, 2009.

[26] M. V. Ottermo, M. Ovstedal, T. Lango, O. Stavdahl, Y. Yavuz, T. A. Johansen, and R. Marvik, "The role of tactile feedback in laparoscopic surgery," *Surgical Laparoscopy Endoscopy & Percutaneous Techniques,* vol. 16, pp. 390-400, 2006.

[27] G. S. Fischer, T. Akinbiyi, S. Saha, J. Zand, M. Talamini, M. Marohn, and R. Taylor, "Ischemia and Force Sensing Surgical Instruments for Augmenting Available Surgeon Information," in *Biomed. Rob. and Biomechatronics, 2006. BioRob 2006. The 1st IEEE/RAS-EMBS Int. Conf. on*, 2006, pp. 1030-1035.

[28] C. E. Reiley, "Evaluation of Augmented Reality Alternatives to Direct Force Feedback in Robot-Assisted Surgery: Visual Force Feedback and Virtual Fixtures," in *Department of Computer Science*. vol. Master of Science: The Johns Hopkins University, 2007.

[29] M. Kitagawa, D. Dokko, A. M. Okamura, and D. D. Yuh, "Effect of sensory substitution on suture-manipulation forces for robotic surgical systems," *Journal of Thoracic and Cardiovascular Surgery,* vol. 129, pp. 151-158, 2005.

[30] M. Tavakoli, R. V. Patel, and M. Moallem, "Haptic interaction in robot-assisted endoscopic surgery: a sensorized end-effector," *Int J Med Robot,* vol. 1, pp. 53-63, 01/01 2005.

[31] D. Murphy, B. Challacombe, T. Nedas, O. Elhage, K. Althoefer, L. Seneviratne, and P. Dasgupta, "Equipment and technology in robotics," *Arch Esp Urol,* vol. 60, pp. 349-55, 2007.

[32] A. Uneri, M. A. Balicki, J. Handa, P. Gehlbach, R. H. Taylor, and I. Iordachita, "New steady-hand eye robot with micro-force sensing for vitreoretinal surgery," in *Biomedical Robotics and Biomechatronics (BioRob), 2010 3rd IEEE RAS and EMBS International Conference on*, 2010, pp. 814-819.

[33] S. Sokhanvar, M. Packirisamy, and J. Dargahi, "A multifunctional PVDF-based tactile sensor for minimally invasive surgery," *Smart Materials and Structures,* vol. 16, pp. 989-998, 2007.

[34] J. Dargahi, N. P. Rao, and S. Sokhanvar, "Design and microfabrication of a hybrid piezoelectric-capacitive tactile sensor," *Sensor Review,* vol. 26, pp. 186-192, 2006.

[35] A. Okamura, L. Verner, C. Reiley, M. Mahvash, M. Kaneko, and Y. Nakamura, "Haptics for Robot-Assisted Minimally Invasive Surgery Robotics Research." vol. 66: Springer Berlin / Heidelberg, 2010, pp. 361-372.

[36] S. Shimachi, S. Hirunyanitiwatna, Y. Fujiwara, A. Hashimoto, and Y. Hakozaki, "Adapter for contact force sensing of the da Vinci robot," *The International Journal of Medical Robotics and Computer Assisted Surgery,* vol. 4, pp. 121-130, 2008.

[37] N. Zemiti, G. Morel, T. Ortmaier, and N. Bonnet, "Mechatronic design of a new robot for force control in minimally invasive surgery," *IEEE/ASME Transactions on Mechatronics,* vol. 12, pp. 143-153, 2007.

[38] A. L. Trejos, R. V. Patel, and M. D. Naish, "Force sensing and its application in minimally invasive surgery and therapy: a survey," *Proc. of the Inst. of Mech. Eng., Part C: J. of Mechanical Engineering Science,* vol. 224, pp. 1435–1453, 2009.

[39] U. Seibold, Kubler, B.,Hirzinger, G., "Prototype of Instrument for Minimally Invasive Surgery with 6-Axis Force Sensing Capability," in *Robotics and Automation, 2005. ICRA 2005. Proceedings of the 2005 IEEE International Conference on*, 2005, pp. 496-501.

[40] S. Shimachi, Y. Fujiwara, and Y. Hakozaki, "New sensing method of force acting on instrument for laparoscopic robot surgery," *International Congress Series,* vol. 1268, pp. 775-780, 2004.

[41] S. Shimachi, Y. Hakozaki, T. Tada, and Y. Fujiwara, "Measurement of force acting on surgical instrument for force-feedback to master robot console," *International Congress Series,* vol. 1256, pp. 538-546, 2003.

[42] J. J. van den Dobbelsteen, R. A. Lee, M. van Noorden, and J. Dankelman, "Indirect measurement of pinch and pull forces at the shaft of laparoscopic graspers," *Medical and Biological Engineering and Computing,* vol. 50, pp. 215-221, 2012.

[43] G. Tholey, A. Pillarisetti, W. Green, and J. Desai, "Design, Development, and Testing of an Automated Laparoscopic Grasper with 3-D Force Measurement Capability," in *Medical Simulation*. vol. 3078 Heidelberg: Springer Berlin, 2004, pp. 38-48.

[44] G.Fischer, T. Akinbiyi, S. Saha, J. Zand, M. Talamini, M.Marohn, and R. Taylor., "Ischemia and Force Sensing Surgical Instruments for Augmenting Available Surgeon Information," in *Biomedical Robotics and Biomechatronics, 2006. BioRob 2006. The First IEEE/RAS-EMBS International Conference on*, 2006, pp. 1030-1035.

[45] V. Van Hemert tot Dingshof, M. Lazeroms, A. Van der Ham, W. Jongkind, and G. Honderd, "Force reflection for a laparoscopic forceps," 1996, pp. 210-211 vol. 1.

[46] B. Kuebler, U. Seibold, and G. Hirzinger, "Development of actuated and sensor integrated forceps for minimally invasive robotic surger," *The International Journal of Medical Robotics and Computer Assisted Surgery,* vol. 1, pp. 96-107, 2005.

[47] A. Saha, "Appropriate degrees of freedom of force sensing in robot-assisted minimally invasive surgery," in *Dept. of Biomedical Enginereing*. vol. MSc Dissertation: Johns Hopkins University, 2006.

[48] A. Wroblewska, "Methods of the force measurement for robotic surgical tools," in *Robot Motion and Control, 2005. RoMoCo '05. Pro. of the 5th Int. Workshop on*, 2005, pp. 51-54.

[49] A. M. Dollar, Wagner, C. R.,Howe, R. D., "Embedded Sensors for Biomimetic Robotics via Shape Deposition Manufacturing," in *Biomedical Robotics and*

Biomechatronics, 2006. BioRob 2006. The First IEEE/RAS-EMBS International Conference on, 2006, pp. 763-768.

[50] J. Rosen, B. Hannaford, M. P. MacFarlane, and M. N. Sinanan, "Force controlled and teleoperated endoscopic grasper for minimally invasive surgery - experimental performance evaluation," *IEEE Transactions on Biomedical Engineering,* vol. 46, pp. 1212-1221, 1999.

[51] G. Tholey, T. Chanthasopeephan, T. Hu, J. Desai, and A. Lau, "Measuring grasping and cutting forces for reality-based haptic modeling," *International Congress Series,* vol. 1256, pp. 794-800, 2003.

[52] P. Valdastri, K. Harada, A. Menciassi, L. Beccai, C. Stefanini, M. Fujie, and P. Dario, "Integration of a miniaturised triaxial force sensor in a minimally invasive surgical tool," *IEEE Transactions on Biomedical Engineering,* vol. 53, pp. 2397-2400, 2006.

[53] T. J. Ortmaier, "Motion Compensation in Minimally Invasive Robotic Surgery ". vol. PhD Munich: Technische Universität München, 2003.

[54] R. Haag and W. Storz, "Surgical Scissors," *Springer Handbook of Medical Technology,* pp. 1291-1319, 2011.

[55] S. M. Shimi, "Dissection techniques in laparoscopic surgery: a review," *Journal of the Royal College of Surgeons of Edinburgh,* vol. 40, pp. 249-259, 1995.

[56] V. Bochkarev, C. D. Ringley, and D. Oleynikov, "Robotic-Assisted Operative Techniques in General Surgery," *Operative Techniques in General Surgery,* vol. 7, pp. 188-200, 2005.

[57] N. L. Shah, S. Kaul, and M. Menon, "Surgical Robotics in Urology: Robotic Assisted Radical Prostatectomy," *Operative Techniques in General Surgery,* vol. 7, pp. 201-208, 2005.

[58] M. Mahvash and A. M. Okamura, "A Fracture Mechanics Approach to Haptic Synthesis of Tissue Cutting with Scissors," in *Proceedings of the First Joint Eurohaptics Conference and Symposium on Haptic Interfaces for Virtual Environment and Teleoperator Systems*: IEEE Computer Society, 2005.

[59] M. Mahvash, L. M. Voo, K. Diana, K. Jeung, J. Wainer, and A. M. Okamura, "Modeling the Forces of Cutting With Scissors," *IEEE Trans. Biomed. Eng.,* vol. 55, pp. 848-856, 2008.

[60] T. Yang, L. Xiong, J. Zhang, L. Yang, W. Huang, J. Zhou, J. Liu, Y. Su, C. K. Chui, C. L. Teo, and S. Chang, "Modeling cutting force of laparoscopic scissors," in *Biomedical Engineering and Informatics (BMEI), 3rd International Conference on*, 2010, pp. 1764-1768.

[61] A. Trejos, S. Jayaraman, R. Patel, M. Naish, and C. Schlachta, "Force sensing in natural orifice transluminal endoscopic surgery," *Surgical Endoscopy,* vol. 25, pp. 186-192, 2011.

[62] K. Y. Ang, P. W. Lucas, and H. T. W. Tan, "Novel way of measuring the fracture toughness of leaves and other thin films using a single inclined razor blade," *New Phytologist,* vol. 177, pp. 830-837, 2008.

[63] B. Chu, E. Gaillard, R. Mongrain, S. Reiter, and J.-C. Tardif, "Characterization of fracture toughness exhaustion in pig aorta," *Journal of the Mechanical Behavior of Biomedical Materials,* vol. 17, pp. 126-136, 2013.

[64] P. Lucas and B. Pereira, "Estimation of the fracture toughness of leaves," *Functional Ecology,* pp. 819-822, 1990.

[65] C. Gokgol, C. Basdogan, and D. Canadinc, "Estimation of fracture toughness of liver tissue: Experiments and validation," *Medical Engineering & Physics,* vol. 34, pp. 882-891, 2012.

[66] S. Y. Chong, L. A. Chong, and H. Ariffin, "Accurate prediction of the needle depth required for successful lumbar puncture," *The American Journal of Emergency Medicine,* vol. 28, pp. 603-606, 2010.

[67] A. G. Atkins and Y. W. Mai, "On the guillotining of materials," *Journal of Materials Science,* vol. 14, pp. 2747-2754, 1979.

[68] N. Ragavendra, J. W. Ju, J. W. Sayre, S. Hirschowitz, I. Chopra, and M. W. Yeh, "In vivo analysis of fracture toughness of thyroid gland tumors," *Journal of Biological Engineering,* vol. 2, 2008.

[69] M. Mahvash, J. Gwilliam, R. Agarwal, B. Vagvolgyi, S. Li-Ming, D. D. Yuh, and A. M. Okamura, "Force-Feedback Surgical Teleoperator: Controller Design and Palpation Experiments," in *Haptic interfaces for virtual environment and teleoperator systems, 2008. haptics 2008. symposium on*, 2008, pp. 465-471.

[70] S. K. Prasad, M. Kitagawa, G. S. Fischer, J. Zand, M. A. Talamini, R. H. Taylor, and A. M. Okamura, "A modular 2-DOF force-sensing instrument for laparoscopic surgery," Montreal, Que., Canada, 2003, pp. 279-286.

[71] V. B. Chial, S. Greenish, and A. M. Okamura, "On the Display of Haptic Recordings for Cutting Biological Tissues," in *IEEE Com. Soc. Proc. of the 10th Symp. on Haptic Interfaces for Virtual Environment and Teleoperator Systems*, 2002.

[72] T. Azar and V. Hayward, "Estimation of the Fracture Toughness of Soft Tissue from Needle Insertion," in *Proc. of the 4th int. symp. on Biomedical Simulation* London, UK: Springer-Verlag, 2008.

[73] P. Mucksavage, D. C. Kerbl, D. L. Pick, J. Y. Lee, E. M. McDougall, and M. K. Louie, "Differences in Grip Forces Among Various Robotic Instruments and da Vinci Surgical Platforms," *Journal of Endourology,* vol. 25, pp. 523-528, 2011.

[74] S. Greenish, V. Hayward, V. Chial, A. M. Okamura, and T. Steffen, "Measurement, Analysis and Display of Haptic Signals during Surgical Cutting," *Presence: Teleoper. Virtual Environ.,* vol. 11, pp. 626-651, 2002.

[75] S. Greenish, "Acquisition and Analysis of Cutting Forces of Surgical Instruments for Haptic Simulation," in *Department of Electrical and Computer Engineering*: McGill University, 1998.

[76] D. H. Slatter, *Textbook of small animal surgery* vol. 2: Elsevier Health Sciences, 2003.

[77] M. I. Tiwana, S. J. Redmond, and N. H. Lovell, "A review of tactile sensing technologies with applications in biomedical engineering," *Sensors and Actuators A: Physical,* vol. 179, pp. 17-31, 2012.

[78] K. J. Rebello, K. S. Lebouitz, and M. Migliuolo, "MEMS Tactile Sensors for Surgical Instruments," San Francisco, CA, United States, 2003, pp. 55-60.

[79] K. J. Rebello, "Applications of MEMS in surgery," *Proceedings of the IEEE,* vol. 92, pp. 43-55, 2004.

[80] S. Richmond, "Minimizing the risk of infection in the operating department: a review for practice," 2009.

[81] W. A. Rutala and D. J. Weber, "Guideline for disinfection and sterilization of prion-contaminated medical instruments," *Infection control and hospital epidemiology,* vol. 31, pp. 107-117, 2010.

[82] J. Dargahi and S. Najarian, "An endoscopic force-position sensor grasper with minimum sensors," *Electrical and Computer Engineering, Canadian Journal of,* vol. 28, pp. 155-161, 2003.

[83] S. Misra, Okamura, Allison M., Ramesh, K. T., "Force Feedback is Noticeably Different for Linear versus Nonlinear Elastic Tissue Models," in *EuroHaptics Conference, 2007 and Symposium on Haptic Interfaces for Virtual Environment and Teleoperator Systems. World Haptics 2007. Second Joint*, 2007, pp. 519-524.

[84] A. Hamed, S. C. Tang, H. Ren, A. Squires, C. Payne, K. Masamune, G. Tang, J. Mohammadpour, and Z. T. H. Tse, "Advances in Haptics, Tactile Sensing, and Manipulation for Robot-Assisted Minimally Invasive Surgery, Noninvasive Surgery, and Diagnosis," *Journal of Robotics,* vol. 2012, p. 14, 2012.

[85] A. Mendez, "Fiber Bragg grating sensors: a market overview," in *Third European Workshop on Optical Fibre Sensors*, 2007, pp. 661905-661905-6.

[86] Y.-L. Park, S. Elayaperumal, B. Daniel, S. C. Ryu, M. Shin, J. Savall, R. J. Black, B. Moslehi, and M. R. Cutkosky, "Real-Time Estimation of 3-D Needle Shape and Deflection for MRI-Guided Interventions," *IEEE/ASME Trans. Mechatronics,* vol. 15, pp. 906-915, 2010.

[87] H. Su and G. S. Fischer, "A 3-axis optical force/torque sensor for prostate needle placement in magnetic resonance imaging environments," in *Technologies for Practical Robot Applications, 2009. TePRA 2009. IEEE International Conference on*, 2009, pp. 5-9.

[88] P. Yong-Lae, R. Seok Chang, R. J. Black, K. K. Chau, B. Moslehi, and M. R. Cutkosky, "Exoskeletal Force-Sensing End-Effectors With Embedded Optical Fiber-Bragg-Grating Sensors," *Robotics, IEEE Transactions on,* vol. 25, pp. 1319-1331, 2009.

[89] Y.-J. Rao, "In-fibre Bragg grating sensors," *Meas. Sci. and Tech.,* vol. 8, pp. 355-375, 1997.

[90] R. Maaskant, T. Alavie, G. Tadros, S. Rizkalla, and A. Guha-Thakurta, "Fiber-optic Bragg grating sensors for bridge monitoring," *Cement and Concrete Composites,* vol. 19, pp. 21-33, 1997.

[91] D. J. Callaghan, M. M. McGrath, G. Rajan, E. Coyle, Y. Semenova, and G. Farrell, "Analysis of strain transfer to FBG's for sensorized telerobotic end-effector applications," in *Advances in Robotics Research*: Springer, 2009, pp. 65-75.

[92] M. Majumder, T. K. Gangopadhyay, A. K. Chakraborty, K. Dasgupta, and D. K. Bhattacharya, "Fibre Bragg gratings in structural health monitoring - Present status and applications," *Sensors and Actuators A: Physical,* vol. 147, pp. 150-164, 2008.

[93] L. Z. Karam, A. P. G. Franco, P. Tomazinho, L. Signorini, L. Carvalho, M. H. Fernandes, M. B. Hecke, and H. J. Kalinowski, "Evaluation of the efficacy and influence of the decontamination and sterilization of FBGs exposed to S. aureus and E. coli," in *International Conference on Applications of Optics and Photonics*, 2011, pp. 800134-800134-6.

[94] L. Zen Karam, A. P. Franco, P. Tomazinho, and H. J. Kalinowski, "Validation of a Sterilization Methods in FBG Sensors for in vivo Experiments," in *Latin America Optics and Photonics Conference*, 2012.

[95] V. Mishra, N. Singh, U. Tiwari, and P. Kapur, "Fiber grating sensors in medicine: Current and emerging applications," *Sensors and Actuators A: Physical,* vol. 167, pp. 279-290, 2011.

[96] E. Udd, *Fiber optic smart structures*: Wiley New York, 1995.

[97] R. Monfaredi, R. Seifabadi, G. Fichtinger, and I. Iordachita, "Design of a decoupled MRI-compatible force sensor using fiber bragg grating sensors for robot-assisted prostate interventions," in *SPIE Medical Imaging*, 2013, pp. 867118-867118-9.

[98] K. O. Hill and G. Meltz, "Fiber Bragg grating technology fundamentals and overview," *J. Lightwave Tech.,* vol. 15, pp. 1263-1276, 1997.

[99] J. Kim, Y. Lee, Y. Park, and C. Kim, "Temperature-compensated strain measurement of full-scale small aircraft wing structure using low-cost FBG interrogator," in *SPIE Smart Structures and Materials+ Nondestructive Evaluation and Health Monitoring*, 2013, pp. 86922P-86922P-7.

[100] K. Kuang, S. Quek, C. Koh, W. Cantwell, and P. Scully, "Plastic optical fibre sensors for structural health monitoring: a review of recent progress," *Journal of sensors,* vol. 2009, 2009.

[101] Q. Wang, G. Farrell, T. Freir, G. Rajan, and P. Wang, "Low-cost wavelength measurement based on a macrobending single-mode fiber," *Opt. Lett.,* vol. 31, pp. 1785-1787, 2006.

[102] G. R. Sutherland, P. B. McBeth, and D. F. Louw, "NeuroArm: an MR compatible robot for microsurgery," *Int. Congress Series,* vol. 1256, pp. 504-508, 2003.

[103] M. S. Mueller, L. Hoffmann, T. Christopher Buck, and A. Walter Koch, "Fiber Bragg Grating-Based Force-Torque Sensor with Six Degrees of Freedom," *Int. J. Optomech.,* vol. 3, pp. 201 - 214, 2009.

[104] I. Iordachita, Z. Sun, M. Balicki, J. Kang, S. Phee, J. Handa, P. Gehlbach, and R. Taylor, "A sub-millimetric, 0.25 mN resolution fully integrated fiber-optic force-sensing tool for retinal microsurgery," *Int. J. Comp. Assist. Radiology and Surg.,* vol. 4, pp. 383-390, 2009.

[105] S. Hoseok, K. Heechul, J. Juwon, and L. Jungju, "Development of FBG sensor system for force-feedback in minimally invasive robotic surgery," in *Sensing Technology (ICST), 2011 Fifth International Conference on*, pp. 16-20.

[106] I. Kuru, B. Gonenc, M. Balicki, J. Handa, P. Gehlbach, R. H. Taylor, and I. Iordachita, "Force sensing micro-forceps for robot assisted retinal surgery," in *Engineering in Medicine and Biology Society (EMBC), 2012 Annual International Conference of the IEEE*, pp. 1401-1404.

[107] B. W. Darvell, P. K. D. Lee, T. D. B. Yuen, and P. W. Lucas, "A portable fracture toughness tester for biological materials," *Measurement Science and Technology,* vol. 7, p. 954, 1996.

[108] B. P. Pereira, P. W. Lucas, and T. Swee-Hin, "Ranking the fracture toughness of thin mammalian soft tissues using the scissors cutting test," *J. Biomechanics,* vol. 30, pp. 91-94, 1997.

[109] T. Atkins, "Science and Engineering of Cutting - The Mechanics and Processes of Separating, Scratching and Puncturing Biomaterials, Metals and Non-Metals," Butterworth-Heinemann, 2009.

[110] B. Darvell, P. Lee, T. Yuen, and P. Lucas, "A portable fracture toughness tester for biological materials," *Measurement Science and Technology,* vol. 7, p. 954, 1996.

[111] T. Chanthasopeephan, J. P. Desai, and A. C. W. Lau, "Modeling Soft-Tissue Deformation Prior to Cutting for Surgical Simulation: Finite Element Analysis and Study of Cutting Parameters," *Biomedical Engineering, IEEE Transactions on,* vol. 54, pp. 349-359, 2007.

[112] A. M. Okamura, R. J. Webster III, J. T. Nolin, K. W. Johnson, and H. Jafry, "The haptic scissors: cutting in virtual environments," in *Robotics and Automation, 2003. Proc. ICRA '03. IEEE Int. Conf. on*, Taipei, 2003, pp. 828-833.

[113] V. I. Lozinsky, L. G. Damshkaln, B. L. Shaskol'skii, T. A. Babushkina, I. N. Kurochkin, and I. I. Kurochkin, "Study of cryostructuring of polymer systems: 27. Physicochemical properties of poly(vinyl alcohol) cryogels and specific features of their macroporous morphology," *Colloid Journal,* vol. 69, pp. 747-764, 2007.

[114] C. L. Lester, S. M. Smith, C. D. Colson, and C. A. Guymon, "Physical properties of hydrogels synthesized from lyotropic liquid crystalline templates," *Chemistry of materials,* vol. 15, pp. 3376-3384, 2003.

[115] C. Hassan and N. Peppas, "Structure and applications of poly (vinyl alcohol) hydrogels produced by conventional crosslinking or by freezing/thawing methods," *Biopolymers· PVA Hydrogels, Anionic Polymerisation Nanocomposites,* pp. 37-65, 2000.

[116] N. Peppas, P. Bures, W. Leobandung, and H. Ichikawa, "Hydrogels in pharmaceutical formulations," *European journal of pharmaceutics and biopharmaceutics,* vol. 50, pp. 27-46, 2000.

[117] G. Reinholz, L. Lu, D. Saris, M. Yaszemski, and S. O'Driscoll, "Animal models for cartilage reconstruction," *Biomaterials,* vol. 25, pp. 1511-1521, 2004.

[118] A. Kharine, S. Manohar, R. Seeton, R. G. M. Kolkman, R. A. Bolt, W. Steenbergen, and F. F. M. de Mul, "Poly (vinyl alcohol) gels for use as tissue phantoms in photoacoustic mammography," *Physics in medicine and biology,* vol. 48, p. 357, 2003.

[119] K. Surry, H. Austin, A. Fenster, and T. Peters, "Poly (vinyl alcohol) cryogel phantoms for use in ultrasound and MR imaging," *Physics in medicine and biology,* vol. 49, p. 5529, 2004.

[120] C. T. McCarthy, M. Hussey, and M. D. Gilchrist, "On the sharpness of straight edge blades in cutting soft solids: Part I - indentation experiments," *Engineering Fracture Mechanics,* vol. 74, pp. 2205-2224, 2007.

[121] A. N. Gent, *Engineering with rubber: how to design rubber components*: Hanser Verlag, 2001.

[122] H. Maaß and U. Kühnapfel, "Noninvasive Measurement of Elastic Properties of Living Tissue," in *13th Int. Congress on Computer Assisted Radiology and Surgery (CARS '99)* Paris, 1999, pp. 865-870.

[123] J. A. Stammen, S. Williams, D. N. Ku, and R. E. Guldberg, "Mechanical properties of a novel PVA hydrogel in shear and unconfined compression," *Biomaterials,* vol. 22, pp. 799-806, 2001.

[124] K. C. Chu and B. K. Rutt, "Polyvinyl alcohol cryogel: An ideal phantom material for MR studies of arterial flow and elasticity," *Magnetic Resonance in Medicine,* vol. 37, pp. 314-319, 1997.

[125] O. A. Shergold and N. A. Fleck, "Experimental Investigation Into the Deep Penetration of Soft Solids by Sharp and Blunt Punches, With Application to the Piercing of Skin," *Journal of Biomechanical Engineering,* vol. 127, pp. 838-848, 2005.

[126] A. Atkins, X. Xu, and G. Jeronimidis, "Cutting, by 'pressing and slicing,'of thin floppy slices of materials illustrated by experiments on cheddar cheese and salami," *Journal of Materials Science,* vol. 39, pp. 2761-2766, 2004.

[127] D. J. Adams, K. M. Brosche, and J. L. Lewis, "Effect of Specimen Thickness on Fracture Toughness of Bovine Patellar Cartilage," *Journal of Biomechanical Engineering,* vol. 125, pp. 927-929, 2003.

[128] A. Atkins, "Toughness and cutting: a new way of simultaneously determining ductile fracture toughness and strength," *Engineering fracture mechanics,* vol. 72, pp. 849-860, 2005.

[129] C. F. Doran, B. A. O. McCormack, and A. Macey, "A Simplified Model to Determine the Contribution of Strain Energy in the Failure Process of Thin Biological Membranes during Cutting," *Strain,* vol. 40, pp. 173-179, 2004.

[130] M. Mahvash and V. Hayward, "Haptic Rendering of Cutting: A Fracture Mechanics Approach," *Haptics-e: The Electronic Journal of Haptics Research,* vol. 2, 2001.

[131] H. L. Cox, "The elasticity and strength of paper and other fibrous materials," *British Journal of Applied Physics,* vol. 3, pp. 72-79, 1952.

[132] K. T. Wan, C. K. Y. Leung, and N. G. Olson, "Investigation of the strain transfer for surface-attached optical fiber strain sensors," *Smart Materials and Structures,* vol. 17, p. 035037, 2008.

[133] G. Rajan, "A macro-bend fiber based wavelength demodulation system for optical fiber sensing applications," *Doctoral,* p. 60, 2008.

[134] W. Li, C. Cheng, and Y. Lo, "Investigation of strain transmission of surface-bonded FBGs used as strain sensors," *Sensors and Actuators A: Physical,* vol. 149, pp. 201-207, 2009.

[135] Y-L. Park, S. Elayaperumal, B.L. Daniel, E. Kaye, K.B. Pauly, R.J. Black, and M.R. Cutkosky, "MRI-compatible Haptics: Feasibility of using optical fiber Bragg grating strain-sensors to detect deflection of needles in an MRI environment," in *International Society for Magnetic Resonance in Medicine (ISMRM) 2008, 16th Scientific Meeting and Exhibition,* Toronto, Canada, 2008.

[136] F. Casagrande, P. Crespi, A. M. Grassi, A. Lulli, R. P. Kenny, and M. P. Whelan, "From the Reflected Spectrum to the Properties of a Fiber Bragg Grating: A

Genetic Algorithm Approach with Application to Distributed Strain Sensing," *Appl. Opt.,* vol. 41, pp. 5238-5244, 2002.

[137] A. S. Paterno, V. de Oliveira, T. S. Figueredo, and H. J. Kalinowski, "Multiplexed Fiber Bragg Grating Interrogation System Using a Modulated Fiber Bragg Grating and the Tunable-Filter Method," *Sensors Journal, IEEE,* vol. 6, pp. 1662-1668, 2006.

[138] Q. Wang, G. Rajan, G. Farrell, P. Wang, Y. Semenova, and T. Freir, "Macrobending fibre loss filter, ratiometric wavelength measurement and application," *Measurement Science and Technology,* vol. 18, p. 3082, 2007.

[139] Y. Zhu, P. Shum, C. Lu, M. Lacquet, P. Swart, A. Chtcherbakov, and S. Spammer, "Temperature insensitive measurements of static displacements using a fiber Bragg grating," *Opt. Express,* vol. 11, pp. 1918-1924, 2003.

[140] H. H. Mabie and C. B. Rogers, "Transverse vibrations of double-tapered cantilever beams with end support and with end mass," *The Journal of the Acoustical Society of America,* vol. 55, pp. 986-991, 1974.

[141] M. Le Blanc, S. Y. Huang, M. M. Ohn, and R. M. Measures, "Tunable chirping of a fibre Bragg grating using a tapered cantilever beam," *Electronics Letters,* vol. 30, pp. 2163-2165, 1994.

[142] P. L. Fuhr, S. J. Spammer, and Y. Zhu, "A novel signal demodulation technique for chirped Bragg grating strain sensors," *Smart Materials and Structures,* vol. 9, p. 85, 2000.

[143] A. G. Atkins, "On the mechanics of guillotining ductile metals," *Journal of Materials Processing Technology,* vol. 24, pp. 245-257, 1990.

[144] D. Callaghan, G. Rajan, M. McGrath, E. Coyle, Y. Semenova, and G. Farrell, "Investigation and experimental measurement of scissor blade cutting forces using fiber Bragg grating sensors," *Smart Materials and Structures,* vol. 20, p. 105004, 2011.

[145] S. Mathews, D. Callaghan, Y. Semenova, G. Rajan, and G. Farrell, "Photonic crystal fiber strain sensors for laparoscopic surgical devices," in *Proc. Photonics Global Conference 2012* Singapore, 2012.